DISS. ETH NO. 22914

Voltage Source Converter Based HVDC – Modelling and Coordinated Control to Enhance Power System Stability

A thesis submitted to attain the degree of

DOCTOR OF SCIENCES of ETH ZURICH

(Dr. sc. ETH Zurich)

presented by

MARKUS CHRISTIAN IMHOF

MSc ETH EEIT, ETH Zurich
born on 13.01.1983
citizen of
Bürglen UR and Zürich ZH, Switzerland

accepted on the recommendation of

Prof. Dr. Göran Andersson, examiner
Prof. Dr. Christian Rehtanz, co-examiner

2015

Dedicated to my parents Peter & Barbara.

Abstract

The power systems of today are large complex structures where electrical power is transported from large generators over AC transmission lines to loads in the distribution system. The classical top-down power flow is changing with the so called *Energiewende* as more decentralized and intermittent renewable energy sources are integrated at all system levels. As a result, power system operation faces new challenges to ensure system stability and reliability.

Voltage source converter-based HVDC (VSC-HVDC) may provide an attractive solution to add flexibility that can enhance the future power system performance. During normal operation, VSC-HVDC can add additional controllability to the AC system. Transmission system operators can optimize the VSC-HVDC set-points in order to optimize the AC power flow and avoid congestions. During a disturbance in the AC system, VSC-HVDC links are able to enhance power system stability by modulating their active and reactive power with the help of a grid controller.

This thesis investigates how the active and reactive power of VSC-HVDC links can be modulated in a coordinated way in order to enhance power system stability after a disturbance. First, appropriate VSC-HVDC models are developed for steady state analysis and dynamic studies. The steady state models are used for power flow and optimal power flow calculations. Two dynamic models are introduced. The detailed dynamic model is based on the dynamic power response of an ABB black-box benchmark model. It includes dynamic elements as well as a detailed converter control. It is further shown how the controller of the model may be tuned according to a benchmark model. The simplified dynamic model maintains the basic dynamic response of

the power with a reduced number of states. Both dynamic models can
be used for power stability studies.

Most operation schemes for VSC-HVDC links use a constant power ref-
erence at the converters. It is typically changed according to the mar-
ket by the system operator. Existing power system stability controllers
use local measurements for controlling the active and reactive power
of VSC-HVDC links and do not coordinate their control. This thesis
introduces model predictive control (MPC) based control schemes for
inter-area oscillation damping and voltage stability control. The advan-
tage of a MPC-based controller compared to a local rule based controller
is, that it is possible to predict the system response of the control ac-
tions of the VSC-HVDC links and coordinate the control actions of all
the VSC-HVDC links to enhance power system stability. It is shown
in small and large networks that the MPC-based inter-area oscillation
damping controller and the MPC-based voltage stability controller ben-
eficially modulate the active and reactive power of the VSC-HVDC links
to enhance power system stability.

Controlled islanding is the last resort of emergency control in order
to prevent a large disturbance to spread throughout the system and
causing a system-wide blackout. Power exchange between the islands
with AC transmission line is not possible. Hence, this thesis develops a
controlled islanding algorithm based on k-means clustering, considering
VSC-HVDC links in the system, in order to connect the islands with
DC connections. Thus, the exchange of power between the islands is
possible in order to minimize the generation-load imbalance. Therefore
load shedding and generator tripping can be prevented to reduce the
economic cost of a large disturbance.

In conclusion, VSC-HVDC links are able to enhance power system sta-
bility if they are controlled in a coordinated way. Simulation studies of
the European system have shown, that even with a small VSC-HVDC
transmission capacity compared to the entire network, VSC-HVDC links
can significantly improve power system stability.

Kurzfassung

Heutige elektrische Energiesysteme sind grosse komplexe Strukturen, in welchen elektrische Energie von grossen Generatoren zu den Lasten im Verteilnetz mittels Wechselstrom (AC) Übertragungsleitungen transportiert wird. Der klassische unidirektionale Leistungsfluss von den Generatoren zu den Lasten ändert sich mit der *Energiewende* zu einem bidirektionalen Fluss, da vermehrt dezentrale und intermittierende neue erneuerbaren Energiequellen in allen Spannungsebenen installiert werden. Demzufolge begegnen Übertragungsnetzbetreiber neuen Herausforderungen, um die Systemstabilität und Zuverlässigkeit zu gewährleisten.

Spannungsgeführte Hochspannungsgleichstromübertragung (HGÜ) kann eine attraktive Lösung sein, um die Flexibilität im elektrischen Übertragungsnetz zu erhöhen und die Systemstabilität zu steigern. Im Normalbetrieb kann eine HGÜ Verbindung zusätzliche Steuerbarkeit bieten, indem der Übertragungsnetzbetreiber die Sollwerte so einstellt, dass der AC–Leistungsfluss optimiert wird und Netzengpässe vermieden werden. Während einer Störung im System können HGÜ Verbindungen die Netzstabilität verbessern, indem sie die Wirk- und Blindleistung dynamisch regulieren. Dies kann entweder lokal oder durch einen übergeordneten Netzregler geschehen.

Diese Doktorarbeit untersucht wie die Wirk- und Blindleistung von HGÜ Verbindungen koordiniert moduliert werden sollen, um die Netzstabilität nach einer Störung zu verbessern. Es wurden geeignete HGÜ Modelle für stationäre Analysen und dynamische Studien entwickelt. Die stationären Modelle werden vorwiegend für Lastfluss und optimale Lastflussberechnungen genutzt. Die dynamischen Modelle werde vorwiegend für Netzstabilitätsstudien verwendet. Ein detailliertes dynamische Modell basiert auf der Antwort eines ABB Blackbox–Bezugsmodells.

Es beinhaltet dynamische Elemente sowie eine detaillierte Umrichterre-
gelung. Es wird weiter gezeigt, wie der Umrichterregler gemäss dem
Bezugsmodell eingestellt werden kann. Ein vereinfachtes dynamische
Modell bildet die wichtigsten dynamischen Eigenschaften der Wirk- und
Blindleistungsantwort nach einer Änderung ab, während die Anzahl dy-
namischen Zustände reduziert wurden.

Die meisten Betriebspläne für HGÜ–Verbindungen sehen eine konstan-
te Leistungsreferenz an den Umrichtern vor. Typischerweise werden sie
vom Netzbetreiber nach den Vorgaben des Markts verändert. Es gibt
hingegen schon Stabilitätsregler für das Energienetz welche die Wirk-
und Blindleistung der HGÜ gemäss lokalen Messwerten, das heisst ohne
koordinierte Regelung, verändern. Diese Doktorarbeit präsentiert mo-
dellprädiktive Regelsysteme (MPC) welche die Wirk- und Blindleistung
von HGÜ Verbindungen modulieren um Netzpendelungen zu dämpfen
und die Spannungsstabilität verbessern. Der Vorteil von MPC-basierten
Reglern gegenüber regelbasierten Reglern ist, dass sie das Systemver-
halten inklusiv das Verhalten der HGÜs vorhersagen können, sowie
die HGÜs aufeinander abgestimmt geregelt werden können. In klei-
nen und grossen Netzen wird gezeigt, dass der MPC–basierte Netz-
pendelungsdämpfungsregler sowie der MPC–basierter Spannungsstabi-
litätsregler die Wirk- und Blindleistung vorteilhaft modulieren um die
Netzstabilität zu erhöhen.

Kontrollierter Inselbetrieb von elektrischen Energiesystemen ist das
letzte Mittel der Notfallsteuerung um zu verhindern, dass sich eine
grosse Störung im gesamten Netz verbreitet und letztendlich zu einem
Stromausfall des gesamten Systems führt. Der Austausch von Leistung
zwischen zwei Netzinseln über AC–Leitungen ist jedoch nicht möglich.
Diese Doktorarbeit stellt eine Methode basierend auf k-means Cluste-
ring vor, welche beim Bilden des kontrollierten Inselbetriebes die ver-
schiedenen Netzinseln mit HGÜs verbindet. Somit ist es möglich elektri-
sche Energie zwischen den Netzinseln auszutauschen um das Ungleich-
gewicht zwischen Erzeugung und Verbrauch zu verringern. Somit kann
der Lastabwurf und die Genratorenabschaltung verringert werden.

Abschliessend kann gesagt werden, dass HGÜ–Verbindungen in der La-
ge sind die Netzstabilität zu erhöhen, falls die Wirk- und Blindleistung
aufeinander abgestimmt geregelt werden. Simulationsstudien mit dem
europäischen System haben gezeigt, dass die Netzstabilität sogar mit
relative geringer HGÜ–Übertragungskapazität, verglichen zur Gesamt-
kapazität vom Netz, bedeutend erhöht werden kann.

Preface

This thesis was written during my time as a researcher and assistant at the Power Systems Laboratory of the ETH Zurich between 2009 and 2015.

I would like to thank Prof. Dr. Göran Andersson for providing the opportunity to be a member of the PSL and complete my doctoral studies under his guidance. His time for questions and suggestions was highly appreciated. My special thanks goes also to Prof. Dr. Christian Rehtanz for being co-examiner for my thesis. The comments he had were very generous, and provided great input. Further I am very grateful about the possibility to spend time for research under the supervision of Prof. Dr. Ian Hiskens at the University of Michigan.

I also want to thank my project partners Dr. Mats Larsson from ABB, Dr. Walter Sattinger from swissgrid, Dr. Martin Kauert from swisselectric research and Dr. Sandro Dinser from axpo for the fruitful discussions and their inputs from the perspective of the industry.

Further I want to thank Alexander Fuchs from the automatic control laboratory of the ETH Zurich, the fellow PhD on this project, for the close collaboration and the nice working environment we had together. I also want to thank Dr. Turhan Demiray for all the support and input he gave me on the dynamic simulation tool.

I also would like to thank all members of the PSL for their inputs, their friendship and the very nice working environment they created. A special thank goes to my office mates of the ETL G22 "The HVDC competence center" for the great time together.

Finally, I would like to thank my family for all the support during these years.

Contents

List of Symbols

Notation

Scalar physical quantities (e.g. R, L, C) or numerical variables (e.g. x, y, z) are italic.

Complex quantities or variables are underlined (e.g. $\underline{U}$, $\underline{I}$, $\underline{S}$).

Matrices and vectors are boldface (e.g. $\mathbf{A}$, $\mathbf{B}$, $\mathbf{x}$, $\mathbf{y}$).

Unit symbols are written using roman type (e.g. Hz, MW, kV).

Standard mathematical functions are written using roman type (e.g. sin, cos).

Subscripts relating to objects are written using roman type (e.g. $\underline{I}_{\mathrm{line}}$, $\underline{I}_{\mathrm{trafo}}$, U_{dc}).

Subscripts relating to physical quantities or numerical variables are written using italic type (e.g. a_{ij}, $\underline{U}_i$).

Superscripts d, q refer to the direct- and quadrature-axis components.

Superscripts a, b, c refer to the three AC phase components.

Lower case symbols normally denote instantaneous values (e.g. u, i).

Upper case symbols normally denote root mean square (RMS) or peak values (e.g. U, I).

Acronyms

AC	alternating current
ALEGrO	Aachen Liège Electric Grid Overlay
AVR	automatic voltage regulator
COI	center of inertia
CSC	current source converter
CSC-HVDC	current source converter-based HVDC
DC	direct current
DFIG	doubly-fed induction generator
EMT	electromagnetic transient
ENTSO-E	European Network of Transmission System Operators for Electricity
FACTS	flexible AC transmission systems
GOV	governor
HVDC	high voltage DC
IGBT	insulated gate bipolar transistor
IGCT	integrated gate-commutated thyristor
inelfe	France-Spain Electrical Interconnection
IPFC	intertie power flow controller
MPC	model predictive control
MMC	modular multilevel converter
OPF	optimal power flow
OBDD	ordered binary decision diagram
OH	overhead
PD	proportional differential

PI	proportional integral
PF	power flow
PSS	power system stabilizer
p.u.	per-unit
PV	photovoltaics
PWM	pulsewidth modulation
RES	renewable energy sources
SM	submodule
SSSC	static synchronous series compensator
STATCOM	static synchronous compensator
TSO	transmission system operator
UFLS	under-frequency load shedding
UPFC	unified power flow controller
VSC	voltage source converter
VSC-HVDC	voltage source converter-based HVDC
WAMS	wide-area measurement system

Symbols

Scalars

Symbol	Unit	Description
α		Line weight for the VSC-HVDC grouping
α_i		Scaling factor of the zeros of a transfer function
β		Line weight for the slow coherency grouping
β_i		Scaling factor of the poles of a transfer function
γ		Line weight for the rotor angle deviation grouping
ζ		Damping ratio of a second-order transfer function
η		Line weight for the rotor angle deviation grouping
θ	rad	Frequency angle
ϑ		Line weight for the generation-load power balance grouping
κ		Line weight for the VSC-HVDC injection-bus power imbalance grouping
λ		Eigenvalue
σ		Mode of the eigenvalue analysis
σ_{j}		Deviation of the objective function
σ_{ω}	p.u., Hz	Frequency deviation from the average system frequency
σ_{u}	p.u., kV	Voltage deviation from the desired VSC-HVDC AC terminal voltage set-point
τ	s	Rise time of a first order transfer function
φ_i	rad	AC voltage angle
ψ_{ij}		Shortest path between node i and node j

Symbol	Unit	Description
ω_{n}	p.u., 1/s	Undamped natural frequency of a second-order transfer function
ω_{s}	p.u., 1/s	Angular frequency of the system
$\overline{\omega}$	p.u., 1/s	Average angular frequency of the system
b_i	p.u.	Imaginary part of the series admittance Y_i
C_{cable}	p.u.	DC cable capacitance
$C_{\mathrm{converter}}$	p.u.	DC converter capacitance of the VSC
C_{dc}	p.u.	Total DC capacitance of the VSC-HVDC link
E_i	p.u., kV	Internal generator voltage behind transient reactance
f_{s}	p.u., Hz	Standard system frequency
g_i	p.u.	Real part of the series admittance Y_i
H	s	Inertia constant of the entire power system
H_i	s	Inertia constant of a synchronous generator
$\underline{i}_1$	p.u.	dq-current at the rectifier of the VSC-HVDC link
$\underline{i}_2$	p.u.	dq-current at the inverter of the VSC-HVDC link
$\underline{I}$	p.u.	AC current flowing into the HVDC link
I_{cable}	p.u.	DC current in the DC cable or overhead line of the HVDC link
$I_{\mathrm{dc},1}$	p.u.	DC current at the rectifier
$I_{\mathrm{dc},2}$	p.u.	DC current at the inverter
I_{dc}	p.u.	Total DC current in the DC cable or overhead line of the HVDC link
j		Imaginary unit that satisfy the equation $j^2 = -1$
K_0		Modulation constant of the rectangular pulsewidth modulation
K_{D}	p.u.	Derivative gain of a PD-controller

Symbol	Unit	Description
K_p	p.u.	Proportional gain of a PI-controller
K_i	p.u.	Integral gain of a PI-controller
L_dc	p.u.	Inductance of the DC cable of the VSC-HVDC link
L_r	p.u.	Inductance of the phase reactor of the VSC-HVDC link
L_t	p.u.	Inductance of the step-down transformer of the VSC-HVDC link
m		Modulation signal
m_i	s^2	Normalized inertia constant with system frequency
$\underline{m}_i$		dq-part of the modulation signal
M_p		Maximum overshoot of the step-response of a second-order function
n_gen		Number of generators in the power system
n_hvdc		Number of VSC-HVDC links in the power system
n_line		Number of AC lines in the power system
n_node		Number of AC busses in the power system
n_sys		Total nodes in the system including internal AC nodes of the VSC-HVDC links
N		Prediction horizon
N_isl		Number of islands
ΔP_1	p.u., MW	Change of Active power of the VSC-HVDC link at the rectifier side of the system
P_1	p.u., MW	Active power absorption of the VSC-HVDC link at the rectifier side of the system
$P_{1,\mathrm{ref}}$	p.u., MW	Active power reference of the VSC-HVDC link at the rectifier side of the system
$P_{1,\mathrm{ref}}^\mathrm{post}$	p.u., MW	Active power reference of the VSC-HVDC link at the rectifier side after the set-point change

Symbol	Unit	Description
P_2	p.u., MW	Active power absorption of the VSC-HVDC link at the inverter side of the system
P_{ac}	p.u., MW	AC active power
P_{dc}	p.u., MW	DC active power
P_{gen}	p.u., MW	Active power output of a generator
P_{vsc}	p.u., MW	Active power at the AC side of the VSC
Q_1	p.u., Mvar	Reactive power absorption of the VSC-HVDC link at the rectifier side of the system
$Q_{1,ref}$	p.u., Mvar	Reactive power reference of the VSC-HVDC link at the rectifier side of the system
Q_2	p.u., Mvar	Reactive power absorption of the VSC-HVDC link at the inverter side of the system
$Q_{2,ref}$	p.u., Mvar	Reactive power reference of the VSC-HVDC link at the inverter side of the system
Q_{vsc}	p.u., Mvar	Reactive power at the AC side of the VSC
R_r	p.u.	Resistance of the phase reactor of the VSC-HVDC link
R_{dc}	p.u.	DC resistance of the HVDC cable or overhead line
s		Complex frequency of the Laplace transformation
S_B	MW	Base power
t	s	Time
t_p	s	Peak time of the step-response of a second-order function
T_{mpc}	s	Samping intervall of the MPC-based controller
T_s	s	Period of the modulation signal

Symbol	Unit	Description
$\underline{u}_i$	p.u., kV	dq-internal voltage at the inner current controller
$\underline{u}_\mathrm{c}$	p.u., kV	dq-voltage at the AC VSC terminal bus of the VSC-HVDC link
$\underline{u}_\mathrm{r}$	p.u., kV	dq-voltage over the phase reactor of the VSC-HVDC link
$\underline{u}_\mathrm{s}$	p.u., kV	dq-voltage at the AC system terminal bus of the VSC-HVDC link
$\underline{u}_\mathrm{t}$	p.u., kV	dq-voltage at the AC step-down terminal bus of the VSC-HVDC link
$U_{\mathrm{c},i}$	p.u., kV	AC voltage amplitude at the VSC terminal bus of the VSC-HVDC link model
$U_{\mathrm{dc},2,\mathrm{ref}}$	p.u., kV	DC voltage amplitude reference at the VSC inverter side bus of the VSC-HVDC link
$U_{\mathrm{dc},i}$	p.u., kV	DC voltage amplitude at the VSC terminal bus of the VSC-HVDC link model
$U_{\mathrm{s},i}$	p.u., kV	AC voltage amplitude at the AC system terminal bus of the VSC-HVDC link model
w		Weight of an undirected graph
X_r	p.u.	Impedance of the phase reactor of the VSC-HVDC link
X_trafo	p.u.	Impedance of the step-down transformer of the VSC-HVDC link
X_d'	p.u.	Transient reactance of a synchronous machine
Y_i	p.u.	Series admittance
$\underline{Z}_\mathrm{ac}$	p.u.	Combined impedance of step-down transformer impedance and phase reactor impedance of the VSC-HVDC link
$\underline{Z}_\mathrm{r}$	p.u.	Phase reactor impedance of the VSC-HVDC link
$\underline{Z}_\mathrm{trafo}$	p.u.	Step-down transformer impedance of the VSC-HVDC link

Vectors and Matrices

Symbol	Unit	Description
φ	rad	AC voltage angles
$\mathbf{A}$		Linear system matrix
$\hat{\mathbf{A}}$		Discretized system matrix
$\mathbf{A}_{\mathrm{adj}}$		Adjacency matrix
$\mathbf{B}$		Linear input system matrix
$\hat{\mathbf{B}}$		Discretized input system matrix
$\mathbf{C}$		Linear output of the state variables
$\hat{\mathbf{C}}$		Discretized output of the state variables
$\mathbf{D}$		Linear output of the input variables
$\hat{\mathbf{D}}$		Discretized output of the input variables
$\mathbf{D}_{\mathrm{dist}}$		Distance matrix which defines the shortest distance to each node of a graph
$\mathbf{e}_{\mathrm{A}}$	p.u.	Voltages at the generators behind the transient reactance
$\mathbf{f}_0$		Initial derivative of linearization
$\mathbf{G}$		Permuted grouping matrix
$\mathbf{G}_{\mathrm{gen}}$		Grouping matrix where all generators are assigned to a coherent group
$\mathbf{h}$		Normalized inertia vector of the entire power system
$\mathbf{i}_{\mathrm{A}}$	p.u.	Current injections of the generators
$\mathbf{J}$		Parks' derivative transformation matrix
$\mathbf{l}_{\mathrm{bus}}$		Load busses
$\mathbf{L}$		Lower triangular matrix of the Gaussian elimination with complete pivoting
$\mathbf{M}$		Normalized inertia matrix of the entire power system
$\mathbf{M}_{\mathrm{h}}$	s^2	Inertia matrix of the entire power system
$\mathbf{p}_{\mathrm{cumulative}}$	p.u., MW	Cumulative active power consumption of the loads

Symbol	Unit	Description
$\mathbf{p}_{\text{gen}}$	p.u., MW	Active power output of the generators
$\mathbf{p}_{\text{loads}}$	p.u., MW	Active power consumptions of the loads
$\mathbf{p}_{\text{vsc}}$	p.u., MW	Active power injection of the VSC
$\mathbf{P}$		Row permutations of the Gaussian elimination with complete pivoting
$\mathbf{q}_{\text{gen}}$	p.u., Mvar	Reactive power output of the generators
$\mathbf{p}_{\text{vsc}}$	p.u., MW	Reactive power injection of the VSC
$\mathbf{Q}$		Column permutations of the Gaussian elimination with complete pivoting
$\mathbf{T}_{\text{abc}}$		Park's inverse transformation matrix
$\mathbf{T}_{\text{dq0}}$		Park's transformation matrix
$\mathbf{u}$	p.u.	Input of the power system
$\hat{\mathbf{u}}$	p.u.	Linearized input of the power system
$\mathbf{u}_0$	p.u.	Steady state of the input of the power system
$\mathbf{u}_{\text{ac}}$	p.u., kV	AC bus voltage amplitude
$\mathbf{u}_{\text{dc},1}$	p.u., kV	DC voltage amplitude at the rectifier
$\mathbf{U}$		Upper triangular matrix of the Gaussian elimination with complete pivoting
$\mathbf{V}$		Eigenbasis matrix
$\mathbf{x}$		Dynamic states of the power system
$\hat{\mathbf{x}}$		Linearized dynamic states of the power system
$\mathbf{x}_0$		Steady state of the dynamic states of the power system
$\mathbf{y}$		System outputs of the dynamic power system model
$\hat{\mathbf{y}}$		Linearized system outputs of the dynamic power system model
$\mathbf{y}_0$		Steady state of system outputs of the dynamic power system model
$\mathbf{Y}_{\text{int}}$	p.u.	Internal admittance matrix

Sets

Symbol	Description
$\mathcal{E}$	Edges
$\mathcal{G}$	Undirected graph
$\mathcal{P}$	Shortest path in a graph
$\mathcal{V}$	Vertices
$\mathcal{W}$	Weights
$\mathbb{N}$	Natural numbers
$\mathbb{R}$	Rational numbers

Functions

Symbol	Description
$f\left(\mathbf{x}\right)$	Objective function of optimization formulation
$f\left(\mathbf{x}(t), \mathbf{u}(t)\right)$	Differential and algebraic equations of the power system
$g\left(\mathbf{x}\right)$	Equality constraints
$g\left(\mathbf{x}(t), \mathbf{u}(t)\right)$	Function of the output values of the power system
$G_{\mathrm{id},i}(s)$	Transfer function of the d-current controller
$G_{\mathrm{iq},i}(s)$	Transfer function of the q-current controller
$G_{\mathrm{P},1}(s)$	Transfer function of the linear plant model for the active power
$G_{\mathrm{Udc}}(s)$	Transfer function of the DC voltage
$h\left(\mathbf{x}\right)$	Inequality constraints
$H_{\mathrm{Udc}}(s)$	Closed loop transfer function of the DC plant and the PI controller
$H_{\mathrm{id},i}(s)$	Closed loop transfer function of the inner control loop for the d-axis
$H_{\mathrm{iq},i}(s)$	Closed loop transfer function of the inner control loop for the q-axis
$H_{\mathrm{P},i}(s)$	Closed loop transfer function including plant and PI-controller

Symbol	Description
$H_{\mathrm{PT1}}(s)$	First-order transfer function
$H_{\mathrm{PT2}}(s)$	Second-order transfer function
$H_{\mathrm{Q},i}(s)$	Closed loop transfer function including plant and PI-controller
$J(t)$	Total objective function of the MPC controller
$J_{\omega}(t)$	Cost function for the damping of the MPC controller
$J_{\mathrm{u}}(t)$	Cost function for the voltage controller of the MPC controller
$J_{\delta}(t)$	Cost function for the slack variables of the MPC controller
$K_{\mathrm{dc}}(s)$	Linear transfer function of the DC voltage controller
$K_{\mathrm{id},i}(s)$	Linear transfer function of the d-current controller
$K_{\mathrm{iq},i}(s)$	Linear transfer function of the q-current controller
$l_{\mathrm{Udc}}(s)$	Open loop transfer function of the DC plant and the PI controller
$l_{\mathrm{id},i}(s)$	Open loop transfer function of the inner control loop for the d-axis
$l_{\mathrm{iq},i}(s)$	Open loop transfer function of the inner control loop for the q-axis
$l_{\mathrm{P},i}(s)$	Open loop transfer function including plant and PI-controller for the active power
$l_{\mathrm{Q},i}(s)$	Open loop transfer function including plant and PI-controller for the reactive power

List of Figures

List of Tables

Chapter 1

Introduction

This chapter gives a brief background about high voltage DC and power systems dynamics and motivates why voltage source converter-based HVDC is a good solution for power system stability control. The main contributions of this thesis are stated and a list of publications is given.

1.1   Background and Motivation

The electric power system is one of the biggest engineering achievements of the 20th century. The conversion of primary energy to electrical energy allowed us to build our modern industry and society. Electrical power is indispensable for our daily life. It is used for telecommunication, heating, transportation, medical care, water supply, and is essential for our economy. We depend on a reliable supply of electrical power and a secure operation of the power system for the stability of our society.

The first power system was built by Thomas Edison in New York and began its operation in 1882. It was a DC system. However, the lack of technology to transform the DC voltage to higher voltages prevented the DC system to transport power over long distances. With the development of a polyphase AC system by Nikola Tesla and the development of the transformer, the AC system became more attractive for transporting power over long distances [1]. This so called "War of the Currents" was won by Tesla in the mid 1890's and thus the power system was built in AC. For the first 60 years of power transmission, DC did not play any

significant role until in the early 1950's mercury valves were developed, which allowed high voltage DC (HVDC) transmission system become economical in certain situations [2, 3]. However, it took another 20 years for the first HVDC rectifier based on semiconductor switches to go into operation. In the spring of 1970 the first thyristor based HVDC transmission link went into operation connecting the island of Gotland with the mainland of Sweden [4]. This HVDC converter technology is called current source converter-based HVDC (CSC-HVDC). With the vast development of the semiconductor technology, the voltage level as well as the power rating increased. A big milestone was in the mid 80's when the 6 300 MW HVDC link from the Itaipu power plant to Sao Paolo was put into operation. It showed that the CSC-HVDC link is a reliable technology. With the further development of other semiconductor elements such as insulated gate bipolar transistors (IGBTs), ABB energized in 1996 the first voltage source converter-based HVDC (VSC-HVDC) link on the island of Gotland and started a new era for HVDC transmission. This technology seems very suitable to connect renewable energy sources and approach upcoming transmission challenges, therefore a lot of research has been committed.

The HVDC technologies can be classified into two categories based on their terminal voltage and current waveforms at their DC side, the current source converter (CSC) and the voltage source converter (VSC). The CSC keeps the DC current at the same polarity and therefore the direction of the power flow through the converter is determined by the polarity of the DC voltage. These converters are built with semi-controllable switches such as thyristors. Thyristors can only control the instant (firing angle) at which the current starts to conduct by a gate signal. However the current interruption is only determined by the zero-crossing of the AC voltage. The DC side of a CSC is typically connected in series of large smoothing reactors that maintain the current continuity [5, 6]. The CSC generates voltage and current harmonics on the AC side. Large AC filters are needed to remove those types of harmonics. Today power ratings up to 10 000 MW with a DC voltage of ±1 100 kV and a transmission distance of more than 3 000 km are possible [7]. On the contrary, the VSC keeps the DC voltage at the same polarity and the direction of the power flow is determined by the polarity of the DC current. These converters are built with fully controllable switches such as IGBTs. These switches are able to conduct and interrupt the current at any instant by a gating command. The DC side of a VSC is typically connected in parallel with a relatively large capacitor that resembles a
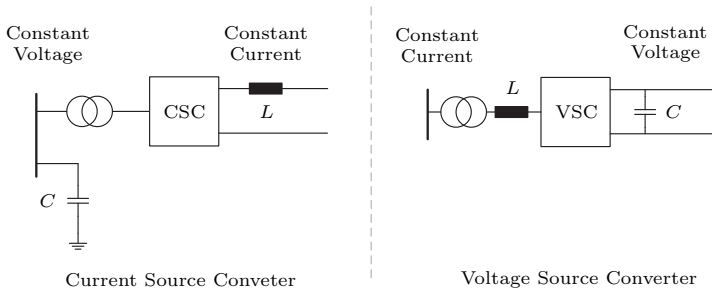
Figure 1.1: Comparison of the CSC and VSC structure [11].

voltage source [5]. In more recent converter designs, so called modular multilevel converter (MMC), the DC side capacitor is split into levels to reduce the AC harmonics [8, 9]. The VSC generates much less voltage and current harmonics on the AC side. Hence, only small filters are needed or with more recent converter design they could even be omitted. Because of this, the size of the converter stations are reduced dramatically. This opens up a new area to the HVDC technology like offshore converters or converter stations in urban areas. Nowadays VSC-HVDC links of up to 2 600 MW with a DC voltage of up to ±525 kV and a transmission distance of more than 1 500 km are possible [10]. In Figure 1.1 a comparison of the different structure of a CSC and a VSC is shown. Table 1.1 gives a brief comparison of the two technologies. The main difference between CSCs and VSCs is that the VSCs are able to control the active and reactive power injections independent from each other as well as from the system state. This property makes VSC-HVDC links attractive for real-time power system control. They are also able to reverse power quicker than CSC-HVDC links, because they do not need to change the voltage polarity of the DC cable and thereby to discharge and charge the DC capacitor [12, 11]. Another advantage of VSCs is that they can be connected to weak AC networks. Theoretically, they are able to connect to an AC bus with a short-circuit ratio of 0, whereas CSCs need at least a short-circuit ratio of around 2 [13]. Voltage source converters are very important during a grid restoration. Since they do not need any short-circuit capacity in order to connect to the grid, they can start immediately and provide voltage support [14]. Current source converters on the other hand can only start with sufficient short-circuit

Table 1.1: Comparison of CSC and VSC technology.

Characteristic	CSC	VSC
Commutation process	line-commutated	forced-commutated
Switch type	semi-controllable	fully controllable
Semiconductor	thyristor	IGBT
Minimum short-circuit ratio	> 2	0
Power control	active only	active and reactive independently
Station losses	lower	higher
Harmonics	large AC and DC filters	small AC and DC filters
Switching losses	lower	higher
Controllability	slower	fast
Station size	large (200%)	small (100%)
Black start capability	no	yes

capacity.

Both converter technologies are nowadays used in power systems for different applications. One application is compensation: A power-electronic compensator can be used to increase the power-transfer capacity of the line, to maximize the efficiency of the power transfer, to enhance voltage and angle stability, to improve power quality, or to fulfill a combination of the foregoing objectives [5]. This compensation techniques are known under the general term of flexible AC transmission systems (FACTS). The FACTS controllers include the static synchronous compensator (STATCOM), the static synchronous series compensator (SSSC), the intertie power flow controller (IPFC), the unified power flow controller (UPFC), and the semiconductor-controlled phase shifter [15]. However, the main application is to exchange power between two converters in a controlled manner with HVDC lines. A HVDC converter controls not only the power on the DC line, but is also capable to ensure that certain requirements, for example the frequency, voltage magnitude or power factor, are met. High voltage DC transmission systems are used with different lengths and power rating in various application.
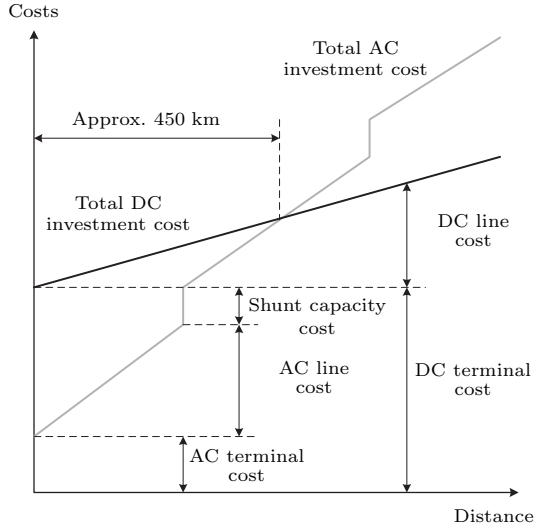
Figure 1.2: Transmission distance and total investment costs for AC over-
head lines (gray line) and DC overhead lines(black line) power
transmission lines. Own illustration based on [6].

Two HVDC converter connected without any line or cable are called
back-to-back HVDC systems. They are able to transfer power between
two asynchronous AC systems or even between systems with different
frequencies. Point-to-point HVDC systems connect two distant points
in either synchronous or asynchronous AC systems. The two convert-
ers are connected with either overhead lines or cables. These types of
HVDC systems are used for very high power and ultra-long distance
transmission, for long under-sea cable transmission, for flexible power
transmission or to transfer power from a variable-frequency wind-power
park to the power system [16, 17, 18, 19].

The reasons to choose DC over AC transmission are diverse. The overall
costs of the HVDC transmission system for the transmission of bulk
power over long distances is lower and the losses are lower than for the
AC transmission. A major advantage of the DC link is that there is
no stability limit related to the amount of power or the transmission
distance. Figure 1.2 shows the transmission distance and investment

costs for AC and DC overhead transmission lines [6]. The gray line depicts the costs for an AC line and the black line the costs for a DC line. It shows that the initial DC costs are much bigger than the AC terminal costs. This is due to the higher valve costs of the HVDC converter. In addition, the DC line costs per km are lower compared to the AC line cots. In case of the AC transmission, additionally shunt capacitors must be installed every 100 km to 200 km. Thus, for the same amount of power, AC overhead-line transmission is favorable for distances less then about 450 km and high voltage DC overhead-line transmission is favorable if the distance exceeds 450 km [6]. For the transmission of power with cables the break-even distance is much shorter. Generally AC cables are economical feasible up to a distance of about 50 km.

Another major advantage of HVDC systems is the controllability of the power flow. In AC systems the power over a line depends on the angle difference at the sending and receiving end of the line. This angle difference cannot be influenced and therefore the power flow is given by the operating point of the system. In HVDC systems the flow of active power over the HVDC link is controlled and therefore independent of the operating point of the system. It is also possible to control the reactive power injection or absorption of the HVDC terminal. Due to the ability to control the reactive power, the HVDC link can also be used for voltage control. Another advantage of HVDC systems is the environmental benefit. The visual impact for a DC line is lower, because the towers are smaller compared to the towers of an AC line with the same power rating. Figure 1.3 shows the right-of-way widths to transmit 6 000 MW for AC and DC systems. For a 765 kV AC system three single-circuit lines are needed which use about 240 m of land. A 500 kV AC systems needs even seven power lines to transmit the same amount of power. On the other hand, a HVDC system with ±500 kV needs only about 110 m. This is not even half the right-of-way of the AC system. A HVDC system with ±800 kV only needs 80 m which is three times less then the corresponding AC system [20]. A HVDC system not only uses less land, but also much less copper because fewer conductors are needed. The process of getting a transmission corridor approved is getting longer and longer, due to political and legal reasons. Therefore HVDC is a very promising solution since the smaller right-of-way or cable solution can help to shorten the approval process.

There are as well some disadvantages of HVDC transmission systems. High voltage DC systems are still not economical feasible for short distances. The converter control with its valves is quite complex with pos-
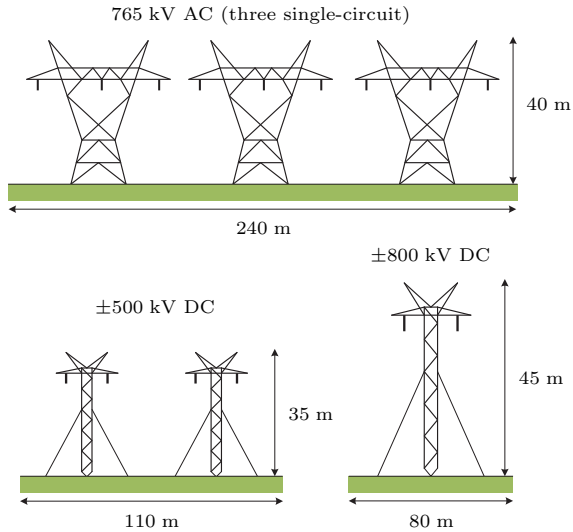
Figure 1.3: Comparison of 6 000 MW right-of-way widths for different technologies of overhead lines.

sible risk for misoperations. However, one of the biggest challenges is to find a DC circuit breaker [21]. A DC circuit breaker would be needed to build meshed DC grids like the North Sea HVDC Grid [22], or the idea of the global grid [23]. This gives the possibility to better integrate the renewable energy sources (RES) such as wind or photovoltaics (PV).

The operation of an electric power system is not a static process, rather a dynamic one. The dynamic phenomena can be classified into different time frames [24]. Figure 1.4 depicts the classification of power system dynamics. The time range of the power system transients varies between a few microseconds (wave phenomena) up to hours (thermodynamic phenomena). Caused by lightning and switching overvoltages, the fast wave phenomena occurs exclusively in the network and do not propagate beyond the transformer windings. The electromagnetic phenomena or electromagnetic transients (EMTs), which may be caused by power electronic equipment, equipment failure or faults, propagate usually confined in the electrical equipment such as transmission lines, transformers and protective devices. For an accurate simulation of EMTs these de-
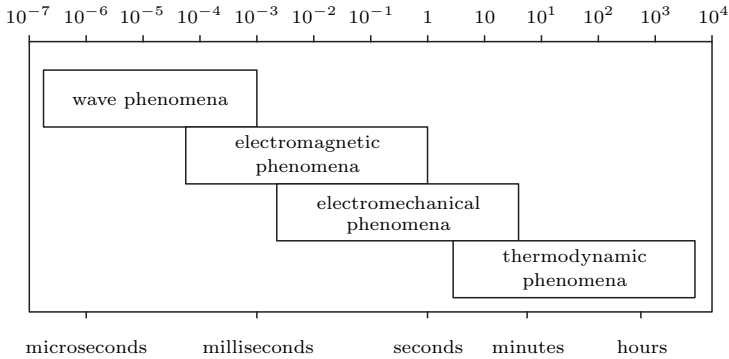
Figure 1.4: Time frame of basic power system phenomena, own illustration based on [24].

vices have to be modelled in great detail. The slower electromechanical transients are mainly caused due to the interaction between the mechanical energy stored in the rotating machines and the electrical energy stored in the electrical system. A mismatch between the mechanical energy and the electrical energy involves the oscillation of machine rotors due to an unbalance between the generator and turbine torque. An important role play the generator control systems such as the automatic voltage regulator (AVR), the power system stabilizer (PSS), and the turbine governor (GOV) systems. The long term thermodynamic transients involve phenomena such as boiler thermal dynamics of a power plant or thermal line ratings.

Power system stability may be defined as "the property of a power system that enables it to remain in a state of operating equilibrium under normal operation conditions and to regain an acceptable state of equilibrium after being subjected to a disturbance" [1]. In the evaluation of stability the interest is the performance of the power system when subjected to a disturbance. The disturbance may be small or large. Small disturbances occur continually in the form of load changes. The system must operate adequately under these conditions. It must also be able to survive numerous large disturbances. The most prominent ones are short-circuit on a transmission line, loss of a large generator or load, or
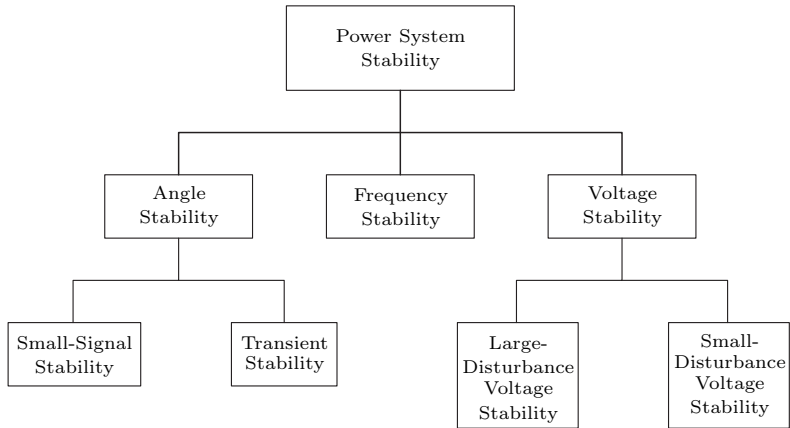
Figure 1.5: Classification of power system stability, own illustration based on [1].

loss of a tie line between two subsystems. Figure 1.5 shows the different classification of power system stability. The angle stability is the ability of interconnected synchronous machines of a power system to remain synchronism [1]. It is divided into small-signal stability and transient stability. Small-signal stability is the ability to maintain synchronism under small disturbances. The disturbances are here sufficiently small for a linearization of the system equations. Instability may result in two forms: steady increase of rotor angle due to lack of sufficient synchronization torque or rotor oscillations of increasing amplitude due to lack of sufficient damping torque. Transient stability is the ability of the power system to maintain synchronism when subjected to a large disturbance. The resulting system response involves large excursions of generator angles. The response is driven by the nonlinear power-angle relationship. Usually, the system is changed so that the post-disturbance steady-state operation differs from the pre-disturbance one. Another classification of stability is voltage stability. Voltage stability is the ability of a power system to maintain acceptable steady voltages at all busses in the system under normal operation [1]. The main factor of instability is the inability to meet the demand of reactive power. Voltage stability can be divided into two classes, large-disturbance voltage stability and small-disturbance stability. The first is the ability to control voltages following

a large disturbance such as faults or loss of generation. It requires the examination of the nonlinear system over sufficient long period of time, usually some seconds to tens of minutes. The second is the ability to control voltages following a small disturbance such as the incremental changes in system load. This stability is determined by the characteristics of the load and control at a given instant of time. Therefore, steady state analysis may be used. A third classification is the frequency stability, or mid- and long-term stability [1]. It examines that inter-machine synchronizing power oscillations have damped out. The result is a uniform system frequency. Typical ranges are from a few seconds up to tens of minutes.

The power system is in a transition state, we are in the middle of the so called *Energiewende* [25]. The goal of many governments is to decarbonize the energy sector and replace conventional power plants such as nuclear, coal, or gas fired plants by RES like PV and wind. Renewable energy sources such as PV and wind are intermittent sources of power and their energy output is difficult to predict. Therefore additional controllable power plants such as pumped hydro storage or batteries are needed to save excess energy or quickly ramp up to provide the loads with power. However, this induces new challenges to the existing transmission network. The transmission network is not built for constantly exchanging large amount of power but rather to exchange power between countries in case of an emergency [26]. Therefore additional capacity as well as controllability has to be added to the system. This can be done using either AC or DC technology. This thesis will focus on the DC technology, specifically on VSC-HVDC links. They add additional transmission capacity to the system as well as controllability of the active and reactive power flow. These VSC-HVDC links can be used for real-time power oscillation damping, or voltage stability control by modulating their active and reactive power. This thesis investigates their potential of being used as a power system stabilizer. It is shown on large networks, that VSC-HVDC links, together with appropriate control, can add additional damping and voltage controllability. It was difficult to have suitable public VSC-HVDC model available. The manufacturers only provide black-box models, where the detailed model structure and internal control algorithm are unknown. Therefore suitable steady-state and dynamic models are developed where the active and reactive power can be easily controlled by an external controller. This external control entity may be a local damping controller, or a global grid controller which coordinates the control of several VSC-HVDC links in a large

power system.

1.2 Contributions

The main contributions of this PhD thesis can be summarized as follows:

- A VSC-HVDC steady-state model that can be used in power flow or optimal power flow calculations.

- A detailed VSC-HVDC nonlinear dynamic model, which considers the physical dynamic elements as well as the converter control. This model may be used in power system stability studies.

- A linearized VSC-HVDC control model to easily parametrize the VSC-HVDC non-linear dynamic model.

- A simplified VSC-HVDC dynamic model which captures the main active and reactive power characteristics. This model can be used in large power system studies or it can be used as a simple model for a model predictive control (MPC) prediction model.

- A global MPC controller which controls the active and reactive power references of the VSC-HVDC links to be used for inter-area oscillation damping and voltage stability control.

- A controlled islanding method based on k-means clustering which splits the power system in a such a way that the different islands are connected with VSC-HVDC links. This allows the exchange of power between the islands and minimizes load shedding and generator tripping.

- A local controller in order to control the active and reactive power of the VSC-HVDC links during controlled islanding.

1.3 Thesis Outline

This thesis is divided into the following chapters:

Chapter 2 gives an overview of the VSC technology.

Chapter 3 introduces three different VSC-HVDC models and how they are tuned. The first model is a steady-state model for power flow calculations. The second and third models are dynamic VSC-HVDC models. They are based on the response of an ABB black-box model. They are able to control the active and reactive power based on a set-point from a supervisory grid controller.

Chapter 4 shows how a MPC-based grid controller is able to damp inter-area oscillations by modulating the active and reactive power of VSC-HVDC links. This is demonstrated on a small system as well on a reduced dynamic model of the European Network of Transmission System Operators for Electricity (ENTSO-E) continental system.

Chapter 5 introduces a MPC-based grid controller which is able to damp inter-area oscillations as well as to control the AC voltages within certain bounds by modulating the active and reactive power of VSC-HVDC links. This is shown on a small system as well as on a large scale system for voltage stability.

Chapter 6 shows how VSC-HVDC links are able to add additional damping when more RES are introduced while reducing the capacity of thermal generation on the European system. The overall system inertia is reduced, which leads to higher frequency dynamics. However, with an appropriate control of the VSC-HVDC active and reactive power set-points it is possible to mitigate this effect and add additional damping.

Chapter 7 introduces a controlled islanding algorithm, which considers VSC-HVDC in order to exchange power between the islands. By exchanging power with VSC-HVDC links between the islands it is possible to reduce load shedding and generator tripping and add additional controllability.

Chapter 8 gives a conclusion of this thesis and suggest directions for future research.

1.4   List of Publications

The work presented in this thesis has been reported by the following publications:

1. M. Imhof and G. Andersson, *Dynamic modeling of a VSC-HVDC Converter*, 48th UPEC 2013, Dublin, 2013, DOI: 10.1109/UPEC.2013.6714935

2. A. Fuchs, M. Imhof, T. Demiray and M. Morari, *Stabilization of Large Power Systems Using VSC-HVDC and Model Predictive Control*, IEEE Transactions on Power Delivery, Vol. 29 No. 1, 2014, DOI: 10.1109/TPWRD.2013.2280467

3. M. Imhof, A. Fuchs, G. Andersson and M. Morari, *Voltage Stability Control using VSC-HVDC Links and Model Predictive Control*, XIII SEPOPE 2014, Foz do Iguaçu, 2014

4. M. Imhof and G. Andersson, *Power System Stability Control using Voltage Source Converter Based HVDC in Power Systems with a High Penetration of Renewable*, 18th PSCC 2014, Wroclaw, 2014, DOI: 10.1109/PSCC.2014.7038493

5. M. Imhof, E. Iggland and G. Andersson, *A Simplified Second-Order Model of a VSC-HVDC Link for Dynamic Studies*, Cigré International Symposium, Across Borders - HVDC Systems and Market Integration, Lund, 2015

6. R. Wiget, M. Imhof, M. Bucher and G. Andersson, *Overview of a Hierarchical Controller Structure for Multi-Terminal HVDC Grids*, Cigré International Symposium, Across Borders - HVDC Systems and Market Integration, Lund, 2015

7. M. Imhof, O. Valgaev and G. Andersson, *Controlled Islanding Using VSC-HVDC to Minimize Load Shedding*, IEEE PowerTech 2015, Eindhoven, 2015, DOI: 10.1109/PTC.2015.7232357

Other publications:

1. L. Mackay, M. Imhof, R. Wiget and G. Andersson, *Voltage Dependent Pricing in DC Distribution Grids*, IEEE PowerTech 2013, Grenoble, 2013, DOI: 10.1109/PTC.2013.6652227

2. M. Vrakopoulou, S. Chatzivasileiadis, E. Iggland, M. Imhof, T. Krause, O. Mäkelä, J. L. Mathieu, L. Roald, R. Wiget and G. Andersson, *A Unified Analysis of Security-Constrained OPF Formulations Considering Uncertainty, Risk, and Controllability in Single and Multi-area Systems*, IX IREP 2013, Rethymnon, 2013, DOI: 10.1109/IREP.2013.6629409

Chapter 2

VSC-HVDC Technology: An Overview

This chapter gives an overview of the voltage source converter-based HVDC technology. It illustrates how the basic setup of a voltage source converter-based HVDC link is implemented. A detailed explanation of the basic voltage source converter structure is given on the semiconductor level. Further the PQ capability of a voltage source converter is shown.

2.1   VSC-HVDC Link Structure

A VSC-HVDC link is composed of three parts, an AC and a DC circuit and the VSCs. In Figure 2.1 a simplified schematic of an entire VSC-HVDC link is shown. The link is connected with three phases to the AC transmission network through a step down transformer on both sides. The step down transformer transforms the AC voltage to the desired voltage level for the VSC. A three phased phase reactor, depicted in red, drives the AC current in order to have a current source characteristics on the AC side. The VSC rectifier converts the AC voltage to DC and the VSC inverter back to AC. For each converter there are two control degrees. The rectifier controls the active power over the DC link as well as the reactive power at the AC side of the converter. This is equivalent to controlling the AC voltage at the converter. The inverter
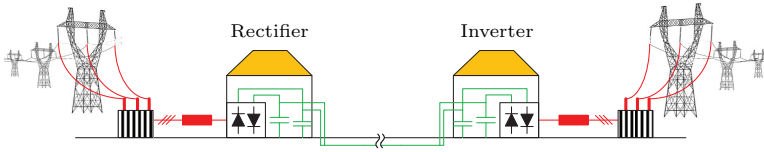
Figure 2.1: Schematic structure of a VSC-HVDC link. The AC part is colored red and the DC part green.

is also able to control the reactive power at the AC side of the converter. In addition, it also controls the DC voltage at the DC side of the converter. Large capacitors are installed at the DC side of both converters. They smoothen the DC voltage and make sure that the DC side reacts like a voltage source, depicted in green. Both converter are connected with either a bipolar overhead line, underground cable or sea-cable.

Therefore a VSC-HVDC link is able to connect two distant points in an AC grid and is able to control the active and reactive power at the terminals. This is why these transmission lines are very interesting not only for power transmission, but also for power system control.

2.2   Converter Structure

Voltage source converter-based HVDC technology uses full controllable switches, such as IGBT or integrated gate-commutated thyristor (IGCT). In contrast, the CSC-HVDC technology uses semi controllable switches like thyristors. Figure 2.2 depicts the schematic diagram of a three-phase two-level VSC. The converter consists of three half-bridges, one for each phase. The AC voltage is switched by the IGBTs either to the positive ($+$) or to the negative ($-$) DC pole. The fundamental voltage of the AC side is usually controlled by pulsewidth modulation (PWM) [27]. The carrier signal for VSC has a switching frequency of around 2 000 Hz. Figure 2.3 shows the behavior of one switch and the converter voltage U_{c} over one duty cycle of the carrier signal. The switch is triggered by the modulation signal when to conduct or to block. The potential of the converter voltage U_{c} is switched from $-\frac{U_{\mathrm{dc}}}{2}$ to $\frac{U_{\mathrm{dc}}}{2}$, depending on the position of the switch.
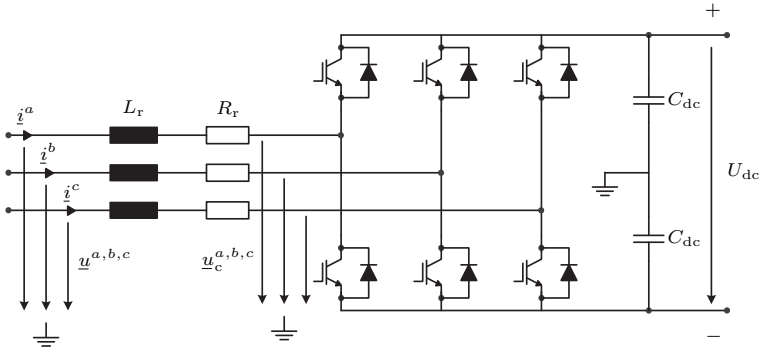
Figure 2.2: Schematic diagram of a three-phase two-level VSC.
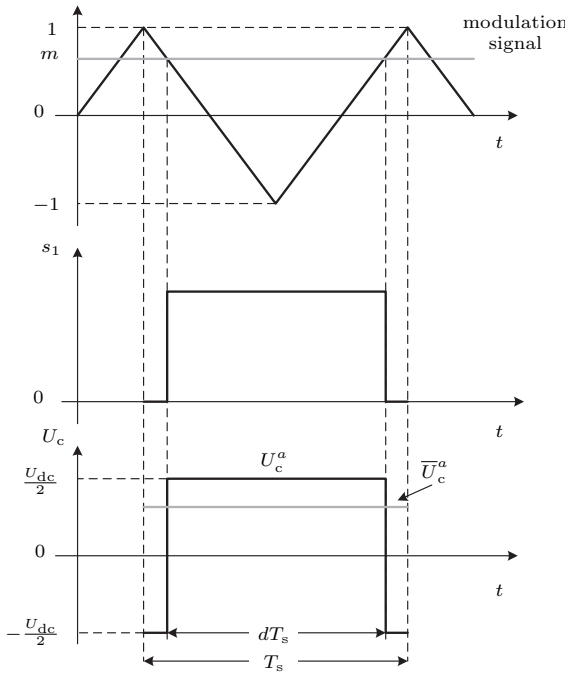
Figure 2.3: Generation of the switching signal with a desired duty ratio, own illustration based on [5].

In order not to model every switching state of the converter, the converter averaged switched model is used in this thesis [5, 27]. It assumes that the modulation signal $m(t)$ during one switching cycle is constant. Therefor the converter voltage U_c can be averaged using

$$\overline{U}_c = \frac{1}{T_s} \int_{t-T_s}^{t} u_c(\tau)d\tau \qquad (2.1)$$

to calculate $\overline{U}_c$, where T_s is the period of the modulation signal. The averaging method may be applied when the switching frequency is sufficiently high compared to the frequency of the modulation signal. For VSC in power system the switching frequency is about 20 times higher, which is satisfactory. When using the converter averaged model, the relation between AC and DC voltage is given with

$$\overline{U}_c(t) = m(t)\frac{U_{dc}}{2} \quad , \qquad (2.2)$$

where $m(t)$ is the modulation signal with the form

$$m(t) = K_0 \cos{(\omega_s t + \varphi)} \qquad (2.3)$$

K_0 is the modulation constant and depends on the PWM method. In case of sinusoidal modulation the factor K_0 is [28]:

$$K_0 = \frac{\sqrt{3}}{2\sqrt{2}} \qquad (2.4)$$

In case of rectangular modulation the factor K_0 is [28]:

$$K_0 = \frac{\sqrt{6}}{\pi} \qquad (2.5)$$

A more recent converter structure is the MMC. It was first introduced by Siemens about 10 years ago. The idea of this topology is, that the converter arms act as a controllable voltage source with n possible discrete voltage steps which allows to approximate the AC sine wave at the AC terminal [29]. Figure 2.4 shows the schematic diagram of a MMC VSC with n so called submodules (SMs) per arm. The converter consists of six arms, whereas each arm is built from series connected submodules. Each submodule contains an IGBT half- or full-bridge as a switching element and a DC storage capacitor [30], as depicted in Figure 2.5. As
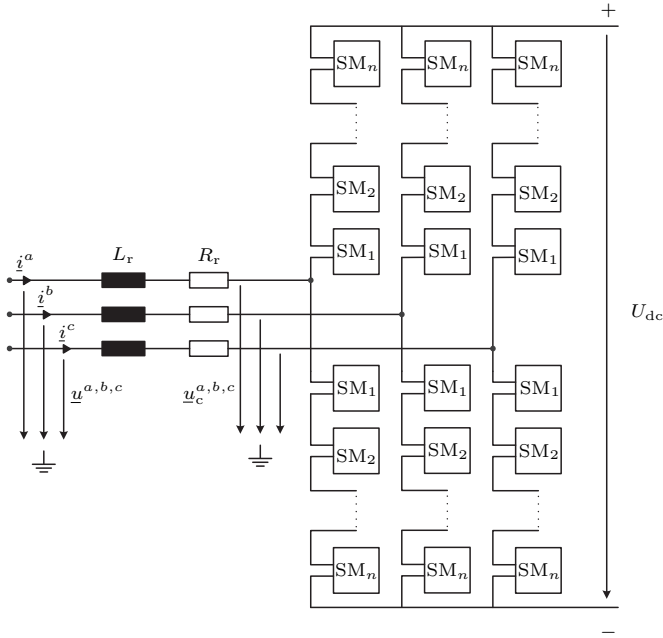
Figure 2.4: Schematic diagram of a MMC VSC with n submodules per arm.

the two-level structure a phase reactor $\underline{Z}_r = R_r + L_r$ is connected on the AC side. The main functions of the phase reactor are to reduce the current rise time during faults to protect the IGBTs and to balance the currents between the phases. This has to be done, because the generated DC voltage of the phase modules are not exactly equal [31]. For a half-bridge module there are three different states for a proper operation of a submodule. Both IGBTs are switched off: This can be compared to the blocking condition of a two-level converter. During normal operation such a condition does not occur. If the current flows from the positive DC pole in the direction of the AC terminal, the current flows through the capacitor of the submodule and charges the capacitor. When it flows in the opposite direction the current bypasses the capacitor over the diode of the IGBT. The upper IGBT is switched on and the lower IGBT is switched off: Independent of the direction of the
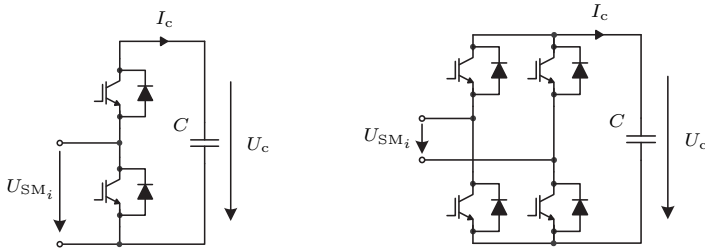
(a) Half-bridge submodule of a MMC VSC.

(b) Full-bridge submodule of a MMC VSC.

Figure 2.5: Different submodule structures for a MMC VSC.

current, the voltage of the storage capacitor is applied to the terminal of the submodule. Depending on the flow of the current, the capacitor is either charged, positive DC current, or discharged, negative DC current. Upper IGBT is switched off and lower IGBT is switched on: Irrespective of the flow of the current, this state ensures that zero voltage is applied to the terminal of the submodule. The voltage of the storage capacitor remains unchanged [31].

The main difference of the full-bridge type and the half-bridge type is, that the terminal voltage U_{SM_i} of the half-bridge can only be switch between zero volts and $+U_{\mathrm{c}}$, whereas the terminal voltage U_{SM_i} of the full-bridge can be switched from $-U_{\mathrm{c}}$ to $+U_{\mathrm{c}}$ [32].

There are some advantages of the MMC over the two-level converter design. The MMC has a highly modular design, which gives good scalability for different voltage levels and power ratings [32]. Because the AC voltage level can be switched in fine DC voltage levels by the submodules, the harmonics generated are minimized and thus AC filters can be omitted in most cases [29]. Due to the low harmonics, standard AC transformers can be used to step down the voltage. The MMC converters have much lower switching frequencies of the IGBT because no more than one submodule per converter leg is switching at any given time. Therefore the system loss are decreased compared to the two-level converters. Furthermore, industry proven standard components like IGBTs and capacitors from the traction industry can be used to reduce the
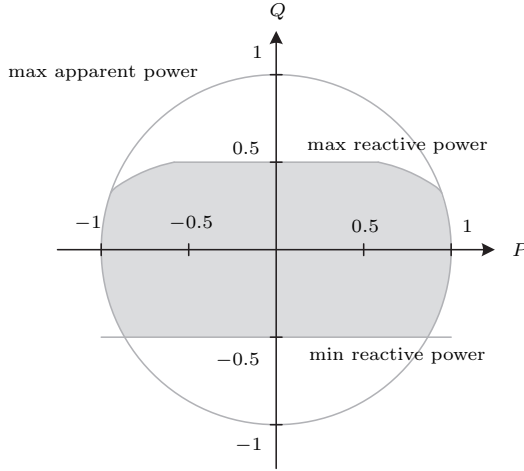
Figure 2.6: *PQ* capability chart.

system costs of a VSC [31].

2.3 PQ Capability

In order to exploit the entire potential of a VSC-HVDC link for power system control by modulating its active and reactive power, the *PQ* capability has to be examined. Figure 2.6 shows the *PQ* diagram according to [33]. The first and fourth quadrants represent the rectifier mode and the second and third quadrants the inverter mode. The *PQ* capability is bounded by some constraints. The first constraint is the maximum apparent power. This is due the limitation of the AC current $\underline{i}$ and is a circle in the *PQ* plane. The current is limited in order not to overheat the IGBT.

The reactive power is constrained by the AC terminal voltage U_c, according to [34]. If the terminal voltage is about 1 p.u. the reactive power can only inject or absorb about 0.5 p.u. of the rated power.

Chapter 3

Modelling of VSC-HVDC Links for Power System Studies

This chapter introduces three different VSC-HVDC models and shows how the parameters of these models can be determined. The first model is a steady-state model for optimal power flow or power flow calculations. The second model is a detailed dynamic model based on the response of an ABB benchmark model. It is also shown, how the controllers of the detailed model may be tuned. The third model is a simplified dynamic model of the latter one. The basic dynamics are maintained, but the number of states is reduced. This chapter is based on the papers "Dynamic Modelling of a VSC-HVDC Converter" presented at UPEC 2013 in Dublin [35] and "A Simplified Second-Order Model of a VSC-HVDC Link for Dynamic Studies" presented at the Cigré HVDC Symposium in Lund 2013 [36].

3.1 Introduction

It is important to have a suitable dynamic VSC-HVDC models for dynamic studies. The complexity of these models varies from very accurate physical models to generic power injection models. This chapter focuses
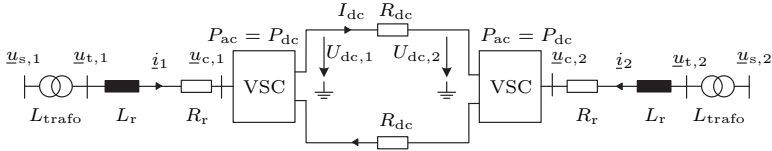
Figure 3.1: Single line diagram of a steady state VSC-HVDC link model.

on three-phase two-level VSC technology. These models are usually controlled based on the PWM technique [27]. However, some of the theory can also be applied to MMC technology. The authors of [27] propose a detailed VSC-HVDC model considering the dynamics of the IGBTs. These models are very accurate but are not well suited for dynamic power system simulations, because they require a high computational effort. Converter averaged models [27, 37] do not consider the dynamics of every switching action, but the averaged waveform over one switching cycle to another. These models reduce the computational complexity significantly and are accurate enough for power system studies. Power injection models [38, 39] are the simplest models. They neglect higher order dynamics, thus they are not of importance for large scale dynamic power system studies rather for steady-state power system studies.

Detailed VSC-HVDC models from manufactures, where the control structure is elaborated, are not available. However, only black-box models are provided. For an academic point of view this is suboptimal. Therefore generic dynamic models have been developed in [5, 40, 41, 42]. However, how the controllers of these models are tuned is not addressed. This chapter presents a steady state model as well as modified dynamic VSC-HVDC models and also elaborates on the tuning of the converter control.

Figure 3.1 shows a single line diagram of the VSC-HVDC steady state model. It can be divided into three parts: The AC part at the rectifier side, the DC part with the two converters and the AC part at the inverter side. Both AC parts consist of a step-down transformer $\underline{Z}_{\mathrm{trafo}} = jL_{\mathrm{trafo}}$ and a phase reactor $\underline{Z}_{\mathrm{r}} = R_{\mathrm{r}} + jL_{\mathrm{r}}$. The DC side is modelled as a bipolar cable with a DC resistance R_{dc}. The VSCs are assumed to be lossless, therefore the power is conserved over the converters:

$$P_{\mathrm{ac}} = P_{\mathrm{dc}} \tag{3.1}$$

Based on this model, a steady-state model and two dynamic models are developed.

3.1.1 ABC Three Phase Representation

In the ABC three phase representation any kind of power system equipment can be modelled. The values are time varying with the system frequency of either 50 or 60 Hz, even during steady-state operation. Normally the three phase quantities are balanced and in positive sequence. This can be formulated as

$$x^{abc}(t) = \begin{bmatrix} \hat{X} \cos{(\theta + \varphi)} \\ \hat{X} \cos{\left(\theta + \varphi - \frac{2\pi}{3}\right)} \\ \hat{X} \cos{\left(\theta + \varphi + \frac{2\pi}{3}\right)} \end{bmatrix} \quad , \tag{3.2}$$

where $\theta = \omega_{\mathrm{s}} t = 2\pi f_{\mathrm{s}} t$ and f_{s} is the system frequency [43]. The value $\hat{X}$ denotes the amplitude of cosine.

3.1.2 Phasor Representation

The steady-state values of a power system can be written in the well-known phasor representation in the complex plane. The time function $x(t)$ corresponds to the rotating phasor $\underline{X}$:

$$x(t) = \hat{X} \cos(\theta + \varphi) \rightarrow \underline{X} = \frac{\hat{X}}{\sqrt{2}} \left(\cos \varphi + j \sin \varphi \right) = X e^{j\varphi} \tag{3.3}$$

The advantage of this representation is that during steady-state operation the values remain constant. The phasor representation is then mainly used for steady-state calculation such as power flow (PF) and optimal power flow (OPF) analysis.

3.1.3 DQ0 Representation

A widely used variable representation in power systems is the DQ0 representation. The DQ0 or Park's transformation is mainly applied in the derivation of electrical machines and is generally referred as a reference frame rotating with the system frequency [1, 44]. An advantage

of the DQ0 representation is that the quantities are orthogonal, unlike in the ABC representation. The DQ0 or Park's transformation is given by the following equation:

$$
\begin{bmatrix} x^d \\ x^q \\ x^0 \end{bmatrix} = \frac{2}{3} \underbrace{\begin{bmatrix} \cos(\theta) & \cos\left(\theta - \frac{2\pi}{3}\right) & \cos\left(\theta + \frac{2\pi}{3}\right) \\ -\sin(\theta) & -\sin\left(\theta - \frac{2\pi}{3}\right) & -\sin\left(\theta + \frac{2\pi}{3}\right) \\ \frac{1}{2} & \frac{1}{2} & \frac{1}{2} \end{bmatrix}}_{\mathbf{T}_{\text{dq0}}} \begin{bmatrix} x^a \\ x^b \\ x^c \end{bmatrix}
$$

$$(3.4)$$

The inverse transformation is given by

$$
\begin{bmatrix} x^a \\ x^b \\ x^c \end{bmatrix} = \underbrace{\begin{bmatrix} \cos(\theta) & -\sin(\theta) & 1 \\ \cos\left(\theta - \frac{2\pi}{3}\right) & -\sin\left(\theta - \frac{2\pi}{3}\right) & 1 \\ \cos\left(\theta + \frac{2\pi}{3}\right) & -\sin\left(\theta + \frac{2\pi}{3}\right) & 1 \end{bmatrix}}_{\mathbf{T}_{\text{abc}}} \begin{bmatrix} x^d \\ x^q \\ x^0 \end{bmatrix} \quad . \quad (3.5)
$$

The derivative of the time dependent transformation matrices $\mathbf{T}_{\text{dq0}}$ and $\mathbf{T}_{\text{abc}}$ is given as

$$
\frac{\mathrm{d}\mathbf{T}_{\text{dq0}}}{\mathrm{d}t} = -\omega_{\text{s}}\left(\mathbf{J} \cdot \mathbf{T}_{\text{dq0}}\right) \tag{3.6}
$$

$$
\frac{\mathrm{d}\mathbf{T}_{\text{abc}}}{\mathrm{d}t} = \omega_{\text{s}}\left(\mathbf{J} \cdot \mathbf{T}_{\text{abc}}\right) \quad , \tag{3.7}
$$

with

$$
\mathbf{J} = \begin{bmatrix} 0 & 1 & 0 \\ -1 & 0 & 0 \\ 0 & 0 & 0 \end{bmatrix} \quad . \tag{3.8}
$$

For balanced steady-state operation x^d and x^q are constant and $x^0 = 0$. For other modes of operation, like electromechanical oscillations, these quantities slowly vary with time (maximum 2 to 3 Hz) [1].

3.2　Steady-State VSC-HVDC Model

The steady-state model should be valid for PF and OPF calculations. It can also be used for the initialization of a dynamic simulation. This

model must have the same properties as the dynamic model in steady-state. A VSC-HVDC link may be operated in different control modes, similar to a generator. The link can be operated either in PU-mode, as a generator where the active power and the AC voltage are controlled, or in PQ-mode, where the active and reactive power are controlled. Thus different steady-state simulations are possible:

1. Classic PF calculation: The set-points of the generators and of the VSC-HVDC links are predefined. Thus only an AC PF is calculated for the network.

2. Semi OPF calculation: The generators have fixed set-points. However, the set-points of the VSC-HVDC links are optimized in order to reduce the losses in the AC system.

3. Classic OPF calculation: The set-points of the generators and of the VSC-HVDC links are optimized for a given cost function.

The formulation of an OPF problem can be formulated as follows [45]:

$$\min_{\mathbf{x}} f(\mathbf{x}) \tag{3.9}$$

subject to

$$g(\mathbf{x}) = 0 \tag{3.10}$$
$$h(\mathbf{x}) \leq 0 \tag{3.11}$$
$$\mathbf{x}_{\min} \leq \mathbf{x} \leq \mathbf{x}_{\max} \tag{3.12}$$

The objective function $f(\mathbf{x})$ defines the costs of the generators. It is minimized subject to equality (3.10) and inequality constraints (3.11) and the box constraints (3.12). The optimization vector $\mathbf{x}$ for standard OPF formulation consists of the voltage angles φ and magnitudes $\mathbf{u}_{\mathrm{ac}}$ as well as the generator real and reactive power injections $\mathbf{p}_{\mathrm{gen}}$ and $\mathbf{q}_{\mathrm{gen}}$:

$$\mathbf{x} = \begin{bmatrix} \varphi \\ \mathbf{u}_{\mathrm{ac}} \\ \mathbf{p}_{\mathrm{gen}} \\ \mathbf{q}_{\mathrm{gen}} \end{bmatrix} \tag{3.13}$$

The goal of the steady-state model is to find a formulation which fits the already existing OPF framework. Figure 3.2 depicts the steady-state

Figure 3.2: Steady-state model of a VSC-HVDC link.

model of a VSC-HVDC link. The transformer reactance $\underline{Z}_{\text{trafo}}$ and the phase reactor $\underline{Z}_{\text{r}}$ are lumped into the impedance $\underline{Z}_{\text{ac}}$. The AC side of the VSC is modelled as a generator which absorbs or injects active and reactive power $P_{\text{vsc},i}$ and $Q_{\text{vsc},i}$. The index $i \in \{1, 2\}$ denotes the rectifier side or the inverter side of the VSC-HVDC link, respectively. The DC side of the VSC is modelled as a voltage source $U_{\text{dc},i}$. The DC connection is modelled as a bipolar DC cable or overhead line with the resistance R_{dc}.

For each link, additionally to the AC voltage magnitudes and angles of the internal AC busses, new state variables are introduced and added to the optimization vector $\mathbf{x}$, namely $\mathbf{p}_{\text{vsc}}$, $\mathbf{q}_{\text{vsc}}$ and $\mathbf{u}_{\text{dc},1}$ the DC voltage at the rectifier. This leads to the new optimization vector $\mathbf{x}$:

$$
\mathbf{x} = \begin{bmatrix} \boldsymbol{\varphi} \\ \mathbf{u}_{\text{ac}} \\ \mathbf{p}_{\text{gen}} \\ \mathbf{q}_{\text{gen}} \\ \mathbf{p}_{\text{vsc}} \\ \mathbf{q}_{\text{vsc}} \\ \mathbf{u}_{\text{dc},1} \end{bmatrix} \tag{3.14}
$$

In total a HVDC link adds 13 elements to the state vector. A voltage angel and magnitude for each of the internal busses, one active and reactive power generator state for each of the VSCs and one DC voltage state at the rectifier side.

The power flow of the corresponding AC line from the connected AC node to the VSC is calculated as follows:

$$P_{\mathrm{hvdc},i} = U_{\mathrm{s},i}^2 g_i - U_{\mathrm{s},i} U_{\mathrm{c},i} g_i \cos \varphi_{\mathrm{sc},i} - U_{\mathrm{s},i} U_{\mathrm{c},i} g_i \sin \varphi_{\mathrm{sc},i} \qquad (3.15)$$

$$Q_{\mathrm{hvdc},i} = U_{\mathrm{s},i}^2 b_i + U_{\mathrm{s},i} U_{\mathrm{c},i} b_i \cos \varphi_{\mathrm{sc},i} - U_{\mathrm{s},i} U_{\mathrm{c},i} g_i \sin \varphi_{\mathrm{sc},i} \quad , \qquad (3.16)$$

where $Y_i = Z_{\mathrm{ac},i}^{-1} = g_i + jb_i$ is the series admittance of the AC line. The voltage angle is defined as follows: $\varphi_{\mathrm{sc},i} = \varphi_{\mathrm{s},i} - \varphi_{\mathrm{c},i}$. The flows from the VSC to the AC system node is calculated as:

$$P_{\mathrm{vsc},i} = U_{\mathrm{c},i}^2 g_i - U_{\mathrm{s},i} U_{\mathrm{c},i} g_i \cos \varphi_{\mathrm{cs},i} - U_{\mathrm{s},i} U_{\mathrm{c},i} g_i \sin \varphi_{\mathrm{cs},i} \qquad (3.17)$$

$$Q_{\mathrm{vsc},i} = U_{\mathrm{c},i}^2 b_i + U_{\mathrm{s},i} U_{\mathrm{c},i} b_i \cos \varphi_{\mathrm{cs},i} - U_{\mathrm{s},i} U_{\mathrm{c},i} g_i \sin \varphi_{\mathrm{cs},i} \quad , \qquad (3.18)$$

where power flows (3.17) and (3.18) correspond exactly to the absorbed or produced power of the introduced generators. Since the VSC is assumed to be lossless, the power relationship between the AC and DC side can be formulated as follows:

$$P_{\mathrm{vsc},i} + P_{\mathrm{dc},i} = 0 \qquad (3.19)$$

The two VSCs are connected with a bipolar cable or overhead line. The DC losses are included and the active power at the inverter $P_{\mathrm{dc},2}$ is constraint as

$$P_{\mathrm{dc},1} + P_{\mathrm{dc},2} - 2R_{\mathrm{dc}} I_{\mathrm{dc}}^2 = 0 \quad , \qquad (3.20)$$

where I_{dc} is the current of one pole. The factor 2 of the loss term is deduced from the bipolar operation the DC cable. The DC current is calculated with:

$$I_{\mathrm{dc}} = \frac{P_{\mathrm{dc},1}}{2U_{\mathrm{dc},1}} \qquad (3.21)$$

The DC current is limited due to operational constraints like current rating of the IGBTs and thermal rating of the DC cable to:

$$-I_{\mathrm{dc,max}} \leq I_{\mathrm{dc}} \leq I_{\mathrm{dc,max}} \quad . \qquad (3.22)$$

Using Kirchhoff's law, the DC voltage of the inverter can be computed:

$$U_{\mathrm{dc},2} = U_{\mathrm{dc},1} - R_{\mathrm{dc}} I_{\mathrm{dc}} \qquad (3.23)$$

For the additional states in the state vector, the following bounds are introduced. As introduced in Section 2.3 the VSC has some operational
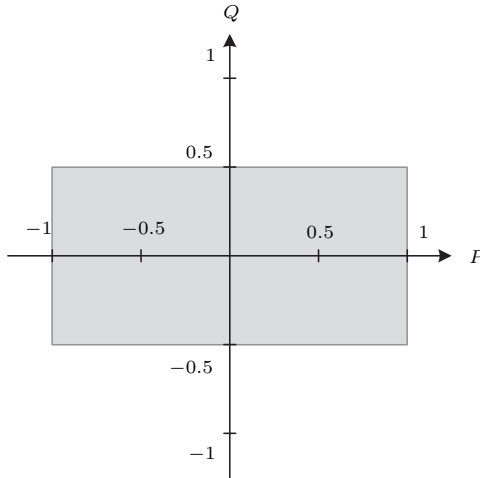
Figure 3.3: Simplified PQ capability chart.

limits. The simplified PQ capability chart is depicted in Figure 3.3, and leads to the following limits:

$$P_{\min} \leq P_{\text{vsc},i} \leq P_{\max} \tag{3.24}$$

$$Q_{\min} \leq Q_{\text{vsc},i} \leq Q_{\max} \tag{3.25}$$

Additionally, the DC voltage at the rectifier and inverter are only allowed to stay within certain bounds, which are given as

$$U_{\text{dc,min}} \leq U_{\text{dc,1}} \leq U_{\text{dc,max}} \tag{3.26}$$

$$U_{\text{dc,min}} \leq U_{\text{dc,2}} \leq U_{\text{dc,max}} \quad . \tag{3.27}$$

The introduced generators of the VSC-HVDC link do not add any additional costs to the objective function $f(\mathbf{x})$. With these equations, the OPF formulation, according to (3.9) to (3.12), is built and the optimization is solved.

For the classical PF calculation, the power injections of the generators and the VSC-HVDC link are given. Therefore the generator limits and the VSC-HVDC limits, (3.24) and (3.25), are set to their set-points and
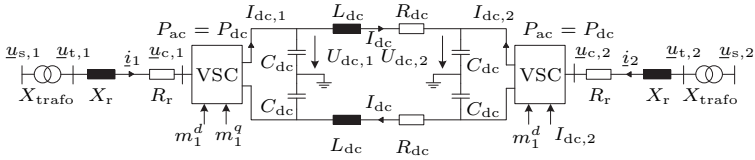
Figure 3.4: Single line diagram of the VSC-HVDC dynamic model.

the AC power flows of the system are determined. The second simulation case is the semi OPF. It minimizes the overall system losses with the installed VSC-HVDC links when the power injections of the generators are fixed. In this case, (3.24) and (3.25) are set to the operational limits of the VSC and the AC and DC power flows are determined. The third simulation case is the classical OPF formulation, where the overall production costs are minimized. In this case, the limits of the generators and the VSC-HVDC links are set to their operational limits to calculate the voltages of the system as well as the power flows.

3.3 Dynamic VSC-HVDC Model

It is difficult to have access to detailed dynamic VSC-HVDC models. Manufactures, like ABB or Siemens, only provide the industry and universities with black-box models. Especially the control structure of these links is not transparent. Therefore generic VSC-HVDC models have to be made accessible to study the effects of VSC-HVDC links on the power system. Some generic dynamic models have been presented in [40, 41] and [46].

The modelling of a VSC-HVDC link is a two staged process. First a dynamic model of the physical part such as AC filter, DC cable and VSC including the converter control has to be developed. Secondly the converter control has to be tuned. This section presents a dynamic model of a VSC-HVDC link based on the publication "Dynamic Modeling of a VSC-HVDC Converter" [35], which is a modified and expanded model description of [40] and [42], and shows how the converter control can be tuned according the response of an ABB black-box benchmark model.

The dynamic VSC-HVDC model consists of two parts: The components such as AC filters, VSC and DC cables, depicted in Figure 3.4, and the
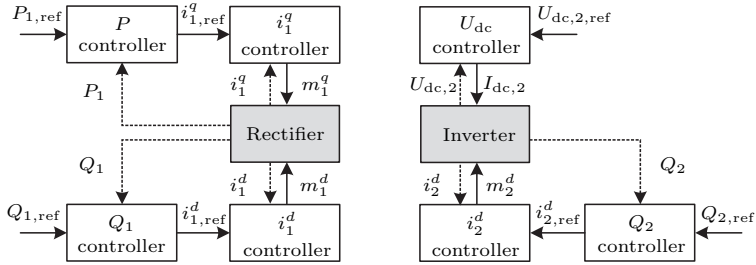
Figure 3.5: Control scheme of the VSC-HVDC link: Controller blocks with saturated PI controllers (white boxes), physical converter models (grey boxes), measurement signals (dashed arrows) and reference values (solid arrows).

converter control, shown in Figure 3.5 . The model includes the dynamics of the AC phase reactor, the DC converter capacitance, the DC cable as well as the dynamics of the converter control. The VSC is modelled as a two-level PWM controlled converter where the modulation signal $\underline{m}$ is the actuating variable. The converter has a cascaded control structure, consisting of an inner and an outer control loop [47]. The inner loop controls the AC currents and calculates the modulation signal $\underline{m}$ for the converter. The outer loop controls the AC powers and calculates the current references for the inner loop. Figure 3.5 shows the control structure of the VSC-HVDC link. The link is controlled by four external control signals. The rectifier controls the active and reactive power at the AC terminal and the inverter controls the reactive power at the AC terminal and regulates the DC voltage. The DC voltage controller consists of a single control loop.

All values are represented in the DQ0 reference frame. However, the zero component is neglected, thus only balanced operation of the VSC-HVDC link is considered. The values in the DQ reference frame are written as $\underline{x} = x^d + jx^q$.

3.3.1   Components Modelling

The components of the VSC-HVDC link can be separated into three main subsystems: Two AC systems, two VSC and one DC system.

The AC part of the VSC-HVDC link consists of an ideal step down transformer, represented with the inductance X_{trafo}, which connects the VSC-HVDC link to the AC grid. A phase reactor, represented by $\underline{Z}_{\text{r}} = R_{\text{r}} + jX_{\text{r}}$ connects the VSC with the transformer as depicted in Figure 3.4. The active and reactive power in the DQ reference frame at the AC terminal are calculated as follows [1]:

$$P_i = u_{\text{s},i}^d i_i^d + u_{\text{s},i}^q i_i^q \tag{3.28}$$

$$Q_i = -u_{\text{s},i}^d i_i^q + u_{\text{s},i}^q i_i^d \tag{3.29}$$

where subscript $i \in \{1, 2\}$ stands for the rectifier side and the inverter side, respectively. In order to decouple the powers, (3.28) and (3.29), from their d and q current parts, the q-axis of the rotating DQ reference frame is aligned with the AC terminal voltage $\underline{u}_{\text{s},i}$, hence $u_{\text{s},i}^d = 0$. This enables the converter to independently control the active and reactive power with its corresponding current part. Therefore the voltage at the AC terminal bus is

$$\underline{u}_{\text{s},i} = ju_{\text{s}}^q \quad . \tag{3.30}$$

The dq-current equations of the phase reactor is calculated as follows:

$$u_{\text{r},i}^d = L_{\text{r}} \frac{\mathrm{d}i_i^d}{\mathrm{d}t} - \omega_{\text{s}} L_{\text{r}} i_i^q \tag{3.31}$$

$$u_{\text{r},i}^q = L_{\text{r}} \frac{\mathrm{d}i_i^q}{\mathrm{d}t} + \omega_{\text{s}} L_{\text{r}} i_i^d \quad . \tag{3.32}$$

The dynamics of the AC current are thus calculated as follows, based on Kirchhoff's law:

$$\frac{X_{\text{r}}}{\omega_{\text{s}}} \frac{\mathrm{d}i_i^d}{\mathrm{d}t} - X_{\text{r}} i_i^q = -R_{\text{r}} i_i^d - u_{\text{c},i}^d + u_{\text{t},i}^d \tag{3.33}$$

$$\frac{X_{\text{r}}}{\omega_{\text{s}}} \frac{\mathrm{d}i_i^q}{\mathrm{d}t} + X_{\text{r}} i_i^d = -R_{\text{r}} i_i^q - u_{\text{c},i}^q + u_{\text{t},i}^q \quad , \tag{3.34}$$

where $u_{\text{c},i}^d$ and $u_{\text{c},i}^q$ represent the voltages at the converters, and $u_{\text{t},i}^d$ and $u_{\text{t},i}^q$ the voltage after the step down transformer. The current dynamics $L\frac{\mathrm{d}i}{\mathrm{d}t}$ of the step down transformer are neglected because for all other transformers in the AC system, these dynamics are not modelled either. The voltage equations are

$$u_{\text{t},i}^d = X_{\text{trafo}} i_i^q \tag{3.35}$$

$$u_{\text{t},i}^q = u_{\text{s},i}^q - X_{\text{trafo}} i_i^d \quad . \tag{3.36}$$

Equation (3.36) and (3.35) are substituted into (3.33) and (3.34) which leads to the dynamic AC equations

$$\frac{X_{\mathrm{r}}}{\omega_{\mathrm{s}}}\frac{\mathrm{d}i_i^d}{\mathrm{d}t} = (X_{\mathrm{r}} + X_{\mathrm{trafo}})\, i_i^q - R_{\mathrm{r}}i_i^d - u_{\mathrm{c},i}^d \tag{3.37}$$

$$\frac{X_{\mathrm{r}}}{\omega_{\mathrm{s}}}\frac{\mathrm{d}i_i^q}{\mathrm{d}t} = -(X_{\mathrm{r}} + X_{\mathrm{trafo}})\, i_i^d - R_{\mathrm{r}}i_i^q - u_{\mathrm{c},i}^q + u_{\mathrm{s},i}^q \quad . \tag{3.38}$$

The DC circuit of the VSC-HVDC link consists of the converter capacitance $C_{\mathrm{converter}}$ and a bipolar DC cable. The cable is modelled as a π-equivalent with the elements R_{dc}, L_{dc} and C_{cable}. The equivalent DC capacitance C_{dc}, as depicted in Figure 3.4, is calculated as

$$C_{\mathrm{dc}} = C_{\mathrm{converter}} + \frac{1}{2}C_{\mathrm{cable}} \quad . \tag{3.39}$$

The dynamic circuit equations of the DC side are

$$C_{\mathrm{dc}}\frac{\mathrm{d}U_{\mathrm{dc},1}}{\mathrm{d}t} = I_{\mathrm{dc},1} - I_{\mathrm{cable}} \tag{3.40}$$

$$C_{\mathrm{dc}}\frac{\mathrm{d}U_{\mathrm{dc},2}}{\mathrm{d}t} = I_{\mathrm{dc},2} + I_{\mathrm{cable}} \tag{3.41}$$

$$L_{\mathrm{dc}}\frac{\mathrm{d}I_{\mathrm{cable}}}{\mathrm{d}t} = U_{\mathrm{dc},1} - U_{\mathrm{dc},2} - R_{\mathrm{dc}}I_{\mathrm{cable}} \quad . \tag{3.42}$$

It is assumed that the VSCs are lossless two-level PWM converters. They are modelled as average switched converter models [5], thus the higher harmonics of the switching of the IGBTs are neglected. The relationship between the AC and DC voltage is given as

$$\underline{u}_{\mathrm{c},i} = K_0 \cdot \underline{m}_i \cdot 2 \cdot U_{\mathrm{dc},i} \quad , \tag{3.43}$$

where $\underline{m}_i = m_i^d + jm_i^q$ represents the modulation signal of the converter. It is the output of the current controller to control the converter voltage $\underline{u}_{\mathrm{c},i}$. It is assumed that the converter operates in rectangular modulation and therefore the modulation constant is $K_0 = \frac{\sqrt{6}}{\pi}$ [28]. For other modulation methods and constants please refer to Chapter 2.2. Because of the assumption of a lossless converter, the constraint for the power balance of the AC and DC side is given by:

$$u_{\mathrm{c},i}^d i_i^d + u_{\mathrm{c},i}^q i^q = P_{\mathrm{ac},i} \overset{!}{=} P_{\mathrm{dc},i} = 2 \cdot I_{\mathrm{dc},i}U_{\mathrm{dc},i} \tag{3.44}$$

Each converter has two control inputs. The rectifier is controlled by m_1^d and m_1^q and the inverter by m_2^d and $I_{\mathrm{dc},2}$. Unlike in [42] there is no q-current controller at the inverter side, as shown in Figure 3.5, since this would over-determine the system. Therefore the q-part of current $\underline{i}_2$ is calculated using the power equality (3.44).

3.3.2   Converter Control

The aim of the converter control is to independently control the active power P_1 at the AC terminal bus at the rectifier side, the DC voltage $U_{\mathrm{dc},2}$ at the inverter side and either the active power Q_i or the AC terminal bus voltage U_{s} at both sides. Because of the alignment of the AC terminal bus voltage with the q-axis according to (3.30) the active and reactive power are controlled independently by the corresponding currents

$$P_i = u_{\mathrm{s},i}^q \cdot i_i^q \tag{3.45}$$

$$Q_i = u_{\mathrm{s},i}^q \cdot i_i^d \quad . \tag{3.46}$$

The converter control is a two stage control of two cascaded PI-controller, as depicted in Figure 3.5. All PI-controllers have the form

$$K(s) = \left(K_{\mathrm{p}} + \frac{K_{\mathrm{i}}}{s} \right) \quad , \tag{3.47}$$

where K_{p} is the proportional gain and K_{i} is the integral gain.

Outer Control Loop

The active power at the rectifier and the reactive power or AC terminal voltage at both sides are controlled by the outer control loop, as depicted in Figure 3.6. Both controllers calculate the current reference for the inner control loop. Figure 3.6a shows the active power controller. A PI-controller, with a proportional gain $K_{\mathrm{p}} = K_{\mathrm{p,P}}$ and an integral gain $K_{\mathrm{i}} = K_{\mathrm{i,P}}$, controls the active power to a given set-point. The q-current is limited to

$$-i_{1,\mathrm{max}}^q \leq i_1^q \leq i_{1,\mathrm{max}}^q \tag{3.48}$$

in order to keep the current within the rating limits of the IGBTs. The calculated q-current reference serves as an input for the underlying current controller.
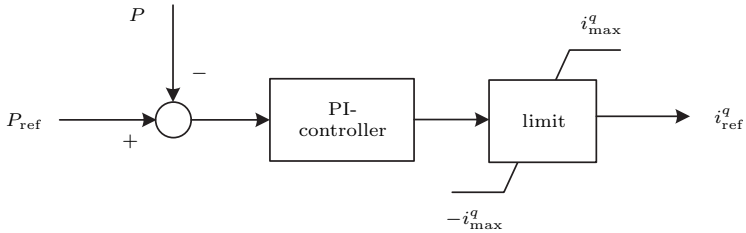
(a) Active power controller for the rectifier.
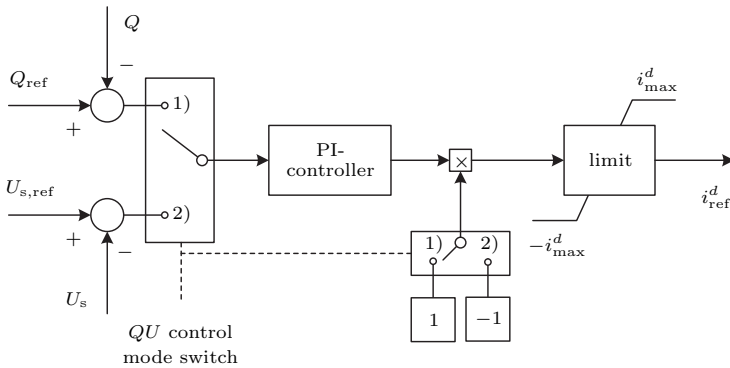
(b) Reactive power or AC voltage controller for the rectifier and inverter. There are two control modes. 1) is for reactive power control mode and 2) for AC voltage control mode.

Figure 3.6: Block diagram of the outer control loop.

The VSC can either be operated in *PQ*- or *PU*-mode. Figure 3.6b shows the combined reactive power and AC terminal voltage controller. The controller can switch between controlling the reactive power (1) and controlling the AC terminal bus voltage (2). A PI-controller with a proportional gain $K_{\mathrm{p}} = K_{\mathrm{p,QU},i}$ and an integral gain $K_{\mathrm{i}} = K_{\mathrm{i,QU},i}$ controls the desired values to a given reference value. The *d*-current is limited to

$$-i_{i,\mathrm{max}}^{d} \leq i_{i}^{d} \leq i_{i,\mathrm{max}}^{d} \quad . \tag{3.49}$$

Inner Control Loop

The inner control loop controls the currents to the reference value received from the outer controller. Due to the DQ reference frame, the *d* and *q* values are coupled according to the transformation (3.6). In order to control the *d*- and the *q*-current independently from each other, a current decoupling feed-forward term, as depicted in Figure 3.7, is introduced [5].

The control structure of the inner loop for the rectifier is shown in Figure 3.7a. Two PI-controllers, in the form of (3.47), control the *d*- and *q*-current to its reference value and calculate the internal voltage $\underline{u}_{1}$. The parameters of the *d*-current controller are $K_{\mathrm{p}} = K_{\mathrm{p,id},1}$ for the proportional gain and $K_{\mathrm{i}} = K_{\mathrm{i,id},1}$ for the integral gain. For the *q*-current controller the gains are defined as $K_{\mathrm{p}} = K_{\mathrm{p,iq},1}$ and $K_{\mathrm{i}} = K_{\mathrm{i,iq},1}$. The internal voltage $\underline{u}$ is limited by

$$u_{\mathrm{min}}^{d} \leq u_{1}^{d} \leq u_{\mathrm{max}}^{d} \tag{3.50}$$

$$u_{\mathrm{min}}^{q} \leq u_{1}^{q} \leq u_{\mathrm{max}}^{q} \quad . \tag{3.51}$$

The modulation indices m_{1}^{d} and m_{1}^{q} are calculated and sent to the VSC to be applied. The control structure of the inverter is shown in Figure 3.7b. The *d*-current is controlled as the inverter with the controller parameter $K_{\mathrm{p}} = K_{\mathrm{p,id},2}$ for the proportional gain and $K_{\mathrm{i}} = K_{\mathrm{i,id},2}$ for the integral gain. The second PI-controller controls the DC voltage to its desired value with the controller parameters $K_{\mathrm{p}} = K_{\mathrm{p,dc}}$ and $K_{\mathrm{i}} = K_{\mathrm{i,dc}}$. To avoid overheating of the cable and the IGBTs the DC current is limited:

$$-I_{\mathrm{dc,max}} \leq I_{\mathrm{dc},2} \leq I_{\mathrm{dc,max}} \tag{3.52}$$
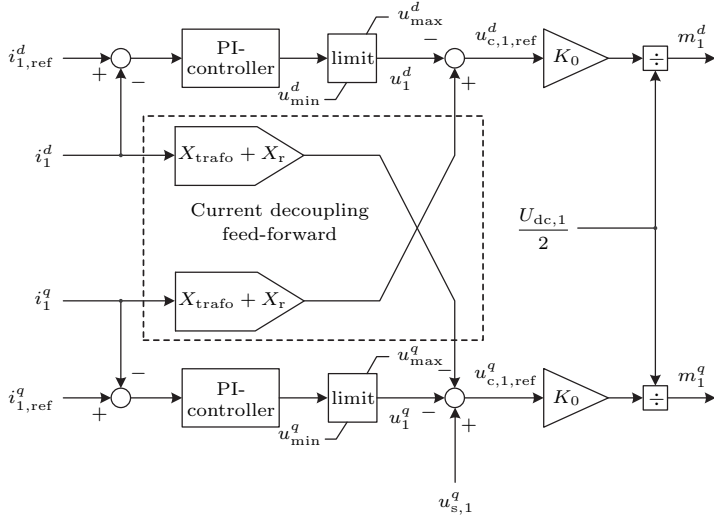
(a) Block diagram of the inner dq-current controller of the rectifier.
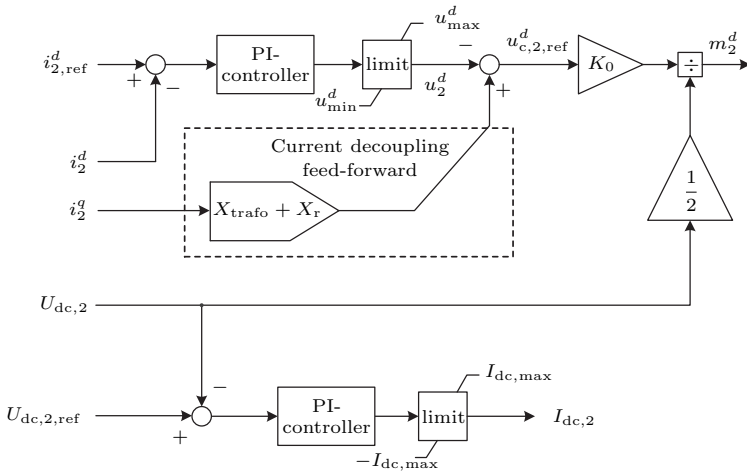
(b) Block diagram of the inner d-current controller and DC voltage controller of the inverter.

Figure 3.7: Block diagram of the inner control loop.

3.3.3 Controller Tuning

In order to have a realistic response of the VSC-HVDC link, the controllers have to be tuned. The tuning is based on the response of a VSC-HVDC light black-box model from ABB [33].

In order to determine the parameters of the controllers, a linear control model is developed. First the VSC-HVDC link is linearized and then the linear transfer function including the controllers is derived.

Linerization of the VSC-HVDC Link

The AC and converter model from Section 3.3.1 is linearized at the current operating point x_0. This results in the following combined linearized AC plant

$$
\begin{bmatrix} \frac{X_{\mathrm{r}}}{\omega} \dot{\hat{i}}_i^d \\ \frac{X_{\mathrm{r}}}{\omega} \dot{\hat{i}}_i^q \end{bmatrix} = \begin{bmatrix} -R_{\mathrm{r}} & X_{\mathrm{r}} + X_{\mathrm{trafo}} \\ -(X_{\mathrm{r}} + X_{\mathrm{trafo}}) & -R_{\mathrm{r}} \end{bmatrix} \begin{bmatrix} \hat{i}_i^d \\ \hat{i}_i^q \end{bmatrix}
$$
$$
+ \begin{bmatrix} -2K_0 U_{\mathrm{dc},0,i} & 0 \\ 0 & -2K_0 U_{\mathrm{dc},0,i} \end{bmatrix} \begin{bmatrix} \hat{m}_i^d \\ \hat{m}_i^q \end{bmatrix} \tag{3.53}
$$
$$
+ \begin{bmatrix} 0 & -2K_0 m_{0,i}^d \\ 1 & -2K_0 m_{0,i}^q \end{bmatrix} \begin{bmatrix} \hat{u}_{\mathrm{s},i}^q \\ \hat{U}_{\mathrm{dc},i} \end{bmatrix} \quad,
$$

where $\hat{i}_i^d$, $\hat{i}_i^q$, $\hat{m}_i^d$, $\hat{m}_i^q$, $\hat{u}_{\mathrm{s},i}^q$ and $\hat{U}_{\mathrm{dc},i}$ denote the linearized values in the form of $\hat{x} = x - x_0$, where x_0 is the steady state and $\hat{x}$ denotes the deviation from the steady state. This leads to the transfer function for the d-current

$$
\begin{aligned}
G_{\mathrm{id},i}(s) &= \frac{\hat{i}_i^d(s)}{\hat{m}_i^d(s)} \\
&= -2K_0 U_{\mathrm{dc},0,i} \bigg(2K_0 m_{0,i}^q \hat{U}_{\mathrm{dc},i}(s) \\
&\quad + (X_{\mathrm{r}} + X_{\mathrm{trafo}}) \hat{i}_i^d(s) + \frac{1}{\frac{X_{\mathrm{r}}}{\omega} s + R_{\mathrm{r}}} \bigg) \quad,
\end{aligned} \tag{3.54}
$$

and for the q-current

$$
\begin{aligned}
G_{\mathrm{iq},i}(s) &= \frac{\hat{i}_i^q(s)}{\hat{m}_i^q(s)} \\
&= -2K_0 U_{\mathrm{dc},0,i}\bigg(2K_0 m_{0,i}^d \hat{U}_{\mathrm{dc},i}(s) \\
&\quad - (X_{\mathrm{r}} + X_{\mathrm{trafo}})\hat{i}_i^q + \hat{u}_{\mathrm{s},i}^q + \frac{1}{\frac{X_{\mathrm{r}}}{\omega}s + R_{\mathrm{r}}} \bigg) \quad .
\end{aligned}
\tag{3.55}
$$

The DC model of Section 3.3.1 is linearized at its operating point which leads to

$$
\begin{bmatrix} C_{\mathrm{dc}}\dot{\hat{U}}_{\mathrm{dc},1} \\ C_{\mathrm{dc}}\dot{\hat{U}}_{\mathrm{dc},2} \\ L_{\mathrm{dc}}\dot{\hat{I}}_{\mathrm{cable}} \end{bmatrix} = \begin{bmatrix} -\frac{P_{\mathrm{dc},1,0}}{U_{\mathrm{dc},1,0}^2} & 0 & -1 \\ 0 & 0 & 1 \\ 1 & -1 & -R_{\mathrm{dc}} \end{bmatrix} \begin{bmatrix} \hat{U}_{\mathrm{dc},1} \\ \hat{U}_{\mathrm{dc},2} \\ \hat{I}_{\mathrm{cable}} \end{bmatrix}
$$
$$
+ \begin{bmatrix} 0 \\ 1 \\ 0 \end{bmatrix} \hat{I}_{\mathrm{dc},2} + \begin{bmatrix} \frac{1}{U_{\mathrm{dc},1,0}} \\ 0 \\ 0 \end{bmatrix} \hat{P}_{\mathrm{dc},1} \quad .
\tag{3.56}
$$

The transfer function for the DC voltage, assuming that $\hat{P}_{\mathrm{dc},1} = 0$, has the form

$$
G_{\mathrm{Udc}}(s) = \frac{\hat{U}_{\mathrm{dc},2}(s)}{\hat{I}_{\mathrm{dc},2}(s)} = \frac{\alpha_2 s^2 + \alpha_1 s + \alpha_0}{\beta_3 s^3 + \beta_2 s^2 + \beta_1 s + \beta_0} \quad .
\tag{3.57}
$$

The values α_2, α_1, α_0 and β_3, β_2, β_1, β_0 are listed in Table 3.1.

Linearized Current Controller Tuning

With the linearization of the controllers, saturation, anti-windup and the limits of the PI-controllers are neglected and only (3.47) is considered. The linear transfer function for the d-current controller is:

$$
\begin{aligned}
K_{\mathrm{id},i}(s) &= \frac{\hat{i}_{\mathrm{ref},i}^d(s)}{\hat{m}_i^d(s)} \\
&= \frac{1}{2K_0 U_{\mathrm{dc},0,i}}\bigg(2K_0 m_{0,i}^d \hat{U}_{\mathrm{dc},i}(s) \\
&\quad + (X_{\mathrm{r}} + X_{\mathrm{trafo}})\hat{i}_i^q(s) - \frac{K_{\mathrm{p},\mathrm{id},i}s + K_{\mathrm{i},\mathrm{id},i}}{s} \bigg)
\end{aligned}
\tag{3.58}
$$

Table 3.1: Transfer function values for $G_{\text{Udc}}(s)$.

α_2	$=$	$2C_{\text{dc}}L_{\text{dc}}U_{\text{dc},1,0}^2$
α_1	$=$	$2C_{\text{dc}}R_{\text{dc}}U_{\text{dc},1,0}^2 + L_{\text{dc}}P_{\text{dc},1,0}$
α_0	$=$	$R_{\text{dc}}P_{\text{dc},1,0} + 2U_{\text{dc},1,0}^2$
β_3	$=$	$2C_{\text{dc}}^2 L_{\text{dc}}U_{\text{dc},1,0}^2$
β_2	$=$	$2C_{\text{dc}}^2 R_{\text{dc}}P_{\text{dc},1,0} + C_{\text{dc}}L_{\text{dc}}P_{\text{dc},1,0}$
β_1	$=$	$4C_{\text{dc}}U_{\text{dc},1,0}^2 + C_{\text{dc}}R_{\text{dc}}P_{\text{dc},1,0}$
β_0	$=$	$P_{\text{dc},1,0}$

and for the q-current controller for the rectifier is

$$
\begin{aligned}
K_{\text{iq},1}(s) &= \frac{\hat{i}_{\text{ref},1}^q(s)}{\hat{m}_1^q(s)} \\
&= \frac{1}{2K_0 U_{\text{dc},0,1}}\left(2K_0 m_{0,1}^q \hat{U}_{\text{dc},1}(s) + \hat{u}_{\text{s},1}^q(s)\right. \\
&\left. - (X_{\text{r}} + X_{\text{trafo}})\hat{i}_1^d(s) - \frac{K_{\text{p,iq},1}s + K_{\text{i,iq},1}}{s}\right) \quad .
\end{aligned}
\tag{3.59}
$$

The open loop transfer function of the inner control loop, as depicted in Figure 3.5, is derived. For the d-axis we obtain

$$
l_{\text{id},i}(s) = K_{\text{id},i}(s) \cdot G_{\text{id},i}(s) = \frac{K_{\text{p,id},i}\left(s + \frac{K_{\text{i,id},i}}{K_{\text{p,id},i}}\right)}{s\frac{X_{\text{r}}}{\omega}\left(s + R_{\text{r}}\frac{\omega}{X_{\text{r}}}\right)} \quad .
\tag{3.60}
$$

By choosing the negative zero of the controller to

$$
-\frac{K_{\text{i,id},i}}{K_{\text{p,id},i}} = -R_{\text{r}}\frac{\omega}{X_{\text{r}}} \quad ,
$$

the negative pole of the reactor is canceled. This leads to the closed loop transfer function

$$
H_{\text{id},i}(s) = \frac{\hat{i}_i^d(s)}{\hat{i}_{\text{ref},i}^d(s)} = \frac{1}{s\frac{X_{\text{r}}}{\omega K_{\text{p,id},i}} + 1} = \frac{1}{\tau_{\text{id}}s + 1} \quad .
\tag{3.61}
$$

The response from $i_i^d(s)$ to $i_{\text{ref},i}^d(s)$ is based on a first-order transfer function whose rise time is given by τ_{id}, is a design parameter that

can be freely chosen. It should be sufficiently small for a fast current controller. Therefore the parameters for the PI-controller are

$$K_{\mathrm{p,id},i} = \frac{X_{\mathrm{r}}}{\omega} \quad , \qquad\qquad K_{\mathrm{i,id},i} = \frac{R_{\mathrm{r}}}{\tau_{\mathrm{id}}} \quad . \qquad (3.62)$$

For the q-current controller tuning, the same design procedure is applied with a rise time of $\tau_{1\mathrm{q}}$.

It has been shown, that the choice of $\tau_{i,\mathrm{d}} = \tau_{1\mathrm{q}} = 50$ ms for all current controllers is reasonably fast and gives good overall responses. The calculated PI-parameters for the current controller can be found in Appendix A.2.3.

Linearized Active and Reactive Power Controller Tuning

Since the inner controller is much faster than the outer one, it can be assumed that the linear plant for the response from $i_{\mathrm{ref},1}^{q}$ to P_1 is only driven by (3.61). This leads to the following plant model:

$$G_{\mathrm{P},1}(s) = \frac{\hat{P}_1(s)}{\hat{i}_{\mathrm{ref},1}^{q}(s)} = u_{\mathrm{s},1,0}^{q} \frac{1}{s\tau_{1\mathrm{q}} + 1} + i_{1,0}^{q} \hat{u}_{\mathrm{s},1}^{q}(s) \quad . \qquad (3.63)$$

For tuning purposes, we assume that the disturbance $\hat{u}_{\mathrm{s},1}^{q}(s)$ is small and can be neglected. This leads to the open loop transfer function including the PI-controller for the active power of the form of (3.47)

$$l_{\mathrm{P},1}(s) = k_{\mathrm{P},1}(s) \cdot G_{\mathrm{P},1}(s) = \frac{u_{\mathrm{s},1,0}^{q}(K_{\mathrm{p,P},1}s + K_{\mathrm{i,P},1})}{s(s\tau_{1\mathrm{q}} + 1)} \quad , \qquad (3.64)$$

which brings us to the closed loop transfer function

$$H_{\mathrm{P},1} = \frac{\hat{P}_1(s)}{\hat{P}_{\mathrm{ref}}(s)} = \frac{\frac{1}{\tau_{1\mathrm{q}}} u_{\mathrm{s},1,0}^{q}(K_{\mathrm{p,P},1}s + K_{\mathrm{i,P},1})}{s^2 + \frac{u_{\mathrm{s},1,0}^{q}K_{\mathrm{p,P},1} + 1}{\tau_{1\mathrm{q}}}s + \frac{u_{\mathrm{s},1,0}^{q}K_{\mathrm{i,P},1}}{\tau_{\mathrm{iq}}}} \quad . \qquad (3.65)$$

The active power response follows a second-order transfer function. According to [48] it can be written in the standard form as

$$H_{\mathrm{P},1} = \frac{\left(\frac{s}{\alpha_0 \zeta \omega_{\mathrm{n}}}\right) + 1}{\left(\frac{s}{\omega_{\mathrm{n}}}\right)^2 + 2\zeta\left(\frac{s}{\omega_{\mathrm{n}}}\right) + 1} \quad , \qquad (3.66)$$

where ζ is the damping ratio, ω_{n} the undamped natural frequency and α_0 is a scaling factor of the zero. A coefficient comparison gives

$$\alpha_0 = \frac{2K_{\mathrm{i,P,1}}\tau_{\mathrm{1q}}}{\left(K_{\mathrm{p,P,1}}u_{\mathrm{s,1,0}}^q + 1\right)K_{\mathrm{p,P,1}}} \quad , \quad \omega_n^2 = \frac{u_{\mathrm{s,1,0}}^q K_{\mathrm{i,P,1}}}{\tau_{\mathrm{1q}}} \quad , \qquad (3.67)$$

$$2\zeta\omega_{\mathrm{n}} = \frac{u_{\mathrm{s,1,0}}^q K_{\mathrm{p,P,1}} + 1}{\tau_{\mathrm{1q}}} \quad . \qquad\qquad (3.68)$$

Standard quantities like the peak time t_{p} or the overshoot M_{p} express the transfer function and can be defined. Reference [48] gives a formula for both quantities in relation to ζ and ω_{n}. They can be solved for ζ and ω_{n} leading to:

$$\zeta = -\ln(M_{\mathrm{p}})\frac{1}{\sqrt{\ln(M_{\mathrm{p}})^2 + \pi^2}} \quad , \quad \omega_{\mathrm{n}} = \frac{\pi}{t_{\mathrm{p}}\sqrt{1-\zeta^2}} \qquad (3.69)$$

and substituted into (3.66) to solve for the PI-parameters:

$$K_{\mathrm{p,P,1}} = \frac{2\zeta\omega_{\mathrm{n}}\tau_{\mathrm{1q}} - 1}{u_{\mathrm{s,1,0}}^q} \quad , \qquad K_{\mathrm{i,P,1}} = \frac{\omega_n^2\tau_{\mathrm{1q}}}{u_{\mathrm{s,1,0}}^q} \quad . \qquad (3.70)$$

If α_0 is large, the zero will be far removed from the poles and thus the zero will have little effect on the response. The effect of the zero is to increase the overshoot M_{p}. Reference [48] shows that the zero has little effect if $\alpha_0 \geq 3$. If the desired design parameters fulfill this constraint then $K_{\mathrm{p,P,1}}$ and $K_{\mathrm{i,P,1}}$ can be chosen according to (3.70). Otherwise a numeric pole zero placement has to be performed to achieve the design requirements.

For the reactive power controller, the same design procedure can be used with the assumption that the disturbance $\hat{u}_{\mathrm{s},i}^q(s)$ is zero.

The control parameters are calculated according the response of an ABB VSC-HVDC light M1 link whose data are reported in Appendix A. The ABB black-box dynamic model is simulated in DIgSILENT Power Factory with the original controllers. The controller tuning and simulation of the response of the introduced dynamic model are done using MAT-LAB. The active power controller is tuned according to the step response of the ABB Model as depicted in Figure 3.8 with a peak time of $t_{\mathrm{p}} = 100$ ms and an overshoot of $M_{\mathrm{p}} = 0.14$. The PI-parameters are shown in Appendix A.2.3. Figure 3.8 shows the step responses of the ABB VSC-HVDC light M1 model (solid red curve), the nonlinear dynamic VSC-HVDC model (dashed blue curve), and the linearized

Active Power Response
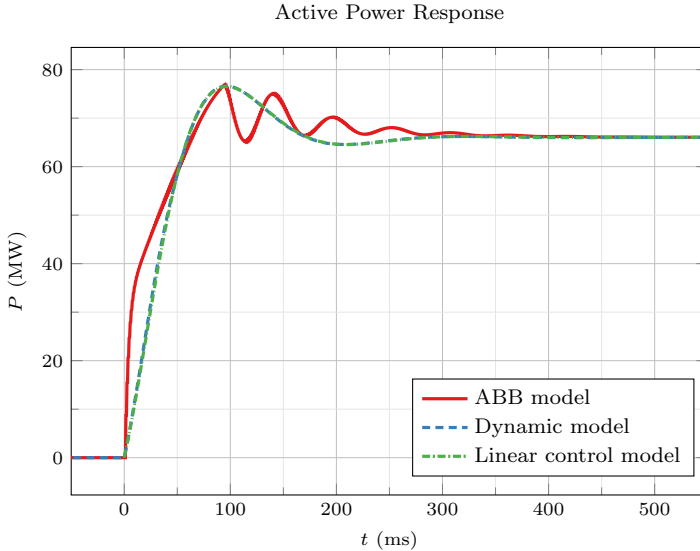
Figure 3.8: Active power step response of different VSC-HVDC models. The
red solid curve is the response of the ABB HVDC Light model
in power factory, the dashed blue curve is the response of the
introduced nonlinear VSC-HVDC model and the dash-dotted
green line is the response of the linearized control model.

control mode (dash-dotted green curve). It is seen that the nonlinear dy-
namic model and the linearized control model are very similar. The non-
linear dynamic model fulfills the design goals, rise time and overshoot,
of the ABB model. The new steady state in both models is reached in
about 250 ms.

The reactive power controller could not be tuned analytically. The re-
sponse of the reactive power in the ABB model does not have a second-
order response (red solid curve), as is seen in Figure 3.9. The response
time is quite fast. It takes about 100 ms to reach the new steady state.
This results in limiters and saturations being activated. The linear con-
trol model (dash-dotted green curve) does not have the same response
as the nonlinear dynamic model (dashed blue curve). The parameters
for the PI controllers were tuned using the MATLAB SISO design tool
and are shown in Appendix A.2.3. In Figure 3.10 the poles and zeros
of the reactive power response are shown. The negative pole/zero can-

Reactive Power Response
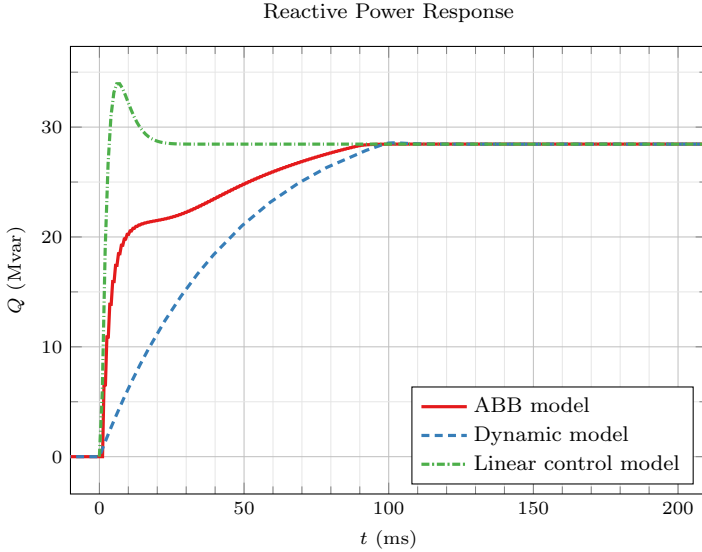
Figure 3.9: Reactive power step response of different VSC-HVDC models. The red solid curve is the response of the ABB HVDC Light model in power factory, the dashed blue curve is the response of the introduced nonlinear VSC-HVDC model and the dash-dotted green line is the response of the linearized control model.

cellation as described in the current controller can be clearly seen. This leads to a response of the reactive power controller which is similar to the one of the ABB Model. The steady states are reached at the same time. However the initial response to the step is slower. Since the ABB VSC-HVDC light model is a black-box model it is unclear what kind of control structure and limiters are used.

Linearized DC Voltage Controller Tuning

The fourth control loop comprises of the DC voltage controller. The linearized transfer function of the plant is given in (3.57). The open loop transfer function including the PI-controller is:

$$l_{\mathrm{dc}}(s) = k_{\mathrm{Udc}}(s) \cdot G_{\mathrm{Udc}}(s) = \frac{\alpha_3 s^3 + \alpha_2 s^2 + \alpha_1 s + \alpha_0}{\beta_4 s^4 + \beta_3 s^3 + \beta_2 s^2 + \beta_1 s + \beta_0} \quad , \quad (3.71)$$
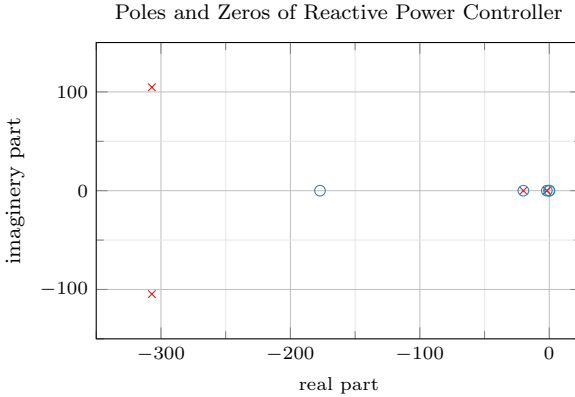
Figure 3.10: Pole zero placement of the controlled closed loop reactive power response. Poles are represented by red crosses and zero by blue circles.

where the values α_3, α_2, α_1, α_0 and β_3, β_2, β_1, β_0 are listed in Table A.3.

This leads to following closed-loop transfer function

$$H_{\mathrm{Udc}}(s) = \frac{\hat{U}_{\mathrm{dc},2}(s)}{\hat{U}_{\mathrm{dc,ref}}(s)} = \frac{\alpha_3 s^3 + \alpha_2 s^2 + \alpha_1 s + \alpha_0}{\beta_4 s^4 + \beta_3 s^3 + \beta_2 s^2 + \beta_1 s + \beta_0} \quad , \quad (3.72)$$

where the values α_3, α_2, α_1, α_0 and β_3, β_2, β_1, β_0 are listed in Table A.4.

The PI-parameters are evaluated using pole zero placement of (3.72). The poles and zeros are shown in Figure 3.11 and the parameter values are reported in Appendix A.2.3.

Figure 3.12 shows the dynamic response of $U_{\mathrm{dc},2}$ after a change of the reference value. The ABB model (red curve) is compared to the dynamic model (dashed blue curve). The overshoot of the ABB model seems quite high with $M_{\mathrm{p}} = 1.09$ with a peak of $U_{\mathrm{dc},2} = 1.2$ p.u., compared to the dynamic model of $M_{\mathrm{p}} = 1.03$ with a peak value of $U_{\mathrm{dc},2} = 1.13$ p.u.. However, the settling time is quite similar. The control response of the dynamic model is less aggressive and thus has a lower overshoot and less oscillations, which seems more reasonable than the ABB model response. The voltage response of the ABB black-box model might not be optimally tuned.
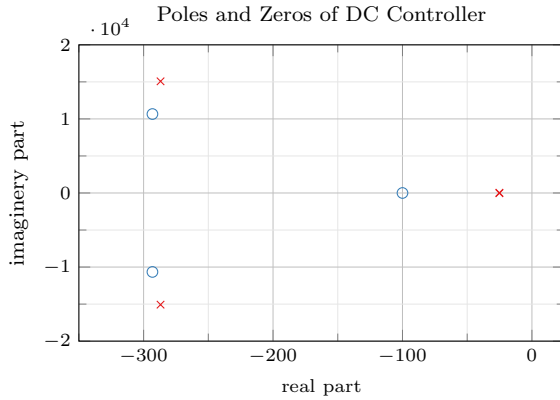
Figure 3.11: Pole zero placement of the controlled closed loop DC system.
Poles are represented by red crosses and zero by blue circles.
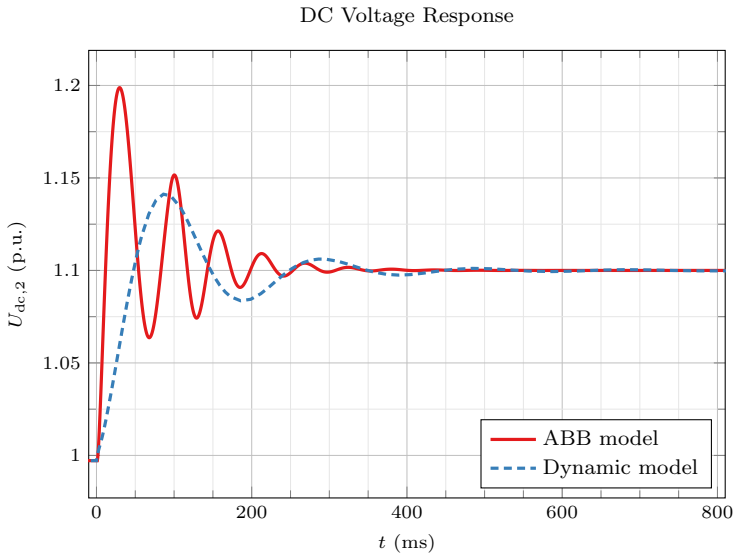
Figure 3.12: Dynamic response of the DC voltage controller after a change
in the reference value. The response of the ABB model is shown
in the red line and the response of the dynamic model with the
dashed blue line.

3.4   Simplified   Dynamic   VSC-HVDC Model

When performing studies on large power systems, simple models without significant loss of accuracy allow quicker calculations and thus a faster simulation times. This section presents a simplified HVDC model based on a second-order and first-order approximation of the dynamics and is based on the paper: *A Simplified Second Order Model of a VSC-HVDC Link for Dynamic Studies* [36]. Dynamic elements such as capacitors or inductances are replaced with their AC phasor reactances. The dynamic effect of other elements, such as the controllers, as depicted in Figure 3.5, are not modelled explicitly. However, their effect on the dynamics is modelled implicitly. The dynamic active power response is modelled by a second-order approximation, while a first order approximation models the dynamic response of the reactive power. This approximation reflects the main dynamics for large scale electromechanical transients transmission system studies.

The advantages of this approximation is a far less computational model with fewer dynamic states, and the tuning of the converter controllers is less complicated. This simple model means that the HVDC link model has a similar complexity than the generator model, which are usually described using the swing-equation [1], or forth to sixth order equivalents when including generator control.

3.4.1   Basis for simplification

A HVDC-link can be used to stabilize large power systems. Any such action will be activated by changes in the external control signals. The calculation of these set-points will be performed by an external controller, for example by a global grid controller or a local power system stabilizer. Generally, a set-point change can be considered as a step change ΔP_1, as shown in (3.73) for a change in the active power reference,

$$
P_{1,\text{ref}}^{\text{post}} = P_{1,\text{ref}} + \Delta P_1
$$
$$
\Delta P_1 = P_{1,\text{ref}}^{\text{post}} - P_{1,\text{ref}} \quad . \tag{3.73}
$$

In stability simulations of large power system studies we are normally only interested on the dynamic response of the trajectory ΔP_1 between

the initial set-point $P_{1,\text{ref}}$ and the new set-point $P_{1,\text{ref}}^{\text{post}}$ for the active and reactive power of the HVDC link.

As can be seen from Figure 3.13a, the active power step response of the detailed black-box model supplied by ABB, shown by the solid red curve, can be approximated by a second-order response, shown with the dashed blue curve. The suitable tuning of the second-order response is done in the next section. Figure 3.13b shows the reactive power step response. The solid red curve shows again the response of the full-detailed ABB black-box model. It has approximately the same nature as a first-order response, dashed blue curve. The suitable tuning of the first-order response is shown in the next section.

The simplified dynamic model of the HVDC link is shown in Figure 3.14. All dynamic elements, such as capacitors or inductances, are replaced by their phasor equivalents on the AC side. Capacitors are substituted by an open circuit, and inductances by a short circuit on the DC side.

3.4.2   Simplified VSC-HVDC Model including Control Structure

The proposed simplified system structure is shown in Figure 3.15. The HVDC voltage controller is assumed to be ideal and therefore $U_{\text{dc},2}$ can be assumed to be constant. The active power response is approximated by a second-order transfer function $H_{\text{P}}(s)$ and the reactive power responses by first-order transfer functions $H_{\text{Q1}}(s)$ and $H_{\text{Q2}}(s)$. There are two different control modes for the reactive power references. Either the converter is in voltage control mode, where the voltage at the system bus is controlled to a reference voltage and the reactive power reference is calculated by a PI-controller, or the converter is in reactive power control mode. In this mode, the reactive power reference is given by an external controller.

All AC components are modelled in the rotating dq-reference frame. The q-axis of the rotating reference frame is aligned with the AC system voltage $\underline{u}_{\text{s},i}$, hence $u_{\text{s},i}^d = 0$. By aligning the dq-reference frame to the system voltage, the following equations for the active and reactive power can be derived:

$$P_i = u_{\text{s},i}^q \cdot i_i^q \tag{3.74}$$

$$Q_i = u_{\text{s},i}^q \cdot i_i^d \tag{3.75}$$

Active Power Step

(a)

Reactive Power Step

(b)
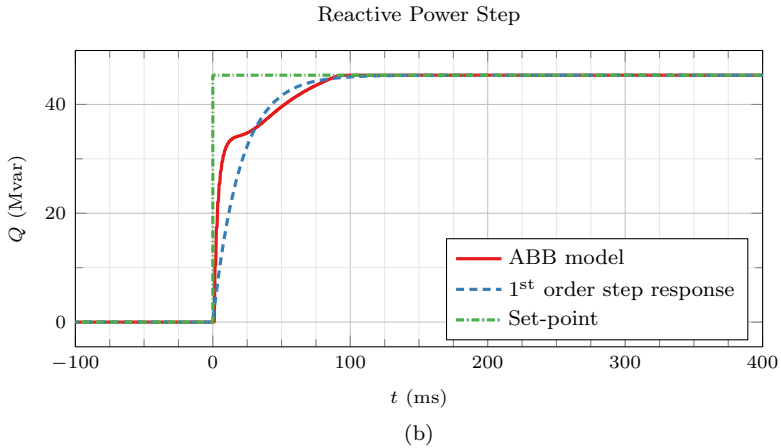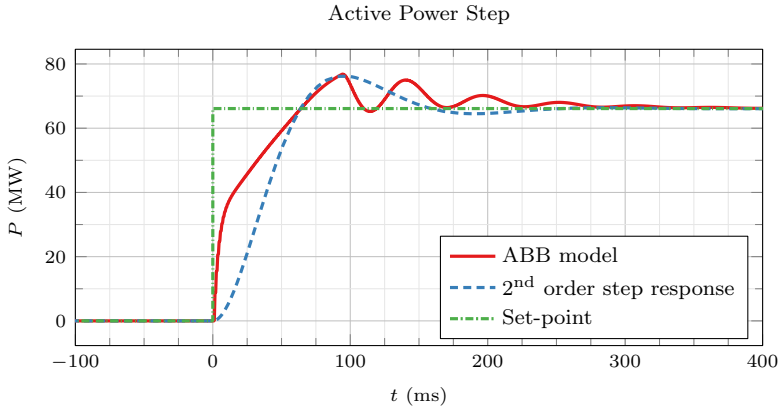
Figure 3.13: Step response for (a) active power step response of ABB HVDC light black-box model (solid red curve), second-order model fit (dashed blue curve), set-point (dash-dotted green curve) and (b) reactive power step response of ABB HVDC light black-box model (solid red curve), first-order model fit (dashed blue curve), set-point (dash-dotted green curve).
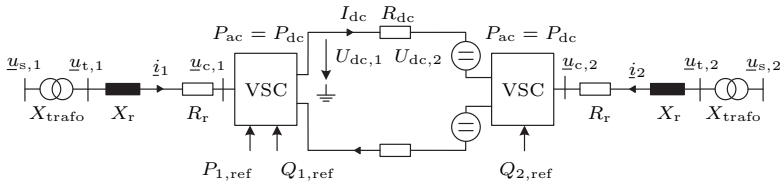
Figure 3.14: Single line diagram of the simplified VSC-HVDC dynamic model.
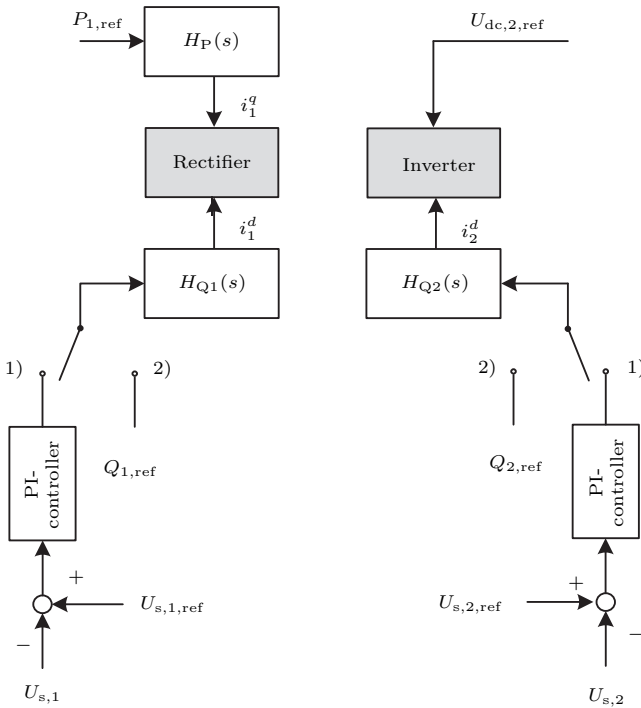
Figure 3.15: Simplified control scheme of the VSC-HVDC link.

The equations (3.74) and (3.75) show that the active and reactive power can be controlled independently by the corresponding currents i^q and i^d.

Active Power Response

A second-order system $H_{\mathrm{PT2}}(s)$ can be written in standard form

$$H_{\mathrm{PT2}}(s) = \frac{K}{s^2 + 2\zeta\omega_{\mathrm{n}}s + \omega^2} \quad , \tag{3.76}$$

where ζ is the damping ratio, ω_{n} is the undamped natural frequency and K is a scaling factor [48]. Measurable quantities like the peak time t_{p} and the overshoot M_{p} can be used to express the transfer function, with the relationships given in (3.77) and (3.78):

$$\zeta = -\log\left(M_{\mathrm{p}}\right) \frac{1}{\sqrt{\log\left(M_{\mathrm{p}}\right)^2 + \pi^2}} \tag{3.77}$$

$$\omega_{\mathrm{n}} = \frac{\pi}{t_{\mathrm{p}}\sqrt{(1 - \zeta^2)}} \tag{3.78}$$

From (3.74) it follows that the active power P_1 is controlled by i_1^q. This leads to following active power controller:

$$H_{\mathrm{P}}(s) = \frac{i_1^q(s)}{P_{\mathrm{ref}}(s)} = \frac{K}{s^2 + 2\zeta\omega_{\mathrm{n}}s + \omega_{\mathrm{n}}^2} \cdot \frac{1}{u_{\mathrm{s}}^q(s)} \tag{3.79}$$

The input is the reference power and the output is the q-current. The parameters are obtained from the step response of the ABB black-box model depicted in Figure 3.13a and are stated in Appendix A.3. Therefore the damping ζ and natural frequency ω_{n} can be calculated using (3.77) and (3.78). The gain K can be calculated by the final value theorem

$$\lim_{t\to\infty} h_{\mathrm{P}}(t) = \lim_{s\to 0} H_{\mathrm{P}}(s) = u_{\mathrm{s}}^q(s) \quad , \tag{3.80}$$

which leads to

$$K = \omega_{\mathrm{n}}^2 \quad . \tag{3.81}$$

Reactive Power Response

A first-order response can be written as:

$$H_{\mathrm{PT1}}(s) = \frac{1}{\tau_{\mathrm{Q}} s + 1} \tag{3.82}$$

where τ_{Q} is the settling time and a tuning parameter. Equation (3.75) shows that the reactive power Q_i is controlled by i_i^d. This leads to following reactive power controller:

$$H_{\mathrm{Q}i}(s) = \frac{i_i^d(s)}{Q_{i,\mathrm{ref}}(s)} = \frac{1}{\tau_{\mathrm{Q}} s + 1} \cdot \frac{1}{u_{\mathrm{s}}^q(s)} \tag{3.83}$$

The input is the reference value of the reactive power and the output is the d-current of the VSC terminal. The parameters are derived from the step response of the ABB model shown in Figure 3.13b and are stated in Appendix A.3.

Verification

In order to verify the simplified model, a case study is performed. The ABB HVDC light M1 model was chosen for the case study. The parameters of the M1 model are given in Appendix A.3. The ABB black-box model is simulated using DIgSILENT Power Factory. Furthermore the dynamic model derived in Section 3.3 was also compared to the simplified model.

The dynamic performance of the different VSC-HVDC models after an active power step is shown in Figure 3.16. The dynamic response of the active power of the ABB black-box model is shown in solid red, the response of the dynamic model in dashed blue and of the simplified model in dash-dotted green. The response of the ABB benchmark model has higher-order harmonics which are not well-represented by the dynamic model and cannot be represented with the simplified model. However, the settling time t_{p} and the overshoot M_{p} of all the models are the same. The difference of the dynamic response of the active power between the dynamic and the simplified model is minor and the simplified model seems to be a good representation of the dynamic model.

Figure 3.17 shows the dynamic performance of the reactive power after a step change for the different VSC-HVDC models. The solid red

Active Power Response
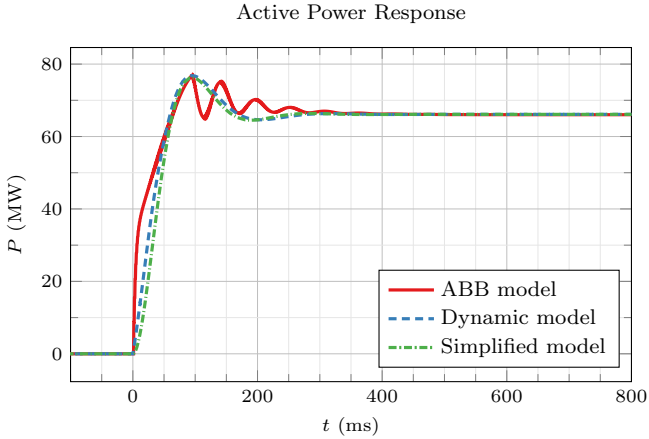
Figure 3.16: Dynamic performance of the active power for the different VSC-HVDC models after a step change of the active power reference. The solid red curve is the response of the ABB black-box model, the dashed blue curve the dynamic model and the dash-dotted green curve the simplified model.

Reactive Power Response
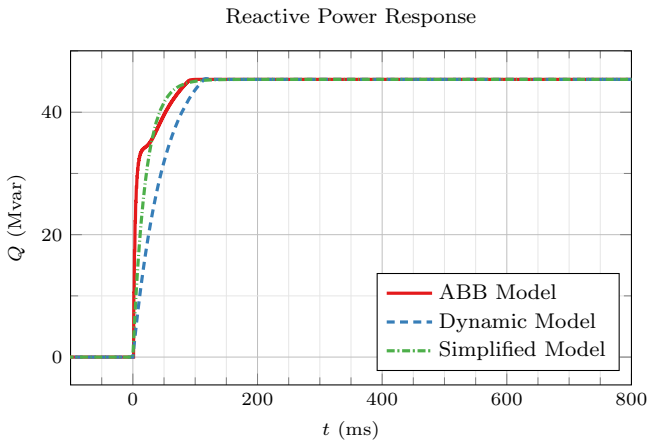
Figure 3.17: Dynamic performance of the active power for the different VSC-HVDC models after a step change of the active power reference. The solid red curve is the response of the ABB black-box model, the dashed blue curve the dynamic model and the dash-dotted green curve the simplified model.
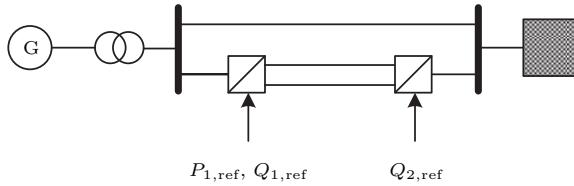
Figure 3.18: Test system with a HVDC link parallel to an AC line connected to a generator and an infinite bus.

curve represents the dynamic response of the ABB black-box model, the dashed blue curve the response of the dynamic model of Section 3.3 and the dash-dotted green the response of the simplified model. The dynamic and the simplified model have been tuned to have the same rise time τ_Q as the ABB model. Both, the dynamic as well as the simplified model, have very similar rise times. The simplified model however, has a steeper gradient and matches the response of the ABB benchmark model better than the dynamic model. However, these differences are minor.

3.4.3 Comparison between the Dynamic and the Simple Model

To compare the performance of the dynamic model with the simple model, they are simulated on a test system. It consists of a single-machine connected to an infinite bus over a 300 km long HVDC line and a 300 km long AC line in parallel. The system is shown in Figure 3.18. Both cases are simulated in MATLAB using the enhanced dynamic simulation tool based on the work of [43]. A test signal is applied to the rectifier to change the active and reactive power references $P_{1,\text{ref}}$ and $Q_{1,\text{ref}}$ at the rectifier side and the dynamic performance of the two models is compared.

Figure 3.19 (a) and (b) show the active power profile at the system bus for the rectifier and the inverter, respectively. The response of the simple model, shown by the dash-dotted green curve, has a similar behavior as the dynamic model, shown by the dashed blue curve. Some of the detailed dynamics of the dynamic model can obviously not be
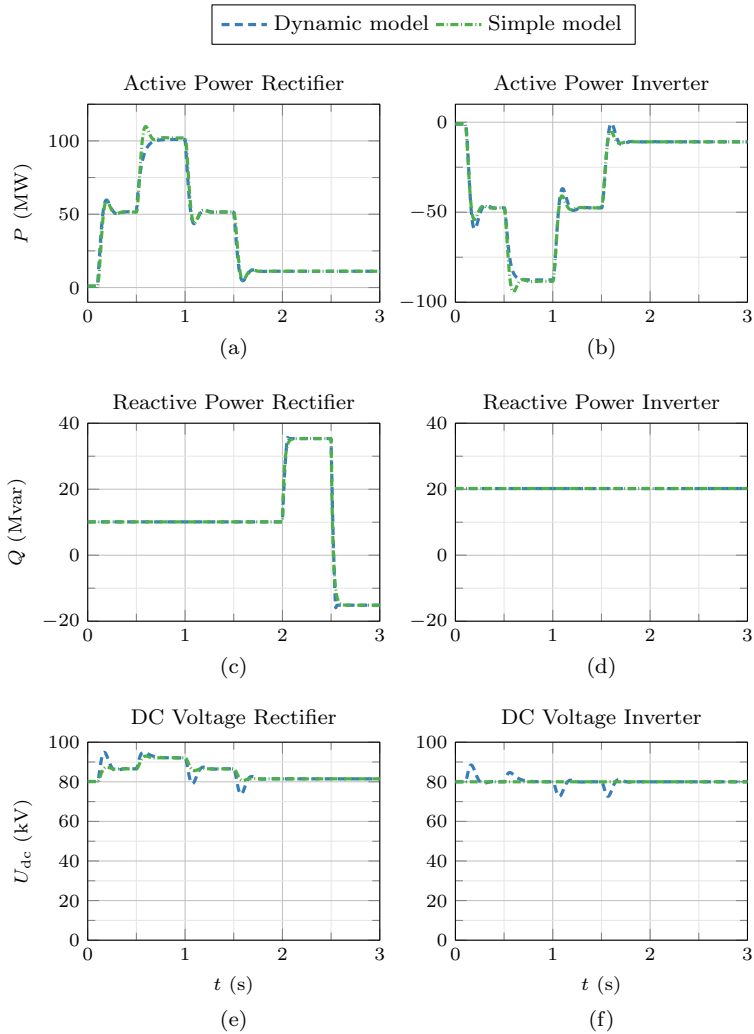
Figure 3.19: Comparison of the dynamic model (dashed blue curve) and the simple model (dash-dotted green curve). Plot (a) shows the dynamic performance of the active power at the rectifier and (b) at the inverter. Plot (c) shows the dynamic performance of the reactive power at the rectifier and (d) at the inverter. Plot (e) shows the DC voltage at the rectifier and (f) at the inverter.

captured by the simple model, in particular the response at $t = 0.5$ s. The dynamic model also captures the saturation of the PI-controllers as well as the limitations of the reference current $i_{1,\text{ref}}^q$ for the input of the current controller, seen at about $t = 0.6$ s. This is captured by the over damped system response of the dynamic model. The simple model does not consider it and therefore diverges from the response of the dynamic model.

Figure 3.19 (c) and (d) show the reactive power injection at the system bus of the rectifier and the inverter. The reactive power at the rectifier side is changed at $t = 2$ s and $t = 3$ s. The performance of the simple model compares well with the dynamic model. What also can be seen is that the active and reactive power are controlled completely independently from each other and do not interfere with each other.

Figure 3.19 (e) and (f) show the DC voltages at the rectifier and inverter, respectively. In this case, the simple model does not capture the dynamics of the DC voltage controller of the dynamic model at the inverter side. The assumption for the simple model is to have an ideal DC voltage controller at the inverter and is modelled as a DC voltage source. However, the fundamental response is included, as seen at the rectifier side. The primary interest of the simple model is the active and reactive power performance on the AC side, and the HVDC voltages are only of secondary interest.

3.5   Conclusion

This chapter presented three different VSC-HVDC models. The steady-state model can be easily integrated in existing PF or OPF formulations. The VSC is modelled as a controlled generator and only the DC constraints have to be added to an existing PF or OPF formulation.

The introduced VSC-HVDC dynamic model represents the main dynamic elements as well as the detailed converter control structure. It includes the four control loops. It can be either operated in *PQ*-mode, where the active and reactive power are controlled by an external input, or in *PU*-mode, where the active power and the terminal AC voltage is controlled by an external signal. Furthermore, a linear control model was derived from the nonlinear dynamic model to be able to tune the controllers according an ABB VSC-HVDC benchmark model. The developed dynamic model depicts the main dynamic characteristics of the ABB VSC-HVDC benchmark model. This model contains 14 dynamic states, and might not be used for large scale power system simulations or as control model for a MPC-based grid controller because of the computational complexity. Therefore a simple VSC-HVDC dynamic model was developed. The dynamic elements and the control structure are greatly simplified using only four dynamic state. However, the main dynamic characteristics of the behavior of the active and reactive power after a change in set-points according the ABB VSC-HVDC benchmark model is considered. This model may be used for large scale dynamic transient stability studies or as a control model for a MPC-based grid controller.

Chapter 4

Power Oscillation Damping

This chapter introduces a global model predictive control based controller which modulates the active and reactive power of voltage source converter-based HVDC links in a coordinated way in order to damp inter-area oscillations. The performance of the grid controller is shown in a small network as well as in a reduced model of the continental European system. This chapter is based on the publication "Stabilization of Large Power Systems Using VSC-HVDC and Model Predictive Control" in IEEE Transactions on Power Delivery [49].

4.1 Introduction

Electromechanical oscillations in power systems between interconnected synchronous generators are an omnipresent phenomenon. Stabilizing these oscillations is an essential part of the system operators' duty to ensure secure operation of the power system. Oscillation associated with a group of power plants are called inter-area modes and have a frequency in the range of 0.1 to 0.8 Hz [50]. Several techniques address the damping of inter-area oscillations using FACTS and PSS [1, 51, 52]. This chapter focuses on the stabilization of the inter-area modes with the help of VSC-HVDC links by manipulating the active and reactive power at the converter terminals.

Voltage source converter-based HVDC links are traditionally controlled based on local measurements at the converter terminals [40]. With the growing infrastructure for wide-area measurement system (WAMS), it has become possible to add a supervisory control layer, exploiting measurements of the entire power system in a coordinated way as suggested in [53] or [54]. The authors of [55] showed that with measurements from WAMS a predictive frequency stability control is possible. This supervisory layer enables static optimization of the power system's load flow [56] but can also be used to enhance the system during transients as in [57] and [58]. A coordinated approach of controlling HVDC and FACTS devices to damp multiple inter-area oscillations are proposed in [59].

The AC power injections at the VSC-HVDC terminals have to be adjusted carefully, taking into account the principal power system dynamics and the physical limitations of the AC and DC components. MPC has been found to be an efficient approach to this problem [60, 61]. This chapter proposes a MPC-based grid controller. The proposed control objective minimizes the measured instantaneous relative frequency error between the generators of the system. This enables the use of the adjustments of the HVDC injections purely for power oscillations damping. Compensation of global frequency changes due to a mismatch in the generation and load balance remains the task of the generator governor systems and of the secondary control scheme. The MPC-based grid controller repeatedly solves an optimization problem which includes several constraints, capturing the dynamics and limitations of the DC and the AC grid. After the optimization terminates, the optimal active and reactive power reference are applied by the VSC-HVDC link. Following a fixed sampling interval, the optimization is repeated.

4.2   MPC-Based Oscillation Damping Controller

The goal of the grid controller is to enhance the power grid performance during transients by manipulating the power injections of the HVDC links. A classical approach is the design of a controller to damp specific oscillatory modes of the system, based on local measurements at HVDC terminals [62, 63]. The optimal controller tuning depends on the topology of the grid, the HVDC location in the network, and the oscillatory modes of interest. Changes in either of these parameters require an ad-

justment of the controller, or have to be accounted for with sufficient robust tuning.

In contrast, a MPC-based control scheme could react to changes in the system without additional tuning [64]. This MPC-based controller was first proposed in [60]. The approach first obtains an estimate of the system models dynamic states. The future behavior of the system is then predicted and an appropriate HVDC injection is selected. To this end, an optimization problem is solved, using discrete time linear model of the system. The procedure is repeated at a fixed sampling rate.

An estimate of the global dynamic state can be obtained using WAMS, which are typically used on a slower time scale for power system monitoring, but can also operate on a faster scale for power system control [65]. While the local estimation of the grid voltage phasor is sufficiently fast [66], the implementation of the control approach also requires the communication of the measurements to the controller and of the control signals to the VSC. This thesis assumes that the system state can be directly measured and neglects the communication delays.

4.2.1 System Dynamics

To derive the prediction model for the MPC scheme, consider the nonlinear dynamic power system model given by the set of ordinary differential equations:

$$\dot{\mathbf{x}}(t) = f\left(\mathbf{x}(t), \mathbf{u}(t)\right) \qquad \mathbf{f}_0 = f(\mathbf{x}_0, \mathbf{u}_0) \qquad (4.1)$$

$$\mathbf{y}(t) = g\left(\mathbf{x}(t), \mathbf{u}(t)\right) \qquad \mathbf{y}_0 = g(\mathbf{x}_0, \mathbf{u}_0) \qquad (4.2)$$

The state vector $\mathbf{x}(t) \in \mathbb{R}^{n_x}$ contains all dynamic states of the power system. The input vector $\mathbf{u}(t) \in \mathbb{R}^{n_u}$ consists of the n_{hvdc} HVDC active and reactive power injection references ($P_{1,ref}$, $Q_{1,ref}$, $Q_{2,ref}$) that are chosen by the grid controller, and that are depicted as reference values in Figure 3.5 and Figure 3.15. The vector $\mathbf{y}(t) \in \mathbb{R}^{n_y}$ denotes the system output used to formulate the control objective. For the MPC-based controller introduced in this chapter, the frequencies of the n_{gen} are chosen as output:

$$\mathbf{y}(t) = \left[\omega_1, \ldots, \omega_{n_{gen}}\right]^{\mathrm{T}} \qquad (4.3)$$

To obtain a linear system model, the system is linearized around the current operating point $(\mathbf{x}_0, \mathbf{u}_0)$ with the corresponding time derivative

$\mathbf{f}_0$ and the output value $\mathbf{y}_0$. The linear model is given by

$$\dot{\hat{\mathbf{x}}}(t) = \mathbf{A}\hat{\mathbf{x}}(t) + \mathbf{B}\hat{\mathbf{u}}(t) + \mathbf{f}_0 \qquad (4.4)$$
$$\hat{\mathbf{y}}(t) = \mathbf{C}\hat{\mathbf{x}}(t) + \mathbf{D}\hat{\mathbf{u}}(t) \quad , \qquad (4.5)$$

where

$$\hat{\mathbf{x}}(t) = \mathbf{x}(t) - \mathbf{x}_0 \quad , \qquad\qquad \hat{\mathbf{y}}(t) = \mathbf{y}(t) - \mathbf{y}_0 \quad , \qquad (4.6)$$

represent the linearized state and output deviation, when the power system is close to the operating point after a small input change

$$\hat{\mathbf{u}}(t) = \mathbf{u}(t) - \mathbf{u}_0 \quad . \qquad (4.7)$$

The global MPC-based grid controller operates with a constant sampling time T_{mpc}. During one sampling period, the set-points of the HVDC links $\mathbf{u}(t)$ are constant, leading to the discrete time equivalent formulation of (4.4) and (4.5):

$$\hat{\mathbf{x}}_{k+1} = \hat{\mathbf{A}}\hat{\mathbf{x}}_k + \hat{\mathbf{B}}\hat{\mathbf{u}}_k + \hat{\mathbf{f}}_0 \qquad (4.8)$$
$$\hat{\mathbf{y}}_k = \hat{\mathbf{C}}\hat{\mathbf{x}}_k + \hat{\mathbf{D}}\hat{\mathbf{u}}_k \qquad (4.9)$$

The index k denotes the value of the signal at time t_k, that is $\hat{\mathbf{x}}_k = \hat{\mathbf{x}}(t_k)$. The discrete time matrices are computed using the matrix exponential [67]

$$\begin{bmatrix} \hat{\mathbf{A}} & \hat{\mathbf{B}} & \hat{\mathbf{f}}_0 \\ \mathbf{0} & \mathbf{0} & \mathbf{0} \end{bmatrix} = \exp\left(\begin{bmatrix} \mathbf{A} & \mathbf{B} & \mathbf{f}_0 \\ \mathbf{0} & \mathbf{0} & \mathbf{0} \end{bmatrix} \cdot T_{\mathrm{mpc}} \right) \quad , \qquad (4.10)$$

with the zeros denoting all-zero matrices of appropriate size to obtain a quadratic matrix. The discrete time matrices from (4.9) are defined as:

$$\hat{\mathbf{C}} = \mathbf{C} \qquad (4.11) \qquad\qquad\qquad \hat{\mathbf{D}} = \mathbf{D} \qquad (4.12)$$

4.2.2   Control Objective

The primary objective of the HVDC grid controller is to damp power oscillations in the AC network during power system transients. In other words, to minimize the generator frequency deviations from the average system frequency

$$\bar{\omega}(t) = \frac{\sum_{i=1}^{n_{\mathrm{gen}}} H_i \omega_i(t)}{\sum_{i=1}^{n_{\mathrm{gen}}} H_i} \qquad (4.13)$$

weighted with the n_{gen} generators inertia constants H_i. The objective function J is the squared relative frequency error

$$J(t) = \frac{\sum_{i=1}^{n_{\text{gen}}} H_i \left(\omega_i(t) - \bar{\omega}(t)\right)^2}{\sum_{i=1}^{n_{\text{gen}}} H_i} \quad , \tag{4.14}$$

with

$$\sigma_\omega(t) = \sqrt{J(t)} \tag{4.15}$$

measuring the average frequency deviation between the generators of the system. Under the assumption that $\hat{\mathbf{D}}$ from (4.9) is zero, (4.14) can be rewritten in the quadratic matrix expression

$$J_k = J(t_k) = \hat{\mathbf{z}}_k^{\text{T}} \mathbf{Q} \hat{\mathbf{z}}_k \tag{4.16}$$

with the input vector

$$\hat{\mathbf{z}}_k = [\hat{\mathbf{x}}_k^{\text{T}}, 1]^{\text{T}} \quad . \tag{4.17}$$

The matrix $\mathbf{Q}$ is defined as

$$\mathbf{Q} = \mathbf{Z}^{\text{T}} \text{diag}(\mathbf{h}) \mathbf{Z} \tag{4.18}$$

where

$$\mathbf{Z} = [\mathbf{I} - \mathbf{M}] \cdot [\mathbf{C}, \mathbf{y}_0] \tag{4.19}$$

$$\mathbf{M} = [\mathbf{h}, \dots, \mathbf{h}]^{\text{T}} \tag{4.20}$$

$$\mathbf{h} = \frac{\left[H_1, \dots, H_{n_{\text{gen}}}\right]^{\text{T}}}{\sum_{i=1}^{n_{\text{gen}}} H_i} \quad . \tag{4.21}$$

4.2.3 MPC Control Formulation

The global MPC-based grid controller solves for each sampling time k^* the quadratic optimization problem

$$\min_{\hat{\mathbf{u}}_{k^*}, \dots, \hat{\mathbf{u}}_{k^*+N-1}} \sum_{k=k^*}^{k^*+N} \hat{\mathbf{z}}_k^{\text{T}} \mathbf{Q} \hat{\mathbf{z}}_k \tag{4.22}$$

$$\text{subject to} \quad \forall k \in \{k^*, k^*+1, \dots, k^*+N\}$$

$$\hat{\mathbf{x}}_{k+1} = \hat{\mathbf{A}} \hat{\mathbf{x}}_k + \hat{\mathbf{B}} \hat{\mathbf{u}}_k + \hat{\mathbf{f}}_0 \tag{4.23}$$

$$\mathbf{u}_{\min} \leq \hat{\mathbf{u}}_k + \mathbf{u}_0 \leq \mathbf{u}_{\max} \tag{4.24}$$

$$\mathbf{d}_{\min} \leq \hat{\mathbf{u}}_{k+1} - \hat{\mathbf{u}}_k \leq \mathbf{d}_{\max} \tag{4.25}$$

The future behavior of the system is considered over the prediction horizon of N time steps. The power modulation of the VSC-HVDC links that best enhances the power system behavior is given by $\hat{\mathbf{u}}_{k^*}$, the first element of the optimization sequence. Inequality constraint (4.24) insures that the power rating limits of the VSC-HVDC link are not violated and (4.25) is a ramping constraint that defines how large the HVDC power adjustment compared to the previous control action can be. The new reference values $\mathbf{u}_{k^*} = \hat{\mathbf{u}}_{k^*} + \mathbf{u}_0$ for active and reactive power are applied to each VSC-HVDC terminal and is kept constant for the entire sampling interval $[t_{k^*}, t_{k^*} + T_{\mathrm{mpc}}]$, until a new reference value from the MPC-based grid controller is obtained.

4.3   Local Control Formulation

In order to compare the performance of the MPC-based control scheme, it is compared to the local controller introduced in [63]. The local damping controller changes the power injections of the VSC-HVDC links based on measurements obtained locally at the converter terminals. The local controller chooses the HVDC's active power adjustment ΔP_1 with a proportional differential (PD)-controller and a low-pass filter. The required measurement is the difference of the frequencies (ω_1, ω_2) at the two VSCs. The resulting transfer function of the controller is

$$\Delta P_1 = \left(K_{\mathrm{P}} + \frac{sK_{\mathrm{D}}}{1 + sT_{\mathrm{D}}} \right) \cdot (\omega_1 - \omega_2) \tag{4.26}$$

The gains of the PD-controller are selected, as in [63], to $K_{\mathrm{P}} = 150$, $K_{\mathrm{D}} = 20$ and $T_{\mathrm{D}} = 0.05$ s.

The reactive power of the VSCs at both ends are controlled in U-control mode, as defined in Figure 3.6 and Figure 3.15. The AC terminal voltage U_{s} is controlled to a reference value using a PI-controller with the notation of (3.47). The following parameters were used: proportional gain $K_{\mathrm{p}} = 12.8$ and integral gain $K_{\mathrm{i}} = 1151.7$.

4.4   Two Area System

The MPC-based grid controller from Section 4.2 is compared to the local controller of Section 4.3 and simulated on the two area system from [1].
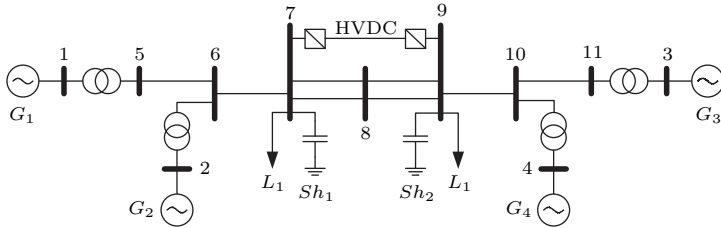
Figure 4.1: Two area 11 bus system with one VSC-HVDC link connecting the two areas at bus 7 and 9.

It consists of four thermal power plants, two load busses, two shunt compensators, and one VSC-HVDC link connecting the two areas in parallel with two AC lines from bus 7 to bus 9. The generators are modelled with a 6th order model including the subtransient states according to [24]. The governor includes a simple droop control for the frequency, and the turbine is modelled as a single reheat steam turbine according to [68]. The AVR is chosen to be an IEEE DC1A according to [1]. The loads as well as the shunts are modelled with constant impedances. The VSC-HVDC link is modelled according to the model in Section 3.3 with a length of 200 km. It has a power rating of 100 MW and a DC voltage rating of ±80 kV. The parameters of the two area system can be found in Appendix B.1.1.

The system is simulated in MATLAB with the enhanced dynamic simulator based on the work of [43]. The system is disturbed at $t = 500$ ms by loosing one of the parallel AC lines between busses 7 and 8 and between busses 8 and 9. The MPC-based grid controller operates with a sampling time of $T_{\mathrm{mpc}} = 100$ ms and a prediction horizon of $N = 10$, i.e. 1 s. The absolute power injection limits, (4.24) are 0.9 p.u. for the active power and 0.5 p.u. for the reactive power. The power ramping constraint (4.25) is set to 0.1 p.u./T_{mpc} for both the active and reactive power. The controller optimizes the VSC-HVDC active and reactive power injections in order to damp inter-area oscillations. The local controller continuously controls the voltage at the AC terminals and modulates the active power in order to damp inter-area oscillations. As a reference, a third case which does not adjust the set-points of the active and reactive power at the VSC-HVDC link was used to compare

the control strategies.

Figure 4.2 shows the frequency oscillations of the four generators for the three different simulation cases. It can be seen that for all three cases, the generators G_1 and G_2 of area 1 and the generators G_3 and G_4 of area 2 start to oscillate in different modes. If the VSC-HVDC does not modify the active and reactive power, the generators' oscillation is weakly damped and fades out in about 50 s, Figure 4.2a. The local controller is able to add additional damping to the system. The oscillations fade out after about 15 s and the initial swing has a lower amplitude, as seen in Figure 4.2b. However, the generators still oscillate in different modes. The MPC-based controller further increases the damping of the system and the initial swing has a reduced amplitude compared to the local control. The decay of the damping takes about the same time as with the local controller. However, the generators oscillate in the same mode after about 2 s, shown in Figure 4.2c. Because of the design of the MPC-based grid controller, these oscillations cannot be detected by the MPC-based grid controller and the generator control will damp these oscillations.

For a more readable comparison, Figure 4.3a shows the average grid frequency as defined in (4.13) and Figure 4.3b shows the average frequency deviation σ_ω as defined in (4.15). It can be seen that the MPC-based controller is able to minimize the frequency deviation between the generators (4.14) down to zero with the appropriate modulation of active and reactive power injections in about 2 s. The system with the local controller and no control has less damped inter-area oscillations which is shown with σ_ω. Figure 4.4 shows the AC terminal voltage of the VSC-HVDC link at bus 7, (a) and bus 9, (b), when it is not controlled, controlled with the local controller, and with the MPC-based controller. The local voltage controller is able to improve the voltage significantly compared to the case where the power injections of the VSC-HVDC link is not controlled. The MPC-based grid controller is able to control the voltages faster then the local controller, even though it is not part of its objective. Figure 4.5 shows the active and reactive power injections of the HVDC link when it is operated with the local controller, (a), and with the MPC-based controller, (b). It can be seen that in both simulation cases the active as well as the reactive power is modulated. It is also seen that the reactive power at both terminal is limited by the internal VSC control at about $t = 1$ s and after about $t = 8$ s for the local control mode. During the MPC-based controller the reactive power at the rectifier is as well limited at about $t = 1$ s.
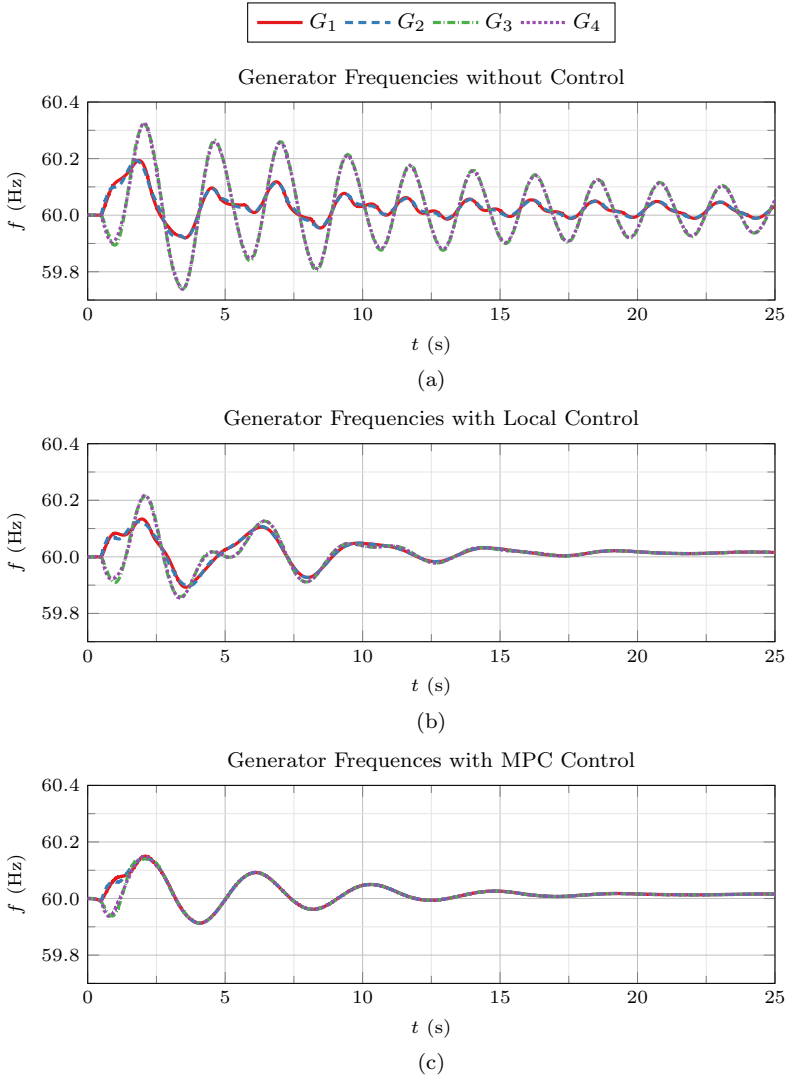
Figure 4.2: Frequency trajectories of the four generators in the two area system. (a) VSC-HVDC active and reactive power injections constant, (b) VSC-HVDC active power injections and AC terminal voltage controlled with local controller, (c) VSC-HVDC active and reactive power injections controlled by MPC-based grid controller.
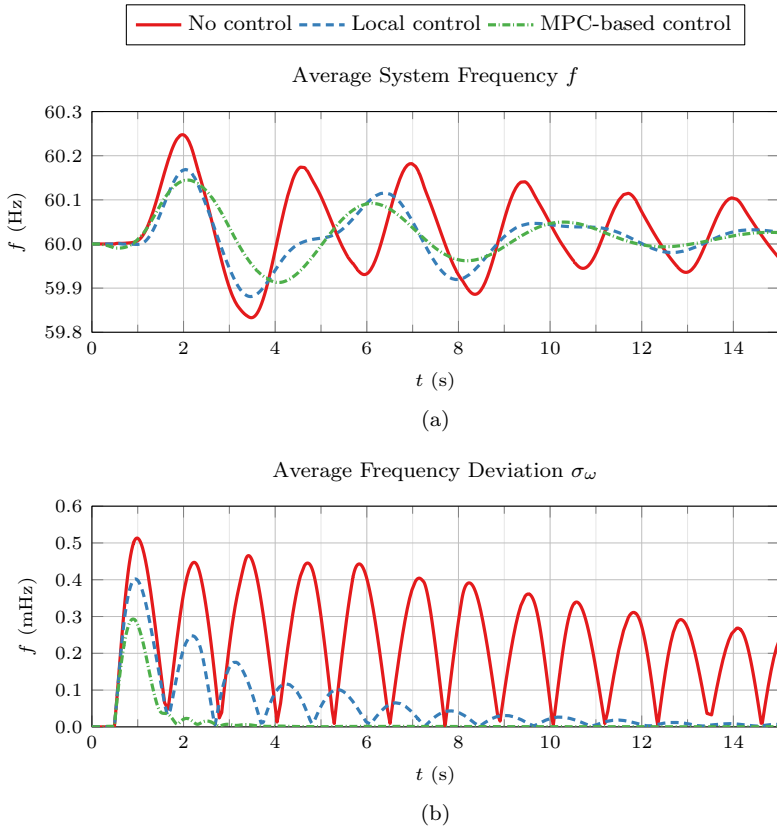
Figure 4.3: Average system frequency for the three control methods (a), and
average frequency deviation (b).
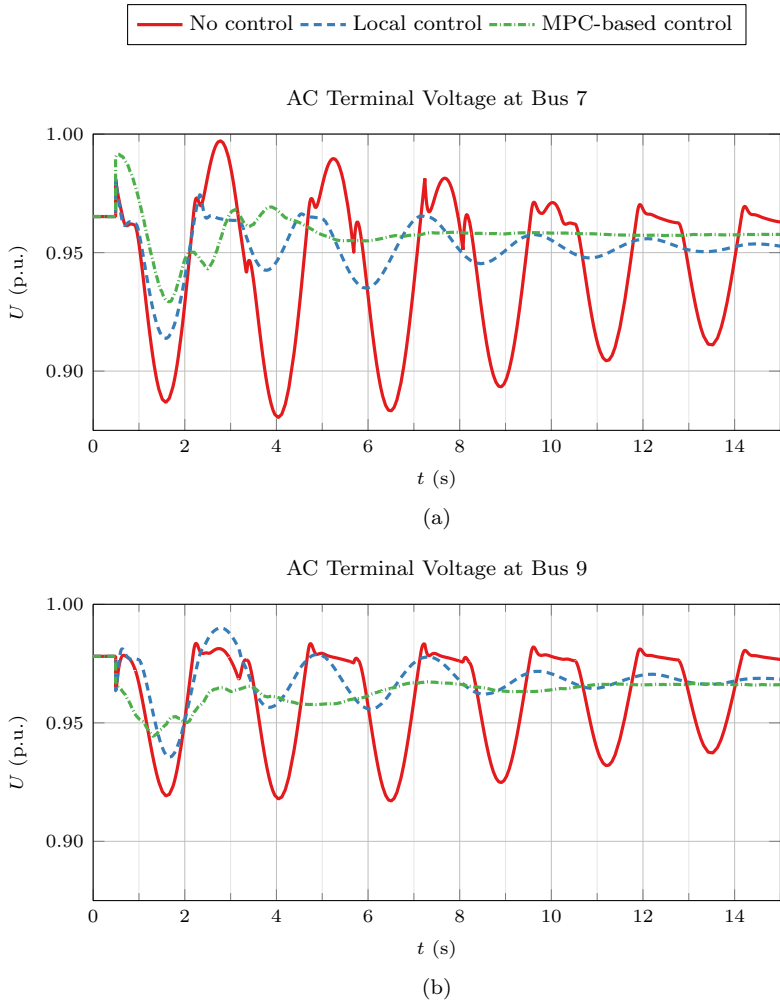
Figure 4.4: AC terminal voltage (a) at bus 7 and (b) at bus 9, where the red solid curve is without the control of the HVDC power injections, the blue dashed curve with local control and the green dash-dotted curve with MPC-based control.
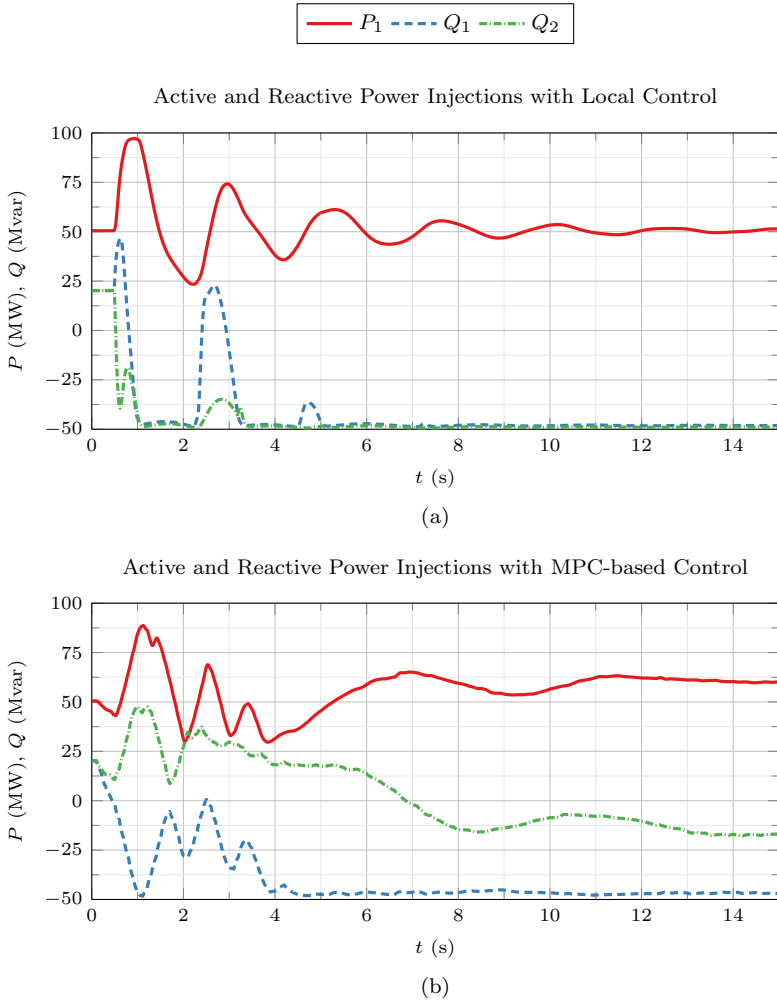
Figure 4.5: Power injections of the VSC-HVDC link when it is controlled locally, (a), or MPC-based, (b). The active power P_1, red solid curve, and reactive Q_1 are measured at bus 7, and the reactive power Q_2, green dash-dotted curve, at bus 9.
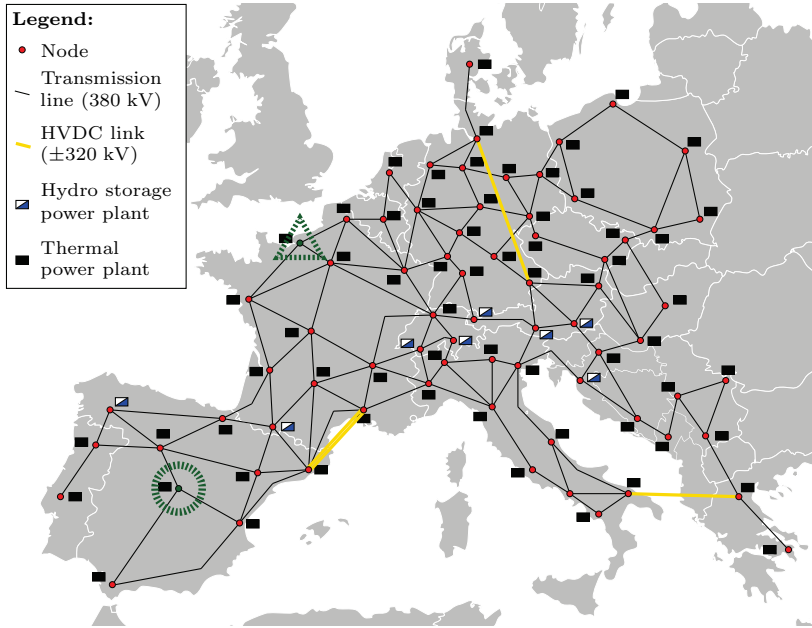
Figure 4.6: European power system.

We showed on a simple system that the MPC-based grid controller achieves better performances than in the case where the power injections of the VSC-HVDC link are not controlled and with the local control case. We now move on to a larger more realistic case study on the European system.

4.5   European System

The MPC-based grid controller is tested on a reduced dynamic model of the ENTSO-E continental grid developed in [69] and kindly provided by swissgrid, the Swiss transmission system operator (TSO). The power system topology is illustrated in Figure 4.6. It consists of 74 busses, each connected to an aggregated power plant and a load. Two different types of generation, thermal units and hydro storage units, are installed in the system. The nodes are connected by 131 AC transmission lines with a nominal voltage of 380 kV. The initial operation point of the simulated

stressed scenarios are derived from measurements of the ENTSO-E grid, with a total installed generation capacity of about 350 GW and with a load demand of about 260 GW.

The power plant models consist of an electrical and a mechanical part [69]. The electrical model comprises the AVR and the electrical part of the synchronous generator. The mechanical model comprises the primary frequency control, the turbine model, and the mechanical part of the synchronous generator. The steam power plant model with seven dynamic states includes a three-staged turbine model and a steam circuit. It provides the mechanical torque to the turbine and can be controlled by the steam valve. The hydro storage power plant model with four dynamic states contains a reservoir with a head to the turbine. The water flows via a pen-stock gallery to the turbine. The mechanical torque of the turbine is controlled by the gate valve. The synchronous generators are modelled with the standard nonlinear 6th-order model [24]. Each generator is equipped with an AVR and a governor. The ENTSO-E grid model of [69] is well damped, with PSS at all generators and with dynamic load models. To investigate HVDC-based damping in a more challenging scenario with stronger power oscillations, no PSS are incorporated in the model. Dynamic load models can both improve and deteriorate the power oscillation damping [70]. For the purpose of this chapter, loads are represented by a static model, as constant impedance loads [1], to weaken the system even more.

Four bipolar VSC-HVDC links with a DC voltage of ± 320 kV are placed in the European system as illustrated in Figure 4.6. They are modelled according the model in Section 3.3. They are placed using planned VSC-HVDC links or already existing CSC-HVDC corridors. Two parallel links connect the South of France with the Northeast of Spain. This connection is based on the France-Spain Electrical Interconnection (inelfe) project, commissioned in 2015 [71]. The inelfe transmission links use a multilevel converter arrangement. The links are 67 km long and have in total power rating of 2 432 MW. The second VSC-HVDC link connects the North of Germany with its South. It transfers the power generated by offshore wind farms in the North to load centers in the South. The link has a rated power of 1 216 MW and a length of 700 km. The third link connects southern Italy with Greece by an undersea cable. A single pole CSC-HVDC link with a power rating of 500 MW already connects Italy with Greece [72]. In this chapter, the CSC-HVDC connection is replaced with a bipolar VSC-HVDC link with a power rating of 1 216 MW. The undersea and land cables have a total

Table 4.1: HVDC links in the European system.

Location	Name	Length	Rated Power	DC Voltage
France to Spain	HVDC 1	67 km	2 432 MW	±320 kV
North to South of Germany	HVDC 2	700 km	1 216 MW	±320 kV
Italy to Greece	HVDC 3	316 km	1 216 MW	±320 kV

length of 316 km. An overview of the parameters of the VSC-HVDC links is given in Table 4.1. Note, that the total installed DC transmission capacity is relatively small, less than 2% of the total load demand and less then 8% of the total nominal load exchange.

The system is simulated in MATLAB using the enhanced dynamic simulation framework based on [43]. Two different disturbances are simulated, the loss of the nuclear power plant Paluel in France, depicted with the green triangle in Figure 4.6, and the loss of a large load in Madrid, illustrated with the green circle in Figure 4.6. For each disturbance, three different controllers to manipulate the HVDC's power injections are compared. The first controller does not control the VSC-HVDC setpoints and keeps the power injections for the entire simulation constant. The second controller uses only local measurements and is based on the controller of Section 4.3. Each VSC-HVDC link is controlled independently and there is no coordination between them. The third controller, is the proposed MPC-based grid controller. It uses global measurements and the power injections of the different VSC-HVDC links are controlled in a coordinated way. The controller operates with a sampling time of $T_{\mathrm{mpc}} = 500$ ms and a prediction horizon of $N = 10$, i.e. 5 s. The absolute power injection limits, (4.24), are 0.9 p.u. for the active power injection and 0.5 p.u. for the reactive power injections. For the power ramping constraint (4.25), 0.1 p.u./T_{mpc} for both active and reactive power is chosen.

4.5.1   Case Study: Loss of a Power Plant

This case study considers the loss of the nuclear power plant Paluel in the north of France at $t = 0.5$ s, depicted with the green triangle in Figure 4.6. The power plant has a pre-fault operating point of 1100 MW.

Figure 4.7 shows the frequency trajectories for the generators that re-
main active after the disturbance. In all three cases the system starts
to oscillate after the disturbance. There are two dominant inter-area
modes in the system: A North-South and a East-West mode. Without
a supervising grid controller, all frequencies initially decrease and result
in an unstable oscillation. The damping can be improved by the local
damping controller. However, it still remains unstable. The MPC-base
grid controller provides an effective way to stabilize and damp the oscil-
lations. For a more readable comparison, Figure 4.8a shows the average
grid frequency as defined in (4.13). The MPC-based controller is able to
damp the initial frequency drop as well as the global oscillation. Since
all VSC-HVDC links are in the same synchronous area, they are not
able to provide any primary frequency control, this is still done with
the local governors. Figure 4.8b shows the average frequency deviation
σ_ω, (4.15). This is as well a measure of the performance of the MPC-
based controller, since it reflects the objective function J, (4.14). After
about $t = 20$ s the inter-area oscillations are damped out. Furthermore,
Figure 4.9 illustrates the power exchanged through the AC network at
two internal frontiers of the ENTSO-E network. The oscillations be-
come particularly apparent near the boundaries of the network. The
injected power trajectories of the three VSC-HVDC links, controlled by
the MPC-based grid controller, are depicted in Figure 4.10. The two
parallel VSC-HVDC links, HVDC 1, connecting Spain with France are
controlled with the same control signal and the total power injections
are depicted in Figure 4.10a. The power injections of the VSC-HVDC
links in Germany, HVDC 2, and between Italy and Greece, HVDC 3,
are illustrated in Figure 4.10b, and Figure 4.10c, respectively. The dis-
crete changes of the reference value can be seen in power injections of
all links. The controller uses the controllability of both active and re-
active power of all the installed VSC-HVDC links. Figure 4.11 depicts
the VSC-HVDC power injections changed by the local grid controller.
The local grid controller modulates the set-points of the VSC-HVDC
links much less, and therefore not fully utilizing the controllability of
the VSC-HVDC links.
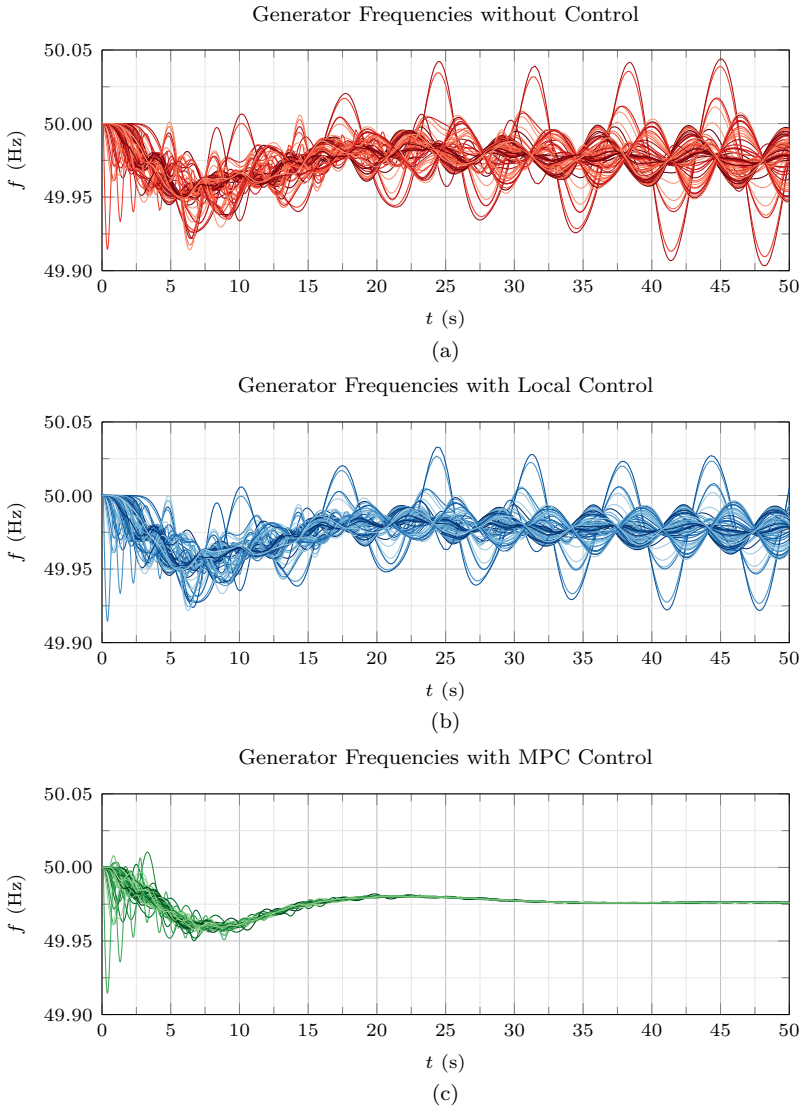
Figure 4.7: Frequency trajectories of all the generators. (a) HVDC power injections kept constant, (b) damping controller using local measurements, (c) MPC-based grid controller.
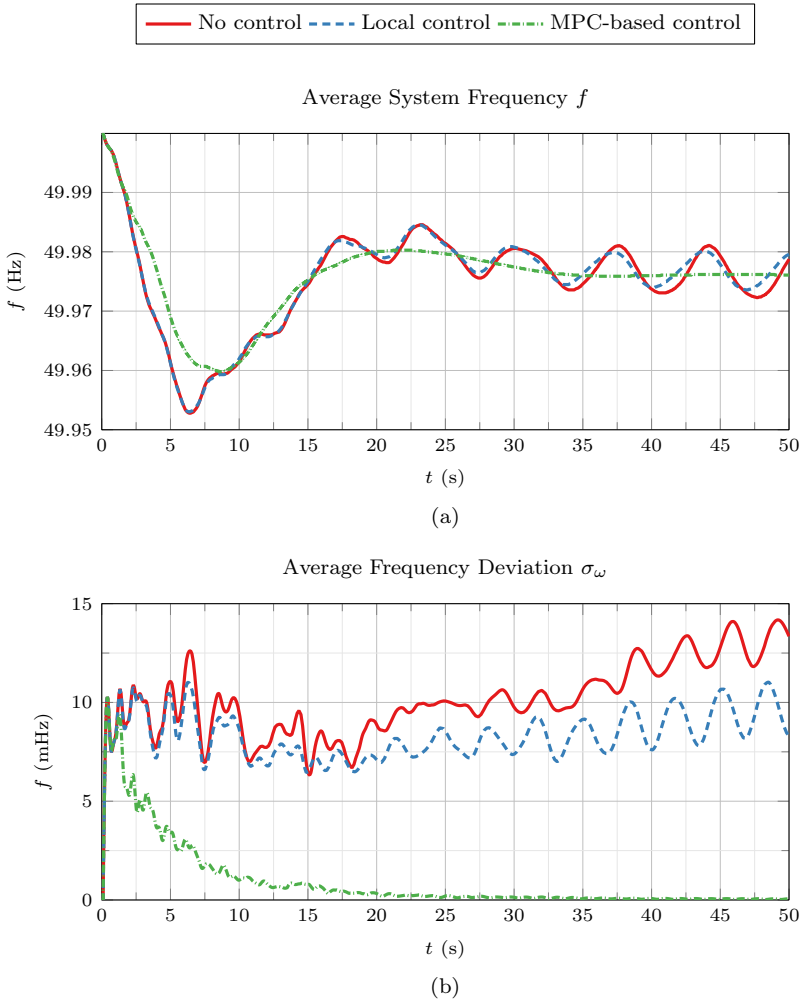
Figure 4.8: Average frequency f, (a), and average frequency deviation σ_ω, (b), when HVDC injections kept constant (red solid curve), HVDC injections controlled locally (blue dashed curve), and HVDC injections controlled by MPC-based controller (green dash-dotted curve).
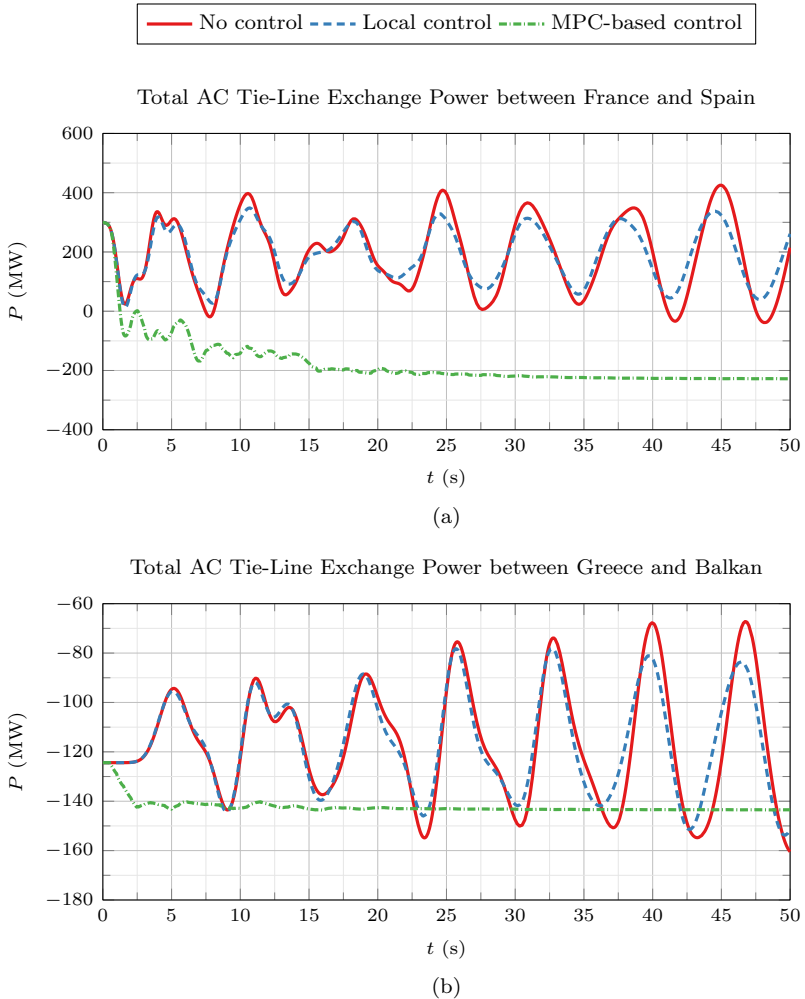
Figure 4.9: Total active power AC tie-line flows from France to Spain, (a), and from Balkan to Greece, (b), when HVDC injections kept constant (red solid curve), HVDC injections controlled locally (blue dashed curve), and HVDC injections controlled by MPC-based controller (green dash-dotted curve).
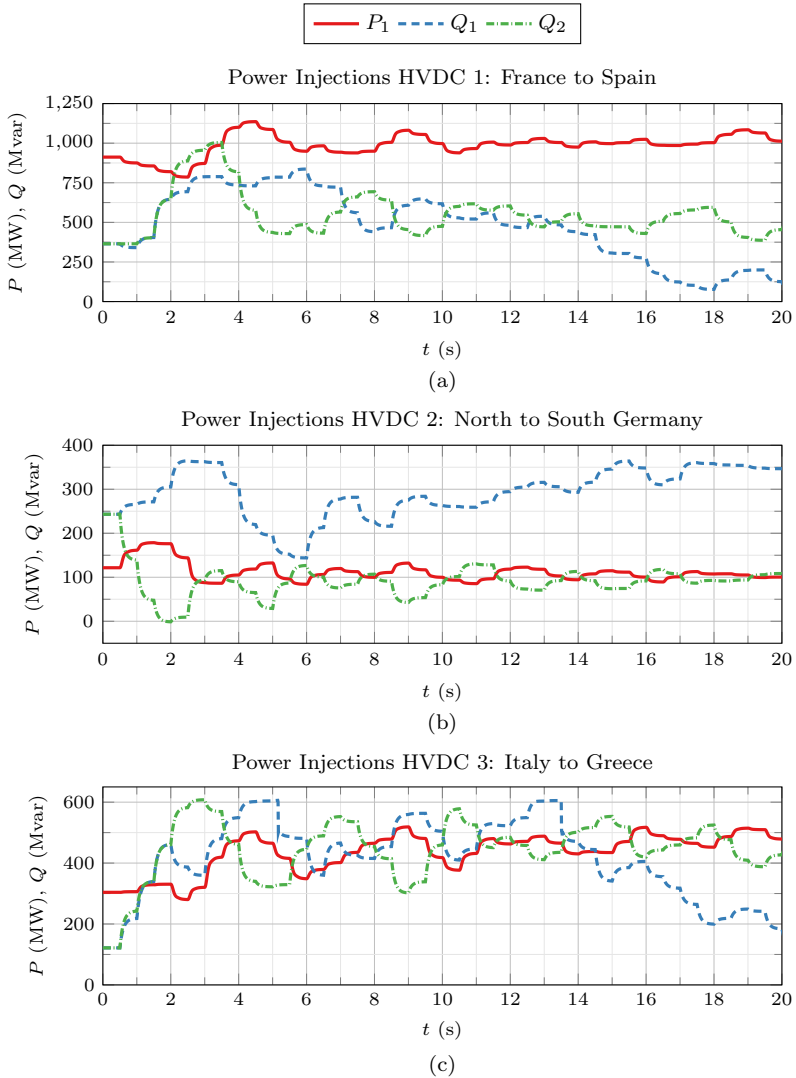
Figure 4.10: Power injections of the three HVDC links, modulated by the MPC-based grid controller, active power (red solid) and reactive power (blue dashed) at the rectifier side and reactive power at the inverter side (green dash-dotted).
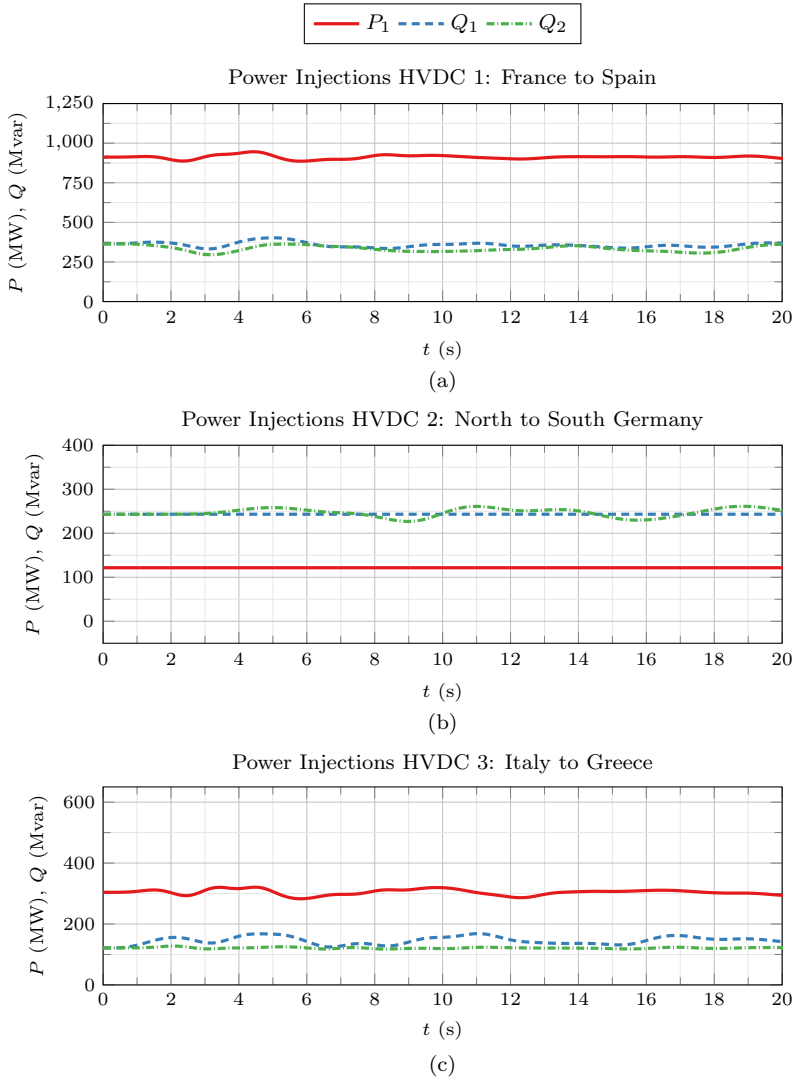
Figure 4.11: Power injections of the three HVDC links, modulated by the local grid controller, active power (red solid) and reactive power (blue dashed) at the rectifier side and reactive power at the inverter side (green dash-dotted).

4.5.2   Case Study: Loss of a Load

Consider the loss of a 500 MW load in the center of Spain, illustrated
with a circle in Figure 4.6, which accounts for about 10% of the load at
this node. Figure 4.12a shows the mean frequency, as defined in (4.13), of
the ENTSO-E system for the three different control cases. If the HVDC
terminals do not adapt the power injections, the system is unstable.
The local controller is able to add additional damping to the system
and stabilize it. However, not enough to efficiently damp the inter-area
oscillations. In contrast, the MPC-based controller not only reduces the
first swing response, but also efficiently damps the inter-area oscilla-
tions. Again, the VSC-HVDC are not able to participate on the primary
frequency control because they are within the same synchronous area.
The generators still provide the primary frequency control and guide the
system to a new equilibrium. Figure 4.12b shows the average frequency
deviation σ_ω. It demonstrates, that the MPC-based controller is able
to minimize the frequency deviation between the generators, according
the objective J, and therefore minimize the inter-area oscillations. Fig-
ure 4.13 shows the total AC tie-line power flows between France and
Spain, (a), and between Greece and the Balkan, (b). If the power of the
VSC-HVDC links is not modulated, strong power oscillations of peak-to-
peak values of up to 700 MW occur. The MPC-based controller is able
to reduce and cancel these oscillations. Figure 4.14 shows the modulated
power injections by the MPC-based grid controller for all three installed
VSC-HVDC links. All three VSC-HVDC links modulated their active
and reactive power and contribute to the damping of the system. The
reactive power at the rectifier of the connection Italy-Greece, depicted
in Figure 4.14c, sometimes reaches the reactive power limits of 0.5 p.u..
Figure 4.15 shows the power injections of the three VSC-HVDC links
when they are controlled by the local grid controller. As in the previous
section, the local controller is not able to utilize the full controllability
of the VSC-HVDC links and does not modulate the active and reactive
power in a large extent.
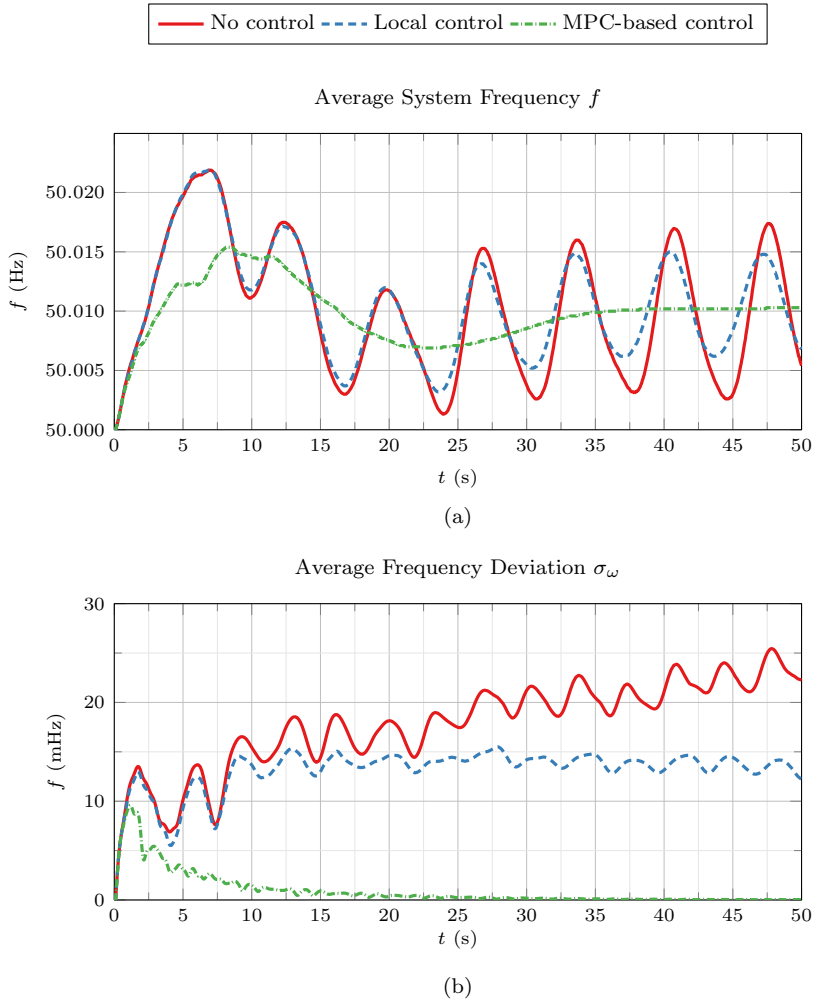
Figure 4.12: Average frequency f, (a), and frequency deviation σ_ω, (b), when the HVDC injections kept constant(red solid curve), HVDC injections controlled locally (blue dashed curve), and HVDC injections controlled by MPC-based controller (green dash-dotted curve).
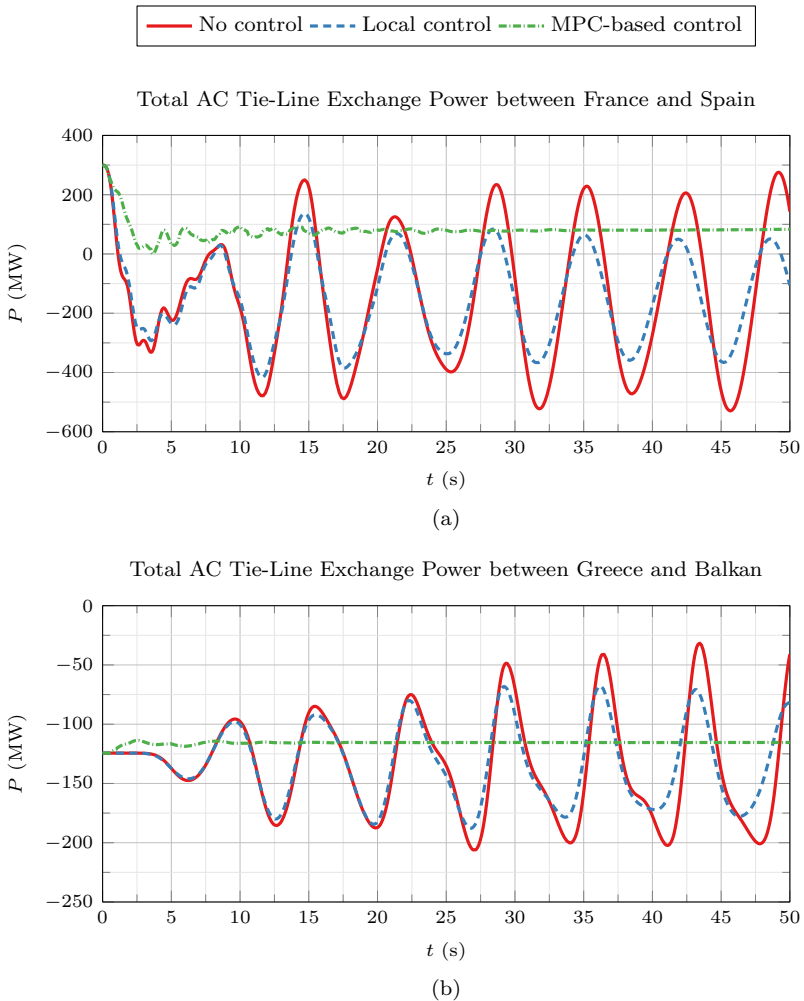
Figure 4.13: Total active power AC tie-line flows from France to Spain, (a), and from Balkan to Greece, (b), when the HVDC injections kept constant(red solid curve), HVDC injections controlled locally (blue dashed curve), and HVDC injections controlled by MPC-based controller (green dash-dotted curve).
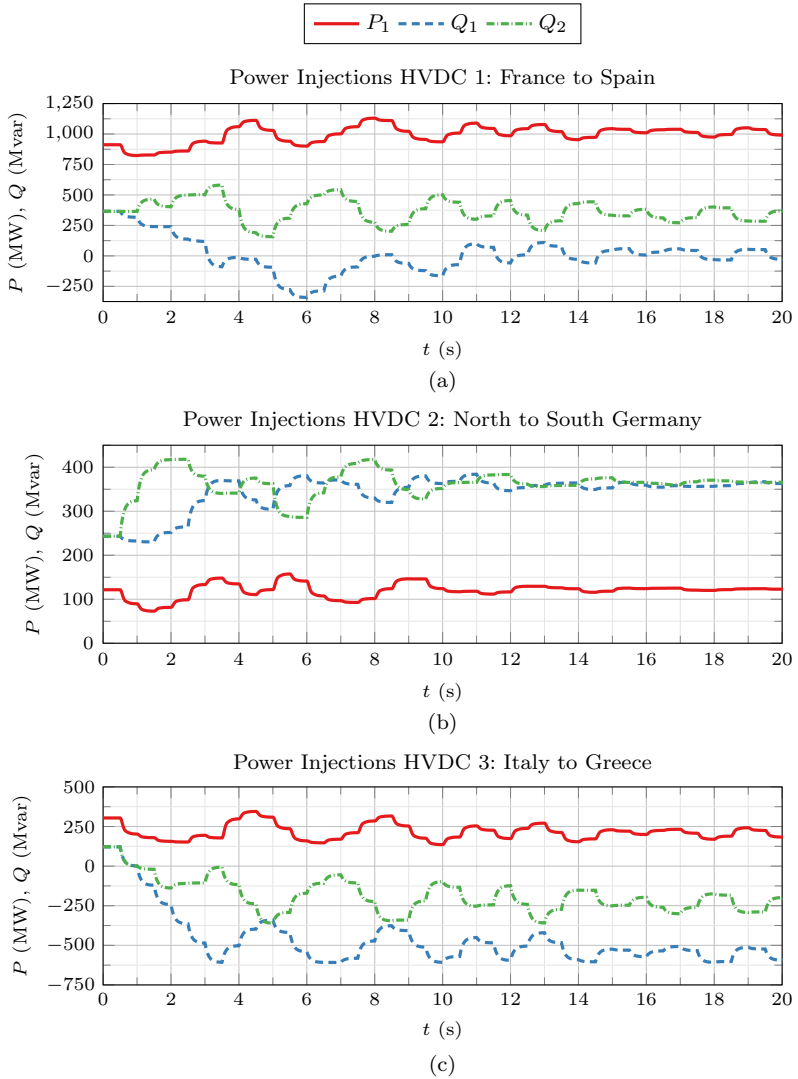
Figure 4.14: Power injections of the three HVDC links, modulated by the MPC-based grid controller, active power (red solid) and reactive power (blue dashed) at the rectifier side and reactive power at the inverter side (green dash-dotted).
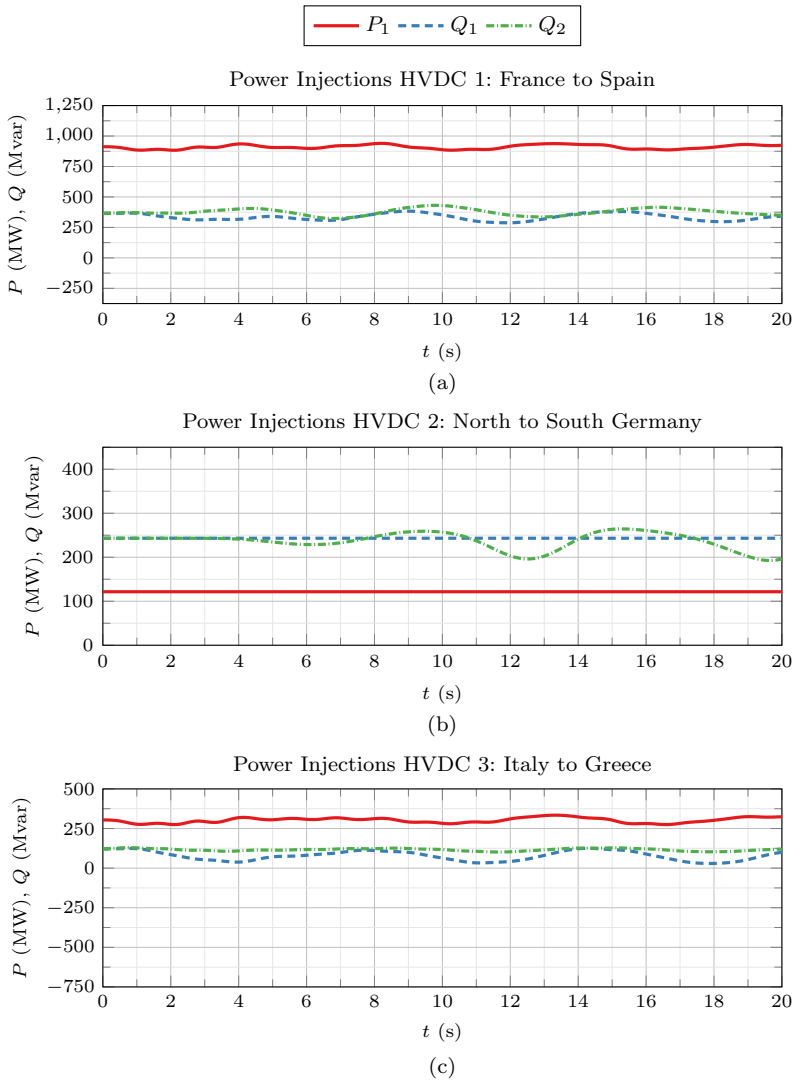
Figure 4.15: Power injections of the three HVDC links, modulated by the local grid controller, active power (red solid) and reactive power (blue dashed) at the rectifier side and reactive power at the inverter side (green dash-dotted).

4.6 Conclusion

This chapter presented a modified MPC-based grid controller based on [60]. The goal was to modulate the active and reactive power of VSC-HVDC links in a coordinated way in order to minimize the frequency deviation of all generators. This is equivalent to the goal of damping inter-area oscillations. The MPC-based grid controller takes measurements from the entire system, and builds a control model. This control model is simulated over a prediction horizon and the best VSC-HVDC active and reactive power injections which minimize the objective function are sent to the VSC-HVDC links. The MPC-based grid controller only changes the set-points with a certain sampling time. During this interval, the VSC-HVDC set-points are kept constant.

The ability of the MPC-based grid controller to damp inter-area oscillations was shown in two test systems, where one is a reduced dynamic model of the ENTSO-E continental system. Three VSC-HVDC links are placed similar as to existing HVDC projects. It had been shown, that not only the MPC-based grid controller was able to damp inter-area oscillations, but also that only three VSC-HVDC links with a total capacity of 4.8 GW were able to control the entire ENTSO-E continental system with a total load of 260 GW. It was also shown that the links like the inelfe project or the planed Germany North-South interconnector contribute a lot to damp the European system. The authors of [34] showed, that those links contribute the best damping for the existing modes in Europe.

Chapter 5

Voltage Stability Control

This chapter extends the damping controller introduced in Chapter 4 to a combined voltage stability and inter-area oscillation controller based on model predictive control. It controls the power injections of the voltage source converter-based HVDC links in the system in a coordinated way and therefore the links can provide enough damping and voltage support to reach a stable equilibrium. The controller is tested on a small network as well as on the Nordic 32 test system. This chapter is based on the publication "Voltage Stability Control using VSC-HVDC Links and Model Predictive Control" in XIII SEPOPE 2014 [73].

5.1   Introduction

Voltage instability is a major risk of blackout in a power system. For example the blackout in southern Sweden and eastern Denmark on September 23, 2003 was caused by voltage instability. A double busbar fault at a 400 kV substation in Sweden caused a triggering of events resulting in a voltage collapse in southern Sweden and eastern Denmark. The result of the blackout was a non-supplied demand of around 10 GWh in Sweden and 8 GWh in Denmark, one of the most severe disturbance in the last 30 years in Europe [74].

Voltage instability is the inability of the transmission system and generators to provide the loads with enough power [75]. This dynamic phenomena is largely driven by the load response on the voltage. Voltage

instability can be divided into two categories: Short and long-term instability [76]. The short-term voltage instability has a time scale of a few seconds and is linked with the angle instability. It may be caused by fast load recovery of induction motors and possibly HVDC systems. Long-term instability is driven by slow dynamics of a time scale of minutes. It may be caused by load tap changers, overexcitation limits of generators and load self-restorations [76]. Voltage instability can be countered either by preventive actions or emergency coordinated control. Emergency coordinated control considers switching of capacitor banks, tap changer operations and as last resort load shedding [77]. These are normally rule based and use only local measurements. The author of [78] showed that a coordinated voltage control of tap changers is beneficial for voltage stability. In [79] the authors further showed that MPC of tap changer actions is improving voltage stability. The nonlinear nature of the problem promotes a method based on a dynamic system model in order to obtain the optimal control actions.

This chapter investigates the capability of modulating the active and reactive power of VSC-HVDC links in order to enhance voltage stability. In order to do so, a MPC-based grid controller is proposed which coordinates the actions of the VSC-HVDC links and is able to predict their impact on the system. The coordination and prediction of the control actions of the VSC-HVDC links is an advantage over rule base local controller, especially in large power systems.

5.2   MPC-Based Voltage Stability Controller

The goal of the grid controller is to modulate the active and reactive power of the HVDC terminals in the system using a MPC-based control scheme.

5.2.1   System Dynamics

To determine the prediction model of the power system for the MPC scheme, consider the following set of ordinary differential equations:

$$\dot{\mathbf{x}}(t) = f\left(\mathbf{x}(t), \mathbf{u}(t)\right) \qquad \mathbf{f}_0 = f(\mathbf{x}_0, \mathbf{u}_0) \qquad (5.1)$$

$$\mathbf{y}(t) = g\left(\mathbf{x}(t), \mathbf{u}(t)\right) \qquad \mathbf{y}_0 = g(\mathbf{x}_0, \mathbf{u}_0) \qquad (5.2)$$

The state vector $\mathbf{x}(t) \in \mathbb{R}_{n_\mathrm{x}}$ contains all dynamic states of the power system. The input vector $\mathbf{u}(t) \in \mathbb{R}_{n_\mathrm{u}}$ consists of the n_hvdc HVDC's active and reactive power references

$$\begin{aligned}
\mathbf{u}(t) = [&P_{1,\mathrm{ref},1}(t), Q_{1,\mathrm{ref},1}(t), Q_{2,\mathrm{ref},1}(t), \dots, \\
&P_{1,\mathrm{ref},n_\mathrm{hvdc}}(t), Q_{1,\mathrm{ref},n_\mathrm{hvdc}}(t), Q_{2,\mathrm{ref},n_\mathrm{hvdc}}(t)]^T
\end{aligned} \qquad , \qquad (5.3)$$

which are manipulated by the MPC-based grid controller and are depicted as reference values in Figure 3.5 and Figure 3.15 for each VSC-HVDC link. The output vector $\mathbf{y}(t) \in \mathbb{R}_{n_\mathrm{y}}$ denotes the system outputs used to formulate the control objective. For the MPC-based voltage stability controller, the frequencies of the n_gen generators and n_node bus voltages magnitudes are chosen as outputs.

$$\mathbf{y}(t) = \left[\omega_1(t), \dots, \omega_{n_\mathrm{gen}}(t), U_1(t), \dots, U_{n_\mathrm{node}}(t)\right] \qquad (5.4)$$

To obtain the linear prediction model of the power system, (5.1) and (5.2) are linearized around the current operating point $\mathbf{x}_0$ with the corresponding time derivative $\mathbf{f}_0$ and the output value $\mathbf{y}_0$. Then the time discrete power system model, similar to (4.4) – (4.12), is computed:

$$\hat{\mathbf{x}}_{k+1} = \hat{\mathbf{A}}\hat{\mathbf{x}}_k + \hat{\mathbf{B}}\hat{\mathbf{u}}_k + \hat{\mathbf{f}}_0 \qquad (5.5)$$

$$\hat{\mathbf{y}}_k = \hat{\mathbf{C}}\hat{\mathbf{x}}_k + \hat{\mathbf{D}}\hat{\mathbf{u}}_k \qquad (5.6)$$

5.2.2 Control Objective

The primary objective of the MPC-based grid controller is to damp power oscillations, as in the previous chapter, and in addition to keep the AC voltage at the VSC-HVDC terminal at the desired level during power system transient. The controller cost function can be split into three parts. The first objective is the damping controller objective $J_\omega(t)$. It measures the generators' frequency deviation from the average system frequency. The second objective is the voltage controller objective $J_\mathrm{u}(t)$. It measures the voltage error at the VSC-HVDC terminals. The

third objective $J_\delta(t)$, is used to relax the voltage constraints. It is only relevant during strong transients to keep the MPC formulation feasible and also to drive the voltage magnitudes back to the operational limits, if possible. The combined cost function $J(t)$ is defined by

$$J(t) = \alpha \cdot J_\omega(t) + \beta \cdot J_{\mathrm{u}}(t) + \gamma \cdot J_\delta(t) \quad . \tag{5.7}$$

The factors α, β, and γ normalize and weight the different physical units of the three objective functions.

The primary objective of the power oscillation damping controller is to damp the frequency oscillations during transients, or in other words, to minimize frequency deviation of the generators from the average system frequency. The average system frequency $\overline{\omega}(t)$ is weighted by the inertia constants H_i of the generators,

$$\overline{\omega}(t) = \frac{\sum_{i=1}^{n_{\mathrm{gen}}} H_i \omega_i(t)}{\sum_{i=1}^{n_{\mathrm{gen}}} H_i} \quad . \tag{5.8}$$

The objective function $J_\omega(t)$ for the damping, derived in Section 4.2, is the relative squared frequency error

$$J_\omega(t) = \frac{\sum_{i=1}^{n_{\mathrm{gen}}} H_i \left(\omega_i(t) - \overline{\omega}(t)\right)^2}{\sum_{i=1}^{n_{\mathrm{gen}}} H_i} \quad , \tag{5.9}$$

with

$$\sigma_\omega(t) = \sqrt{J_\omega(t)} \tag{5.10}$$

measuring the average frequency deviation between the generators of the system frequency.

The purpose of the objective function $J_{\mathrm{u}}(t)$ is to keep the desired voltage magnitude at the HVDC terminals at a given level. The objective function $J_{\mathrm{u}}(t)$ is the squared voltage error at the HVDC terminals

$$J_{\mathrm{u}}(t) = \frac{1}{2n_{\mathrm{hvdc}}} \sum_{i=1}^{2n_{\mathrm{hvdc}}} \left(U_i(t) - U_{i,\mathrm{ref}}\right)^2 \quad , \tag{5.11}$$

with

$$\sigma_{\mathrm{u}}(t) = \sqrt{J_{\mathrm{u}}(t)} \tag{5.12}$$

measuring the average voltage deviation from the desired voltage setpoint.

Additionally, the voltage constraint

$$\mathbf{U}_{\text{min}} \leq \mathbf{U} \leq \mathbf{U}_{\text{max}} \tag{5.13}$$

ensures that $\mathbf{U} \in \mathbb{R}_{n_{\text{node}}}$, the vector of all bus voltages, stays within the limits given by the vectors $\mathbf{U}_{\text{min}}$ and $\mathbf{U}_{\text{max}}$. Since this is not always possible, for example during a short circuit, the slack variables $\boldsymbol{\delta}$ are introduced to relax the strict voltage bounds to

$$\mathbf{U}_{\text{min}} \leq \mathbf{U} + \boldsymbol{\delta} \leq \mathbf{U}_{\text{max}} \quad . \tag{5.14}$$

The use of these slack variables is minimized through the third term of the objective function

$$J_\delta(t) = \sum_{i=1}^{n_{\text{node}}} \delta_i^2(t) \quad , \tag{5.15}$$

with

$$\sigma_\delta(t) = \sqrt{J_\delta(t)} \tag{5.16}$$

measuring the voltage deviation outside the bounds.

Under the assumption, that $\hat{\mathbf{D}}$ from (5.2) equals zero, the objective functions (5.9) and (5.11) can be rewritten in the quadratic matrix expression

$$J_\omega(t) = \hat{\mathbf{z}}_k^T \mathbf{Q}_\omega \hat{\mathbf{z}}_k \tag{5.17}$$

$$J_{\text{u}}(t) = \hat{\mathbf{z}}_k^T \mathbf{Q}_{\text{u}} \hat{\mathbf{z}}_k \quad , \tag{5.18}$$

with the input vector

$$\hat{\mathbf{z}}_k = \left[\hat{\mathbf{x}}_k^T, 1 \right]^T \quad . \tag{5.19}$$

Also the voltage violation objective function (5.15) is of quadratic form with

$$J_\delta(t) = \hat{\boldsymbol{\delta}}_k^T \mathbf{Q}_\delta \hat{\boldsymbol{\delta}}_k \quad , \tag{5.20}$$

with the slack vector

$$\hat{\boldsymbol{\delta}}_k = \hat{\boldsymbol{\delta}}(t_k) = \left[\hat{\delta}_1(t_k), \dots, \hat{\delta}_{n_{\text{node}}}(t_k) \right]^T \quad . \tag{5.21}$$

To construct the matrices $\mathbf{Q}_\omega$ and $\mathbf{Q}_{\text{u}}$, the output $\mathbf{y}_0$ is partitioned to frequency and voltage outputs as in (5.4) to

$$\mathbf{y}_0 = \begin{bmatrix} \mathbf{y}_{0,\omega} \\ \mathbf{y}_{0,\text{u}} \end{bmatrix} \quad , \tag{5.22}$$

with the corresponding output matrix

$$\mathbf{C} = \left[\begin{array}{c} \mathbf{C}_\omega \\ \mathbf{C}_\mathrm{u} \end{array} \right] \quad . \tag{5.23}$$

The matrix $\mathbf{Q}_\omega$ of the damping controller is constructed as in Section 4.2 with

$$\mathbf{Q}_\omega = \mathbf{Z}_\omega^T \cdot \mathrm{diag}(\mathbf{h}) \cdot \mathbf{Z}_\omega \quad , \tag{5.24}$$

where

$$\mathbf{Z}_\omega = [\mathbf{I} - \mathbf{M}] \cdot [\mathbf{C}_\omega, \mathbf{y}_{0,\omega}] \tag{5.25}$$

$$\mathbf{M} = [\mathbf{h}, \ldots, \mathbf{h}]^T \tag{5.26}$$

$$\mathbf{h} = \frac{\left[H_1, \ldots, H_{n_\mathrm{gen}} \right]}{\sum_{i=1}^{n_\mathrm{gen}} H_i} \quad . \tag{5.27}$$

The matrix $\mathbf{Q}_\mathrm{u}$ of the voltage controller is constructed as

$$\mathbf{Q}_\mathrm{u} = \mathbf{Z}_\mathrm{u}^T \cdot \mathbf{I} \cdot \mathbf{Z}_\mathrm{u} \quad , \tag{5.28}$$

where

$$\mathbf{Z}_\mathrm{u} = [\mathbf{C}_\mathrm{u}, \mathbf{y}_{0,\mathrm{u}} - \mathbf{U}_\mathrm{ref}] \quad . \tag{5.29}$$

Finally, $\mathbf{Q}_\delta$ is given by

$$\mathbf{Q}_\delta = \mathbf{I} \quad . \tag{5.30}$$

In summary, one obtains an equivalent expression for (5.7), the discretized objective function for the MPC-based grid controller, as

$$J_k = J(t_k) = \hat{\mathbf{z}}_k^T \left(\alpha \cdot \mathbf{Q}_\omega + \beta \cdot \mathbf{Q}_\mathrm{u} \right) \hat{\mathbf{z}}_k + \hat{\boldsymbol{\delta}}_k^T \left(\gamma \cdot \mathbf{Q}_\delta \right) \hat{\boldsymbol{\delta}}_k \quad . \tag{5.31}$$

5.2.3 MPC Control Formulation

The MPC-based grid controller solves for each sampling time step k^* the quadratic optimization problem

$$\min_{\hat{\mathbf{u}}_{k^*},\ldots,\hat{\mathbf{u}}_{k^*+N-1}} \sum_{k=k^*}^{k^*+N} J_k \tag{5.32}$$

$$\text{subject to} \quad \forall k \in \{k^*, k^*+1, \ldots, k^*+N\}$$

$$\hat{\mathbf{x}}_{k+1} = \hat{\mathbf{A}}\hat{\mathbf{x}}_k + \hat{\mathbf{B}}\hat{\mathbf{u}}_k + \hat{\mathbf{f}}_0 \tag{5.33}$$

$$\mathbf{U}_{\min} \leq [\mathbf{C}_{\mathrm{u}}, \mathbf{y}_{0,\mathrm{u}}]\,\hat{\mathbf{x}}_k + \hat{\boldsymbol{\delta}}_k \leq \mathbf{U}_{\max} \tag{5.34}$$

$$\mathbf{u}_{\min} \leq \hat{\mathbf{u}}_k + \mathbf{u}_0 \leq \mathbf{u}_{\max} \tag{5.35}$$

$$\mathbf{d}_{\min} \leq \hat{\mathbf{u}}_{k+1} - \hat{\mathbf{u}}_k \leq \mathbf{d}_{\max} \quad . \tag{5.36}$$

The MPC-based controller considers the future behavior of the system over the prediction horizon of N time steps. Inequality constraint (5.34) translates to (5.14) and ensures that all voltages stay within their limits. The constraint (5.35) ensures that the rating limits of the VSC-HVDC link are not violated and (5.36) is a ramping constraint that defines how large the HVDC power adjustment compared to the previous control action can be. The active and reactive power injections of the VSC-HVDC links that best enhance the power system are given with $\hat{\mathbf{u}}_{k^*}$, the first element of the optimization sequence. The new reference value $\mathbf{u}_{k^*} = \hat{\mathbf{u}}_{k^*} + \mathbf{u_0}$ is sent to the VSC-HVDC terminals. The reference value is kept constant for the entire sampling interval $[t_{k^*}, t_{k^*} + T_{\mathrm{mpc}}]$, until a new reference value is obtained by the MPC-based grid controller.

5.3 Case Study: Two Area System

The introduced MPC-based power oscillation damping and voltage stability grid controller from Section 5.2 is tested in the two area 11 bus system from [1], depicted in Figure 4.1. A VSC-HVDC link connects area one with area two from bus 7 to bus 9. The mechanical part of the generators comprises a steam turbine with a governor and primary frequency control. The steam turbine is modelled with single reheat according to [68]. The electrical part of the generator consists of a 6th order synchronous generator model, [1]. For the AVR model, a DC current commutator of the type IEEE DC1A has been chosen [80]. The

Table 5.1: Two area system data.

Two Area data			
Installed capacity	3600 MW	Total consumption	3504 MW
Inter area exchange	407 MW	AC line 7-8 loading	147 MW
VSC-HVDC data			
HVDC rating	500 MW	HVDC loading	162 MW
P_{max}	1 p.u.	Q_{max}	0.5 p.u.
P_{min}	-1 p.u.	Q_{max}	-0.5 p.u.

nonlinear dynamic load model with exponential recovery from [81] is used. The active power has a time constant of $\tau_p = 10$ s and the reactive power of $\tau_q = 15$ s. The VSC-HVDC connection is modelled according the model introduced in Section 3.4. It has a total capacity of 500 MW. The general power system data are listed in Appendix B.1.2. Table 5.1 shows a summary of the most important system parameters.

The system is disturbed by tripping the AC line between bus 7 and 8 at $t = 0.45$ s. Three different cases are simulated. Scenario 1: The VSC-HVDC link is not controlled after the disturbance, i.e. the active and reactive power reference are kept constant. In case 2 the VSC-HVDC link is controlled with a local controller using local measurements. The active power is controlled, using the PD-controller from Section 4.3. The reactive power at both VSC terminals are modulated based on the control signal of the PI-controller, which controls the AC terminal voltage U_s. The values for the controllers are given in Appendix C.2. In the third case, the VSC-HVDC link modulates the active and reactive power controlled by the MPC-based controller introduced in Section 5.2. The MPC-based controller operates with a sampling time $T_{mpc} = 100$ ms and has a prediction horizon $N = 50$ time steps, i.e. 5 s. The active and reactive power limits, (5.35), are shown in Table 5.1. The ramping of the active and reactive power, (5.36), is constrained to ± 0.2 p.u./T_{mpc}. The weights α, β, and γ of the objective function (5.7) are chosen as follows: In the Continental European System the allowed frequency range is between 49.0 Hz and 51.0 Hz [82]. The absolute frequency deviation converted in per unit is between 0.98 p.u. and 1.02 p.u.. Therefore the allowed range is 0.04 p.u.. In contrast, the allowed

voltage range in the Continental European system is between 0.90 p.u. and 1.118 p.u. [82], which gives a range of 0.218 p.u.. α and β normalize these ranges, leading to:

$$\alpha = \left(\frac{1}{0.04}\right)^2 = 625$$

$$\beta = \left(\frac{1}{0.218}\right)^2 = 21.042$$

In comparison to β, the penalty weight γ has to be larger, since $\boldsymbol{\delta}$ is only used for relaxing the voltage constraint (5.34). It is chosen to be

$$\gamma = 1000 \quad .$$

The system is simulated using MATLAB and the optimization of the MPC-based grid controller is solved using the gurobi optimization toolbox for MATLAB [83]. Figure 5.1 shows the response of the frequencies of the generators for all three cases. Figure 5.1a shows the frequencies of the generators for the case without controlling the VSC-HVDC injections. Because of the voltage collapse, the frequencies are not stable. In Figure 5.1b, when they are controlled by the local controller the frequency deviation could be quickly stopped, however the frequency error is reduced after a long time. The MPC-based damping controller is able to minimize the frequency deviation after the fault and to stabilize the frequencies of the generators much faster as the local controller, as depicted in Figure 5.1c. Figure 5.2 shows the voltages for each AC node for all three cases. If the VSC-HVDC link is not controlled, and keeps the power set-points constant, the voltage will collapse, Figure 5.2a. However, if the VSC-HVDC link is controlled by either the local controller or the MPC-based controller the voltage collapse can be prevented and all the voltages cn be kept stable. Figure 5.3 shows the controlled AC terminal voltages at busses 7 and 9, when the power injections are either controlled locally or with the MPC-based controller. If the VSC-HVDC link is controlled locally, the voltages are controlled faster compared to the MPC-based control. The MPC-based controller operates with a constant sampling time $T_{\mathrm{mpc}} = 100$ ms. Hence there is a delay after the fault and only discrete time control actions are performed. The magnifying glass in Figure 5.2b and c shows a more detailed view of the voltages after the disturbance. The voltages in b are controlled much faster, and the time discrete change of the voltages with the MPC-based

Figure 5.1: Frequencies of all four generators. (a) shows the response without control, (b) when the HVDC power injections are controlled locally, and (c) when they are controlled using the MPC-based controller.

Bus Voltages without Control

(a)

Bus Voltages with Local Control

(b)

Bus Voltages with MPC Control

(c)
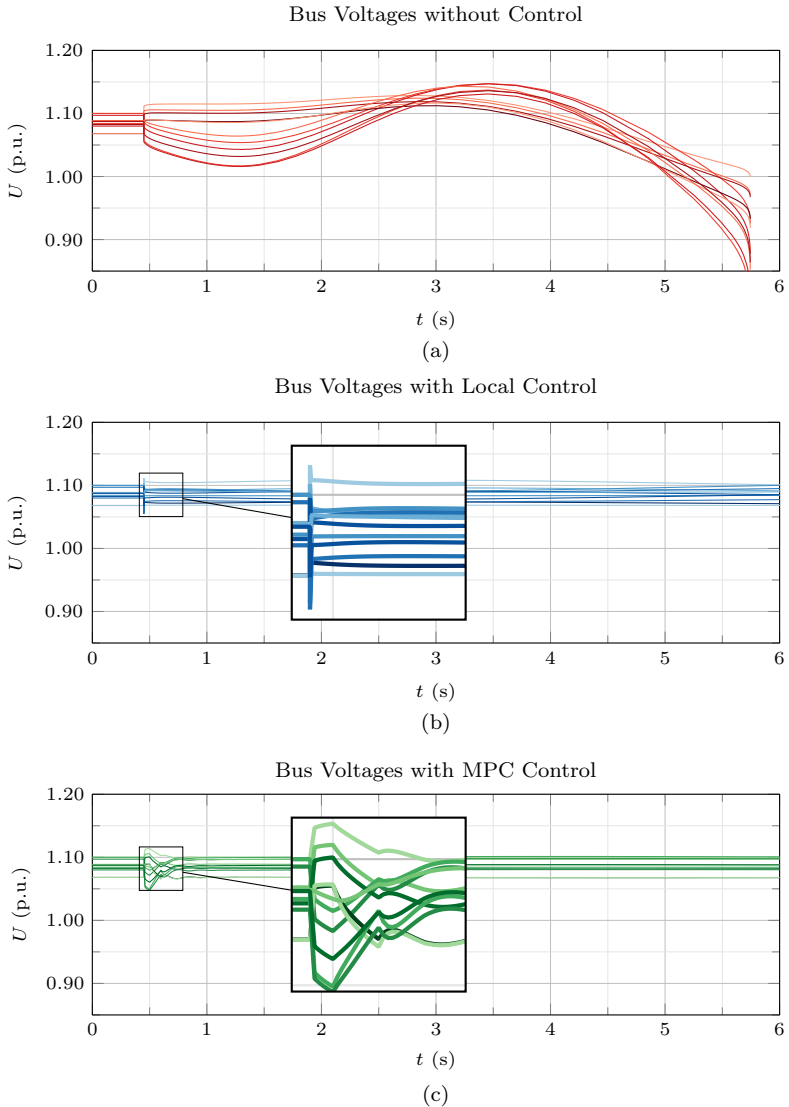
Figure 5.2: AC bus voltages at all AC nodes. (a) shows the response without control, (b) when the HVDC power injections are controlled locally, and (c) when they are controlled using the MPC-based controller.
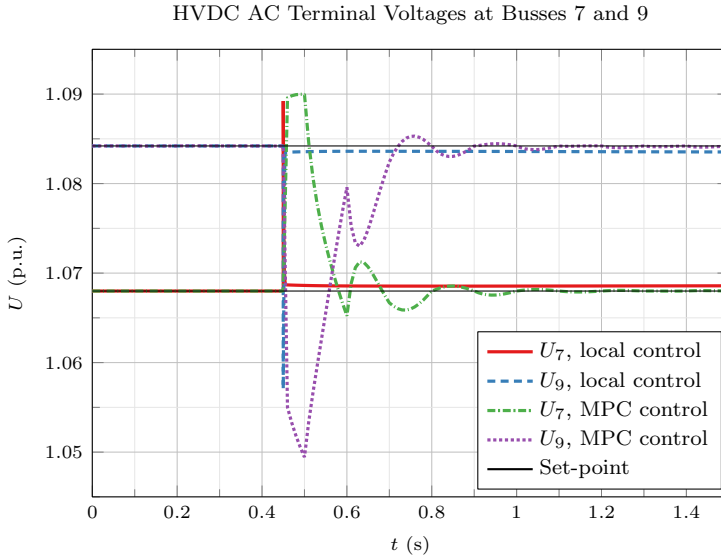
Figure 5.3: Controlled AC bus voltages, U_7 and U_9 at the VSC-HVDC terminal when HVDC power injections are controlled locally oder with the MPC-based controller.

controlled VSC-HVDC link is seen clearly. The predictive behavior of the MPC-based controller can be nicely observed in the voltage profile of U_7, in Figure 5.3. After three control actions, the voltage reaches the desired reference value, and the MPC-based grid controller is able to predict the trajectory of the voltage and stops its descent.

Figure 5.4 and Figure 5.5 show the average frequency deviation σ_ω and the average voltage deviation σ_u. It is a measure how the controllers perform based on our control objective. The local controller is not able to minimize the deviation of both the frequency nor the voltage. The local controller still has a large frequency deviation, however, the voltage deviation is reduced very quickly compared to the MPC-based controller. The discrete nature of the MPC-based controller is clearly seen. The MPC-based controller reduces with every control action the voltage deviation in the system. The global MPC-based grid controller chooses a trade-off between the two different objectives to damp power oscillation and ensure at the same time voltage stability.

Figure 5.6 shows the injected active and reactive power at the
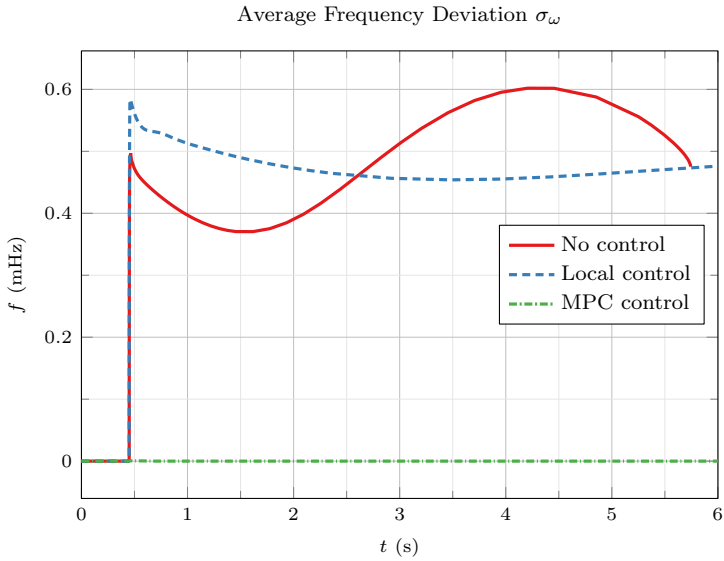
Figure 5.4: Average frequency deviation σ_ω for all three control cases.
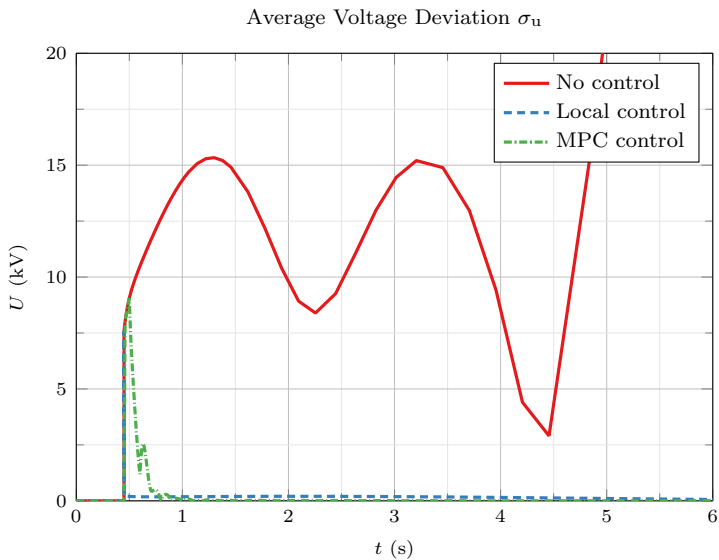
Figure 5.5: Average voltage deviation σ_u for all three control cases.
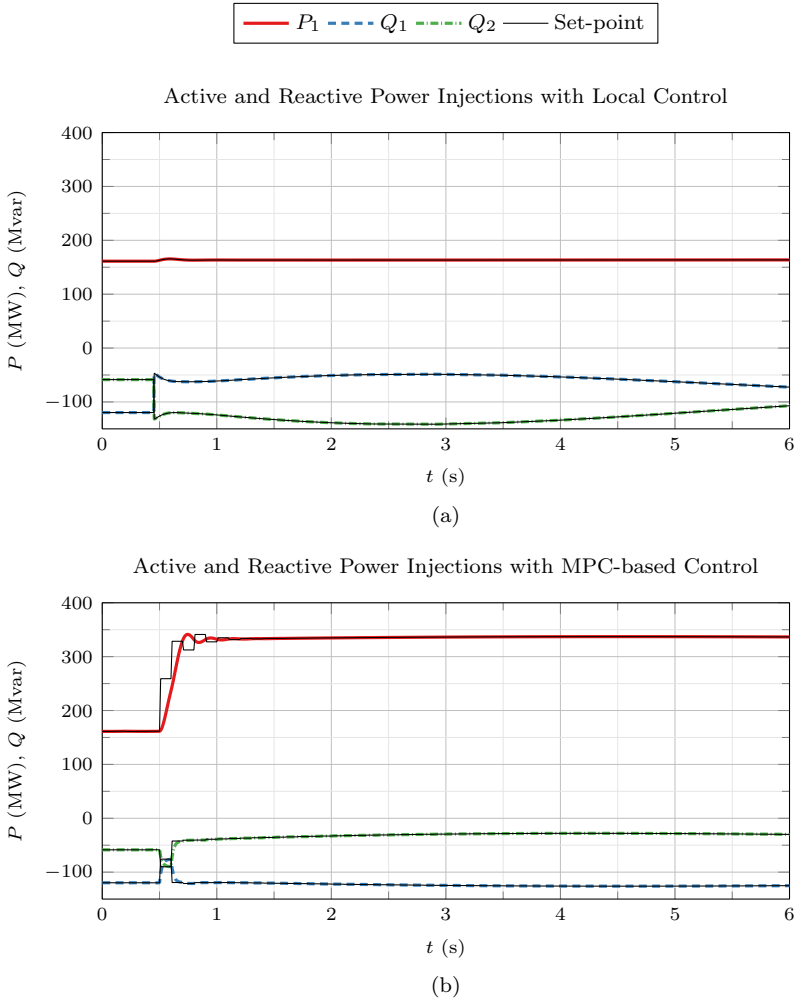
Figure 5.6: Modulated active and reactive power of the VSC-HVDC line.
(a) shows the power modulation with local control, (b) shows
the time discrete power modulation with MPC-based control.

VSC-HVDC terminals when the power injections are controlled locally and with the MPC-based control. The biggest difference is that the set-points for the MPC-based controlled HVDC link changes only with $T_{\mathrm{mpc}} = 100$ ms, whereas with the local controller they change continuously. The VSC-HVDC link, when controlled by the MPC-based controller, is able to compensate the lost transmission capacity of line 7-8 after the disturbance, and thus compensate for the frequency error between the areas much faster. Whereas when the HVDC link which is controlled locally, it does not sufficiently adjust the active power. As for the voltage response, the reactive power modulation of the local control scheme is faster than the reactive power modulation by the MPC-based controller.

Table 5.2: HVDC benchmark data in the Nordic 32 system.

Name	From	To	Length	S_B
HVDC1	4011	4044	500 km	1 216 MW
HVDC2	4031	4045	700 km	1 216 MW

5.4   Case Study: Nordic 32 System

In order to show the capability of the introduced MPC-based power oscillation damping and voltage stability controller, it is tested on the Nordic 32 test system from [84], depicted in Figure 5.7. It is a model of the Scandinavian system with very long AC lines and is often used as a test-system for voltage stability studies. It includes 20 generators, 74 AC busses, 21 tap-changing transformers, 50 AC lines within three different voltage levels and 32 loads and shunts. It consist of 4 parts: a power system equivalent, a northern, a central and a southern part. The power system equivalent and the northern part are connected through very long AC lines with the central and southern parts, where most of the load is located. In the northern and the equivalent system the electrical power production is mostly hydro with only few loads. All generators are equipped with an AVR system. The generators in the north are further equipped with a GOV system including primary frequency control. In addition, most generators damp inter-area oscillations with a PSS. Two VSC-HVDC links have been added with a power rating of 1 216 MW each. HVDC1 connects node 4011 with node 4044 and HVDC2 node 4031 with 4051. Both links connect the northern with the central part. For the VSC-HVDC links, the dynamic model from Section 3.4 is used. Some data of the VSC-HVDC link are shown in Table 5.2. In order to compensate the added capacity of the VSC-HVDC links, a parallel AC line connecting node 4031 and 4041 is removed. Additionally the loads in the central system are increased to 110% of the original data from [84]. The data of the network is shown in Appendix B.2.

The performance of the MPC-based controller is compared to two other control strategies, either by leaving the initial VSC-HVDC set-points constant or by modulating the active and reactive power with a local controller. The MPC-based controller operates with an sampling time of $T_{mpc} = 100$ ms and has a prediction horizon of $N = 9$ time steps, i.e. 0.9 s. The weighting parameters for the objective function α, β and
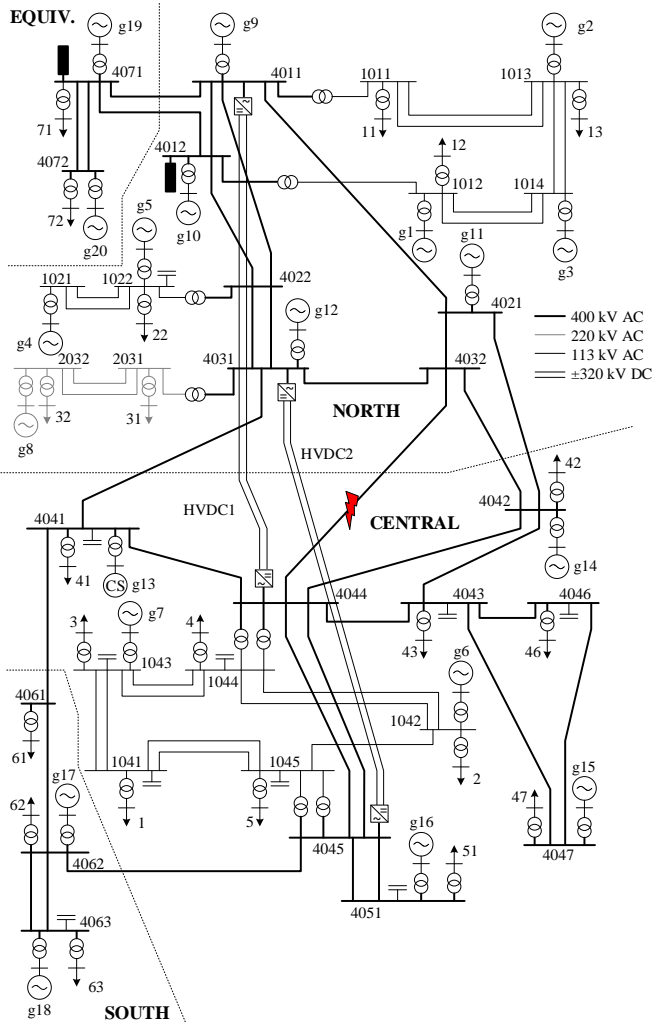
Figure 5.7: Single line diagram of the Nordic 32 test system [84] with two VSC-HVDC links and own modifications.

Table 5.3: Controller Parameters for the MPC-based grid controller.

T_{mpc}	N	α	β	γ	P	Q	d_{P}	d_{Q}
0.1 s	9	$3 \cdot 10^{-3}$	$3 \cdot 10^{-3}$	7500	± 1 p.u.	± 0.5 p.u.	± 0.5 p.u.	± 0.2 p.u.

γ are slightly changed compared to Section 5.3. Due to higher voltage instability of the system, the frequency weight α has to be reduced. In Table 5.3 an overview of the parameters used is given. The active and reactive power of the VSC-HVDC link are limited to ± 1 p.u. for the active power and ± 0.5 p.u. for the reactive power, respectively. The rate of change of the set-points from the previous control section is limited to ± 0.5 p.u./T_{mpc} for the active power and ± 0.2 p.u./T_{mpc} for the reactive power, respectively. The per unit values are referred to the rated power of the VSC-HVDC link. The local controller modulates the active power using the PD-controller from Section 4.3. The reactive power at both VSC-HVDC terminals is modulated based on the control signal of a PI-controller which controls the magnitude of the AC terminal voltage U_{s}. The values for the local controller are given in Appendix C.2.

The system is implemented in MATLAB and simulated using the enhanced dynamic simulator based of [43]. The system is initialized by calculating a semi OPF according to Section 3.2, in order to find the VSC-HVDC initial power flows. The set-points of the generators are fixed, and only the set-points of the VSC-HVDC links are optimized such that the system losses are minimized. The system is disturbed by a short-circuit on the AC line 4032–4044 at about 30% into the line from bus 4044, marked with a flash in Figure 5.7. The fault starts at $t = 100$ ms and is cleared by disconnecting that line after $t = 200$ ms. The initial power flow over that line is 957 MW from north to central. In the cases when the VSC-HVDC links were controlled locally or when the set-points kept constant, the system could not be stabilized and suffered a voltage collapse. Only the MPC-based controller was able to modulate the active and reactive power in order to stabilize the system. Figure 5.8 depicts the frequencies of all 20 generators of the system for all three cases and Figure 5.9 the AC bus voltages of the 74 for busses. If the VSC-HVDC set-points are not controlled, the system voltages collapse about $t = 2$ s after the short-circuit is cleared. The generator frequencies accelerate quite quickly to very high values because the loads are modelled as constant impedance loads. The lower
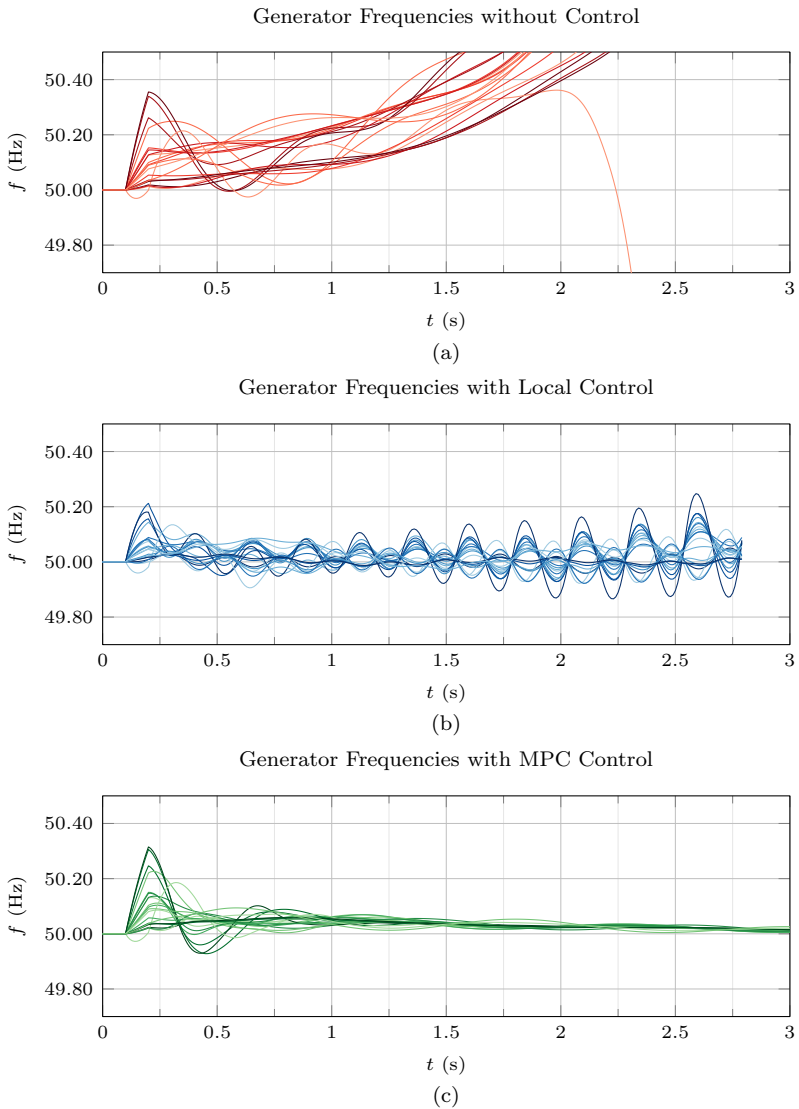
Figure 5.8: Frequency trajectories of the generators. (a) HVDC power injections kept constant, (b) damping controller using local measurements, (c) MPC-based grid controller.

Bus Voltages without Control

(a)

Bus Voltages with Local Control
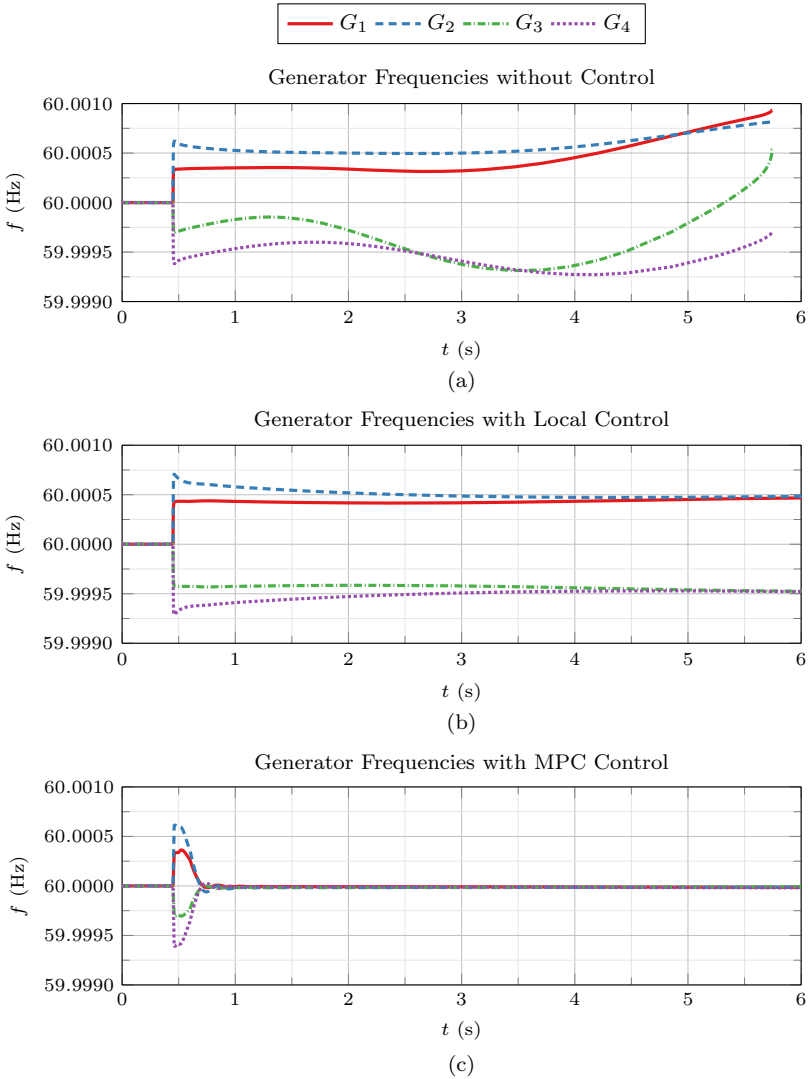

(b)

Bus Voltages with MPC Control

(c)
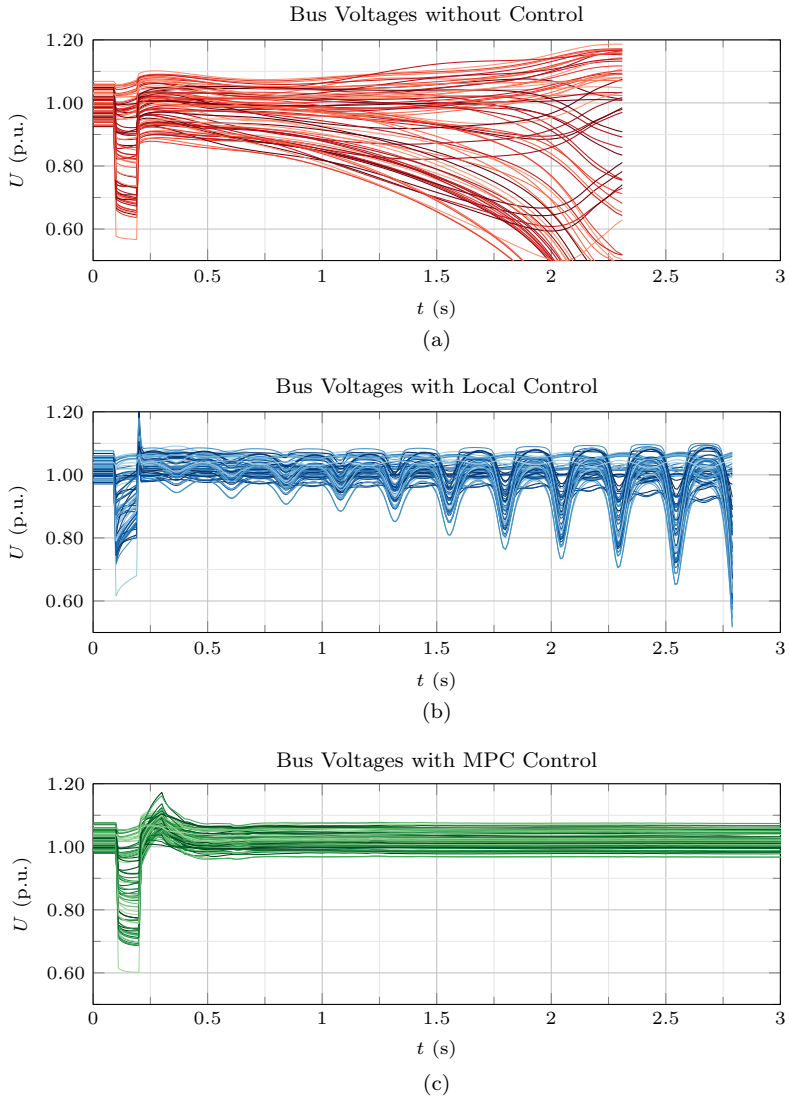
Figure 5.9: AC bus voltages at all AC nodes. (a) shows the response without control, (b) when the HVDC power injections are controlled locally, and (c) when they are controlled using the MPC-based controller.

the voltage at the load bus is, the lower is the consumption of that load. During the voltage collapse, the system load is reduced and the generators accelerate due to the power imbalance. When the active and reactive power of the VSC-HVDC links are modulated by the local controller, the system is still unstable. However, it is not a pure voltage collapse, rather a combination of voltage instability and rotor angle instability. The local controller of the VSC-HVDC link acts destabilizing. The MPC-based grid controller modulates the active and reactive power of the VSC-HVDC links in such a way that oscillations of the generators are damped and that the AC terminal voltage of the VSC-HVDC links are controlled to the desired level. Furthermore the voltages stay within acceptable limits. The AC terminal voltages at bus 4011 and bus 4044 of HVDC1 are shown in Figure 5.10a. The AC terminal voltage at bus 4031 and bus 4045 of HVDC2 are depicted in Figure 5.10b. The desired set-points for each bus are illustrated by the black line. Since the local controller is continuous it is able to react much faster during the fault and tries to drive back the voltage to the desired set-points. The MPC-based controller changes the set-points with the sampling time of $T_{\mathrm{mpc}} = 100$ ms. Therefore it is not able to react during the fault, since the fault just happens after a control action therefore the next control action will be 100 ms after the fault has started. This is the worst case for the controller because the MPC-base controller model is not aware of the fault yet. Shortly after the fault is cleared the local controller is able to control the quicker to the set-points, however in the long term, the voltages start oscillating, and the controller is not able to control these oscillations. After the fault is cleared, the MPC-based controller coordinates the reactive power injections of both links and is able to predict the voltage trajectory and therefore is able to damp the voltage oscillations and controls the voltages to the given set-points. In Figure 5.11 the active and reactive power injections for both VSC-HVDC links are shown when they are controlled locally. The delay between the demanded set-point and the actual power injections is very short, and insignificant compared the discrete set-point change of the MPC-base controller, depicted in Figure 5.12. On the other hand, the MPC-based controller has information about the entire system and is able to find the best solution according to the objective function (5.7) and is able to bring back the voltage to the desired set-point. In Figure 5.13 the frequency deviation σ_ω is shown. The MPC-based controller is able to minimize the frequency deviation of the generators. The frequency oscillations with the local controllers can only be detected by the objective of

(a)

(b)
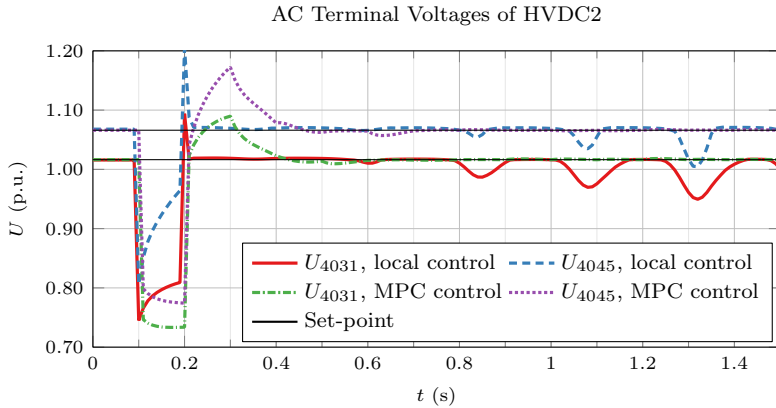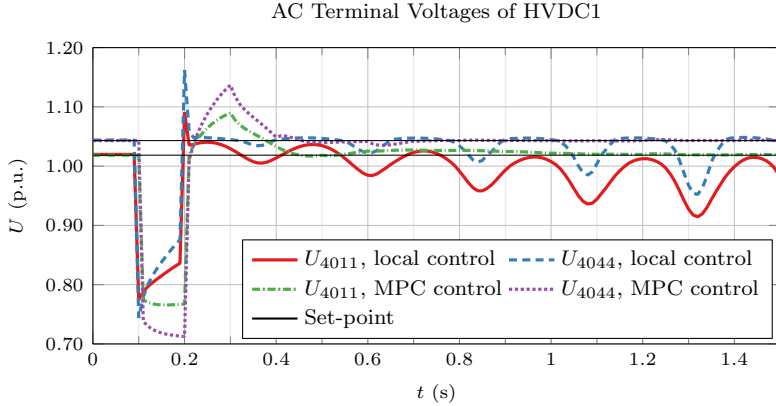
Figure 5.10: Controlled AC bus voltages at the VSC-HVDC terminal when
HVDC power injections are controlled locally or with the MPC-
based controller, (a) for U_{4011} and U_{4044} of HVDC1, and (b)
for U_{4031} and U_{4045} for HVDC2.

Active and Reactive Power Injections of HVDC1 with Local Control

(a)

Active and Reactive Power Injections of HVDC2 with Local Control

(b)
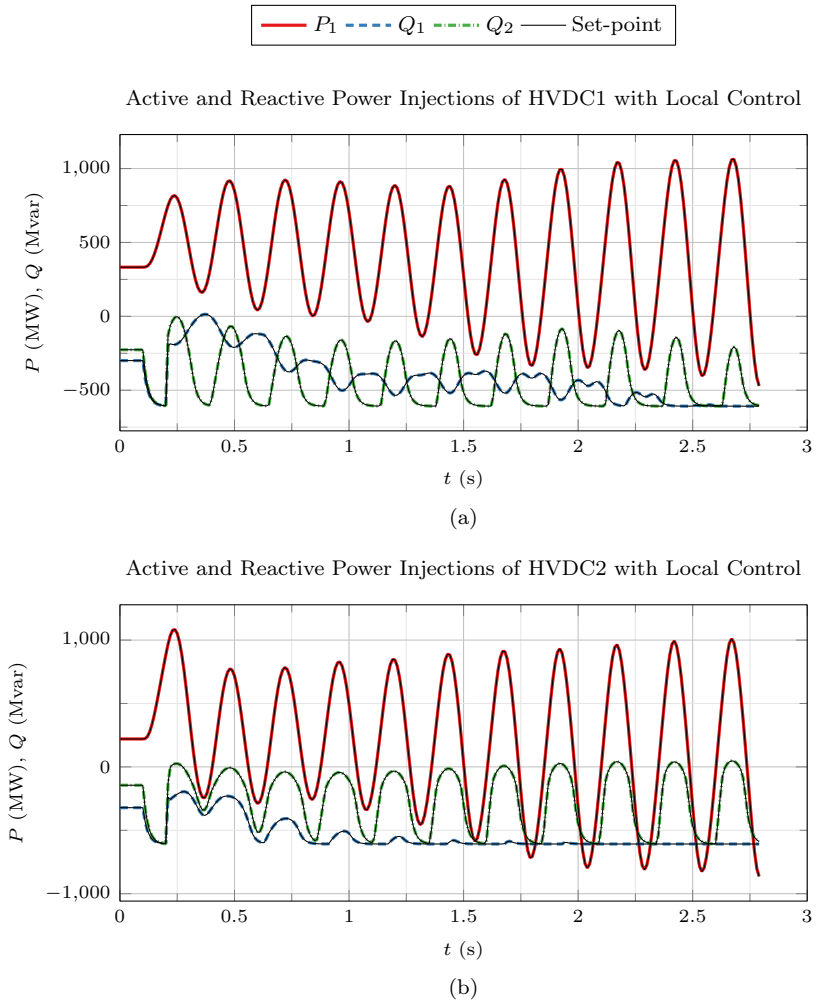
Figure 5.11: Modulated active and reactive power of the VSC-HVDC links when the link are controlled by the local controller for (a) HVDC1, (b) HVDC2.

Active and Reactive Power Injections of HVDC1 with MPC-based Control

(a)

Active and Reactive Power Injections of HVDC2 with MPC-based Control

(b)
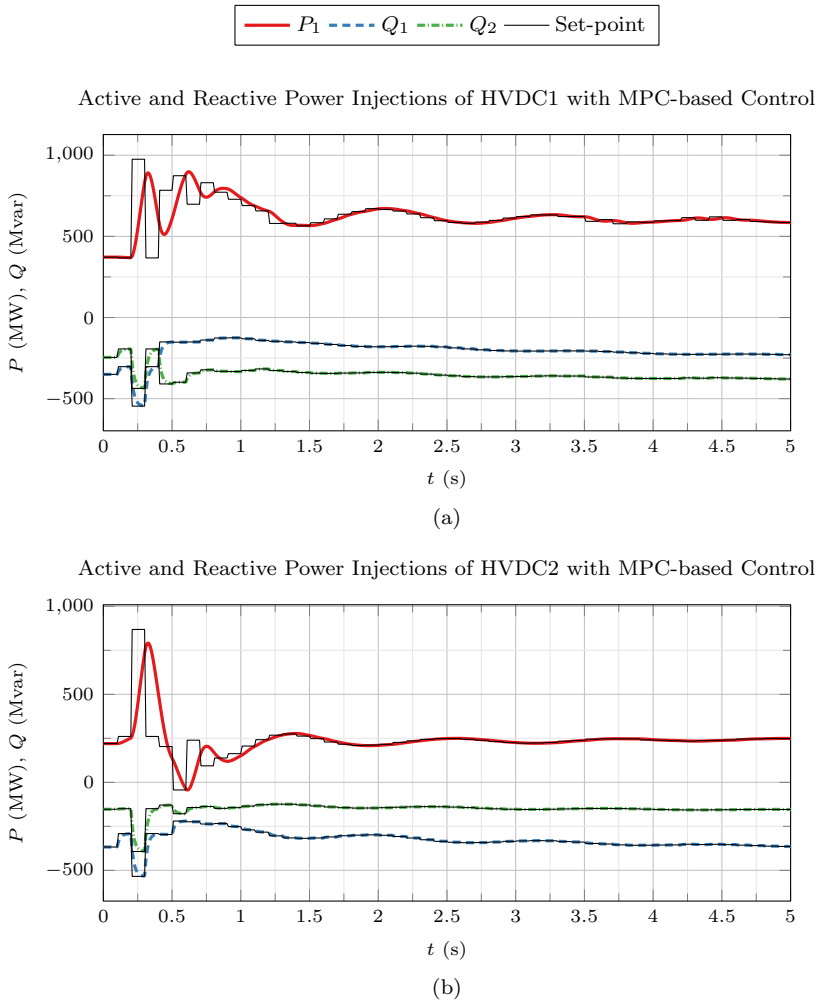
Figure 5.12: Time discrete power modulation of the VSC-HVDC links when the links are controlled by the MPC-based controller for (a) HVDC1, (b) HVDC2.

Average Frequency Deviation σ_ω
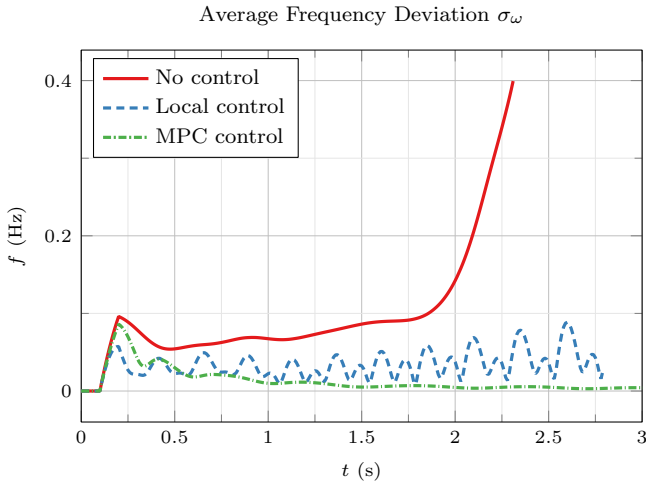
Figure 5.13: Average frequency deviation σ_ω from the mean frequency for all three control cases.

Average Voltage Deviation σ_u
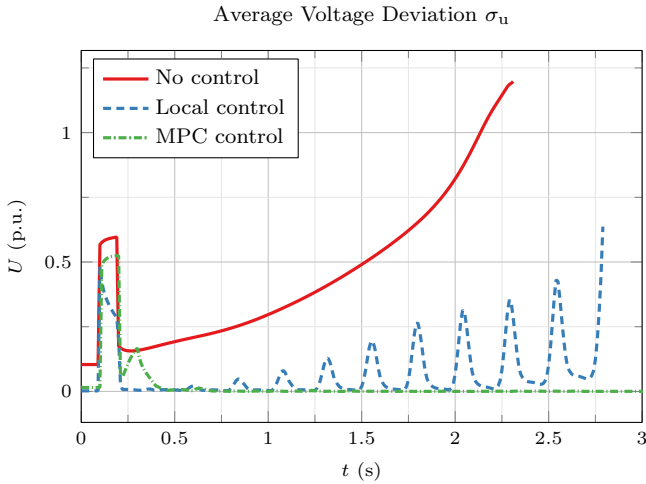
Figure 5.14: Average voltage deviation σ_u of the VSC AC terminal voltage for all three control cases.
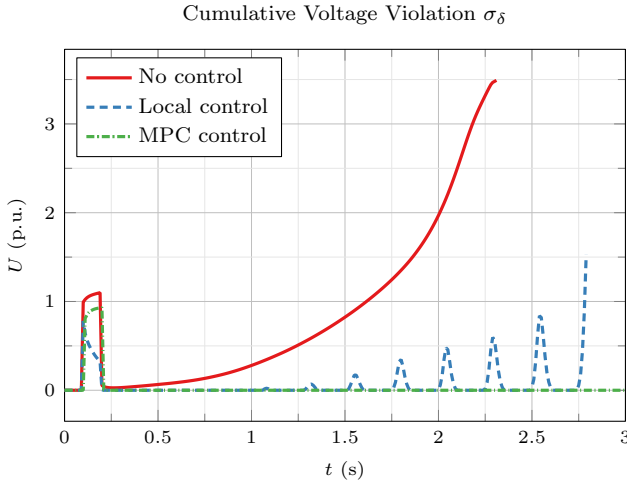
Figure 5.15: Cumulative voltage violation σ_δ from the voltage limits for all three control cases.

the MPC-based controller and therefore they are not able to efficiently damp those oscillations. In Figure 5.14 the average voltage deviation σ_u according (5.12) at the AC bus terminals of the VSCs is shown. The faster control of the AC bus terminal voltage by the local controller, compared to the MPC-based controller is clearly visible. However, after about $t = 1\,\mathrm{s}$ the performance of the local voltage controller is worse compared to the MPC-based grid controller. In Figure 5.15 the cumulative voltage violation σ_δ according to (5.16) are shown. It is a measure of any voltage limit violation of the system. During the fault some voltages are below the minimal acceptable voltage of 0.9 p.u. and the soft constraint (5.34) is activated. The local controller is able to better improve the voltages during the fault compared to MPC-based controller. After the fault is cleared, most voltages are within their bounds and thus (5.34) is not active anymore. The MPC-based controller is able to keep all voltages within the bounds and σ_δ is zero. The voltage collapse is clearly visible if the VSC-HVDC links are not controlled and σ_δ is growing as the voltages in the system collapse.

5.5 Conclusion

This chapter presented a MPC-based grid controller in order to modulate the active and reactive power injections of VSC-HVDC links. The aim was to control the AC terminal voltage of the VSC-HVDC links and keep all AC bus voltages within their acceptable bounds and to simultaneously damp inter-area oscillations. The controller objective consists of three parts: Firstly to minimize the voltage error from their given setpoints at the AC terminal busses of the VSC-HVDC links in order to control the AC voltage of the VSC-HVDC links. Secondly to minimize the frequency error of the generators from the mean system frequency in order to damp inter-area oscillations and thirdly to minimize the slack variables of the soft voltage constraint in order to keep all the AC voltages within their operational limits. The MPC-based grid controller was able to coordinate the control actions of each link and predicted the future behavior of their control actions. Therefor an optimal active and reactive power trajectory could be found to enhance the stability of the power system.

The performance of the controller was shown in the Kundur two area system compared to a local controller. The MPC-based controller was able to control the system, however, the local controller was only slightly worse measured on the MPC control objective. It was also tested on the larger Nordic 32 system used for voltage stability studies. It was shown that the MPC-based controller outperforms the local control scheme due the advantage of a coordinated and predictive control of all VSC-HVDC links in the system.

Chapter 6

Damping Effect of VSC-HVDC in System with High RES Penetration

This chapter shows how voltage source converter-based HVDC links are able to mitigate frequency oscillations induced by large renewable energy sources penetration in the European system. With a coordinated model predictive control based grid controller, four voltage source converter-based HVDC links were able to add enough additional damping to drive the system to a stable equilibrium. This chapter is based on the paper: "Power System Stability Control using Voltage Source Converter Based HVDC in Power Systems with a High Penetration of Renewable" presented at PSCC2014 in Wroclaw [85].

6.1   Introduction

In recent years, the role of RES have become much more prominent. In the last 20 years the amount of energy produced by RES has increased tremendously. Figure 6.1 shows the historic data from 1990 to 2013 of the increasing production of energy from wind and PV [86] as well as
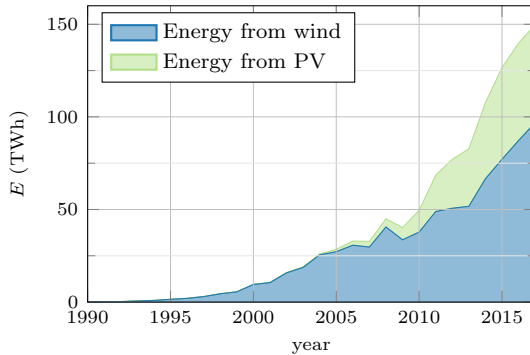
Figure 6.1: Development of energy production of wind and PV in Germany
based on historic data from 1990 up to 2013 [86, 88] and pre-
dicted data until 2016 [87].

the predicted energy production until 2016 [87] in Germany. The energy
production has more than doubled from 2000 to 2010. In 2013 the share
of RES in Germany was 25.3 percent of the total energy production [88]
and is predicted to grow up to 45 percent in the next ten years [88].
Other countries, such as Spain and Italy, made substantial investments
into wind and solar power as well.

With the increasing share of RES, the classical structure of the trans-
mission system changes. Instead of large thermal power units, which
inject power at the highest voltage level, small RES units inject power
directly to the distribution grid [89]. The decommissioning of large ther-
mal units, connected to the power system with synchronous generators,
reduce the amount of inertia of the system. Most RES are connected
either through power converters, such as PV or full converter wind tur-
bines, or through asynchronous generators such as doubly-fed induction
generator (DFIG) wind turbines. They provide no or very little iner-
tia. It is expected that, due to a lower system inertia, deviation form
the nominal frequency will increase. This becomes of increasing con-
cern with the liberalized market, when more power is traded and the
generators change their set-points every 15 minutes.

VSC-HVDC are a viable solution for grid expansion planning. They can
not only be used for power transmission, but also as power system stabi-
lizers. A control entity, such as a TSO, is able to control the set-points of
the VSC-HVDC lines. This chapter investigates the effect of reduced in-

ertia in a large system, like the European system, and how VSC-HVDC links are able to mitigate the decrease of inertia and improve the overall system damping.

6.2 Reduced Inertia Due to Integration of Renewable Energy Sources

In a system consisting mostly of synchronous generators, the system frequency varies with the imbalance between the produced energy of the generators and the consumed energy of the loads. The principal frequency dynamics of a power system can be described by the nonlinear differential equation

$$\frac{\mathrm{d}\Delta\omega}{\mathrm{d}t} = \frac{\omega_0^2}{2HS_{\mathrm{B}}\omega}\left(P_{\mathrm{m}} - P_{\mathrm{e}}\right) \quad , \tag{6.1}$$

where ω is the frequency at the center of inertia (COI):

$$\omega = \frac{\sum_{i=i}^{n_{\mathrm{gen}}} H_i \omega_i}{\sum_{i=1}^{n_{\mathrm{gen}}} H_i} \quad , \tag{6.2}$$

with n_{gen} the number of synchronous generators connected to the system and H_i is the inertia constant of a generator. The frequency ω is further split into

$$\omega = \omega_0 + \Delta\omega \quad , \tag{6.3}$$

where ω_0 is the nominal frequency and $\Delta\omega$ is the frequency deviation from the nominal frequency. The total mechanical power is defined as P_{m} and the total electrical power as P_{e}. The total rating of the system is defined as

$$S_{\mathrm{B}} = \sum_{i_i}^{n_{\mathrm{gen}}} S_{\mathrm{B},i} \quad , \tag{6.4}$$

where $S_{\mathrm{B},i}$ is the power rating for one generator. The total inertia constant H, [1], is defined as

$$H = \frac{\sum_{i=1}^{n_{\mathrm{gen}}} H_i S_{\mathrm{B},i}}{S_{\mathrm{B}}} \quad . \tag{6.5}$$

In the event of a sudden loss of generation or of an abrupt connection of a large load, the system frequency will start decreasing as suggested

by (6.1). The rate of change is determined by the size of the system S_{B} and by the total inertia H of the system. If the inertia is reduced, for example due to the replacement of synchronous generators with RES, as they have no or little inertia, the damping will decrease and frequency oscillations will become more prominent.

The frequency oscillations can be reduced by inertia mimicking, either by the controller of the RES converters, as in [90] or [91], or by using other power stabilizers like VSC-HVDC links. This chapter shows that VSC-HVDC links are capable to add additional damping in a system with reduced inertia.

6.3   European Power System Model with Renewable Energy Sources

To show the effect of a reduced inertia due to an increased share of RES in a large network, the ENTSO-E continental European grid is chosen. Therefore, the power system model from Section 4.5 is modified for this chapter, as depicted in Figure 6.2. It consists of 74 busses connected by 131 AC lines with a nominal voltage of 380 kV. At each node, an aggregated power plant and a load is connected. There are four types of generation technologies: thermal units, hydro storage plants, wind power plants and PV units as depicted in Figure 6.2. The thermal and hydro storage plants are modelled as described in Section 4.5. Each generator is equipped with an AVR and additionally with a PSS. The wind turbines are assumed to be full converter units according to [92] and are modelled as controlled power sources without inertia. The PV installations do not contribute any inertia and are modelled as controlled power sources without inertia as well. It is assumed that the RES do not contribute to the primary frequency control. It is further assumed that due to subsidies they have a feed-in guarantee of their entire production.

Four bipolar VSC-HVDC links are placed in the European system, shown as bold yellow lines in Figure 6.2. The placement of these links was done (a) according to already existing CSC-HVDC corridors, such as the HVDC connection between Italy and Greece (HVDC 1) [72], (b) VSC-HVDC links which are under construction as the inelfe project between France and Spain (HVDC 2) which has been commissioned in 2015 [71], or the Aachen Liège Electric Grid Overlay (ALEGrO) project between Belgium and Germany (HVDC 3) [93], or (c) distant projects,
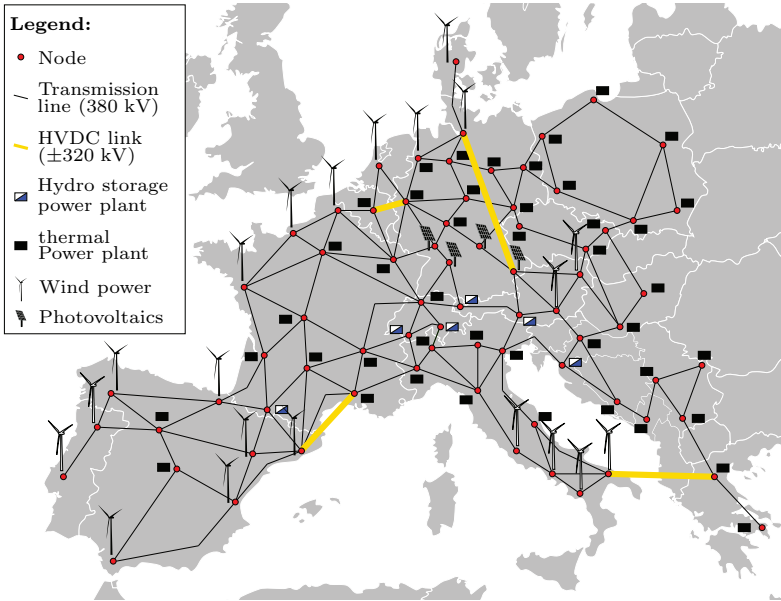
Figure 6.2: European power system with installed RES, namely wind and photovoltaics.

Table 6.1: Location and parameters of the VSC-HVDC links in the European system.

Location	Name	Length	Rated Power
Italy to Greece	HVDC 1	316 km	1 216 MW
France to Spain	HVDC 2	67 km	2 432 MW
Belgium to Germany	HVDC 3	94 km	1 216 MW
Northern to Southern Germany	HVDC 4	700 km	1 216 MW

such as the Germany South link (HVDC 4) [94]. The location, length, and power ratings are depicted in Table 6.1. All VSC-HVDC links have a DC voltage rating of ±320 kV. All four VSC-HVDC links are modelled according the dynamic model in Section 3.4.

6.4   Simulation Results

Three different scenarios of the integration of RES are analyzed. In each scenario the installed capacity of the system is 352 GW and the total load is 256 GW. The initial operating point of the simulated scenarios is derived from a snapshot of real data of the ENTSO-E grid. The three scenarios differ by the amount of RES installed in the system and thus by the total system inertia H. The first scenario is the reference scenario without any RES installed in the system. The total system inertia, obtained with (6.5), sums up to $H = 6.29$ s. In the second scenario the amount of RES is increased to 21% of the total load of the system. Some of the initial production technology, depicted in Figure 4.6, is changed to wind production, depicted with black wind turbines in Figure 6.2. The total system inertia is reduced to $H = 4.96$ s. The production is mainly in the north at the coasts of Germany, Belgium, the Netherlands and France and as well in the south at the coast of Spain. In scenario 3 the energy production of RES is further increased to 32% of the total energy production. The production in the south of Germany is changed to PV, depicted by PV panels in Figure 6.2. In Austria, Portugal and in southern Italy the thermal power plants are replaced with wind turbines. The total system inertia is reduced to $H = 4.20$ s. Each scenario is simulated using the MPC-based grid controller from Section 4.2, which modulates the active and reactive power of all the VSC-HVDC links. The controller operates with a sampling time of $T_{\mathrm{mpc}} = 500$ ms and has a prediction horizon of $N = 10$ time steps, i.e. 5 s. The maximal in-feed of active and reactive power is constraint by the power rating constraint (4.24) to $P_{\max} = 0.9$ p.u. and $P_{\min} = -0.9$ p.u. as well as $Q_{\max} = 0.5$ p.u. and $Q_{\min} = -0.5$ p.u.. The rate of change of the active and reactive power is constraint with (4.25) to $d_{\max} = 0.2$ p.u.$/T_{\mathrm{mpc}}$ and $d_{\min} = -0.2$ p.u.$/T_{\mathrm{mpc}}$. The per unit value are based on the rated power of the VSC-HVDC link. To compare the dynamic performance of the MPC-based controller, another two grid control strategies are simulated. One case does not modulate the active and reactive power and the set-points of the VSC-HVDC links remain constant over the entire simulation. The second case changes the set-points of the VSC-HVDC links only based on local measurements according the controller in Section 4.3. Table 6.2 gives an overview of the different scenarios.

The case studies are simulated using MATLAB. The initial set-points of the VSC-HVDC terminals and the initial conditions of the elements in the ENTSO-E system are determined using an AC power flow solu-

Table 6.2: Overview of simulation scenarios.

Scenario	Installed Capacity of RES	Share of RES	Total System Inertia H	Control Type
1	-	-	6.29 s	no
2a	72.66 GW	21%	4.96 s	no
2b	72.66 GW	21%	4.96 s	local
2c	72.66 GW	21%	4.96 s	MPC
3a	116.85 GW	32%	4.20 s	no
3b	116.85 GW	32%	4.20 s	local
3c	116.85 GW	32%	4.20 s	MPC

tion. The VSC-HVDC loadings are quite low due to the fact that the system is not optimized for a high HVDC utilization. The initial AC power flows is a snapshot from swissgrid in order to reproduce a realistic operation point of the European system The system dynamics are then simulated using the dynamic simulator for MATLAB developed in [43] and the optimization for the MPC-based grid controller is solved using the gurobi optimization toolbox for MATLAB [83].

This simulation case considers the sudden loss of a 1 000 MW load in the middle of Spain. Figure 6.3 shows the mean frequencies for all the scenarios defined in Table 6.2. The solid red curve shows the frequencies for scenario 1 in which no RES are installed. The blue dashed and the orange dashed curves show the results for scenarios 2a and 3a, respectively, where the HVDC set-points are kept constant. As more renewable are integrated, i.e. the inertia is reduced, the frequency deviation increases. The dash-dotted green and dash-dotted yellow curves show the mean frequency profiles for scenarios 2b and 3b where the HVDC active and reactive power injections are modulated by the local damping and voltage controller. The resulting mean frequency profiles are slightly better than without any control. On the other hand, the pink dotted and brown dotted curve show the mean frequency profiles for scenarios 2c and 3c, where the active and reactive power is modulated based of the output of the MPC-based grid controller. After a short acceleration of the system, the MPC-based grid controller is able to effectively damp the system oscillation for both scenarios.

Mean System Frequency f for All Scenarios
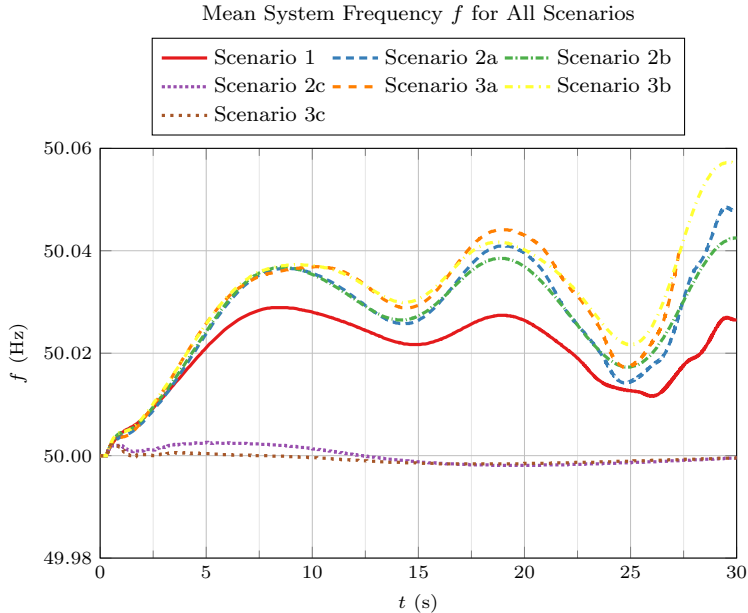
Figure 6.3: Mean system frequency f for all scenarios according Table 6.2.

This is supported by observing the results in Figure 6.4, where the average frequency deviation of the generators from the COI, σ_ω, is shown. The standard deviation for scenarios 1, 2a, and 3a, depicted in Figure 6.4a, grows, which means that the frequencies of the generators diverge if the VSC-HVDC links keep their set-points constant. However, if the set-points are controlled, the HVDC links are able to reduce the standard deviation, shown in Figure 6.4b, and therefore the power oscillations in the system. In both renewable scenarios, the local damping controller is only able to decelerate the divergence of the generators. However, the MPC-based controller is able to stop the divergence of the generators, and damp the inter-area oscillations. The more RES are integrated to the system, the stronger is the initial reaction of the generators, shown in the magnifying glasses shortly after the disturbance. This holds for both control scenarios when the VSC-HVDC links are controlled locally or with the MPC-based grid controller.

The divergence of the generators for scenario 2a can be seen in Figure 6.5a. After about $t = 20\,\mathrm{s}$ two groups of generators enter an insta-

Frequency Deviation σ_ω from Mean System Frequency f

(a)

Frequency Deviation σ_ω from Mean System Frequency f

(b)
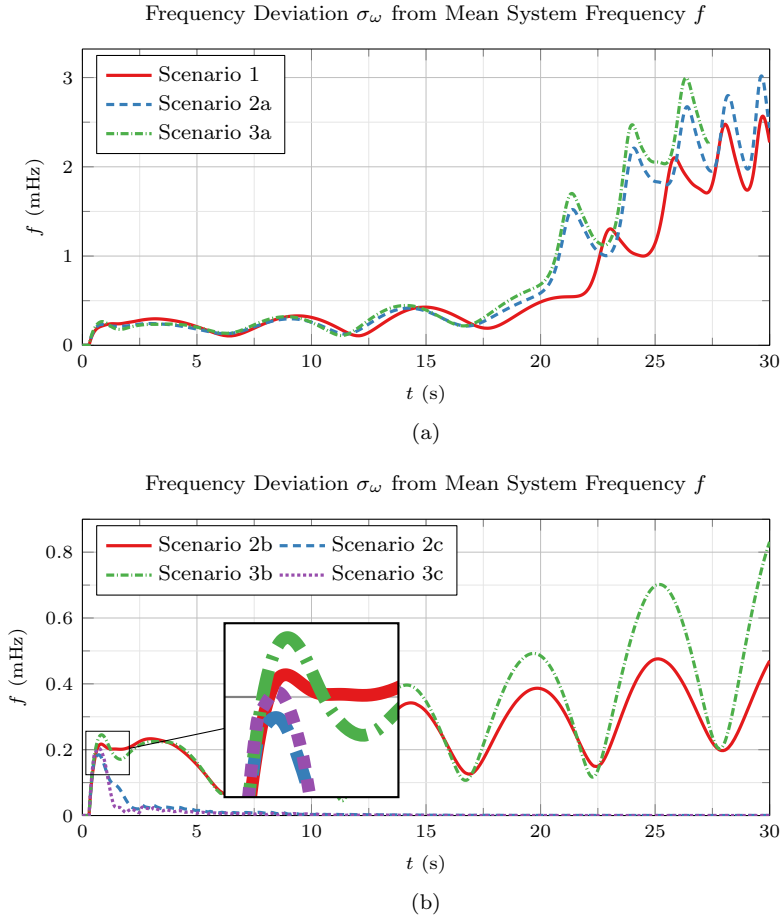
Figure 6.4: Mean frequency deviation σ_ω of the generators from the COI. (a) for the uncontrolled scenarios 1 (base case), scenario 2a (21% RES) and scenario 3a (32% RES), (b) for the controlled scenarios 2b and 3b where the HVDC injections are controlled locally and 2c and 3c with the MPC-based controller.

Generator Frequencies without Control

(a)

Generator Frequencies with Local Control

(b)

Generator Frequencies with MPC Control

(c)
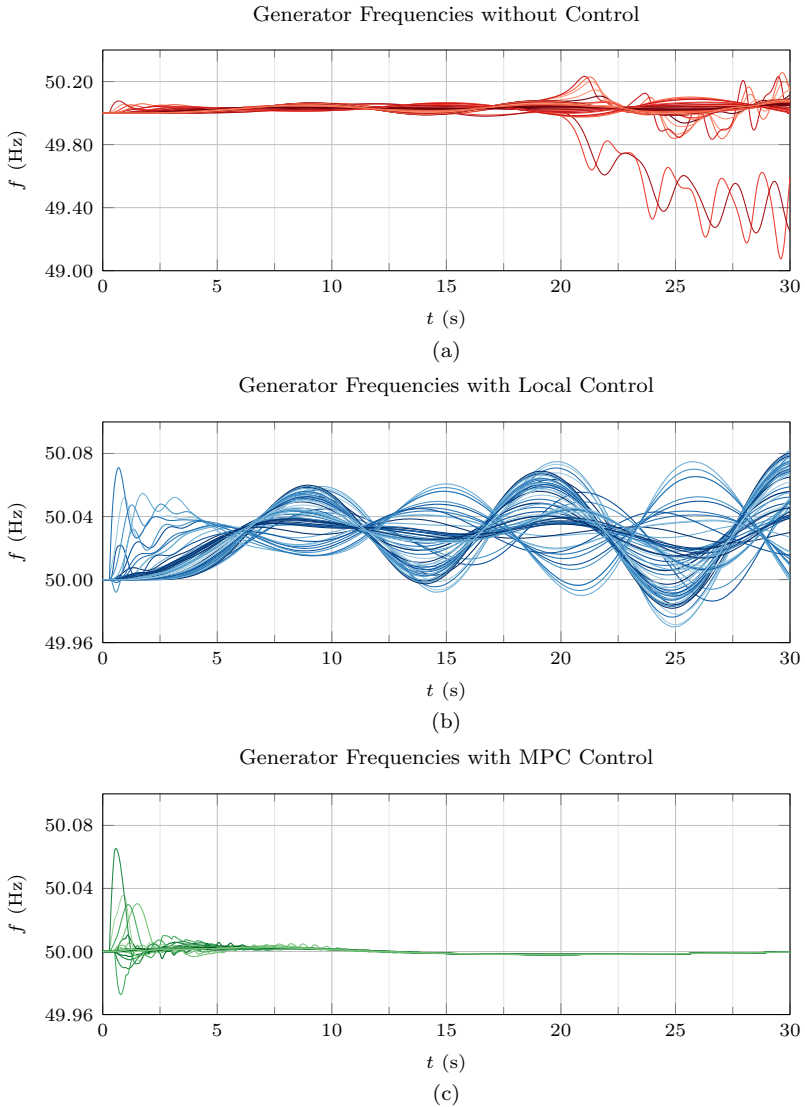
Figure 6.5: Frequency trajectories of the generators. (a) HVDC power injections kept constant, (b) damping controller using local measurements, (c) MPC-based grid controller.

AC Bus Voltages for Scenario 2b

(a)

AC Bus Voltages for Scenario 2c

(b)
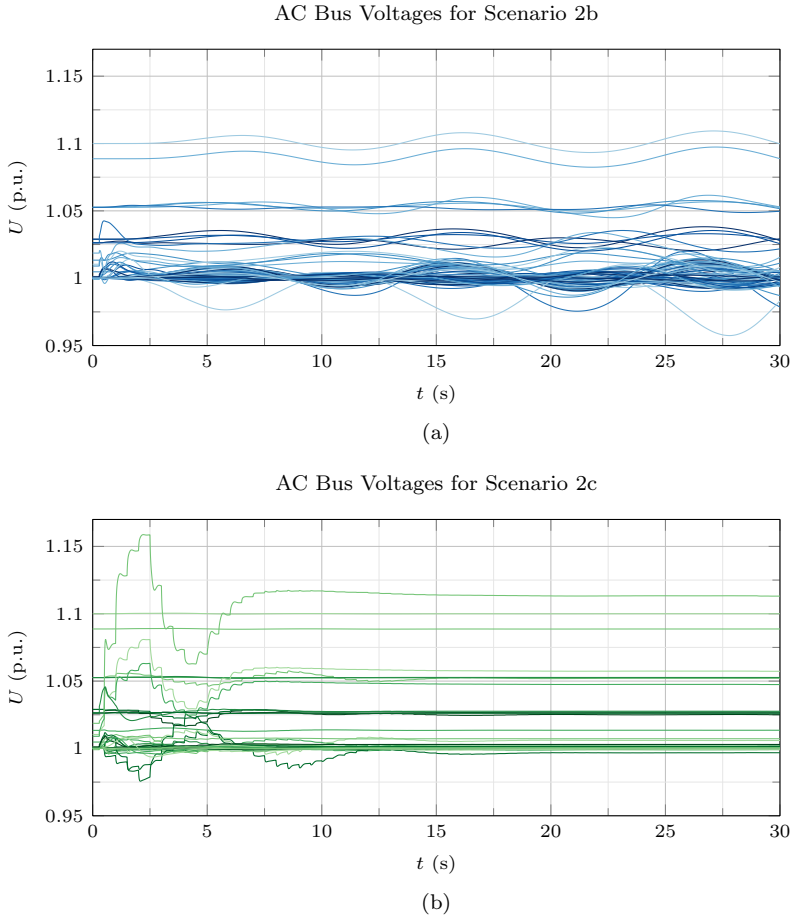
Figure 6.6: AC bus voltages (a) for scenario 2b where the HVDC injections are controlled locally and (b) where the injections are controlled by the MPC-based grid controller.

ble mode. The first group of generators represents the two generators in Greece. They decelerate rapidly and start to oscillate with about 0.6 Hz. The second group represent the seven generators in the Balkan region. They accelerate and start to oscillate with approximately the same frequency. If under-frequency protective devices at the generators in Greece are installed, they would be disconnected due to under-frequency tripping. This would further weaken the system. Figure 6.5b shows the frequency of all generators for scenario 2b. The local damping controllers are able to damp the local inter-area oscillation mode between Greece and the Balkan region. Furthermore, an undamped east-west mode with a frequency of about 0.1 Hz is detected. It also can be examined in the AC bus voltage profile, depicted in Figure 6.6a. The voltages slightly oscillate with the same frequency. The MPC-based controller is able to control the VSC-HVDC power injections in such a manner that after about $t = 10$ s almost all oscillations in the system are damped, and all generators are in stable operating conditions, depicted in Figure 6.5c. The MPC-based controller performs significantly better than the local control scheme. This is due to the fact that the MPC-based controller is able to predict the future behavior of the system. Another reason is, the coordinated control of all four VSC-HVDC links. The MPC-based controller is able to calculate the optimal set-points for all the four VSC-HVDC links in one optimization and thus finds a better solution for the system than the local control scheme which independently controls each link locally. Figure 6.6b shows the AC voltage profile for all the nodes. The discrete control actions of the MPC-based are clearly visible.

Figure 6.7 and Figure 6.8 show the active and reactive power injections for the VSC-HVDC links HVDC 1 and HVDC 2 as well as for HVDC 3 and HVDC 4, respectively. They compare the injection trajectories for the case when 21% RES are installed, if the VSC-HVDC power injections are controlled locally or by the MPC-based grid controller. The capability of changing the active and reactive power is utilized more with the MPC-based controller. HVDC 2, France-Spain, and HVDC 3, Belgium-Germany, contribute the most to the stability of the system. It is an interesting fact that these two VSC-HVDC links are currently being built and are able to contribute to the system stability in the near future. HVDC 1 does not have to change its active power set-points too much, however, it contributes a lot to the system stability with the capability to modulate its reactive power on the Italian side. Currently this link is using the CSC technology. If the converters are changed

Power Injections HVDC 1: Italy - Greece

(a)

Power Injections HVDC 2: France - Spain

(b)
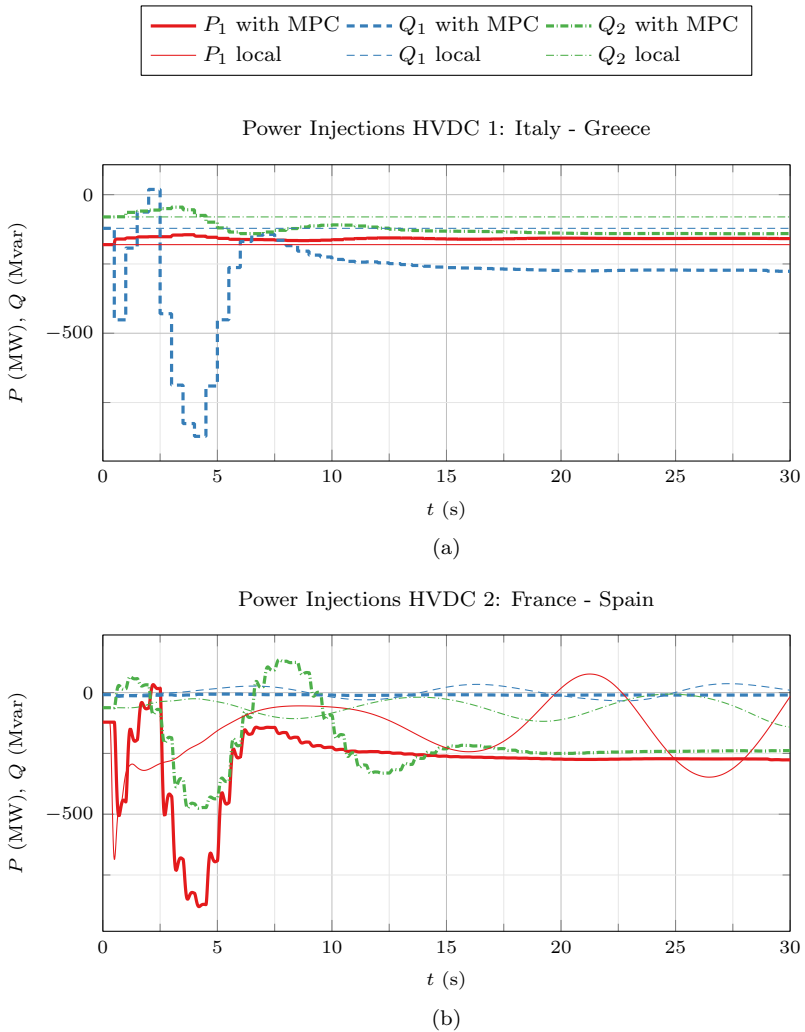
Figure 6.7: HVDC power injections for scenario 2b where the set-points are changed based on local measurements, and 2c based on the MPC-based grid controller (a) for the HVDC link between Italy and Greece, and (b) for the link between France and Spain.

Power Injections HVDC 3: Belgium - Germany

(a)

Power Injections HVDC 4: Northern - Southern Germany

(b)
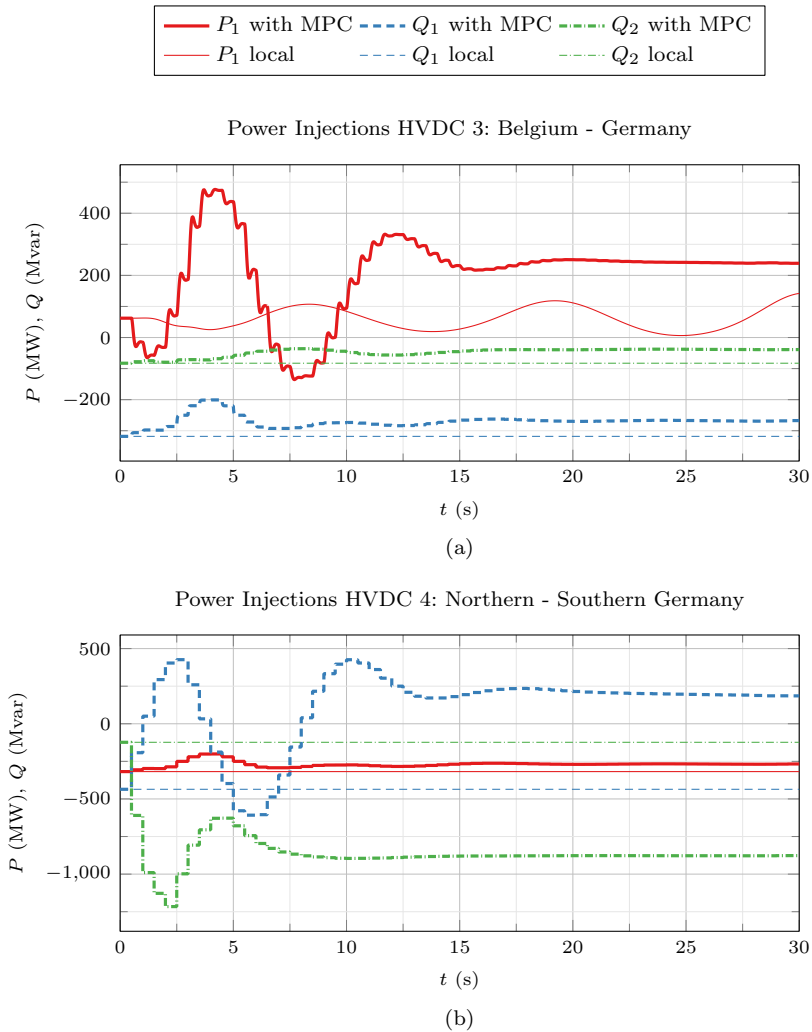
Figure 6.8: HVDC power injections for scenario 2b where the set-points are changed based on local measurements, and 2c based on the MPC-based grid controller (a) for the HVDC link between Belgium and Germany, and (b) for the link within Germany.

to a VSC, the voltage security in southern Italy could be improved by an additional independent reactive power source. HVDC 4, within Germany, contributes reactive power to support the voltage in the south as well as in the north. The system model is designed such that the RES do not provide any voltage support nor primary frequency control. Therefore the VSC-HVDC link have to compensate for their losses. This is nicely seen with the Germany link.

6.5 Conclusion

This chapter showed the effects of VSC-HVDC links in the European system when the amount of RES increases and how the active and reactive power should be controlled. It was shown that with the reduction of the total system inertia, the frequency oscillations will be amplified. If no additional control is added to the system, the system could run into instability, eventually leading to the loss of some synchronous units due to the tripping of under- or over frequency relays. By modulating the power of the VSC-HVDC links with the MPC-based grid controller, the power oscillations can be reduced and the system stabilized.

Building HVDC purely for stability control would generally be prohibitively expensive. However, once they are installed in the system for expanding the transmission capacity, they could also be utilized for stability control, without affecting their primary objective of power transmission. The additional costs for this are usually marginal. Especially the VSC-HVDC links between France and Spain as well as the link between Belgium and Germany prove very effective for the damping of frequency oscillations. These links are currently under construction and could be utilized as power system stabilizer.

It was also shown that with only four VSC-HVDC links in Europe, with a total capacity of 6 300 MVA or 2.5% of the total load, we were able to stabilize the system effectively for the studied contingencies.

Chapter 7

Controlled Islanding Using VSC-HVDC Links to Exchange Power to Reduce Load Shedding

This chapter presents a controlled islanding algorithm which incorporates installed voltage source converter-based HVDC links in order to exchange power between two islands. By exchanging power between islands, load shedding and generator tripping can be reduced which lowers the economic costs of a large disturbance. This chapter is based on the publication "Controlled Islanding Using VSC-HVDC Links to Reduce Load Shedding", presented at POWERTECH 2015 [95].

7.1   Introduction

The analysis of recent blackouts has shown that most major outages are initiated by a single event or unrelated multiple events such as faults of power systems components or relay misoperations [96, 97]. After a disturbance, a sequence of events can lead to uncontrolled cascading outages, followed by an eventual collapse of the entire power system. To

prevent the spread of the disturbance, a number or researchers propose controlled islanding as a control measure.

Several approaches on how to develop an adequate strategy for controlled islanding can be found in the literature. The approach of [98] is based on graph spectral methods. In [99], an off-line method based on slow coherency grouping of the generators is described to determine the minimum cut-set of the AC lines. The identification of the slow coherent generators is based on the method described in [100]. Although the slow coherency method is based on linearized models, results indicate that it captures the dynamic behavior of the nonlinear system fairly well [99]. Several researchers also propose methods for real-time determination of the optimal island boundaries. A graph theoretical approach called ordered binary decision diagram (OBDD) is introduced in [101]. Methods based on graph theory are also presented in [102, 103]. Hybrid methods have also been suggested in literature, where first the dynamic properties of the network are identified off-line, and subsequently the algorithm tries to find the optimal cut-set in real-time. The authors of [104] identify the coherent set with the Krylov Subspace Method off-line and then determine the islands with the least generation-load imbalance in real-time. An approach based on off-line slow coherency grouping and real time rotor angle grouping combined with the least generation-load imbalance based on k-mean clustering is described in [105].

Nowadays, an increasing number of VSC-HVDC links are being built within the same synchronous system [71, 106]. However, VSC-HVDC links also have the advantage to be connected between two asynchronous areas. The idea of this chapter is, to find a method how to form islands in such a way that they are connected with VSC-HVDC links. This allows to continuously exchange power between the islands and therefore prevent load shedding or generator tripping in a case of a generation-load imbalance in an island. Consequently, this would reduce the economic costs of a large disturbance.

The approach presented in this chapter is an extension of the hybrid method of [105, 107]. The proposed algorithm finds islands with an optimal cut-set, such that the terminals of a VSC-HVDC link are located in different islands.

7.2 Controlled Islanding Method

As proposed in [105], controlled islanding can be seen as a clustering problem, where the transmission system is to be split into N_{isl} clusters, i.e. islands. The busses are clustered according to a minimum distance objective function [105]. The purpose of the proposed algorithm is to find clusters which are connected with VSC-HVDC links in order to transfer power between the islands. This reduces the generation-load imbalance in each island and thus reduces load shedding and generator tripping.

The power system can be modelled as a weighted undirected graph $\mathcal{G} = (\mathcal{V}, \mathcal{E})$, where $\mathcal{V} = \{v_1, \ldots, v_{n_{\text{node}}}\}$ is the set of vertices representing the n_{node} power system nodes and $\mathcal{E} = \{e_{ij}\}$ is the set of edges corresponding to the n_{line} power lines. We define $\mathcal{W} = \{w_{ij}\}$ as the set of weights assigned to the edges $\mathcal{E}$. The weighted adjacency matrix $\mathbf{A}_{\text{adj}} = [a_{ij}] \in \mathbb{R}_{n_{\text{node}} \times n_{\text{node}}}$ from $\mathcal{E}$ to $\mathcal{W}$ can be built with

$$a_{ij} = \begin{cases} w_{ij} & \text{if } e_{ij} \in \mathcal{E} \\ 0 & \text{else} \end{cases} .$$

Each weight defines the distance between two nodes in the system. The distance is arbitrarily chosen and does not reflect the physical distance between two nodes of the system. The algorithm modifies the distance between the nodes in order to group the nodes. It gives the opportunity to find an optimal cut-set for the islands. The following rules are used to set the weights:

1. **Voltage source converter-based HVDC grouping:** increase the distance between the terminals of the same VSC-HVDC link.

2. **Slow coherency grouping of generators:** decrease the distance between the generators of the same coherent group.

3. **Rotor angle grouping:** group the generators according to their rotor angles.

4. **Generation-load imbalance:** decrease the distance from the loads to the generator which are fully supplied.

5. **Voltage source converter-based HVDC terminal - bus net-power imbalance:** decrease the distance of the terminal

bus to the neighboring busses which can be supplied by the
VSC-HVDC terminal or provide energy for the VSC-HVDC ter-
minal.

Figure 7.1 depicts the flow chart of the k-means controlled islanding
algorithm. It consists of two parts. The first part is executed off-line
and the second one in real-time after the disturbance occurred.

7.2.1   VSC-HVDC Grouping

To enforce that the terminals of a VSC-HVDC link are in different
islands, the distance between the two terminals is increased. First the
adjacency matrix $\mathbf{A}_{\text{adj}}$ is initialized with:

$$a_{ij} = \begin{cases} 1 & \text{if } e_{ij} \in \mathcal{E} \\ 0 & \text{else} \end{cases}$$

Then $\mathbf{A}_{\text{adj}}$ is modified in such a way that the distance of each edge
e_{ij} in the m shortest paths is increased, where $p = m$ is the degree of
the node where a VSC-HVDC link is connected. This is done with the
following procedure for each VSC terminal.

1. Find the shortest path $\mathcal{P}$ which connects the two VSC-HVDC
   terminal busses v_{vsc1}, v_{vsc2} with the Dijkstra algorithm [108]. It
   is defined as $\mathcal{P} = \{bus_1, bus_2, \ldots, bus_i, \ldots, bus_{n-1}, bus_n\}$, where
   $bus_1 = v_{\text{vsc1}}$ and $bus_n = v_{\text{vsc2}}$.

2. Increase the distance between the VSC-HVDC terminals, by in-
   creasing the weight of each edge with

$$w(bus_1, bus_2) \quad = \quad \alpha \quad ,$$
$$\vdots$$
$$w(bus_i, bus_j) \quad = \quad \alpha \quad ,$$
$$\vdots$$
$$w(bus_{n-1}, bus_n) \quad = \quad \alpha \quad ,$$

where $\alpha > 1$ defines the new line weights. α is an empirical pa-
rameter and has to be tuned.

Weighted adjacency matrix $\mathbf{A}_{\mathrm{adj}}$; weights$= 1$

Crit. 1: HVDC Grouping; Modify weighted adjacency matrix $\mathbf{A}_{\mathrm{adj}}$

Crit. 2: Slow Coherency Grouping; Modify weighted adjacency matrix $\mathbf{A}_{\mathrm{adj}}$

off-line

real-time $\sim\!\!\sim$ —— Disturbance

Rotor angels

Crit. 3: Rotor angle deviation; Modify weighted adjacency matrix $\mathbf{A}_{\mathrm{adj}}$

Create distance matrix $\mathbf{D}_{\mathrm{dist}}$

Active power generation and consumption

Crit. 4: Generation-load active power imbalance; Modify distance matrix $\mathbf{D}_{\mathrm{dist}}$

VSC-HVDC power infeed and bus net-power balance

Crit. 5: HVDC terminal active power imbalance; Modify distance matrix $\mathbf{D}_{\mathrm{dist}}$

k-means controlled islanding: Group the busses

Find the lines to be tripped

Controlled islanding: Trip the lines

Figure 7.1: Flow chart of the k-means controlled islanding algorithm.

3. Remove the edge $\{bus_1, bus_2\}$ from the graph.

4. Repeat steps 1 to 3 until the degree of the vertex v_{vsc1} equals to $p = 0$.

5. Put back all the removed edges.

6. Repeat the whole procedure for the vertex v_{vsc2}.

7.2.2 Slow Coherency

The slow coherency grouping is based on the method presented in [100]. The generators are grouped into N_{isl} groups according to the N_{isl} slowest modes. In order to be able to calculate the coherent groups, the power system model has to be reformulated to use the internal node representation as described in [109], i.e. it is only represented by the internal generator nodes after the transient reactance X_{d}'. The transient reactance X_{d}' is added after the generator node to the network model, according to Figure 7.2. The internal admittance matrix $\mathbf{Y}_{\mathrm{int}}$ is derived in Appendix D leading to the system equation

$$\mathbf{i}_A = \mathbf{Y}_{\mathrm{int}} \cdot \mathbf{e}_A \quad , \tag{7.1}$$

where $\mathbf{e}_A$ is the voltage at the generator behind the transient reactance.

The linear electrical multi-machine power system model, neglecting the damping, can now be defined according to [100] as

$$\ddot{\mathbf{x}} = \mathbf{M}_{\mathrm{h}}^{-1}\mathbf{K}\mathbf{x} = \mathbf{A}\mathbf{x} \quad , \tag{7.2}$$

where $\mathbf{x}$ is a vector with the generator angles δ_i. $\mathbf{M}_{\mathrm{h}}$ is the inertia matrix with

$$\mathbf{M}_{\mathrm{h}} = \mathrm{diag}\left(m_1, \ldots, m_{n_{\mathrm{gen}}}\right) \quad , \tag{7.3}$$

with

$$m_i = \frac{H_i}{\omega_0} \quad .$$

$\mathbf{K}$ is calculated as follows:

$$k_{ij} = E_i E_j B_{ij} \cos\left(\delta_i - \delta_j\right) \tag{7.4}$$

$$k_{ii} = -\sum_{j=1, j\neq i}^{n_{\mathrm{gen}}} k_{ij} \tag{7.5}$$
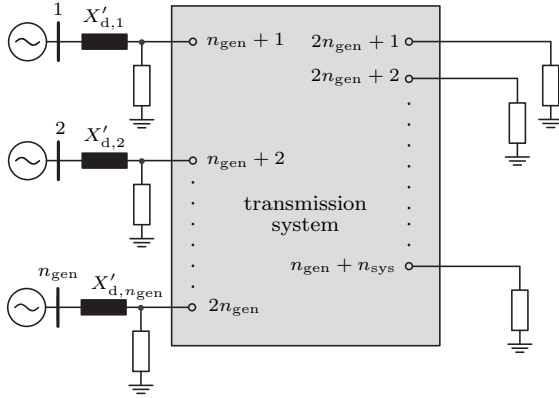
Figure 7.2: Multi-machine power system including internal generator nodes and impedance loads [109].

where E_i and E_j is the voltage at the generator behind the transient reactance and B_{ij} is the reactance from the internal admittance matrix $Y_{\text{int},ij} = G_{ij} + jB_{ij}$. **K** is symmetric if **B** is symmetric, which is true for transmission system without phase shifters [100].

The eigenvalues λ of matrix **A** are calculated. The N_{isl} slowest modes σ are chosen and the eigenvectors **v** belonging to these modes are identified. The eigenbasis matrix **V** from the σ-eigenspace is determined with

$$\mathbf{V} = [\mathbf{v}_1, \ldots, \mathbf{v}_i, \ldots, \mathbf{v}_{N_{\text{isl}}}] \quad , \tag{7.6}$$

where $\mathbf{v}_i$ are the N_{isl} eigenvectors belonging to the N_{isl} slowest modes. In order to obtain the reference states $\mathbf{x}_{\text{ref}}$ the Gaussian elimination with complete pivoting is applied to **V**

$$\mathbf{PVQ} = \mathbf{LU} \quad , \tag{7.7}$$

where **P** tracks the row permutations and **Q** the column permutations. The matrix **L** is the lower triangular and **U** the upper triangular matrix resulting of the Gaussian elimination process. The first N_{isl} states of **P** are defined as reference states $\mathbf{x}_{\text{ref}}$. Now the permuted grouping matrix

$$\mathbf{G} = \mathbf{V}_2 \cdot \mathbf{V}_1^{-1} \tag{7.8}$$

is computed, where $\mathbf{V}_1$ is the eigenspace of the reference states $\mathbf{x}_{\text{ref}}$ and $\mathbf{V}_2$ is the eigenspace of the remaining states. Every element in $\mathbf{G}$ satisfies

$$\sum_{j=1}^{N_{\text{isl}}} G_{ij} = 1, \quad i = 1, 2, \ldots, n_{\text{sys}} - N_{\text{isl}} \quad , \tag{7.9}$$

that is the summation of the entries in each row of $\mathbf{G}$ is equal to 1 [100]. The grouping matrix $\mathbf{G}_{\text{gen}}$ assigns all states to a coherent group. It is constructed as follows:

$$G_{\text{gen},ij} = \begin{cases} 1 & \forall j \quad \max(G_{ij}) \\ 0 & \text{else} \end{cases} \tag{7.10}$$

that is the largest value in each row of $\mathbf{G}$ is set to 1 and all the rest to 0 [100]. This results in each column of $\mathbf{G}_{\text{gen}}$ representing a coherent cluster with the generator states as entry.

Next, the weighted adjacency matrix $\mathbf{A}_{\text{adj}}$ has to be modified. The distance between the generators belonging to the same coherent group is decreased. This is done for every pair of generators within the same group:

1. Find the shortest paths $\mathcal{P}$ connecting two generator busses g_i and g_j within the same coherent group with the Dijkstra algorithm [108]. It is defined as $\mathcal{P} = \{bus_1, bus_2, \ldots, bus_i, \ldots, bus_{n-1}, bus_n\}$ with $bus_1 = g_i$ and $bus_n = g_j$.

2. Decrease the distance between the busses:

$$w(bus_1, bus_2) = \beta \cdot w(bus_1, bus_2) \quad ,$$
$$\vdots$$
$$w(bus_i, bus_j) = \beta \cdot w(bus_i, bus_j) \quad ,$$
$$\vdots$$
$$w(bus_{n-1}, bus_n) = \beta \cdot w(bus_{n-1}, bus_n) \quad ,$$

where $\beta < 1$. β is dependent on the system, and has to be determined empirically.

7.2.3 Rotor Angle Deviation

The generator grouping according to their rotor angles is done in real time after the disturbance. The weighed adjacency matrix $\mathbf{A}_{\mathrm{adj}}$ is modified in such a way, that the distance between two generators with differing angles is increased [105]. The rotor angles δ_i of the generators are grouped into N_{isl} clusters with k-mean clustering according to [110]. The k-mean clustering groups data points whose inter-point distances are small compared with the distance to points outside of the cluster. We define μ_k as a center for each cluster. The goal is to find an assignment of data points to clusters, as well as a set of μ_k such that the sum of the squares of the distances of each data point to this closest μ_k is a minimum [110]. The following objective function can be defined and has to minimized:

$$J = \sum_{n=1}^{n_{\mathrm{gen}}} \sum_{k=1}^{N_{\mathrm{isl}}} r_{nk} \left\| \delta_n - \mu_k \right\|^2 \qquad (7.11)$$

where $r_{nk} \in \{0,1\}$ for $k = 1, \ldots, N_{\mathrm{isl}}$ describes to which of the N_{isl} clusters the rotor angle δ_n is assigned to, so that if the rotor angle δ_n is assigned to cluster k then $r_{nk} = 1$ and $r_{nj} = 0$ for $j \neq k$. The goal is to find values for $\{r_{nk}\}$ and the $\{\mu_k\}$ so as to minimize J. This can be done through an iterative procedure, called the k-means algorithm defined in [110]. The initial centers $\{\mu_k\}$ for the k-means algorithm are the biggest generators of the coherent groups, and the N_{isl} rotor angle groups are calculated.

The adjacency matrix $\mathbf{A}_{\mathrm{adj}}$ is altered as follows:

1. Find all paths $\mathcal{P}$ connecting two generator busses g_i and g_j which belong to a different rotor angle group. Let $\mathcal{P} = \{bus_1, bus_2, \ldots, bus_i, \ldots, bus_{n-1}, bus_n\}$ with $bus_1 = g_i$ and $bus_n = g_j$.

2. Increase for every path only the weight of the first and the last edge with γ:

$$w(bus_1, bus_2) \quad = \quad \gamma \quad ,$$
$$\vdots$$
$$w(bus_{n-1}, bus_n) \quad = \quad \gamma \quad ,$$

where $\gamma > 1$.

3. Find the shortest path $\mathcal{P}$ connecting two generator busses g_i and g_j within the same rotor angle group with the Dijkstra algorithm. We define $\mathcal{P} = \{bus_1, bus_2, \ldots, bus_i, \ldots, bus_{n-1}, bus_n\}$ with $bus_1 = g_i$ and $bus_n = g_j$.

4. Decrease the distance between the busses by η with:

$$
\begin{aligned}
w(bus_1, bus_2) &= \eta \cdot w(bus_1, bus_2) \quad, \\
&\vdots \\
w(bus_i, bus_j) &= \eta \cdot w(bus_i, bus_j) \quad, \\
&\vdots \\
w(bus_{n-1}, bus_n) &= \eta \cdot w(bus_{n-1}, bus_n) \quad,
\end{aligned}
$$

where $\eta < 1$

After this step, the shortest path between each bus in the system according to the modified adjacency matrix $\mathbf{A}_{\text{adj}}$ is calculated and stored in the distance matrix $\mathbf{D}_{\text{dist}}$ with

$$
d_{ij} = \begin{cases} \psi_{ij} &, \forall i, j \\ 0 &, i = j \end{cases} \tag{7.12}
$$

where ψ_{ij} is the shortest distance between node i and node j.

7.2.4   Generation-Load Power Imbalance

The power balance within the islands from the loads and generators should be equalized as much as possible to reduce load shedding or generator tripping. Therefore the distance from the generator to the closest loads which can be fully supplied is reduced [105]. Following steps are executed for each generator:

1. Find all load busses and sort them in ascending order based on their distance.

$$
\mathbf{l}_{\text{bus}} = [bus_1, \ldots, bus_{n_{\text{loads}}}]^T \tag{7.13}
$$

where bus_1 is the load closest to generator i and $bus_{n_{\text{loads}}}$ the load with the longest distance to generator i according to $\mathbf{D}_{\text{dist}}$.

2. Form the vector $\mathbf{p}_{\text{loads}}$ with the consumed active power corresponding to the sorting of the loads

$$\mathbf{p}_{\text{loads}} = \left[P_{bus_1}, \ldots P_{bus_{n_{\text{loads}}}} \right]^T \tag{7.14}$$

Calculate the cumulative sum of $\mathbf{p}_{\text{loads}}$ with

$$\mathbf{p}_{\text{cumulative}} = \begin{bmatrix} P_{bus_1} \\ \vdots \\ \sum_{k=1}^{i} P_{bus_k} \\ \vdots \\ \sum_{k=1}^{n_{\text{loads}}} P_{bus_k} \end{bmatrix} \tag{7.15}$$

3. Subtract from each element in $\mathbf{p}_{\text{cumulative}}$ the active power output P_{gen} of the generator.

$$\mathbf{O} = \left[\ \mathbf{1}_{\text{bus}}, \mathbf{p}_{\text{cumulative}} - P_{\text{gen}} \ \right] \tag{7.16}$$

The busses which can be fully supplied by the generator are defined by the negative elements of the second column of $\mathbf{O}$.

4. Reduce the distance in $\mathbf{D}_{\text{dist}}$ between the generator and those busses by the factor of $\vartheta < 1$.

5. Repeat for all generators.

7.2.5   VSC-HVDC Injection-Bus Power Imbalance

To further reduce the generation-load imbalance of the islands, the power injections of the VSC-HVDC terminals are considered. A VSC-HVDC terminal can behave as a load when it transmits power to the other side of the VSC-HVDC link or as a generator if it injects power to the island. If the VSC-HVDC terminal injects power, for each VSC-HVDC terminal the procedure of Section 7.2.4 repeated with the following modifications:

1. Calculate the net power balance P_{net} for each bus in the system.

2. Find all busses which behave like load busses and sort them in ascending order based on their distance to the VSC-HVDC terminal

$$\mathbf{l}_{\mathrm{bus}} = [bus_1, \ldots, bus_{n_{\mathrm{loads}}}]^T \tag{7.17}$$

where bus_1 is the load bus closest to a VSC-HVDC terminal and $bus_{n_{\mathrm{loads}}}$ the furthest one.

3. Apply steps 2) to 4) from Section 7.2.4. However, the distance in $\mathbf{D}_{\mathrm{dist}}$ to the VSC-HVDC terminal is reduced by the factor $\kappa < 1$.

4. Repeat for all VSC-HVDC terminals.

If the terminal transmits power the other side of the link, the distance matrix $\mathbf{D}_{\mathrm{dist}}$ is modified as follows:

1. Calculate the net power balance P_{net} for each bus in the system.

2. Find all busses which behave like generator busses and sort them in ascending order based on their distance to the VSC-HVDC terminal

$$\mathbf{l}_{\mathrm{bus}} = [bus_1, \ldots, bus_{n_{\mathrm{loads}}}]^T \tag{7.18}$$

where bus_1 is the load bus closest to a VSC-HVDC terminal and $bus_{n_{\mathrm{loads}}}$ the furthest one.

3. Apply steps 2) to 4) from Section 7.2.4 with the opposite sign. Reduce the distance of these busses by the factor $\kappa < 1$.

4. Repeat for all VSC-HVDC terminals.

7.2.6   Forming Islands with k-Means Clustering

The distance matrix $\mathbf{D}_{\mathrm{dist}}$ has been modified and all the nodes are now grouped according the objective in Figure 7.1. The busses can be clustered into N_{isl} islands according the k-means algorithm described in [110]. When the busses for each island are determined, all AC lines connecting these islands are identified. Tripping these lines will form the desired islands, which are only connected with VSC-HVDC links. It allows an exchange of active power between the islands, as well as reactive power support at the terminals.
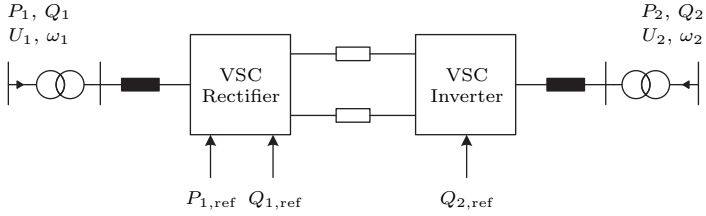
(a) Single line equivalent of VSC-HVDC dynamic model.
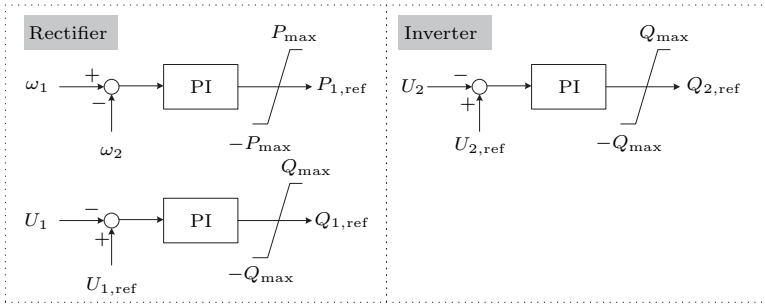
(b) Control structure of the overlying VSC-HVDC power system controller to calculate the power reference values for the rectifier and inverter.

Figure 7.3: VSC-HVDC dynamic model with terminal controller to calculate the new VSC-HVDC set-points.

7.3   VSC-HVDC Controlled Islanding Terminal Control

For the VSC-HVDC links, the dynamic model from Section 3.4 is selected. It considers three control loops: active and reactive power at the rectifier and reactive power at the inverter. The DC voltage controller at the inverter is assumed to be fast and modelled as a voltage source. Figure 7.3a shows the single line diagram of the VSC-HVDC link with the controller inputs. The controller inputs are changed by the overlying controlled islanding terminal controller.

Each VSC-HVDC link operates in *PU*-control mode. Figure 7.3b shows the controlled islanding terminal controller of the VSC-HVDC links.

The goal of this controller is, in case of controlled islanding, to transfer power form an island with a generation surplus to an island with a power deficit. A local measurement, to detect if there is a surplus or a deficit of energy, is the frequency of an island. Each converter measures the frequency ω_i, $i \in \{1, 2\}$ and they compare it with each other, $\Delta\omega = \omega_1 - \omega_2$. The island with the lower frequency has a generation deficit and the island with the higher frequency a generation surplus relatively to each other. The PI-controller depicted in Figure 7.3b tries to minimize the frequency difference $\Delta\omega$ between the terminals and calculates the new reference power $P_{1,\text{ref}}$ which is sent to the internal rectifier controller. The reactive power capability at the rectifier and the inverter is used for local voltage support. A PI-controller controls the AC terminal voltage U_i, $i \in \{1, 2\}$, to the desired reference voltage $U_{\text{ref},i}$.

7.4   Dynamic Simulation

The controlled islanding algorithm has been tested on the IEEE 16 machine 68 bus test system. The static and dynamic data are adopted from [51]. One VSC-HVDC link with a length of 100 km is added connecting bus 52 with bus 68. It has a nominal power rating of 570 MVA and transfers 171 MW from bus 52 to bus 68, depicted in Figure 7.4 and Figure 7.5. All generators are equipped with AVR systems, PSSs and governor droop controller for primary frequency control. The data can be found in Appendix B.3. The loads are modelled as constant impedance loads and for all loads an under-frequency load shedding (UFLS) scheme according to [111] is in action. The values of the UFLS are shown in Table 7.1. The first 5% of the installed load at the bus are shed at a frequency of 49.00 Hz with a delay of 200 ms. Another 10% are shed if the frequency is lower then 48.80 Hz and 48.60 Hz, respectively. Below 48.00 Hz a total of 50% of the installed load at that node will be shed. There is no over-frequency generator tripping installed.

Two cases where the system is split into two islands have been simulated. Case A uses the controlled islanding algorithm of [105]. It does not consider the HVDC criteria 1 and 5 from Figure 7.1. Case B uses the proposed algorithm, including the HVDC criteria 1 and 5 from Section 7.2. Following parameters for the controlled islanding algorithm have been used: $\alpha = 5$, $\beta = 0.8$, $\gamma = 100$, $\eta = 0.1$, $\vartheta = 0.7$ and $\kappa = 0.1$. First the islands are formed, and then the dynamic response of the

Table 7.1: Under frequency load shedding scheme.

Frequency (Hz)	Delay (ms)	Load Shed (%)
49.00	200	5
48.80	200	10
48.60	200	10
48.00	200	25

VSC-HVDC links as well as the entire system is analyzed after switching the AC lines.

Table 7.2 shows the result of both controlled islanding algorithm. It shows for both cases which lines have been switched in order to form the islands. Figure 7.4 depicts the formed islands for case A, where island 1 is colored green and island 2 colored blue. The switched lines are marked with red crosses. In this case study, the two VSC-HVDC terminals are in two different islands and the VSC-HVDC link injects initially 171 MW into island 2. The power balance mismatch in both islands is quite large. Island 1 is 2 531 MW short and island 2 is 2 703 MW long. However, this is not necessarily the case. In Appendix E the RTS96 system with 2 VSC-HVDC links is split into 3 islands, where not all islands are connected with HVDC connections. In Figure 7.5 the results of case B, using the proposed controlled islanding algorithm, are shown. Island 1 is colored green and island 2 blue. The switched lines are marked with red crosses. Table 7.2 lists the switched lines. As expected, the VSC-HVDC terminals are in two different islands and the VSC-HVDC link transfers 171 MW from island 1 to island 2. The power balance mismatch in both islands is much smaller as in case A. Island 1 is 11 MW short and island 2 is 181 MW long.

The dynamic simulation of the system for both cases is done in Neplan using the transient stability toolbox [112]. The system is simulated for 60 s and after 0.5 s it is split into two islands, according to the results of the controlled islanding algorithm in Table 7.2. Both systems could be stabilized. In case A there is a large load surplus for island 1 of 2531 MW and thus the VSC-HVDC link cannot transfer enough power from island 2 to island 1. Therefore the UFLS gets activated and a total of 1307 MW has to be shed at busses 37, 39, and 44. In addition, the average frequency of both islands according to Figure 7.6 deviates from
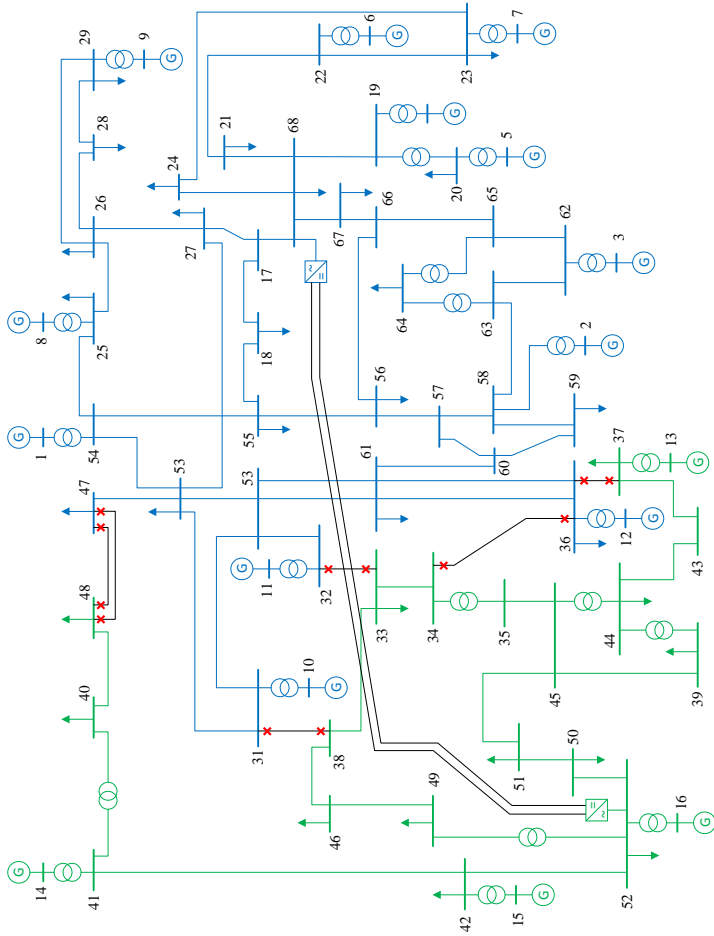
Figure 7.4: Case A: Results of the controlled islanding algorithm without using the HVDC modification for the IEEE 16 machine 68 bus test system including a VSC-HVDC link connecting bus 52 with bus 68.
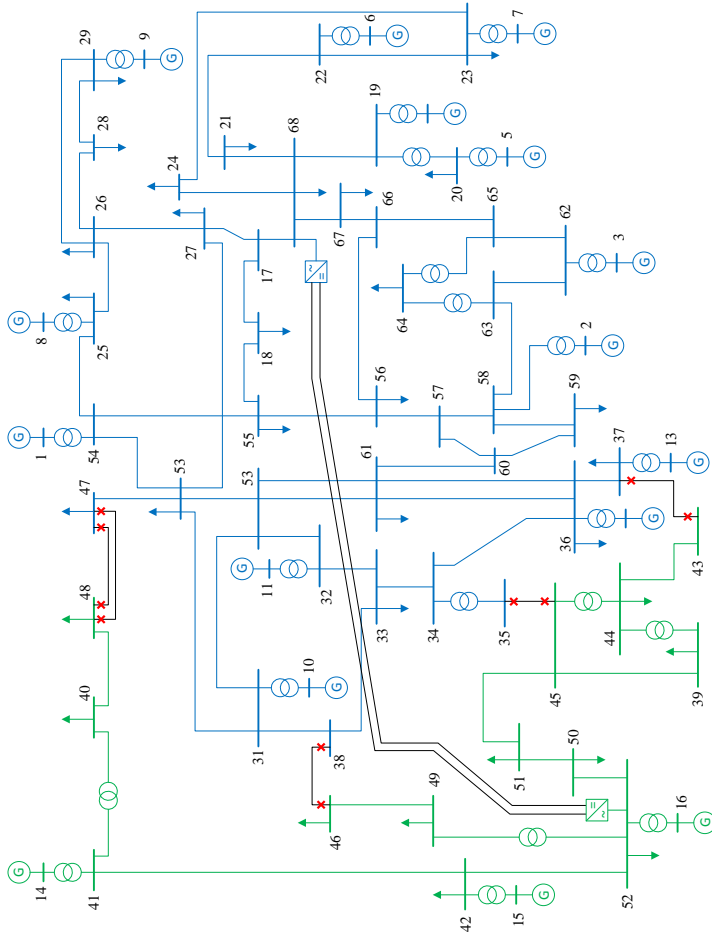
Figure 7.5: Case B: Results of the controlled islanding algorithm with the modification for the VSC-HVDC links for the IEEE 16 machine 68 bus test system including a VSC-HVDC link connecting bus 52 with bus 68.

Table 7.2: Comparison of controlled islanding schemes.

	Case A: Without Using HVDC Criteria		Case B: Using HVDC Criteria	
Controlled Line Switch-Off	31-38, 32-33, 34-36, 36-37, 47-48-a, 47-48-b		35-45, 37-43, 38-46, 47-48-a, 47-48-b	
	Island 1	**Island 2**	**Island 1**	**Island 2**
Total Gen. (MW)	10 373	8 032	6 781	11 623
Total Load (MW)	12 733	5 501	6 621	11 613
Pre-islanding HVDC Injection (MW)	−171	171	−171	171
ΔP (MW)	−2 531	2 703	−11	181
Post-islanding HVDC Injection (MW)	570	−570	−202	202
Shed Load (MW)	1 307	0	0	0

each other. Hence, the secondary control has to drive the frequency to the same value which take some time before the islands can be re-synchronized. In case B, the VSC-HVDC link is able to transfer enough power to islands 1. Therefore, no loads have to be shed. The VSC-HVDC link is not only able to balance the power in both islands, but also controls the frequency to the same value, depicted in Figure 7.6. Thus re-synchronization of both islands can be done faster than in case A.

Figure 7.7 depicts the measured bus frequencies for both cases. It can be seen that the frequencies at nodes 14, 37, 39, 43, and 44 for case A are very low. They fall even below 48 Hz. In consequence the UFLS scheme comes into action. The under-frequency relays open at load 37, 39, and 44 and a total of 1 307 MW is shed. For case B, the frequencies are always above the UFLS threshold of 49 Hz and no loads need to be shed.

In Figure 7.8 the AC bus voltages for both cases are shown. The voltages in case A heavily oscillate and reach unacceptable values, especially in island 1. The nodes in the vicinity of 44 do not have any active voltage support and therefore oscillate the most. In case of under-voltage

Mean Island Frequencies, Case A
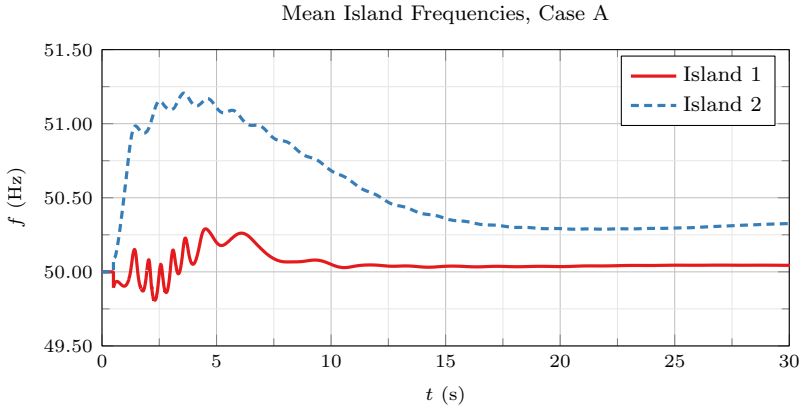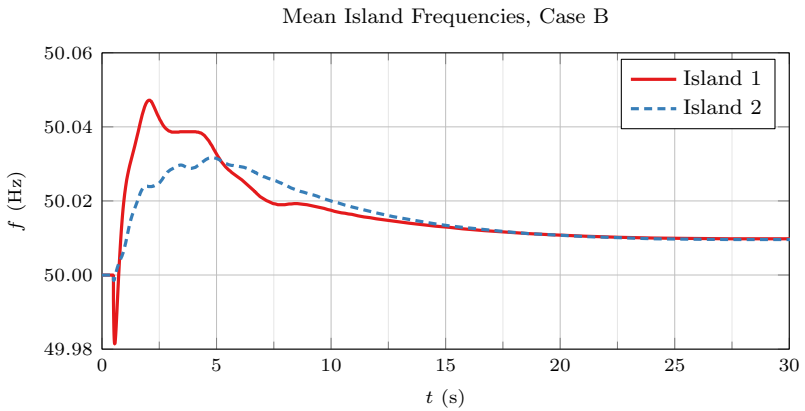
Mean Island Frequencies, Case B

Figure 7.6: Illustration of mean frequencies of the different islands for each case. The red solid curve is the mean frequency of island 1 and the blue dotted curve of island 2. Note the different scales of the frequencies between case A and case B.
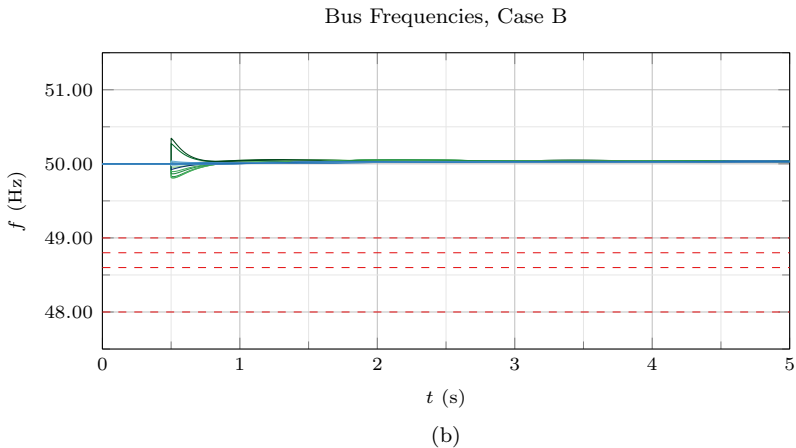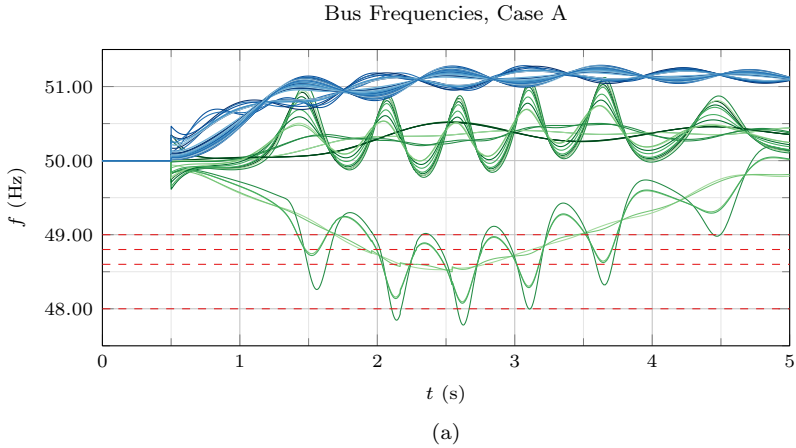
Figure 7.7: Bus frequencies of all 68 busses for each case. The green shaded curves represent the frequencies of island 1 and the blue shaded curves the frequencies of island 2. The red dotted lines are the UFLS frequencies thresholds according Table 7.1.

Bus Voltages, Case A

(a)

Bus Voltages, Case B

(b)
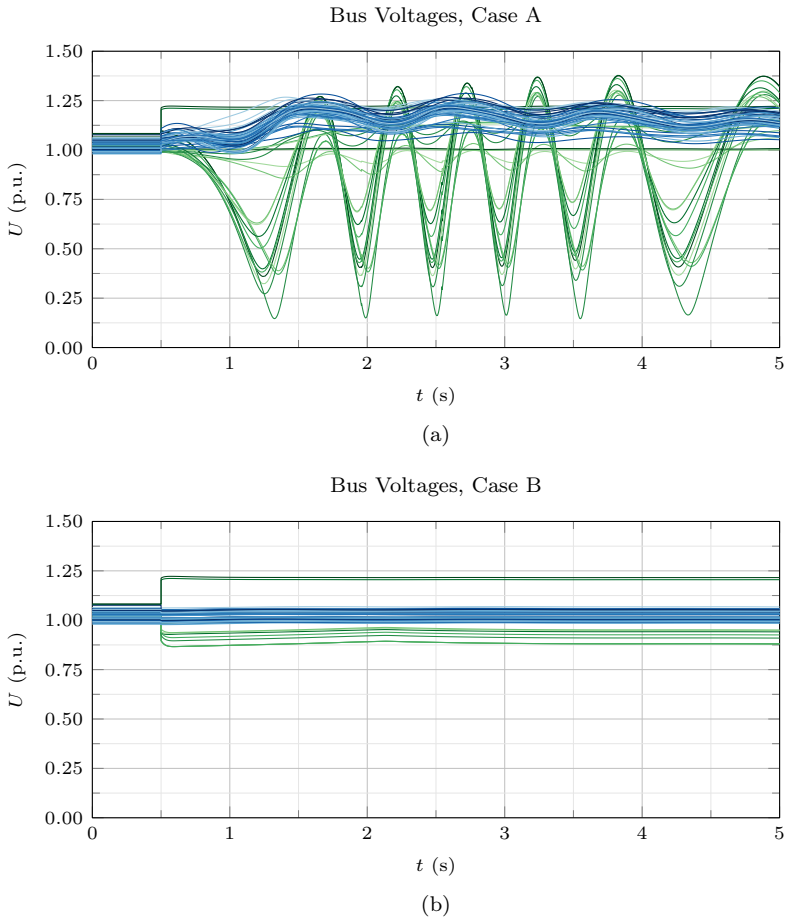
Figure 7.8: AC Bus voltages of all 68 busses for each case. The green shaded curves represent the AC voltages of island 1 and the blue shaded curves the AC voltages of island 2.
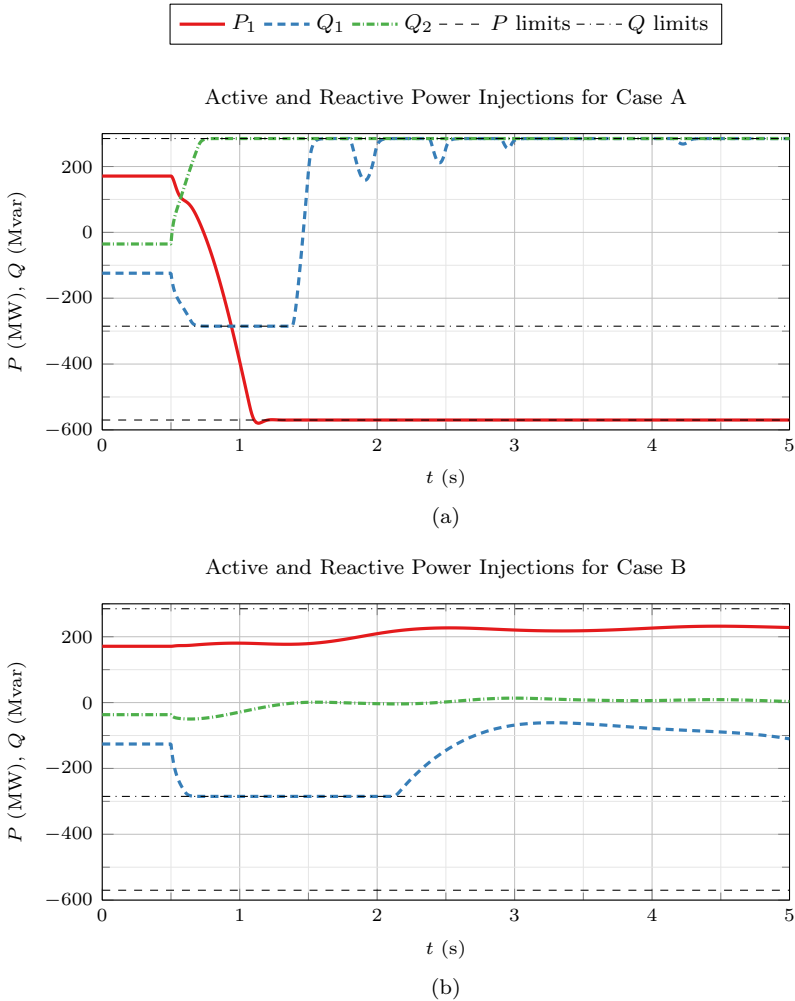
Figure 7.9: Active and reactive power injections of the VSC-HVDC link for
(a) Case A, and (b) Case B. The red solid curve shows the
active power flow P_1 from bus 52 into the VSC-HVDC link.
The blue dotted curve shows the reactive power Q_1 consumed
by the terminal at bus 52 and the green dash-dotted line the
reactive power consumption Q_2 by the terminal at bus 68. The
black dashed line shows the active power limes, and the black
dash-dotted line the reactive power limits of the terminals.

detection these nodes would be tripped and drives the system even further in extrema. On the other hand, in case B most voltages remain of acceptable values with the help of the VSC-HVDC terminal voltage control. However, two voltages have to be pointed out which are quite high, that is the voltage at busses 40 and 48. However, with a tap-changer between bus 41 and bus 40 these voltages could be controlled and reduced to more acceptable values. The lowest voltages are found as well in island 1 around node 44. However, the lowest voltage is 0.88 p.u. and well above the acceptable value of 0.8 p.u..

Figure 7.9 shows the active and reactive power flows over the VSC-HVDC link. In case A, the power of the VSC-HVDC link is reversed in order to supply island 1 with more power. However, the VSC-HVDC link saturates at about 1 s. It is not able to supply island 1 with enough power, which results in load shedding at about 1.5 s. In case B, the VSC-HVDC link hardly changes its active power set-point, because the power imbalance in each island is very small, -11 MW for island 1 and 181 MW for island 2. In both cases, island 1 needs reactive power support after the disturbance and the reactive power Q_1 saturates to support the voltage. However, in case A the reactive power flow has to be reversed after the load shedding in order to control the voltages. In island 2, reactive power has to be absorbed in order to lower the voltage. Because island 1 is always long, the VSC-HVDC terminal is absorbing reactive power.

7.5   Conclusion

This chapter presented an algorithm based on k-means clustering for controlled islanding that can be applied to utilize the capability of a VSC-HVDC link to exchange power between two asynchronous islands. The algorithm tries to form islands based on different objectives with the help of an off-line part and a real-time part. It considers the coherency of the generator and the location of the VSC-HVDC terminals off-line. The generation-load balance, the rotor angle deviation between the generators and the infeed of the VSC-HVDC terminals are considered in the real-time part after a disturbance occurred. With the aim to place VSC-HVDC terminals in two different islands, it is still possible to exchange power between the islands in order to reduce load shedding and generator tripping. Further, a controller which adapts the set-points for active and reactive power at the VSC-HVDC terminal is presented.

The control inputs are based purely on local measurements. Thus, the controller does not rely on a communication systems.

The proposed controlled islanding method was demonstrated on the IEEE 16 machine 68 bus system including a VSC-HVDC link and was compared to the method in [105]. The proposed method successfully split the system into two islands where each VSC-HVDC terminal was in a different island. In a dynamic simulation it was further shown that within the proposed island no loads had to be shed and the system could be stabilized. Because the proposed HVDC controller also controlled the frequency deviation between both islands, the system frequencies of both islands converged, which would simplify the re-synchronization of both islands. This would result in lower costs during the disturbance and the restoration period.

Chapter 8

Conclusion and Outlook

This chapter summarizes the thesis and draws the conclusion of the this work. Finally some suggestions and an outlook for further research is given.

8.1 Summary of the Thesis

This thesis investigated how VSC-HVDC links are able to enhance the power system stability by modulating their active and reactive power. In order to do so suitable VSC-HVDC models have to be developed. In Chapter 3 three different VSC-HVDC models were presented: A steady-state model for PF and OPF studies, a detailed dynamic model for power system stability studies, and a simplified dynamic model which can be used as a control model for a MPC based controller or for power system stability studies.

The detailed dynamic model incorporates dynamic elements as well as the converter control. In order to have a realistic response of the VSC-HVDC link after a change of the power set-points, the model has to be appropriately tuned. A tuning method for the converter control was developed in order to reproduce the active and reactive power response of an ABB black-box benchmark model. The simplified dynamic model only models the dynamic response of the changes in the set-point of the active and reactive power. The converter controller as well as the dynamic elements are only implicitly modelled in a transfer function

which allows to reduce the number of dynamic states significantly. Simultaneously the active and reactive power response of the VSC-HVDC link is similar to the ABB black-box benchmark model.

In order to enhance power system stability by the use of VSC-HVDC links, a global grid controller based on MPC was developed. The advantage of using MPC is that the controller uses an internal dynamic model of the power system with all its components and can therefore predict the behavior of the system over a certain prediction horizon. Another advantage is that if multiple VSC-HVDC links are in one system, the controller is able to coordinate the control actions and calculate the optimal set-points for the VSC-HVDC links based on the controller's objective function. Two MPC-based grid controllers were proposed. In Chapter 4, an inter-area oscillation damping controller was introduced. The MPC objective is to minimize the frequency difference from each generator to the average system frequency. The optimal active and reactive power set-points which damp the inter-area oscillations are sent to the VSCs and the converter control applies the new power references. This controller was tested in a small network to validate the concept and then applied to a system model of the European network. Multiple VSC-HVDC links are controlled in a coordinated way and the power system stability is enhanced. Chapter 5 introduced a second MPC-based grid controller which enhances the voltage stability of the system incorporating VSC-HVDC links. The objective of the controller consists of three parts. First it controls the AC terminal voltage by minimizing the voltage difference of a given set-point, secondly it minimizes the frequency deviation of the generators from the mean system frequency to damp inter-area oscillations, and thirdly it tries to keep all AC bus voltage within the operational limits. Again, the VSC-HVDC links are controlled in a coordinated way and the optimal power injections which enhance the voltage stability are sent to the converters and applied by the converter control. The controller was tested on the small two area system to validate the concept and later on tested on the larger Nordic 32 test system, which is often used for voltage stability studies. It was shown that the MPC-based grid controller was able to improve voltage stability by controlling the VSC-HVDC power injections in a coordinated way, compared to a decentralized local control scheme.

With the *Energiewende* more RES are introduced to the European system. This creates new challenges for the power system operation and its stability. One of the challenges is how to handle the reduced system inertia caused by the decommissioning of large synchronous generators.

These capacities are replaced with RES which have a small or no inertia. This thesis investigated in Chapter 6, if and how VSC-HVDC links can add additional damping to the system and enhance frequency stability in a system with a small inertia. The MPC-based inter-area oscillation controller is applied to the European system with a high share of RES. It was assumed that four VSC-HVDC links are operational in the system and they are used for power oscillation damping. It was shown that these links, even if their installed transfer capacity is only 2.3% of the total load of the system, were able to add sufficient damping to the system in order to enhance frequency stability and drives the system in a stable equilibrium.

Controlled islanding is the last resort of emergency control in order to prevent a large disturbance to spread throughout the system and cause a system-wide blackout. However, it is not possible to exchange power with AC transmission lines between these islands This thesis developed in Chapter 7 a controlled islanding algorithm based in k-means clustering, considering already installed VSC-HVDC links in the system. The goal was to find islands in order to connect them with VSC-HVDC links. Thus, the exchange of power between the islands is possible in order to minimize the generation-load imbalance. Further a controlled islanding VSC-HVDC local controller was introduced, which allows the VSC-HVDC links to change the active and reactive power setpoints after the controlled islanding in order to reduce the generation-loss imbalance and enhance voltage stability. The controlled islanding algorithm and the real-time control of the VSC-HVDC link were tested in the IEEE 16 machine 68 bus system. The system was successfully split into two islands which were connected with a VSC-HVDC link. The local controlled islanding controller was able to modulate the active and reactive power of the VSC-HVDC link in order that no loads were shed and both islands reached a stable equilibrium. The frequency difference of both islands was reduced by the controller, which would simplify the re-synchronization of the islands.

8.2   Conclusions

From the VSC-HVDC modelling part the following conclusions can be drawn:

- Due to the challenge of obtaining open VSC-HVDC dynamic models including the converter control, this thesis developed publicly available VSC-HVDC dynamic models as well as a method for tuning the converter control, which can be used for power system stability studies.

- The developed models reflect the response of the ABB black-box models. However, they can be tuned to any other active and reactive power response based on a different benchmark model. The developed models can also be applied to MMC technologies.

The dynamic simulations with the MPC-based controller provided the following conclusions:

- The proposed MPC-based inter-area as well as the MPC-based voltage stability controller were able to enhance the power system stability by modulating the active and reactive power of the VSC-HVDC links.

- The coordinated and predictive control of multiple VSC-HVDC links proved to be superior compared to the local controller tested in this thesis. This is due to the fact that the MPC-based controller is not rule based and is able prematurely react on the dynamics of the power system.

- It has been shown that even with only a few VSC-HVDC links the power system stability could be enhanced in a large system like the European system. This implies that if VSC-HVDC links are installed within the European system they should be strongly used for power system stability purposes. It is expected that this comes with only marginal additional costs. The planned VSC-HVDC links between Spain and France as well as the link in Germany proved to be very effective in the dynamic studies.

From the controlled islanding algorithm which includes VSC-HVDC links and the local controlled islanding controller following conclusions can be drawn:

- The controlled islanding algorithm based on k-means clustering was able to form islands with a small generation-load imbalance which are connected by VSC-HVDC links. Connecting islands with VSC-HVDC links brings the advantage of exchanging power between the two asynchronous islands. In doing so load shedding is reduced which reduces the economic costs of a disturbance.

- The VSC-HVDC local controller tries to minimize the frequency deviation between the connected islands. Therefore the frequency of both islands might be equal. Therefore the secondary control of the generators does not have to be called which might expedites the re-synchronization of both islands. The faster both islands are re-synchronized the higher will be the system security, since larger systems are more robust to power system disturbances.

- Voltage source converter-based HVDC links in the European system should be included in the controlled islanding scheme. This might prevent a blackout in Europe similar to 2007 where the system was split into three islands. However the islands had a large load-generation mismatch, thus loads and generation had to be tripped [113].

8.3 Outlook

The approach of using a global MPC-based grid controller calls for some strong assumption:

- Full knowledge of the power system including the system topology, power plant topology including the generator control, voltage and power flow measurements and the internal states of the generators, AVR, GOV and PSS.

- No measurement delays are incorporated in the MPC-based grid controller.

- A congruent linear control model of the nonlinear system model is used for the MPC based grid controller.

These assumption might be difficult to defend for real power systems. In order to address the full knowledge of the power system and having one controller, a decentralized MPC-based control approach should be

investigated. This would incorporate the present structure of the power system, where different TSOs operate parts of the system, where only a limited amount of information is shared between these entities. In order to address the measurement delays, the robustness of the MPC-based grid controller on delayed measurements or even lost measurements should be further investigated. If the measurement delays are known, the MPC controller model could be adjusted to design a more robust controller.

This thesis showed that VSC-HVDC links are able to enhance power system stability, when they are controlled optimally in a global manner using a MPC-based controller. The next research question should be, how can they be controlled in a way that the control scheme fits into the current operational scheme of todays power systems. Instead of a global MPC-based grid controller, the focus could be on a decentralized MPC-based controller of the VSC-HVDC links [114]. The power system may be split according to TSO boarders. This would prevent the communication of sensitive data to others, while still obtaining a robust and stable solution.

Appendix A

VSC-HVDC Model Parameters

A.1 Steady State Model

Table A.1: Steady state parameters.

Type	S_{B} (MVA)	$U_{\mathrm{B,ac}}$ (kV)	U_{dc} (kV)	L_{trafo}	L_{r}	R_{r}	R_{dc} (p.u./km)
M1	101	230	± 80	0.113	0.1656	0.001	1.2e-3
M5	570	230	± 195	0.113	0.1640	0	1.977e-5
M9	1216	416	± 320	0.113	0.1656	0.001	9.3813e-05

A.2 Dynamic Model

A.2.1 HVDC Parameters

Table A.2: Dynamic element parameters.

Type	$C_{\text{converter}}$ (p.u.)	C_{cable} (p.u./km)	L_{dc} (p.u./km)
M1	0.004	9.7584e-06	2.2094e-06
M9	0.004	9.5158e-06	1.3063e-06

A.2.2 Linear Control Model Parameter

The linearized transfer function of the plant is given in (3.57). The open loop transfer function with the PI-controller is:

$$l_{\text{dc}}(s) = k_{\text{Udc}}(s) \cdot G_{\text{Udc}}(s) = \frac{\alpha_3 s^3 + \alpha_2 s^2 + \alpha_1 s + \alpha_0}{\beta_4 s^4 + \beta_3 s^3 + \beta_2 s^2 + \beta_1 s + \beta_0} \quad , \quad \text{(A.1)}$$

where the values α_3, α_2, α_1, α_0 and β_3, β_2, β_1, β_0 are listed in Table A.3. The closed-loop transfer function:

$$H_{\text{Udc}}(s) = \frac{\hat{U}_{\text{dc},2}(s)}{\hat{U}_{\text{dc,ref}}(s)} = \frac{\alpha_3 s^3 + \alpha_2 s^2 + \alpha_1 s + \alpha_0}{\beta_4 s^4 + \beta_3 s^3 + \beta_2 s^2 + \beta_1 s + \beta_0} \quad , \quad \text{(A.2)}$$

with the values α_3, α_2, α_1, α_0 and β_3, β_2, β_1, β_0 listed in Table A.4.

A.2.3 Control Parameter

Current Controller

Table A.5: Parameters of d- and q-current controller.

Type	$K_{\text{p,id},i}$	$K_{\text{i,id},i}$	$K_{\text{p,iq},1}$	$K_{\text{i,iq},1}$	$u^d_{i,\text{min,max}}$	$u^q_{1,\text{min,max}}$
M1	0.0088	0.02	0.0088	0.02	± 1	± 1
M9	0.0105	0.02	0.0105	0.02	± 1	± 1

Table A.3: Values of the open loop transfer function $l_{\mathrm{dc}}(s)$.

$$
\begin{aligned}
\alpha_3 &= 2C_{\mathrm{dc}}L_{\mathrm{dc}}U_{\mathrm{dc},1,0}^2 K_{\mathrm{p,dc}}K_{\mathrm{i,dc}} \\
\alpha_2 &= 2C_{\mathrm{dc}}L_{\mathrm{dc}}U_{\mathrm{dc},1,0}^2 K_{\mathrm{i,dc}} + \left(2C_{\mathrm{dc}}R_{\mathrm{dc}}U_{\mathrm{dc},1,0}^2 + L_{\mathrm{dc}}P_{\mathrm{dc},1,0}\right)K_{\mathrm{p,dc}}K_{\mathrm{i,dc}} \\
\alpha_1 &= 2C_{\mathrm{dc}}R_{\mathrm{dc}}U_{\mathrm{dc},1,0}^2 + L_{\mathrm{dc}}P_{\mathrm{dc},1,0}K_{\mathrm{i,dc}} + \left(2U_{\mathrm{dc},1,0}^2 + R_{\mathrm{dc}}P_{\mathrm{dc},1,0}\right)K_{\mathrm{p,dc}}K_{\mathrm{i,dc}} \\
\alpha_0 &= \left(2U_{\mathrm{dc},1,0}^2 + R_{\mathrm{dc}}P_{\mathrm{dc},1,0}\right)K_{\mathrm{i,dc}} \\[6pt]
\beta_4 &= 2C_{\mathrm{dc}}^2 L_{\mathrm{dc}}U_{\mathrm{dc},1,0}^2 \\
\beta_3 &= 2C_{\mathrm{dc}}^2 R_{\mathrm{dc}}U_{\mathrm{dc},1,0}^2 + C_{\mathrm{dc}}L_{\mathrm{dc}}P_{\mathrm{dc},1,0} \\
\beta_2 &= 4C_{\mathrm{dc}}^2 U_{\mathrm{dc},1,0}^2 + C_{\mathrm{dc}}R_{\mathrm{dc}}P_{\mathrm{dc},1,0} \\
\beta_1 &= P_{\mathrm{dc},1,0} \\
\beta_0 &= 0
\end{aligned}
$$

Table A.4: Values of the closed loop transfer function $H_{\mathrm{Udc}}(s)$.

$$
\begin{aligned}
\alpha_3 &= 2C_{\mathrm{dc}}L_{\mathrm{dc}}U_{\mathrm{dc},1,0}^2 K_{\mathrm{p,dc}}K_{\mathrm{i,dc}} \\
\alpha_2 &= 2C_{\mathrm{dc}}L_{\mathrm{dc}}U_{\mathrm{dc},1,0}^2 K_{\mathrm{i,dc}} + \left(2C_{\mathrm{dc}}R_{\mathrm{dc}}U_{\mathrm{dc},1,0}^2 + L_{\mathrm{dc}}P_{\mathrm{dc},1,0}\right)K_{\mathrm{p,dc}}K_{\mathrm{i,dc}} \\
\alpha_1 &= \left(2C_{\mathrm{dc}}R_{\mathrm{dc}}U_{\mathrm{dc},1,0}^2 + L_{\mathrm{dc}}P_{\mathrm{dc},1,0}\right)K_{\mathrm{i,dc}} + \left(2U_{\mathrm{dc},1,0}^2 + R_{\mathrm{dc}}P_{\mathrm{dc},1,0}\right)K_{\mathrm{p,dc}}K_{\mathrm{i,dc}} \\
\alpha_0 &= \left(2U_{\mathrm{dc},1,0}^2 + R_{\mathrm{dc}}P_{\mathrm{dc},1,0}\right)K_{\mathrm{i,dc}} \\[6pt]
\beta_4 &= 2C_{\mathrm{dc}}^2 L_{\mathrm{dc}}U_{\mathrm{dc},1,0}^2 \\
\beta_3 &= 2C_{\mathrm{dc}}^2 R_{\mathrm{dc}}U_{\mathrm{dc},1,0}^2 + C_{\mathrm{dc}}L_{\mathrm{dc}}P_{\mathrm{dc},1,0} + 2C_{\mathrm{dc}}L_{\mathrm{dc}}K_{\mathrm{p,dc}}K_{\mathrm{i,dc}} \\
\beta_2 &= 4C_{\mathrm{dc}}^2 U_{\mathrm{dc},1,0}^2 + C_{\mathrm{dc}}R_{\mathrm{dc}}P_{\mathrm{dc},1,0} + 2C_{\mathrm{dc}}L_{\mathrm{dc}}U_{\mathrm{dc},1,0}^2 K_{\mathrm{i,dc}} + \left(2C_{\mathrm{dc}}R_{\mathrm{dc}}U_{\mathrm{dc},1,0}^2 + 2U_{\mathrm{dc},1,0}^2\right)K_{\mathrm{p,dc}}K_{\mathrm{i,dc}} \\
\beta_1 &= P_{\mathrm{dc},1,0} + \left(2C_{\mathrm{dc}}R_{\mathrm{dc}} + L_{\mathrm{dc}}P_{\mathrm{dc},1,0}\right)K_{\mathrm{i,dc}} + \left(2C_{\mathrm{dc}}R_{\mathrm{dc}}U_{\mathrm{dc},1,0}^2 + 2U_{\mathrm{dc},1,0}^2\right) \\
\beta_0 &= \left(2U_{\mathrm{dc},1,0}^2 + R_{\mathrm{dc}}P_{\mathrm{dc},1,0}\right)K_{\mathrm{i,dc}}
\end{aligned}
$$

Active and Reactive Power Controller

Table A.6: Parameters of active and reactive power controller.

Type	$K_{\mathrm{p,P}}$	$K_{\mathrm{i,P}}$	$i_{1,\mathrm{max}}^{q}$	$K_{\mathrm{p,Q},i}$	$K_{\mathrm{i,Q},i}$	$i_{i,\mathrm{max}}^{d}$
M1	0.7619	64.8693	1	12.8155	1151.7	0.5
M9	0.7619	64.8693	1	12.8155	1151.7	0.5

DC Voltage Controller

Table A.7: Parameters of DC voltage controller.

Type	$K_{\mathrm{p,Udc}}$	$K_{\mathrm{i,Udc}}$	$U_{\mathrm{dc,\,min}}$	$U_{\mathrm{dc,\,max}}$
M1	0.1502	15.03	0.8	1.2
M9	0.1502	15.03	0.8	1.2

A.3   Simple VSC-HVDC Model

Table A.8: Dynamic parameters of simple VSC-HVDC model.

Type	M_{p}	t_{p} (ms)	ω_{p} (1/s)	ζ_{p}	K (1/s)^{2}	τ_{Q} (ms)
M1	0.17	200	41	0.5912	1681.053	100
M5	0.17	180	38.95	0.591	1517.103	100
M9	0.17	40	18.0343	0.4913	325.236	20

Appendix B

System Data

B.1 Two Area System

B.1.1 Inter-Area Oscillation Study

The topology of the two area system is shown in Figure 4.1. All data
are in p.u. with a base power of 100 MVA.

Table B.1: Machine bus data of two area system.

Bus Nr.	U_B (kV)	U	P_g
1	20	1.03	7.00
2	20	1.01	7.00
3	20	1.03	7.17
4	20	1.01	7.00

Table B.2: Bus data of two area system.

Bus Nr.	U_B (kV)	P_l	Q_l	P_{sh}	Q_{sh}
7	230	9.67	1.00	0	-2.00
9	230	17.67	1.00	0	-3.50

Table B.3: AC line data of two area system.

From	To	R	X	B	Tap Ratio
1	5	0	0.1666	0	1
2	6	0	0.1666	0	1
3	10	0	0.1666	0	1
4	11	0	0.1666	0	1
5	6	0.0025	0.0250	0.04375	-
6	7	0.0010	0.0100	0.01750	-
7	8	0.0110	0.1100	0.19250	-
7	8	0.0110	0.1100	0.19250	-
8	9	0.0110	0.1100	0.19250	-
8	9	0.0110	0.1100	0.19250	-
9	10	0.0010	0.0100	0.01750	-
10	11	0.0025	0.0250	0.04375	-

B.1.2   Voltage Stability Study

The topology of the two area system is shown in Figure 4.1. All data are in p.u. with a base power of 100 MVA. The data for the topology, Table B.3, dynamic machine data, Table B.4, and AVR data, Table B.5, are not modified.

B.2   System Data Nordic 32

The topology of the Nordic 32 system is shown in Figure 5.7. All data are in p.u. with a base power of 100 MVA.

Table B.8: Machine bus data of Nordic 32 system.

Bus Nr.	U_{B} (kV)	U_{g}	P_{g} (MW)
$g1$	15	1.0684	600.0
$g2$	15	1.0565	300.0
$g3$	15	1.0595	550.0

Table B.8: Machine bus data of Nordic 32 system.

Bus Nr.	U_B (kV)	UP_g (MW)	
$g4$	15	1.0339	400.0
$g5$	15	1.0294	200.0
$g6$	15	1.0084	360.0
$g7$	15	1.0141	180.0
$g8$	15	1.0498	750.0
$g9$	15	0.9988	668.5
$g10$	15	1.0157	600.0
$g11$	15	1.0211	250.0
$g12$	15	1.0200	310.0
$g13$	15	1.0170	0.0
$g14$	15	1.0454	630.0
$g15$	15	1.0455	1080.0
$g16$	15	1.0531	600.0
$g17$	15	1.0092	530.0
$g18$	15	1.0307	1060.0
$g19$	15	1.0300	300.0
$g20$	15	1.0185	*

Table B.9: Bus data of Nordic 32 system.

Bus Nr.	U_B (kV)	P_L	Q_L	P_sh	Q_sh
1	20	6.6	1.482	0	0
2	20	3.63	0.71	0	0
3	20	2.86	0.838	0	0
4	20	9.26	2.52	0	0
5	20	7.92	1.904	0	0
11	20	2.0	0.688	0	0
12	20	3.0	0.838	0	0
13	20	1.0	0.344	0	0
22	20	2.8	0.799	0	0

Table B.9: Bus data of Nordic 32 system.

Bus Nr.	U_B (kV)	P_L	Q_L	P_{sh}	Q_{sh}
31	20	1.0	0.247	0	0
32	20	2.0	0.396	0	0
41	20	5.94	1.314	0	0
42	20	4.4	1.274	0	0
43	20	9.9	2.546	0	0
46	20	7.7	2.118	0	0
47	20	1.1	0.44	0	0
51	20	8.0	2.582	0	0
61	20	5.0	1.225	0	0
62	20	3.0	0.838	0	0
63	20	5.9	2.646	0	0
71	20	3.0	0.838	0	0
72	20	20.0	3.961	0	0
1011	130	1.64	0.29	0	0
1012	130	2.0	−1.47	0	0
1013	130	4.37	−1.22	0	0
1014	130	24.7	1.23	0	0
1021	130	2.527	1.1856	0	0
1022	130	3.22	0.02	0	−0.5
1041	130	5.0	1.84	0	−2.5
1042	130	2.34	0.84	0	−2.0
1043	130	5.22	1.77	0	0
1044	130	1.04	1.25	0	−2.0
1045	130	0.09	0.88	0	−2.0
2031	220	3.2	1.53	0	0
2032	220	3.29	0.32	0	0
4011	400	0	0	0	0
4012	400	0	0	0	1.0
4021	400	0	0	0	0
4022	400	0	0	0	0

Table B.9: Bus data of Nordic 32 system.

Bus Nr.	U_B (kV)	P_L	Q_L	P_{sh}	Q_{sh}
4031	400	0	0	0	0
4030	400	0	0	0	0
4041	400	0	0	0	−2.0
4042	400	0	0	0	0
4043	400	0	0	0	−2.0
4044	400	0	0	0	0
4045	400	0	0	0	0
4046	400	0	0	0	−1.0
4047	400	0	0	0	0
4051	400	0	0	0	−1.0
4061	400	0	0	0	0
4062	400	0	0	0	0
4063	400	0	0	0	0
4071	400	0	0	0	4.0
4072	400	0	0	0	0

Table B.10: Branch data of Nordic 32 system.

From	To	R	X	B	Tap Ratio
$g1$	1012	0	0.0187	0	1.000
$g2$	1013	0	0.0250	0	1.000
$g3$	1014	0	0.0214	0	1.000
$g4$	1021	0	0.0250	0	1.000
$g5$	1022	0	0.0600	0	0.952
$g6$	1042	0	0.0375	0	0.952
$g7$	1043	0	0.0750	0	0.952
$g8$	2032	0	0.0176	0	0.952
$g9$	4011	0	0.0150	0	0.952
$g10$	4012	0	0.0187	0	0.952
$g11$	4021	0	0.0500	0	0.952

Table B.10: Branch data of Nordic 32 system.

From	To	R	X	B	Tap Ratio
g12	4031	0	0.0429	0	0.952
g13	4041	0	0.0333	0	0.952
g14	4042	0	0.0214	0	0.952
g15	4047	0	0.0125	0	0.952
g16	4051	0	0.0214	0	0.952
g17	4062	0	0.0250	0	0.952
g18	4063	0	0.0125	0	0.952
g19	4071	0	0.0300	0	0.952
g20	4072	0	0.0033	0	0.952
1	1041	0	0.0083	0	1.000
2	1042	0	0.0167	0	1.000
3	1043	0	0.0217	0	0.990
4	1044	0	0.0063	0	1.010
5	1045	0	0.0071	0	1.000
11	1011	0	0.0250	0	0.962
12	1012	0	0.0167	0	0.952
13	1013	0	0.0500	0	0.962
22	1022	0	0.0179	0	0.962
31	2031	0	0.0500	0	0.980
32	2032	0	0.0250	0	0.943
41	4041	0	0.0100	0	0.962
42	4042	0	0.0133	0	0.971
43	4043	0	0.0067	0	0.980
46	4046	0	0.0100	0	0.980
47	4047	0	0.0400	0	0.962
51	4051	0	0.0067	0	0.952
61	4061	0	0.0133	0	0.971
62	4062	0	0.0200	0	0.962
63	4063	0	0.0100	0	0.971
71	4071	0	0.0167	0	0.971

Table B.10: Branch data of Nordic 32 system.

From	To	R	X	B	Tap Ratio
72	4072	0	0.0025	0	0.952
1011	1013	0.010	0.0700	0.0138	-
1011	1013	0.010	0.0700	0.0138	-
1012	1014	0.01402	0.0900	0.01805	-
1012	1014	0.01402	0.0900	0.01805	-
1013	1014	0.006982	0.0500	0.01009	-
1013	1014	0.006982	0.0500	0.01009	-
1021	1022	0.030	0.2000	0.03026	-
1021	1022	0.030	0.2000	0.03026	-
1041	1043	0.010	0.0600	0.01221	-
1041	1043	0.010	0.0600	0.01221	-
1041	1045	0.01497	0.1200	0.02495	-
1041	1045	0.01497	0.1200	0.02495	-
1042	1044	0.03799	0.2800	0.0600	-
1042	1044	0.03799	0.2800	0.0600	-
1042	1045	0.050	0.3000	0.0600	-
1043	1044	0.010	0.0800	0.01593	-
1043	1044	0.010	0.0800	0.01593	-
2031	2032	0.012	0.0900	0.01521	-
2031	2032	0.012	0.0900	0.01521	-
4011	4012	0.001	0.0080	0.2011	-
4011	4021	0.006	0.0600	1.7990	-
4011	4022	0.004	0.0400	1.2010	-
4011	4071	0.005	0.0450	1.4020	-
4012	4022	0.004	0.0350	1.0510	-
4012	4071	0.005	0.0500	1.4980	-
4021	4032	0.004	0.0400	1.2010	-
4021	4042	0.010	0.0600	3.0010	-
4022	4031	0.004	0.0400	1.2010	-
4022	4031	0.004	0.0400	1.2010	-

Table B.10: Branch data of Nordic 32 system.

From	To	R	X	B	Tap Ratio
4031	4032	0.001	0.0100	0.3016	-
4031	4041	0.006	0.0400	2.3980	-
4032	4042	0.010	0.0400	2.0010	-
4032	4044	0.006	0.0500	2.3980	-
4041	4044	0.003	0.0300	0.8997	-
4041	4061	0.006	0.0450	1.3020	-
4042	4043	0.002	0.0150	0.4976	-
4042	4044	0.002	0.0200	0.5982	-
4043	4044	0.001	0.0100	0.3016	-
4043	4046	0.001	0.0100	0.3016	-
4043	4047	0.002	0.0200	0.5982	-
4044	4045	0.002	0.0200	0.5982	-
4044	4045	0.002	0.0200	0.5982	-
4045	4051	0.004	0.0400	1.2010	-
4045	4051	0.004	0.0400	1.2010	-
4045	4062	0.011	0.0800	2.3980	-
4046	4047	0.001	0.0150	0.4976	-
4061	4062	0.002	0.0200	0.5982	-
4062	4063	0.003	0.0300	0.8997	-
4062	4063	0.003	0.0300	0.8997	-
4071	4072	0.003	0.0300	3.0010	-
4071	4072	0.003	0.0300	3.0010	-
1011	4011	0	0.0080	0	1.0530
1012	4012	0	0.0080	0	1.0530
1022	4022	0	0.0120	0	1.0750
2031	4031	0	0.0120	0	1.0000
1044	4044	0	0.0100	0	0.9710
1044	4044	0	0.0100	0	0.9710
1045	4045	0	0.0100	0	0.9620
1045	4045	0	0.0100	0	0.9620

Table B.4: Machine dynamic data in p.u. based on $S = 900$ MVA.

Gen.	X_l	R_a	X_d	X_d'	X_d''	T_{d0}'	T_{d0}''	X_q	X_q'	X_q''	T_{q0}'	T_{q0}''	H	K_D
G_1	0.2	0.025	1.8	0.3	0.25	8	0.03	1.7	0.55	0.25	0.4	0.05	6.5	0
G_2	0.2	0.025	1.8	0.3	0.25	8	0.03	1.7	0.55	0.25	0.4	0.05	6.5	0
G_3	0.2	0.025	1.8	0.3	0.25	8	0.03	1.7	0.55	0.25	0.4	0.05	6.175	0
G_4	0.2	0.025	1.8	0.3	0.25	8	0.03	1.7	0.55	0.25	0.4	0.05	6.175	0

Table B.5: IEEE DC1A exciter system data.

Gen.	T_R	K_F	T_F	T_C	T_B	K_A	T_A	$V_{R,min}$	$V_{R,max}$	A_{ex}	B_{ex}	T_E
G_1	0.05	0.125	1.8	0	0	20	0.55	-5	5	0.0056	1.075	0.36
G_2	0.05	0.125	1.8	0	0	20	0.55	-5	5	0.0056	1.075	0.36
G_3	0.05	0.125	1.8	0	0	20	0.55	-5	5	0.0056	1.075	0.36
G_4	0.05	0.125	1.8	0	0	20	0.55	-5	5	0.0056	1.075	0.36

Table B.6: Modified machine bus data of two area system for voltage stability study.

Bus Nr.	U_B (kV)	U	P_g
1	20	1.100	9.00
2	20	1.089	9.00
3	20	1.100	9.00
4	20	1.097	9.00

Table B.7: Modified bus data of two area system for voltage stability study.

Bus Nr.	U_B (kV)	P_l	Q_l	P_{sh}	Q_{sh}
7	230	13.56	1.00	0	-2.00
9	230	21.57	1.00	0	-3.50

Table B.11: Transformer tap change data of Nordic 32 system.

From	To	R	X	B	Tap ratio	U min	U max	Tap max	Tap min	τ_1	τ_2	Step size
1	1041	0	0.0083	0	1.00	0.99	1.01	1.2	0.88	29	12	0.01
2	1042	0	0.0167	0	1.00	0.99	1.01	1.2	0.88	29	8	0.01
3	1043	0	0.0217	0	0.99	0.99	1.01	1.2	0.88	29	9	0.01
4	1044	0	0.0063	0	1.01	0.99	1.01	1.2	0.88	29	10	0.01
5	1045	0	0.0071	0	1.00	0.99	1.01	1.2	0.88	29	11	0.01
11	1011	0	0.0250	0	0.96	0.99	1.01	1.2	0.88	30	8	0.01
12	1012	0	0.0167	0	0.95	0.99	1.01	1.2	0.88	30	9	0.01
13	1013	0	0.0500	0	0.96	0.99	1.01	1.2	0.88	30	10	0.01
22	1022	0	0.0179	0	0.96	0.99	1.01	1.2	0.88	30	11	0.01
31	2031	0	0.0500	0	0.98	0.99	1.01	1.2	0.88	29	12	0.01
32	2032	0	0.0250	0	0.94	0.99	1.01	1.2	0.88	31	8	0.01
41	4041	0	0.0100	0	0.96	0.99	1.01	1.2	0.88	31	9	0.01
42	4042	0	0.0133	0	0.97	0.99	1.01	1.2	0.88	31	10	0.01
43	4043	0	0.0067	0	0.98	0.99	1.01	1.2	0.88	31	11	0.01
46	4046	0	0.0100	0	0.98	0.99	1.01	1.2	0.88	31	12	0.01
47	4047	0	0.0400	0	0.96	0.99	1.01	1.2	0.88	30	8	0.01
51	4051	0	0.0067	0	0.95	0.99	1.01	1.2	0.88	30	9	0.01

Table B.11: Transformer tap change data of Nordic 32 system

From	To	R	X	B	Tap ratio	U min	U max	Tap max	Tap min	τ_1	τ_2	Step size
61	4061	0	0.0133	0	0.97	0.99	1.01	1.2	0.88	30	10	0.01
62	4062	0	0.0200	0	0.96	0.99	1.01	1.2	0.88	30	11	0.01
63	4063	0	0.0100	0	0.97	0.99	1.01	1.2	0.88	30	12	0.01
71	4071	0	0.0167	0	0.97	0.99	1.01	1.2	0.88	31	9	0.01
72	4072	0	0.0025	0	0.95	0.99	1.01	1.2	0.88	31	11	0.01

Table B.12: HVDC data of Nordic 32 system.

From	To	S_B (MVA)	U_B (kV)	$U_{dc,B}$ (kV)	X_{trafo}	X_r	R_r	R_{dc}
4011	4044	1216	400	320	0.1130	0.165	0.001	1.9802
4031	4045	1216	400	320	0.1130	0.165	0.001	2.7723

Table B.13: HVDC initial power flow data and power flow limits of Nordic 32 system.

From	To	P_1 (MW)	Q_1 (Mvar)	P_2 (MW)	Q_2 (Mvar)	$P_{min,max}$	$Q_{min,max}$	$U_{dc,1}$	$U_{dc,2}$
4011	4044	220.08	-243.84	-187.40	-119.50	±1216	±608	1.1	0.94
4031	4045	101.30	-181.39	-91.60	-50.54	±1216	±608	1.1	1.00

Table B.14: HVDC dynamic data according the simplified VSC-HVDC model of Nordic 32 system.

From	To	M_p	t_p	ζ	ω_n	K_0	τ_Q	$U_{dc,set}$
4011	4044	0.17	15.71	0.491	18.034	0.7797	0.02	0.94
4031	4045	0.17	15.71	0.491	18.034	0.7797	0.02	1.00

Table B.15: Dynamic machine data in p.u. based on $S = 100\text{MVA}$ of synchronous generators in the Nordic 32 system.

Gen.	X_l	R_a	X_d	X'_d	X''_d	T'_{d0}	T''_{d0}	X_q	X'_q	X''_q	T'_{q0}	T''_{q0}	H	K_D
$g6$	2.2	0	0.3	0.3	0.3	7	0.05	2	0.4	0.2	1.5	0.05	6	0
$g7$	2.2	0	0.3	0.3	0.3	7	0.05	2	0.4	0.2	1.5	0.05	6	0
$g14$	2.2	0	0.3	0.3	0.3	7	0.05	2	0.4	0.2	1.5	0.05	6	0
$g15$	2.2	0	0.3	0.3	0.3	7	0.05	2	0.4	0.2	1.5	0.05	6	0
$g16$	2.2	0	0.3	0.3	0.3	7	0.05	2	0.4	0.2	1.5	0.05	6	0
$g17$	2.2	0	0.3	0.3	0.3	7	0.05	2	0.4	0.2	1.5	0.05	6	0
$g18$	2.2	0	0.3	0.3	0.3	7	0.05	2	0.4	0.2	1.5	0.05	6	0

Table B.16: Dynamic machine data in p.u. based on $S = 100$MVA of salient pole generators in the Nordic 32 system.

Gen	X_l	R_a	X_d	X'_d	X''_d	T'_{do}	T''_{do}	X_q	X''_q	T''_{qo}	H	K_D
$g1$	0.1	0	1.10	0.25	0.25	5	0.50	0.7	0.2	0.1	3	0
$g2$	0.1	0	1.10	0.25	0.25	5	0.50	0.7	0.2	0.1	3	0
$g3$	0.1	0	1.10	0.25	0.25	5	0.50	0.7	0.2	0.1	3	0
$g4$	0.1	0	1.10	0.25	0.25	5	0.50	0.7	0.2	0.1	3	0
$g5$	0.1	0	1.10	0.25	0.25	5	0.50	0.7	0.2	0.1	3	0
$g8$	0.1	0	1.10	0.25	0.25	5	0.50	0.7	0.2	0.1	3	0
$g9$	0.1	0	1.10	0.25	0.25	5	0.50	0.7	0.2	0.1	3	0
$g10$	0.1	0	1.10	0.25	0.25	5	0.50	0.7	0.2	0.1	3	0
$g11$	0.1	0	1.10	0.25	0.25	5	0.50	0.7	0.2	0.1	3	0
$g12$	0.1	0	1.10	0.25	0.25	5	0.50	0.7	0.2	0.1	3	0
$g13$	0.1	0	1.55	0.30	0.30	7	0.05	1.0	0.2	0.1	2	0
$g19$	0.1	0	1.10	0.25	0.25	5	0.50	0.7	0.2	0.1	3	0
$g20$	0.1	0	1.10	0.25	0.25	5	0.50	0.7	0.2	0.1	3	0
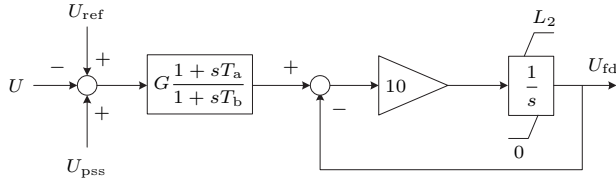
Figure B.1: Model of exciter and AVR system used in the Nordic 32 system.
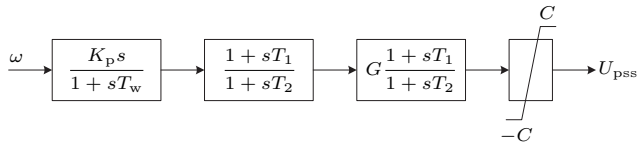
Figure B.2: Model of PSS used in the Nordic 32 system.

Table B.17: Exciter system and AVR data for all generators according the model depicted in Figure B.1.

Gen Nr.	G	T_a	T_b	L_2
$g1$, $g2$, $g3$, $g4$, $g5$, $g8$, $g9$, $g10$, $g11$, $g12$, $g19$, $g20$	70	10	20	4
$g6$, $g7$, $g14$, $g15$, $g16$, $g17$, $g18$,	120	5	12.5	5
$g13$,	50	4	20	4

Table B.18: PSS data for all generators according the model depicted in Figure B.2.

Gen Nr.	K_p	T_w	T_1	T_2	C
$g1$, $g2$, $g3$, $g5$, $g8$, $g9$, $g10$, $g11$, $g12$	75	15	0.20	0.010	0.1
$g4$	150	15	0.20	0.010	0.1
$g6$, $g7$, $g14$, $g15$, $g16$	75	15	0.22	0.012	0.1

Table B.18: PSS data for all generators according the model depicted in Figure B.2.

Gen Nr.	K_p	T_w	T_1	T_2	C
g17, g17	150	15	0.22	0.012	0.1
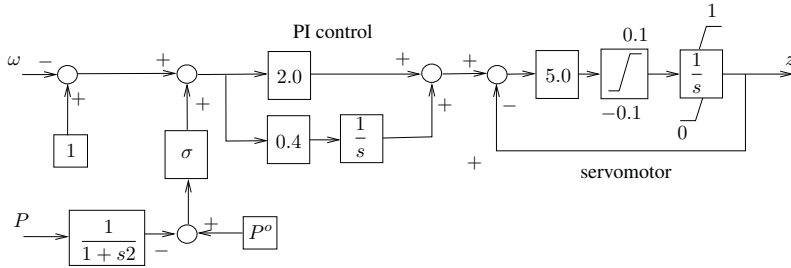
(a) Model of speed governor system [84].
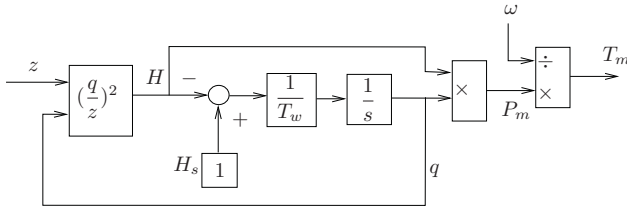
(b) Model of hydro turbine model [84].

Figure B.3: Governor and turbine model of Nordic 32 system.

Table B.19: Speed governor and hydro turbine model data according to block diagrams Figure B.3.

Gen Nr.	T_w	σ
g1, g2, g3, g4, g8, g9, g10, g11, g2	1	0.04
g19, g20	1	0.08

B.3 System Data IEEE68

The topology of the IEEE 16 machine 68 bus test system is shown in Figure 7.5. All data are in p.u. with a base power of 100 MVA

Table B.20: Machine bus data of IEEE 16 machine 68 bus system.

Bus Nr.	U_B (kV)	U	P_g
1	20	1.0450	2.500
2	20	0.9800	5.450
3	20	0.9830	6.500
4	20	0.9970	6.320
5	20	1.0110	5.052
6	20	1.0500	7.000
7	20	1.0630	5.600
8	20	1.0300	5.400
9	20	1.0250	8.000
10	20	1.0100	5.000
11	20	1.0000	10.000
12	20	1.0156	13.500
13	20	1.0110	35.910
14	20	1.0000	17.850
15	20	1.0000	10.000
16	20	1.0000	0.000

Table B.21: Bus data of IEEE 16 machine 68 bus system.

Bus Nr.	U_B (kV)	P_L	Q_L	P_{sh}	Q_{sh}
18	220	1.58	0.3	0	0
20	220	6.8	1.03	0	0
21	220	1.74	1.15	0	0
23	220	1.48	0.85	0	0
24	220	3.09	−0.92	0	0
25	220	2.24	0.47	0	0

Table B.21: Bus data of IEEE 16 machine 68 bus system.

Bus Nr.	U_B (kV)	P_L	Q_L	P_{sh}	Q_{sh}
26	220	1.39	0.17	0	0
27	220	2.81	0.76	0	0
28	220	2.06	0.28	0	0
29	220	2.84	0.27	0	0
33	220	1.12	0	0	0
36	220	1.02	-0.1946	0	0
37	220	60.0	3.0	0	0
39	110	2.67	0.126	0	0
40	220	0.6563	0.2353	0	0
41	110	10.0	2.5	0	0
42	110	11.5	2.5	0	0
44	220	2.6755	0.0484	0	0
45	110	2.08	0.21	0	0
46	220	1.507	0.285	0	0
47	220	2.0312	0.3259	0	0
48	220	2.412	0.022	0	0
49	220	1.64	0.29	0	0
50	110	2.0	-1.47	0	0
51	220	4.37	-1.22	0	0
52	220	24.7	1.23	0	0
53	220	2.527	1.1856	0	0
55	220	3.22	0.02	0	0
56	220	5.0	1.84	0	0
59	220	2.34	0.84	0	0
60	220	5.22	1.77	0	0
61	220	1.04	1.25	0	0
64	60	0.09	0.88	0	0
67	220	3.2	1.53	0	0
68	220	3.29	0.32	0	0

Table B.22: Branch data of IEEE 16 machine 68 bus system.

From	To	R	X	B	Tap Ratio
1	54	0	0.0181	0	0.976
2	58	0	0.0250	0	0.935
3	52	0	0.0200	0	0.935
4	19	0.0007	0.0142	0	0.935
5	20	0.0009	0.0180	0	0.991
6	22	0	0.0143	0	0.976
7	23	0.0005	0.0272	0	1.000
8	25	0.0006	0.0232	0	0.976
9	29	0.0008	0.0156	0	0.976
10	31	0	0.0260	0	0.962
11	32	0	0.0130	0	0.962
12	36	0	0.0075	0	0.962
13	37	0	0.0033	0	0.962
14	41	0	0.0015	0	1.000
15	41	0	0.0015	0	1.000
16	52	0	0.0030	0	1.000
17	18	0.0007	0.0082	0.1319	-
17	27	0.0013	0.0173	0.3216	-
19	20	0.0007	0.0138	0	1.060
21	22	0.0008	0.0140	0.2565	-
22	23	0.0006	0.0096	0.1846	-
23	24	0.0022	0.0350	0.361	-
25	26	0.0032	0.0323	0.531	-
26	27	0.0014	0.0147	0.2396	-
26	28	0.0043	0.0474	0.7802	-
26	29	0.0057	0.0625	1.029	-
28	29	0.0014	0.0151	0.249	-
30	31	0.0013	0.0187	0.333	-
30	32	0.0024	0.0288	0.488	-
31	38	0.0011	0.0147	0.247	-

Table B.22: Branch data of IEEE 16 machine 68 bus system.

From	To	R	X	B	Tap Ratio
32	33	0.0008	0.0099	0.168	-
33	34	0.0011	0.0157	0.202	-
33	38	0.0036	0.0444	0.693	-
34	36	0.0033	0.0111	1.45	-
35	34	0.0001	0.0074	0	0.946
35	45	0.0007	0.0175	1.39	-
36	37	0.0005	0.0045	0.32	-
37	43	0.0005	0.0276	0	-
38	46	0.0022	0.0284	0.43	-
39	44	0	0.0411	0	1.000
39	45	0	0.0839	0	-
41	40	0.006	0.0840	3.15	-
42	41	0.004	0.0600	2.25	-
43	44	0.0001	0.0011	0	-
44	45	0.0025	0.0730	0	-
45	51	0.0004	0.0105	0.72	-
46	49	0.0018	0.0274	0.27	-
47	48	0.0025	0.0268	0.4	-
47	48	0.0025	0.0268	0.4	-
48	40	0.002	0.0220	1.28	-
49	52	0.0076	0.1141	1.16	-
50	51	0.0009	0.0221	1.62	-
50	52	0.0012	0.0288	2.06	-
52	42	0.004	0.0600	2.25	-
53	27	0.032	0.3200	0.41	-
53	30	0.0008	0.0074	0.48	-
53	31	0.0016	0.0163	0.25	-
53	47	0.0013	0.0188	1.31	-
53	54	0.007	0.0822	0.3493	-
54	25	0.007	0.0086	0.146	-

Table B.22: Branch data of IEEE 16 machine 68 bus system.

From	To	R	X	B	Tap Ratio
54	55	0.0013	0.0151	0.2572	-
55	18	0.0011	0.0133	0.2138	-
55	56	0.0013	0.0213	0.2214	-
56	57	0.0008	0.0128	0.1342	-
56	66	0.0008	0.0129	0.1382	-
57	58	0.0002	0.0026	0.0434	-
57	60	0.0008	0.0112	0.1476	-
58	59	0.0006	0.0092	0.113	-
58	63	0.0007	0.0082	0.1389	-
59	60	0.0004	0.0046	0.078	-
60	61	0.0023	0.0363	0.3804	-
61	30	0.0019	0.0183	0.29	-
61	30	0.0019	0.0183	0.29	-
61	36	0.0022	0.0196	0.34	-
61	36	0.0022	0.0196	0.34	-
62	63	0.0004	0.0043	0.0729	-
62	65	0.0004	0.0043	0.0729	-
64	63	0.0016	0.0435	0	1.060
64	65	0.0016	0.0435	0	1.060
65	66	0.0009	0.0101	0.1723	-
66	67	0.0018	0.0217	0.366	-
67	68	0.0009	0.0094	0.171	-
68	17	0.0007	0.0089	0.1342	-
68	19	0.0016	0.0195	0.304	-
68	21	0.0008	0.0135	0.2548	-
68	24	0.0003	0.0059	0.068	-

Table **B.23:** HVDC data of IEEE 16 machine 68 bus system.

From	To	S_B (MVA)	U_B (kV)	$U_{dc,B}$ (kV)	X_{trafo}	X_r	R_r	R_{dc}
52	68	570	230	195	0.1648	0.164	0.113	1.977000e-05

Table **B.24:** HVDC initial power flow data and power flow limits of IEEE 16 machine 68 bus system.

From	To	P_1 (MW)	Q_1 (Mvar)	P_2 (MW)	Q_2 (Mvar)	$P_{min,max}$	$Q_{min,max}$	$U_{dc,1}$	$U_{dc,2}$
52	68	171.29	2.05	-171.29	11.77	$\pm$570	$\pm$285	1.1	1.1

Table **B.25:** HVDC dynamic data according the simplified VSC-HVDC model of IEEE 16 machine 68 bus system.

From	To	M_P	t_P	ζ	ω_n	K_0	τ_Q	$U_{dc,set}$
52	68	0.1	0.1	0.591	38.95	0.7797	0	1.1

Table B.26: Machine dynamic data in p.u. based on $S = 100\text{MVA}$ of IEEE 16 machine 68 bus system.

Gen	X_l	R_a	X_d	X'_d	T'_{d0}	X_q	X'_q	T'_{q0}	H	K_D
G_1	0.0125	0.0000	0.1	0.0310	10.2000	0.07	0.0280	1.5000	42.0	0
G_2	0.035	0.0000	0.295	0.0697	6.5600	0.28	0.0600	1.5000	30.2	0
G_3	0.0304	0.0000	0.2495	0.0531	5.7000	0.24	0.0500	1.5000	35.8	0
G_4	0.0295	0.0000	0.262	0.0436	5.6900	0.26	0.0400	1.5000	28.6	0
G_5	0.027	0.0000	0.33	0.0660	5.4000	0.31	0.0600	0.4400	26.0	0
G_6	0.0224	0.0000	0.254	0.0500	7.3000	0.24	0.0450	0.4000	34.8	0
G_7	0.0322	0.0000	0.295	0.0490	5.6600	0.29	0.0450	1.5000	26.4	0
G_8	0.028	0.0000	0.29	0.0570	6.7000	0.28	0.0500	0.4100	24.3	0
G_9	0.0298	0.0000	0.2106	0.0570	4.7900	0.20	0.0500	1.9600	34.5	0
G_{10}	0.0199	0.0000	0.169	0.0457	9.3700	0.12	0.0450	1.5000	31.0	0
G_{11}	0.0103	0.0000	0.128	0.0180	4.1000	0.12	0.0150	1.5000	28.2	0
G_{12}	0.022	0.0000	0.101	0.0310	7.4000	0.10	0.0280	1.5000	92.3	0
G_{13}	0.003	0.0000	0.0296	0.0055	5.9000	0.03	0.0050	1.5000	248.0	0
G_{14}	0.0017	0.0000	0.018	0.0029	4.1000	0.02	0.0025	1.5000	300.0	0
G_{15}	0.0017	0.0000	0.018	0.0029	4.1000	0.02	0.0025	1.5000	300.0	0
G_{16}	0.0041	0.0000	0.0356	0.0071	7.8000	0.03	0.0060	1.5000	225.0	0

Table B.27: IEEE DC1A exciter system data for all generators.

T_R	K_F	T_F	T_C	T_B	K_A	T_A	$U_{r,min}$	$U_{r,max}$	T_E	K_E
0.01	0.03	1	0.1	0.1	200	0.05	-20	20	0.785	0

Table B.28: Single reheat steam turbine model with governing droop control system for all generators.

R	T_G	T_{CH}	T_{RH}	T_{CO}	F_{HP}	F_{IP}	F_{LP}
0.02	0.2	0.3	10	0.3	0.3	0.4	0.3

Appendix C

Controller Data

C.1 Power Oscillation Damping Controller Data

Local Controller Data

Table C.1: Parameters of the local damping controller used for different power system studies.

System	K_P	K_D	T_D (s)
Two Area System	150	20	0.05
European System	75	20	0.05
European System with RES	150	20	0.05
Nordic 32 System	150	20	0.05

Model Predictive Controller Data

Table C.2: Parameters of MPC-based damping controller used for different power system studies.

System	T_{mpc} (ms)	N	u_{p} min,max	u_{q} min,max	d_{p} min,max	d_{q} min,max
Two Area System	100	10	± 0.9	± 0.5	± 0.1	± 0.1
European System	500	10	± 0.9	± 0.5	± 0.1	± 0.1
European System with RES	500	10	± 0.9	± 0.5	± 0.2	± 0.2

C.2 Voltage Stability Local Controller Data

Local Controller Data

Table C.3: Parameters of the local voltage controller used for different power system studies.

System	K_{P}	K_{I}
Two Area System	150	20
Nordic 32 System	150	20

Model Predictive Controller Data

Table C.4: Parameters of the MPC-based damping and voltage controller used for different power system studies.

System	T_{mpc} (ms)	N	u_{p} min,max	u_{q} min,max	d_{p} min,max	d_{q} min,max	α	β	γ
Two Area System	100	50	± 1	± 0.5	± 0.1	± 0.2	625	21.042	1000
Nordic 32 System	100	9	± 1	± 0.5	± 0.5	± 0.2	3e-3	12e-3	750

Appendix D

Internal Node Representation

Figure D.1 shows a transmission system with n_{sys} nodes numbered $n_{\mathrm{gen}}+1, \ldots, 2n_{\mathrm{gen}}, 2n_{\mathrm{gen}}+1, \ldots, n_{\mathrm{gen}}+n_{\mathrm{sys}}$, of which the last $n_{\mathrm{gen}}-n_{\mathrm{sys}}$
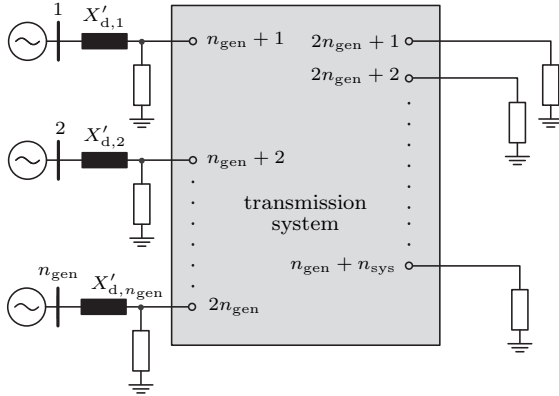

Figure D.1: Multi-machine power system including internal generator nodes and impedance loads [109].

are purely load nodes and the first n_{gen} are generator nodes where there may also be loads. The internal generator nodes are connected to the generator system nodes with the transient reactance X'_{d}. All loads of the system are changed to impedance loads with

$$\underline{Y}_{\text{load}} = \frac{\underline{S}^*_{\text{load}}}{U^2_{\text{load}}} \tag{D.1}$$

where $\underline{S}_{\text{load}}$ is the complex apparent power of the load, and U_{load} the voltage amplitude at the load bus.

The original admittance matrix $\mathbf{Y}_{\text{BUS}} \in \mathbb{C}_{n_{\text{sys}} \times n_{\text{sys}}}$ can be written as

$$\mathbf{Y}_{\text{BUS}} = \left[\begin{array}{cc} \mathbf{Y}_1 & \mathbf{Y}_2 \\ \mathbf{Y}_3 & \mathbf{Y}_4 \end{array} \right] \tag{D.2}$$

where $\mathbf{Y}_1 \in \mathbb{C}_{n_{\text{gen}} \times n_{\text{gen}}}$, $\mathbf{Y}_2 \in \mathbb{C}_{n_{\text{gen}} \times (n_{\text{sys}} - n_{\text{gen}})}$, $\mathbf{Y}_3 \in \mathbb{C}_{(n_{\text{sys}} - n_{\text{gen}}) \times n_{\text{gen}}}$ and $\mathbf{Y}_4 \in \mathbb{C}_{(n_{\text{sys}} - n_{\text{gen}}) \times (n_{\text{sys}} - n_{\text{gen}})}$ [109].

Now $\mathbf{Y}_{\text{BUS}}$ matrix is augmented by the admittances corresponding to the generator transient reactances with

$$\underline{y}_i = \frac{1}{jX'_{\text{d},i}}, \qquad i = 1, 2, \ldots, n_{\text{gen}} \quad . \tag{D.3}$$

to create the internal nodes $1, 2, \ldots, n_{\text{gen}}$. We also add the admittances $y_{\text{load},i}$ corresponding to the loads at the busses $(n_{\text{gen}} + 1), \ldots, (n_{\text{gen}} + n_{\text{sys}})$. This will result in the overall network admittance matrix as

$$\hat{\mathbf{Y}}_{\text{BUS}} = \left[\begin{array}{ccc} \mathbf{Y}_{\text{G}} & -\mathbf{Y}_{\text{G}} & \mathbf{0} \\ -\mathbf{Y}_{\text{G}} & \mathbf{Y}_{\text{G}} + \mathbf{Y}_1 + \mathbf{Y}_{\text{l,g}} & \mathbf{Y}_2 \\ \mathbf{0} & \mathbf{Y}_3 & \mathbf{Y}_4 + \mathbf{Y}_{\text{l,l}} \end{array} \right] \tag{D.4}$$

where

$$\mathbf{Y}_{\text{l,g}} = \text{diag}\left(\frac{\underline{S}^*_{\text{load},i}}{U^2_{\text{load},i}} \right), \quad i = n_{\text{gen}} + 1, \ldots, n_{\text{gen}}$$

$$\mathbf{Y}_{\text{l,l}} = \text{diag}\left(\frac{\underline{S}^*_{\text{load},i}}{U^2_{\text{load},i}} \right), \quad i = 2n_{\text{gen}} + 1, \ldots, n_{\text{gen}} + n_{\text{sys}}$$

$$\mathbf{Y}_{\text{G}} = \text{diag}\left(\frac{1}{jX'_{\text{d},i}} \right), \quad i = 1, 2, \ldots, n_{\text{gen}}$$

In the $\hat{\mathbf{Y}}_{\text{BUS}}$ matrix only the first n_{gen} internal busses are retained and the rest n_{sys} eliminated in order to get the internal node model [109]. For this purpose, we symbolically partition $\hat{\mathbf{Y}}_{\text{BUS}}$ into

$$\hat{\mathbf{Y}}_{\text{BUS}} = \left[\begin{array}{cc} \mathbf{Y}_{\text{A}} & \mathbf{Y}_{\text{B}} \\ \mathbf{Y}_{\text{C}} & \mathbf{Y}_{\text{D}} \end{array} \right] \tag{D.5}$$

where

$$\mathbf{Y}_{\text{A}} = \mathbf{Y}_{\text{G}}$$

$$\mathbf{Y}_{\text{B}} = \left[\begin{array}{cc} -\mathbf{Y}_{\text{G}} & \mathbf{0} \end{array} \right]$$

$$\mathbf{Y}_{\text{C}} = \left[\begin{array}{c} -\mathbf{Y}_{\text{G}} \\ \mathbf{0} \end{array} \right]$$

$$\mathbf{Y}_{\text{D}} = \left[\begin{array}{cc} \mathbf{Y}_{\text{G}} + \mathbf{Y}_1 + \mathbf{Y}_{\text{l,g}} & \mathbf{Y}_2 \\ \mathbf{Y}_3 & \mathbf{Y}_4 + \mathbf{Y}_{\text{l,l}} \end{array} \right] \tag{D.6}$$

The network equations for this augmented network are

$$\left[\begin{array}{c} \mathbf{I}_{\text{A}} \\ \mathbf{0} \end{array} \right] = \left[\begin{array}{cc} \mathbf{Y}_{\text{A}} & \mathbf{Y}_{\text{B}} \\ \mathbf{Y}_{\text{C}} & \mathbf{Y}_{\text{D}} \end{array} \right] \cdot \left[\begin{array}{c} \mathbf{E}_{\text{A}} \\ \mathbf{U}_{\text{D}} \end{array} \right] \tag{D.7}$$

where $\mathbf{E}_{\text{A}}$ is the vector of the voltages behind the transient reactance and $\mathbf{U}_{\text{D}}$ is the vector of physical bus voltages [109]. Retaining the first n_{gen} nodes gives

$$\mathbf{I}_{\text{A}} = \mathbf{Y}_{\text{int}} \cdot \mathbf{E}_{\text{A}} \tag{D.8}$$

where we define the internal admittance matrix with

$$\mathbf{Y}_{\text{int}} = \left(\mathbf{Y}_{\text{A}} - \mathbf{Y}_{\text{B}} \mathbf{Y}_{\text{D}}^{-1} \mathbf{Y}_{\text{C}} \right) \tag{D.9}$$

Appendix E

Controlled Islanding RTS96 Systems

The controlled islanding algorithm is applied to the 3 area RTS96 test system. Two VSC-HVDC links with a capacity of 570 MW are installed between busses 75 and 41 and between busses 89 and 65. Following parameters for the controlled islanding algorithm are used: $\alpha = 5$, $\beta = 0.8$, $\gamma = 100$, $\eta = 0.1$, $\vartheta = 0.6$ and $\kappa = 0.9$. Table E.1 shows the results of the controlled islanding algorithm. Case A does not include the HVDC modification introduced in Chapter 7. Case B includes all the modification of the controlled islanding algorithm introduced in Chapter 7. Figure E.1 depicts the three islands for case A and Figure E.2 for case B.

Table E.1: Comparison of controlled islanding schemes in the RTS96 system.

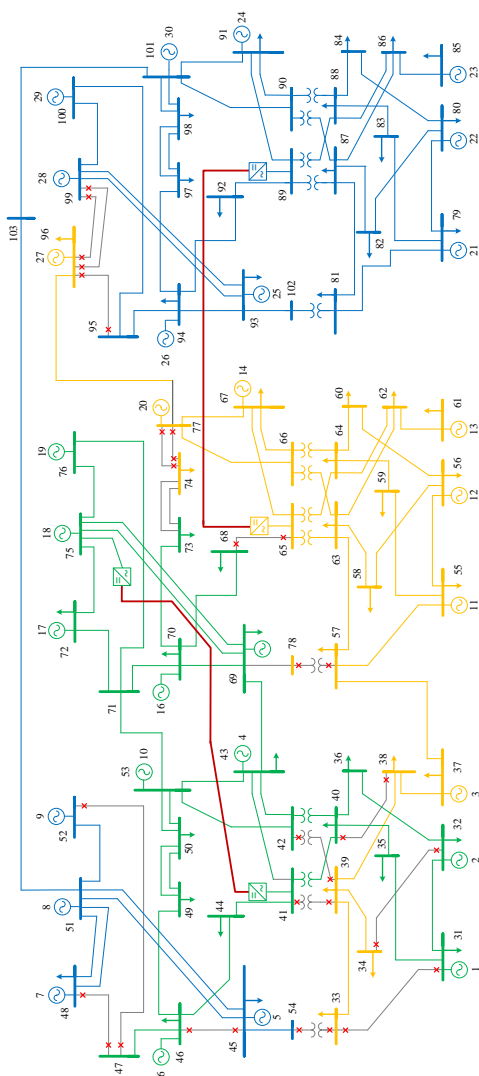|	Case A: Without Using HVDC Criteria		
Controlled Line Switch-Off	31-33, 32-34, 33-54, 38-40, 39-41, 39-42, 45-46, 47-48, 47-52- 57-78, 65-68, 74-77-a, 74-77-b, 95-96, 96-99-a, 96-99-b		
	Island 1	**Island 2**	**Island 3**
Total Gen. (MW)	3822	2379	2478
Total Load (MW)	3167	2728	2655
Total HVDC Injection (MW)	104	-	−104
ΔP (MW)	−551	349	73
	Case B: Using HVDC Criteria		
Controlled Line Switch-Off	41-43, 42-43, 42-53, 45-51-a, 45-51-b, 46-47, 49-50-a, 49-50-b, 65-68, 69-78, 73-74-a, 73-74-b, 95-96, 96-99-a, 96-99-b		
	Island 1	**Island 2**	**Island 3**
Total Gen. (MW)	3192	1880	3607
Total Load (MW)	4182	1518	2850
Total HVDC Injection (MW)	284	180	104
ΔP (MW)	706	−182	−653

Figure E.1: Case A: Results of the controlled islanding algorithm without using the HVDC modification for the RTS96 test system including two VSC-HVDC link connecting bus 41 with bus 75 and bus 68 with bus 89.
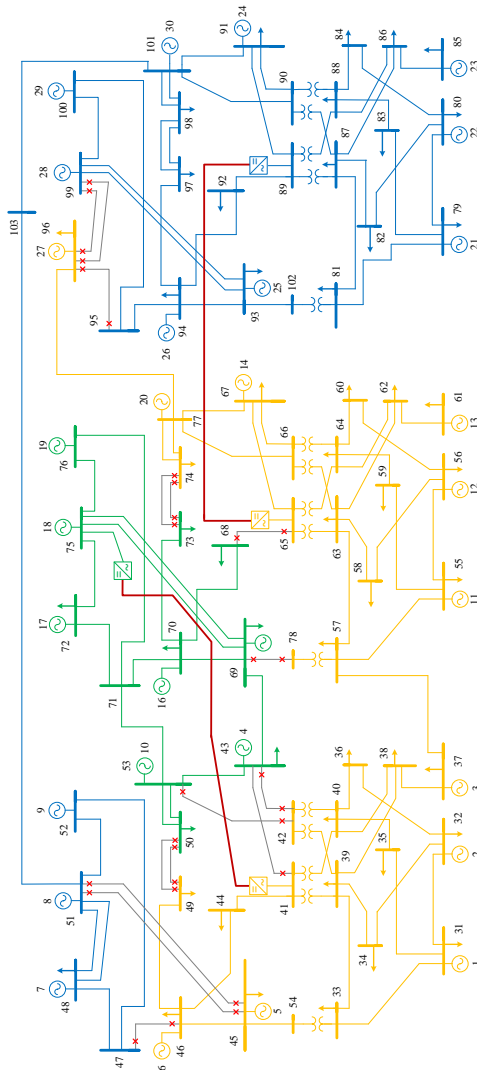
Figure E.2: Case B: Results of the controlled islanding algorithm with the modification for the VSC-HVDC links for the RTS96 test system including two VSC-HVDC link connecting bus 41 with bus 75 and bus 68 with bus 89.

Bibliography

[1] P. Kundur, *Power System Stability and Control*. New York, USA: McGraw-Hill, 1994.

[2] P. Fairley, "DC Versus AC: The Second War of Currents Has Already Begun [In My View]," *IEEE Power and Energy Magazine*, vol. 10, no. 6, pp. 104–103, Nov. 2012.

[3] G. Asplund, C. Lennart, and O. Tollerz, "50 years - Part 1 ABB - from pioneer to world leader," *ABB Review*, pp. 6–8, 2003.

[4] ——, "50 years HVDC - Part II The semiconductor 'takeover'," *ABB Review*, pp. 10–13, 2003.

[5] A. Yazdani and R. Iravani, *Voltage-Sourced Converters in Power Systems - Modeling, Control, and Applications*. Hoboken, NJ, USA: John Wiley & Sons, Inc., 2010.

[6] C.-K. Kim, V. K. Sood, G.-S. Jang, S.-J. Lim, and S.-J. Lee, *HVDC Transmission - Power Conversion Applications in Power Systems*. Singapore: John Wiley & Sons (Asia) Pte Ltd, 2009.

[7] H. Bewa, "ABB develops complete system solution for 1,100 kV HVDC power transmission," 2014. [Online]. Available: http://www.abb.ch/cawp/seitp202/3a8302e9925218a4c1257d3f00451b52.aspx

[8] J.-S. Lai and F. Z. Peng, "Multilevel converters-a new breed of power converters," *IAS '95. Conference Record of the 1995 IEEE Industry Applications Conference Thirtieth IAS Annual Meeting*, vol. 3, pp. 2348–2356, 1995.

[9] A. Lesnicar and R. Marquardt, "An innovative modular multilevel converter topology suitable for a wide power range," in *2003 IEEE Bologna PowerTech - Conference Proceedings*, vol. 3. IEEE, 2003, pp. 272–277.

[10] T. Schmidt and A. Ligi, "ABB launches world's most powerful underground and subsea power transmission cable system," 2014. [Online]. Available: http://www.abb.ch/cawp/seitp202/ 0cea859b5b6e1776c1257d3b002af564.aspx

[11] V. K. Sood, *HVDC and FACTS Controllers: Applications of Static Converters in Power Systems.* Dordrecht, The Netherlands: Kluwer Academic Publischer, 2004.

[12] J. Arrillaga, *High Voltage Direct Current Transmission.* London, UK: IET, 1998.

[13] R. L. Sellick and M. Akerberg, "Comparison of HVDC Light (VSC) and HVDC Classic (LCC) Site Aspects , for a 500MW 400kV HVDC Transmission Scheme," in *10th IET International Conference on AC and DC Power Transmission, ACDC 2012*, Birmingham, UK, 2012, pp. 1–6.

[14] S. G. Johannson, G. Asplund, E. Jansson, and R. Rudervall, "Power System Stability Benefits with VSC DC-Transmission Systems," in *Cigré Devision B4-204*, 2004.

[15] E. Acha, C. R. Fuerte-Esquivel, H. Ambriz-Pérez, and C. Angeles-Camacho, *FACTS.* Chichester, UK: John Wiley & Sons, Ltd, Feb. 2004.

[16] F. J. Ellert and N. G. Hingorani, "Power: HVDC for the long run: High-voltage de transmission may be a viable alternative to ac transmission for long-distance routes," *IEEE Spectrum*, vol. 13, pp. 37–44, 1976.

[17] N. Flourentzou, V. Agelidis, and G. Demetriades, "VSC-Based HVDC Power Transmission Systems: An Overview," *IEEE Transactions on Power Electronics*, vol. 24, no. 3, pp. 592–602, Mar. 2009.

[18] N. B. Negra, J. Todorovic, and T. Ackermann, "Loss evaluation of HVAC and HVDC transmission solutions for large offshore wind

farms," *Electric Power Systems Research*, vol. 76, no. 11, pp. 916–927, Jul. 2006.

[19] M. Hyttinen, J.-O. Lamell, and T. F. Nestli, "New application of voltage source converter (VSC) HVDC to be installed on the gas platform Troll A," in *Cigré Devision B4-210*, Paris, France, 2004.

[20] O. Heyman, L. Weimars, and M.-L. Bohl, "HVDC - A key solution in future transmission systems," in *World Energy Congress, WEC*, Montréal, 2010.

[21] C. M. Franck, "HVDC Circuit Breakers: A Review Identifying Future Research Needs," *IEEE Transactions on Power Delivery*, vol. 26, no. 2, pp. 998–1007, Apr. 2011.

[22] T. K. Vrana, R. E. Torres-Olguin, B. Liu, and T. M. Haileselassie, "The North Sea super grid - a technical perspective," in *9th IET International Conference on AC and DC Power Transmission ACDC 2010*, London, UK, 2010.

[23] S. Chatzivasileiadis, D. Ernst, and G. Andersson, "The Global Grid," *Renewable Energy*, vol. 57, pp. 372–383, 2013.

[24] J. Machowski, J. Bialek, and J. Bumby, *Power System Dynamics - Stability and Control: Stability and Control*, 2nd ed. West Sussex, UK: John Wiley & Sons, Ltd, 2008.

[25] T. Bührke, *Erneuerbare Energie : Konzepte für die Energiewende*, 3rd ed. Weinheim: Wiley-VCH, 2012.

[26] UCTE, "The 50 Year Success Story - Evolution of a European Interconnected Grid," Secretariat of UCTE, Brussels, Tech. Rep., 2009. [Online]. Available: https://www.entsoe.eu/news-events/former-associations/ucte/Pages/default.aspx

[27] N. Mohan, T. M. Undeland, and W. P. Robbins, *Power Electronics: Converters, Applications, and Design*, 3rd ed. John Wiley & Sons, Inc., 2003.

[28] "DIgSILENT Technical Documentation - PWM Converter," DIgSILENT GmbH, Tech. Rep., 2014.

[29] K. Friedrich, "Modern HVDC PLUS application of VSC in Modular Multilevel Converter topology," in *IEEE International Symposium on Industrial Electronics*, 2010, pp. 3807–3810.

[30] R. Marquardt and A. Lesnicar, "New Concept for High Voltage - Modular Multilevel Converter," in *PESC 2004*, Aachen, Germany, 2004.

[31] J. Dorn, H. Huang, and D. Retzmann, "Novel Voltage-Sourced Converters for HVDC and FACTS Applications," in *Cigré Symposium Osaka*, Osaka, 2007.

[32] C. C. Davidson and D. R. Trainer, "Innovative Concepts for Hybrid Multi-Level Converters for HVDC Power Transmission," in *9th IET International Conference on AC and DC Power Transmission (ACDC 2010)*, 2010, pp. 1–5.

[33] "It's time to connect - technical description of HVDC light technology," Grid Systems - HVDC, ABB, Tech. Rep., 2008. [Online]. Available: www.abb.com/hvdc

[34] A. Fuchs, "Coordinated Control of Power Systems with HVDC Links," PhD Thesis, ETH Zürich, 2015.

[35] M. Imhof and G. Andersson, "Dynamic modeling of a VSC-HVDC converter," in *2013 48th International Universities' Power Engineering Conference (UPEC)*, no. Vsc 2.   IEEE, Sep. 2013, pp. 1–6.

[36] M. Imhof, E. Iggland, and G. Andersson, "A Simplified Second-Order Model of a VSC-HVDC Link for Dynamic Studies," in *Cigré International Symposium - Across Borders - HVDC Systems and Market Integration*, Lund, Sweden, 2015.

[37] P. Krein, J. Bentsman, R. Bass, and B. Lesieutre, "On the use of averaging for the analysis of power electronic systems," *IEEE Transactions on Power Electronics*, vol. 5, pp. 182–190, 1990.

[38] A. Pizano-Martinez, C. R. Fuerte-Esquivel, H. Ambriz-PÉrez, and E. Acha, "Modeling of VSC-Based HVDC Systems for a Newton-Raphson OPF Algorithm," *IEEE Transactions on Power Systems*, vol. 22, no. 4, pp. 1794–1803, Nov. 2007.

[39] H. Ambriz-Pérez, E. Acha, and C. Fuerte-Esquivel, "High voltage direct current modelling in optimal power flows," *International Journal of Electrical Power & Energy Systems*, vol. 30, no. 3, pp. 157–168, Mar. 2008.

[40] D. Jovcic, L. Lamont, and L. Xu, "VSC transmission model for analytical studies," in *2003 IEEE Power Engineering Society General Meeting*.   IEEE, 2003, pp. 1737–1742.

[41] Y. Wang, S.-Z. Zhao, C. Huangfu, and J.-J. Ruan, "Dynamic Model and Control of Voltage Source Converter Based HVDC," *2009 Asia-Pacific Power and Energy Engineering Conference*, pp. 1–5, Mar. 2009.

[42] S. Cole, "Steady-State and Dynamic Modelling of VSC HVDC Systems for Power System Simulation," Ph.D. dissertation, Katholike Univeriteit Leuven, 2010.

[43] T. Demiray, "Simulation of Power System Dynamics using Dynamic Phasor Models," PhD Thesis, ETH Zurich, 2008.

[44] R. H. Park, "Two-Reaction Theory of Synchronous Machines Generalized Method of Analysis-Part I," *Transactions of the American Institute of Electrical Engineers*, vol. 48, no. 3, pp. 716–727, 1929.

[45] H. Dommel and W. Tinney, "Optimal Power Flow Solutions," *IEEE Transactions on Power Apparatus and Systems*, vol. PAS-87, no. 10, 1968.

[46] S. Cole, J. Beerten, and R. Belmans, "Generalized Dynamic VSC MTDC Model for Power System Stability Studies," *IEEE Transactions on Power Systems*, vol. 25, no. 3, pp. 1655–1662, Aug. 2010.

[47] M. Kazmierkowski and L. Malesani, "Current control techniques for three-phase voltage-source PWM converters: a survey," *IEEE Transactions on Industrial Electronics*, vol. 45, no. 5, pp. 691–703, 1998.

[48] G. F. Franklin, D. J. Powell, and A. Emami-Naeini, *Feedback control of dynamic systems*, 5th ed.   Upper Saddle River: Prentice Hall PTR, 2006.

[49] A. Fuchs, M. Imhof, T. Demiray, and M. Morari, "Stabilization of Large Power Systems Using VSC-HVDC and Model Predictive Control," *IEEE Transactions on Power Delivery*, vol. 29, no. 1, pp. 480–488, Feb. 2014.

[50] M. Klein, G. J. Rogers, and P. Kundur, "A fundamental study of inter-area oscillations in power systems," *IEEE Transactions on Power Systems*, vol. 6, no. 3, pp. 914–921, 1991.

[51] R. Sadikovic, "Use of FACTS Devices for Power Flow Control and Damping of Oscillations in Power Systems," PhD Thesis, ETH Zurich, 2006.

[52] M. E. Aboul-Ela, A. A. Sallam, J. D. McCalley, and A. A. Fouad, "Damping controller design for power system oscillations using global signals," *IEEE Transactions on Power Systems*, vol. 11, no. 2, pp. 767–773, 1996.

[53] J. Pan, R. Nuqui, K. Srivastava, T. Jonsson, P. Holmberg, and Y.-J. Hafner, "AC Grid with Embedded VSC-HVDC for Secure and Efficient Power Delivery," *2008 IEEE Energy 2030 Conference*, pp. 1–6, Nov. 2008.

[54] X.-P. Zhang, C. Rehtanz, and B. Pal, *Flexible AC Transmission Systems: Modelling and Control.* Heidelberg, Germany: Springer-Verlag, 2012.

[55] M. Larsson and C. Rehtanz, "Predictive frequency stability control based on wide-area phasor measurements," *IEEE Power Engineering Society Summer Meeting,*, vol. 1, pp. 233–238, 2002.

[56] G. Hug-Glanzmann, "Coordinated Power Flow Control to Enhance Steady-State Security in Power Systems," Phd Thesis, ETH Zurich, 2008.

[57] H. Latorre, M. Ghandhari, and L. Söder, "Active and reactive power control of a VSC-HVdc," *Electric Power Systems Research*, vol. 78, no. 10, pp. 1756–1763, Oct. 2008.

[58] R. Preece, A. M. Almutairi, O. Marjanovic, and J. V. Milanović, "Damping of electromechanical oscillations by VSC-HVDC active power modulation with supplementary wams based modal LQG controller," in *IEEE Power and Energy Society General Meeting*, San Diego, USA, 2011.

[59] Y. Li, C. Rehtanz, S. Rüberg, L. Luo, and Y. Cao, "Wide-area robust coordination approach of HVDC and FACTS controllers for damping multiple interarea oscillations," *IEEE Transactions on Power Delivery*, vol. 27, pp. 1096–1105, 2012.

[60] A. Fuchs, S. Mariethoz, M. Larsson, and M. Morari, "Grid stabilization through VSC-HVDC using wide area measurements," in *2011 IEEE Trondheim PowerTech*. IEEE, Jun. 2011, pp. 1–6.

[61] P. Mc Namara, R. R. Negenborn, B. De Schutter, and G. Lightbody, "Optimal coordination of a multiple HVDC link system using centralized and distributed control," *IEEE Transactions on Control Systems Technology*, vol. 21, no. 2, pp. 302–314, 2013.

[62] T. Smed and G. Andersson, "Utilizing HVDC to damp power oscillations," *IEEE Transactions on Power Delivery*, vol. 8, no. 2, pp. 620–627, Apr. 1993.

[63] R. Eriksson, "Security-centered Coordinated Control in AC/DC Transmission Systems," PhD Thesis, KTH Stockholm, 2008.

[64] J. Maciejowski, *Predictive Control: With Contstraints*. Harlow, UK: Pearson Education, 2002.

[65] J. De La Ree, V. Centeno, J. S. Thorp, and A. G. Phadke, "Synchronized Phasor Measurement Applications in Power Systems," *IEEE Transactions on Smart Grid*, vol. 1, no. 1, pp. 20–27, Jun. 2010.

[66] M. Balabin, K. Görner, Y. Li, I. E. Naumkin, and C. Rehtanz, "Evaluation of PMU performance during transients," in *2010 International Conference on Power System Technology: Technological Innovations Making Power Grid Smarter, POWERCON2010*, Hangzhou, China, 2010.

[67] C. Van Loan, "Computing integrals involving the matrix exponential," *IEEE Transactions on Automatic Control*, vol. 23, no. 3, pp. 395–404, Jun. 1978.

[68] G. Andersson, "Dynamics and Control of Electric Power Systems," ETH Zurich, 2014.

[69] T. Haase, "Anforderungen an eine durch Erneuerbare Energien geprägte Energieversorgung - Untersuchung des Regelverhaltens von Kraftwerken und Verbundnetzen Dissertation," PhD Thesis, Universität Rostock, 2006.

[70] J. V. Milanovic and I. A. Hiskens, "Effects of dynamic load model parameters on damping of oscillations in power systems," *Electric Power Systems Research*, vol. 33, no. 1, pp. 53–61, 1995.

[71] "inelfe - France-Spain Electrical Interconnection Project," 2014. [Online]. Available: www.inelfe.eu

[72] A. Giorgi, R. Rendina, G. Georgantzis, C. Marchiori, G. Pazienza, S. Corsi, C. Pincella, M. Pozzi, K. G. Danielsson, H. Jonasson, A. Orini, and R. Grampa, "The Italy-Greece HVDC Link," in *Cigré Devision 14-116*, Paris, France, 2002.

[73] M. Imhof, A. Fuchs, G. Andersson, and M. Morari, "Voltage Stability Control using VSC-HVDC Links and Model Predictive Control," in *XIII Symposium of Specialists in Electric Operational and Expension Planning, XIII SEPOPE*, Foz do Iguassu, Brazil, 2014.

[74] S. Larsson and A. Danell, "The black-out in southern Sweden and eastern Denmark, September 23, 2003," in *2006 IEEE PES Power Systems Conference and Exposition, PSCE 2006 - Proceedings*, 2006, pp. 309–313.

[75] T. Van Cutsem and C. D. Vournas, *Voltage Stability of Electrical Power Systems*. Kluwer Academic Publischer, 1998.

[76] ——, "Emergency Voltage Stability Controls: an Overview," *2007 IEEE Power Engineering Society General Meeting*, pp. 1–10, Jun. 2007.

[77] D. Popović, I. A. Hiskens, and D. J. Hill, "Investigations of load-tap changer interaction," *International Journal of Electrical Power and Energy Systems*, vol. 18, no. 2, pp. 81–97, 1996.

[78] M. Larrson, "Coordinated Voltage Control in Electric Power Systems," PhD Thesis, Lund University, 2000.

[79] M. Larsson, D. J. Hill, and G. Olsson, "Emergency voltage control using search and predictive control," *International Journal of Electrical Power & Energy Systems*, vol. 24, no. 2, pp. 121–130, Feb. 2002.

[80] "IEEE Recommended Practice for Excitation System Models for Power System Stability Studies," *IEEE Std 421.5-1992*, p. 0_1, 1992.

[81] D. Hill, "Nonlinear dynamic load models with recovery for voltage stability studies," *IEEE Transactions on Power Systems*, vol. 8, no. 1, pp. 166–176, 1993.

[82] "ETNSO-E Network Code for Requirements for Grid Connection Applicable to all Generators," entso-e, Brussels, Tech. Rep., 2013. [Online]. Available: https://www.entsoe.eu/major-projects/network-code-development/requirements-for-generators/Pages/default.aspx

[83] "Gurobi Optimizer 5.6," 2013. [Online]. Available: www.gurobi.com

[84] T. Van Cutsem and L. Papangellis, "Description , Modeling and Simulation Results of a Test System for Voltage Stability Analysis," University of Liège, Liège, Belgium, Tech. Rep. November, 2013.

[85] M. Imhof and G. Andersson, "Power System Stability Control using Voltage Source Converter Based HVDC in Power Systems with a High Penetration of Renewables," in *18th Power Systems Computation Conference, PSCC*, Wroclaw, Poland, 2014.

[86] D. Böhme, W. Dürrschmidt, and M. van Mark, "Erneuerbare Energien in Zahlen - Nationale und internationale Entwicklung," Bundesministerium für Umwelt, Naturschutz und Reaktorsicherheit (BMU), Berlin, Germany, Tech. Rep., 2012.

[87] M. Reichmuth, L. Kyriakos, G. Schröder, A. Scheuermann, A. Schiffler, and A. Weber, "Endbericht: Mittelfristprognose zur deutschlandweiten Stromerzeugung aus regenerativen Kraftwerken bis 2016 - Prognose der Stromeinspeisung und der Vergütung im," Leipziger Institut für Energie GmbH, Leipzig, Germany, Tech. Rep., 2011.

[88] "Erneuerbare Energien in Zahlen Nationale und internationale Entwicklungen im Jahr 2013," Bundesministerium für Wirtschaft und Energie (BMWi), Berlin, Germany, Tech. Rep., 2013.

[89] REN21, "Renewables 2012 Global Status Report," 2012. [Online]. Available: www.ren21.net

[90] H. D. Mathur, L. B. F. Leite, H. Siguerdidjane, and Y. K. Bhateshvar, "Study of impact of wind power penetration on frequency stabilization in multi-area power system," *2013 8Th International Symposium on Advanced Topics in Electrical Engineering (Atee)*, pp. 1–6, May 2013.

[91] F. M. Gonzalez-Longatt, "Effects of the synthetic inertia from wind power on the total system inertia: simulation study," *2012 2nd International Symposium On Environment Friendly Energies And Applications*, pp. 389–395, Jun. 2012.

[92] "Generic models and model validation for wind and solar pv generation; technical update," EPRI, Palo Alto, CA, Tech. Rep., 2011.

[93] A. Pollet and B. Verhagen, "Electricity interconnection project between Belgium and Germany: Authorisation process begins," 2013. [Online]. Available: www.eliagroup.eu

[94] P. Fairley, "Germany Takes the Lead in HVDC," 2013. [Online]. Available: http://spectrum.ieee.org/energy/renewables/germany-takes-the-lead-in-hvdc

[95] M. Imhof, O. Valgaev, and G. Andersson, "Controlled Islanding Using VSC-HVDC To Minimize Load Shedding," in *IEEE PowerTech 2015*, Eindhoven, The Netherlands, 2015.

[96] G. Beck, D. Povh, and D. Retzmann, "Global Blackouts - Lessons Learned," *Power-Gen Europe*, vol. 28, p. 30, 2005.

[97] P. Pourbeik, P. Kundur, and C. Taylor, "The anatomy of a power grid blackout - Root causes and dynamics of recent major blackouts," *IEEE Power and Energy Magazine*, vol. 4, no. 5, pp. 22–29, Sep. 2006.

[98] H. Li, G. W. Rosenwald, J. Jung, and C.-C. Liu, "Strategic Power Infrastructure Defense," *Proceedings of the IEEE*, vol. 93, no. 5, pp. 918–933, May 2005.

[99] H. You, V. Vittal, and X. Wang, "Slow Coherency-Based Islanding," *IEEE Transactions on Power Systems*, vol. 19, no. 1, pp. 483–491, Feb. 2004.

[100] J. H. Chow, *Lecture Notes in Control and Information Sciences Time-Scale Modeling of Dynamic Networks with Applications to Power Systems*, A. V. Balakrishnan and M. Thoma, Eds. Berlin, Germany: Springer-Verlag, 1982.

[101] K. Sun, D.-Z. Zheng, and Q. Lu, "A Simulation Study of OBDD-Based Proper Splitting Strategies for Power Systems Under Consideration of Transient Stability," *IEEE Transactions on Power Systems*, vol. 20, no. 1, pp. 389–399, Feb. 2005.

[102] A. Peiravi and R. Ildarabadi, "A fast algorithm for intentional islanding of power systems using the multilevel kernel k-means approach," *Journal of Applied Sciences*, vol. 9, no. 12, pp. 2247–2255, 2009.

[103] C. Wang, B. Zhang, J. Shu, P. Li, and Z. Bo, "A fast method for power system splitting boundary searching," *2009 IEEE Power & Energy Society General Meeting*, pp. 1–8, Jul. 2009.

[104] S. Najafi, "Evaluation of interconnected power systems controlled islanding," in *2009 IEEE Bucharest PowerTech*. IEEE, Jun. 2009, pp. 1–8.

[105] S. Koch, S. Chatzivasileiadis, M. Vrakopoulou, and G. Andersson, "Mitigation of cascading failures by real-time controlled islanding and graceful load shedding," in *2010 IREP Symposium Bulk Power System Dynamics and Control - VIII (IREP)*. IEEE, Aug. 2010, pp. 1–19.

[106] "ALEGrO - The first direct electricity interconnetion between Belgium and Germany," 2014. [Online]. Available: www.elia.be/alegro

[107] O. Valgaev, "Controlled Islanding with VSC-HVDC Links," Master Thesis, ETH Zurich, 2014.

[108] E. W. Dijkstra, "A Note on Two Problems in Connexion with Graphs," *Numerische Mathematik*, vol. 1, no. 1, pp. 269–271, 1959.

[109] M. A. Pai, *Energy Function Analysis for Power System Stability*, T. A. Lipo, Ed. Boston, MA: Springer US, 1989.

[110] C. M. Bishop, *Pattern recognition and machine learning*. New York: Springer, 2009.

[111] Entso-e, "Continental Europe Operational Handbook," european network of transmission system operators for electricity, Tech. Rep., 2010.

[112] BCP Busarello + Cott + Partner AG, "Neplan 5.5.3," 2014. [Online]. Available: www.neplan.ch

[113] "Final Report - System Disturbance on 4 November 2006," UCTE, Brussels, Tech. Rep., 2007. [Online]. Available: https://www.entsoe.eu/news-events/former-associations/ucte/other-reports/Pages/default.aspx

[114] T. H. Kim and T. Sugie, "Robust decentralized MPC algorithm for a class of dynamically interconnected constrained systems," in *Proceedings of the 44th IEEE Conference on Decision and Control, and the European Control Conference, CDC-ECC '05*, vol. 2005, Seville, Spain, 2005, pp. 290–295.

Curriculum Vitae

2009 - 2015	Assistant at the Power Systems Laboratory, ETH Zurich, Switzerland; PhD Thesis under the supervision of Prof. Dr. Göran Andersson
Feb - June 2014	Academic visit to Prof. Dr. Ian Hiskens at University of Michigan, USA
2009	Master of Science in Electrical Engineering and Information Technology, ETH Zurich, Switzerland
2008 - 2009	Studies of electrical engineering at ETH Zurich in Zurich, Switzerland
2008	Bachelor of Science in Electrical Engineering and Information Technology, ETH Zurich, Switzerland
2003 - 2008	Studies of electrical engineering at ETH Zurich in Zurich, Switzerland
Jan - Feb 2008	Internship at Levitronix GmbH in Zurich, Switzerland
Sep - Dez 2007	Internship at Electricity Generating Authority of Thailand (EGAT), Bangkok, Thailand
2003	Matura, Kantonsschule Pfäffikon/Nuolen
1998 - 2003	Kantonsschule Pfäffikon/Nuolen in Pfäffikon SZ, Switzerland

2000 - 2001	High School Exchange at Knox Community High School, Knox, IN, USA
1996 - 1998	Secondary school, Bezirksschule Lachen, Switzerland
1991 - 1996	Primary school in Wollerau, Switzerland
1990 - 1991	Primary school in Adliswil, Switzerland
January 13, 1983	Born in Zurich, Switzerland